

MODELING PHOTOLYTIC ADVANCED OXIDATION PROCESSES FOR THE
REMOVAL OF TRACE ORGANIC CONTAMINANTS

by

Tianqi Zhang

Copyright © Tianqi Zhang 2017

A Dissertation Submitted to the Faculty of the

DEPARTMENT OF CHEMICAL AND ENVIRONMENTAL ENGINEERING

In Partial Fulfillment of the Requirements

For the Degree of

DOCTOR OF PHILOSOPHY

In the Graduate College

THE UNIVERSITY OF ARIZONA

2017

THE UNIVERSITY OF ARIZONA
GRADUATE COLLEGE

As members of the Dissertation Committee, we certify that we have read the dissertation prepared by Tianqi Zhang, titled Modeling Photolytic Advanced Oxidation Processes for the Removal of Trace Organic Contaminants and recommend that it be accepted as fulfilling the dissertation requirement for the Degree of Doctor of Philosophy.

_____ Date: 04/11/17
A. Eduardo Sáez

_____ Date: 04/11/17
Robert G. Arnold

_____ Date: 04/11/17
Kimberly Ogden

_____ Date: 04/11/17
Avelino F. Arellano

Final approval and acceptance of this dissertation is contingent upon the candidate's submission of the final copies of the dissertation to the Graduate College.

I hereby certify that I have read this dissertation prepared under my direction and recommend that it be accepted as fulfilling the dissertation requirement.

_____ Date: 04/11/17
Dissertation Director: A. Eduardo Sáez

STATEMENT BY AUTHOR

This dissertation has been submitted in partial fulfillment of the requirements for an advanced degree at the University of Arizona and is deposited in the University Library to be made available to borrowers under rules of the Library.

Brief quotations from this dissertation are allowable without special permission, provided that an accurate acknowledgement of the source is made. Requests for permission for extended quotation from or reproduction of this manuscript in whole or in part may be granted by the head of the major department or the Dean of the Graduate College when in his or her judgment the proposed use of the material is in the interests of scholarship. In all other instances, however, permission must be obtained from the author.

SIGNED: Tianqi Zhang

ACKNOWLEDGEMENTS

I would like to express my deepest appreciation to all the people who have played a positive role to my education during my whole life. I try to remember all these people with a humbling feeling of gratitude, as I approach to finish my doctorate. In this list of people, I would foremost need to include my mother, who has spent majority of her life to mentor, inspire and support her children. I would also like to include my father and sister, who provide me never-ending supports and encouragements to inspire me to study.

I would specially like to thank my advisor Dr. Eduardo Sáez for his invaluable guidance, never-ending supports, and many invaluable opportunities he gave me throughout my entire graduate career. I also would like to thank Dr. Robert Arnold for his guidance, quick smile and many invaluable advices and opportunities he gave me to expend my knowledge and skills. At this point, I would like to say that the luckiest thing I have had during my whole Ph.D. is having Dr. Sáez as my advisor, in the meantime, having Dr. Arnold as my co-advisor. I would also like to thank Dr. Kimberly Ogden and Dr. Avelino Arellano for their support and quick smile.

I am greatly thankful to all my research team for their tireless helps in the lab: Long Cheng, Bingfeng Dong, Itzel Marquez, Fanchao Meng, Yichen Guo, Monem Aldhaif, Matthew Potzler, Luke Avetian, Jeremiah Traeger. I would also thank to Armando Durazo for his tireless supports of instruments training.

Finally, I have special gratitude to my wife, kids and friends. Because of all of you, the years in Tucson are wonderful and the experience in graduate school is full of fun.

DEDICATION

*To my wife Jingmin, whose encouragement over these
years has make this work possible;*

*my children Sarah and Luke, without whom this work can
be done earlier but with much less fun.*

TABLE OF CONTENTS

ABSTRACT	10
1 INTRODUCTION	12
1.1 Water reuse.....	12
1.2 Advanced oxidation processes	13
1.3 Hydrogen peroxide photolysis (UV/H ₂ O ₂)	14
1.4 Sunlight-driven photolysis	16
1.5 Fe-based photocatalysis	16
1.6 Research objectives	18
1.7 Dissertation format	19
2 PRESENT STUDY	22
3 CONCLUSIONS.....	37
APPENDIX A: MODELING THE OXIDATION OF PHENOLIC COMPOUNDS BY HYDROGEN PEROXIDE PHOTOLYSIS	40
Abstract.....	41
Introduction.....	42
Materials and methods	45
Chemicals	45
Experimental procedure	45
Analytics.....	46
Proposed mechanism.....	47
Kinetic model	48
Results and discussion	51
Actinometry. Hydrogen peroxide photolysis	52
<i>p</i> -Cresol and 4-methylcatechol direct photolysis	52
Model predictions: <i>p</i> -cresol degradation.....	52
Model predictions: 4-methylcatechol degradation.....	56
Concluding remarks	56
References	57
Tables	61

Figures.....	63
APPENDIX B: MODELING THE UV/H ₂ O ₂ OXIDATION OF PHENOLIC COMPOUNDS IN A CONTINUOUS-FLOW REACTOR WITH REFLECTIVE WALLS.....	75
Abstract.....	76
Introduction.....	77
Materials and methods	79
Experimental	79
Reactor model	80
Results and discussion	84
Actinometry at 254 nm.....	84
Direct photolysis in monochromatic light.....	84
Dichromatic light experiments	85
Model predictions: significance of reflection.....	86
Concluding remarks	87
Acknowledgments.....	87
References	88
Figures.....	90
APPENDIX C: FATE OF TRACE ORGANICS IN A WASTEWATER EFFLUENT DEPENDENT STREAM.....	101
Abstract.....	102
Introduction.....	103
Materials and methods	107
Chemicals and reagents.....	107
Sample collection and preparation	108
Yeast estrogen screen (YES) bioassay method	111
Gas chromatography–mass spectroscopy.....	113
Liquid chromatography–mass spectrometry	113
Photodegradation of estrogenic activity in secondary effluent	114
Results and discussion	115
Trace organics attenuation in the Santa Cruz River.....	115

In-stream attenuation of estrogenic activity	117
Phototransformation effects	119
Trace organics in monitoring wells along the SCR	121
Trace organics in riverbed sediments.....	122
Estrogenic activity in riverbed sediments	123
Conclusions.....	124
Acknowledgment	125
References.....	126
Tables.....	132
Figures.....	142
APPENDIX D: KINETIC STUDY OF THE PHOTO-FENTON PROCESS.....	153
Abstract.....	154
Introduction.....	155
Materials and methods	157
Chemicals	157
Solution preparation	158
Experimental setup and procedure	158
Analytical	159
Modeling.....	160
Kinetic model	160
Prediction of iron speciation	164
Absorption spectrum calculation.....	165
Results and discussion	165
Conclusions.....	173
References.....	175
Tables.....	179
Figures.....	181
APPENDIX E: EFFECTIVENESS OF ENGINEERED AND NATURAL WASTEWATER TREATMENT PROCESSES FOR THE REMOVAL OF TRACE ORGANICS IN WATER REUSE.....	196
Abstract.....	197

Introduction.....	198
Methods.....	203
TOrC selection criteria.....	203
Physicochemical properties.....	204
Biodegradability predictions.....	205
UV ₂₅₄ photolysis.....	206
Activated carbon adsorption.....	209
Membrane separations.....	211
Sunlight photolysis.....	211
Statistical analysis.....	213
Results and discussion.....	213
BioWin biodegradability predictions.....	214
UV ₂₅₄ direct photolysis.....	216
Advanced oxidation.....	217
Carbon adsorption.....	219
Membrane separations.....	220
Direct sunlight photolysis.....	221
Implication for process design.....	222
Limitations of the analysis.....	223
Conclusions.....	224
References.....	227
Tables.....	232
Figures.....	250
REFERENCES.....	266

ABSTRACT

Advanced oxidation processes (AOPs) are commonly used for the destruction of persistent trace organic contaminants (TOrcs) that survive conventional wastewater treatment processes. Three types of AOPs, UV/H₂O₂, sunlight photolysis and photo-Fenton are experimentally investigated and mathematically quantified to anticipate the fate of TOrcs during oxidation processes, specifically addressing the significant effect of reaction by-products and water matrix on oxidation efficiencies.

Hydrogen peroxide UV photolysis is among the most widely used AOPs for the destruction of TOrcs in waters destined for reuse. Previous kinetic models of UV/H₂O₂ focus on the dynamics of hydroxyl radical production and consumption, as well as the reaction of the target organic with hydroxyl radicals. In this work, we build a predictive kinetic model for the destruction of *p*-cresol by hydrogen peroxide photolysis based on a complete reaction mechanism that includes reactions of intermediates with hydroxyl radicals. The results show that development of a predictive kinetic model to evaluate process performance requires consideration of the complete reaction mechanism, including reactions of intermediates with hydroxyl radicals. Applying the model to an annular flow-through reactor with reflecting walls, the model mathematically demonstrates that the wall reflectivity significantly enhances the rate of conversion of the target, accounting for the UV light reflection from the reacting walls, as well as the hydrodynamics of the annular flow.

Direct and indirect sunlight photolysis is critically important in the breakdown of contaminants in effluent wastewater. The fate of a suite of TOrcs and estrogenic activity

were investigated in an effluent-dependent stream. Some TOrCs, which are not sufficiently attenuated through biodegradation and soil adsorption were destructed obviously with distance of travel in the stream. Independent experiments, conducted in batch reactor with 17 α -ethinylestradiol (EE₂) spiked in effluent showed that attenuation of estrogenic compounds maybe due in part to indirect photolysis caused by formation of reactive species from sunlight absorption. Further investigation was conducted using selective probe compounds to characterize reactive species. And results showed that singlet oxygen generated from excited state of effluent organic matter was responsible for essentially all observed transformations of targets in the effluent in Tucson.

To mathematically quantify the photo-Fenton AOP, a kinetic model is proposed for the photolysis of Fe³⁺ hydroxo complexes at low pH (pH \leq 3.0). The model incorporates elementary reactions of the Fenton-like and UV/H₂O₂ system. Iron speciation and photochemical parameters, including the molar absorptivities of light-absorbing species and the quantum yields of Fe³⁺ and FeOH²⁺ hydrolysis are experimentally validated. However, the predicted, time-dependent Fe²⁺ concentrations during Fe³⁺ photolysis are much lower than measured. The possible missing elements in the model could be (i) quenching of OH radicals by unknown species, or/and (ii) shielding of Fe²⁺ by unknown compounds at the beginning of the process.

1 INTRODUCTION

1.1 Water reuse

Wastewater reclamation is one of the most important potential methods to preserve water resources, especially in arid and semi-arid regions such as the U.S. Southwest. In Tucson, AZ, the need to reuse water has become greatly exacerbated by population growth and drought in the Colorado River system. In particular, wastewater treatment plants in most of Southern Arizona, including the cities of Tucson and Green Valley, utilize aquifer recharge, since natural water bodies are absent. However, conventional wastewater treatment processes are not designed to transform or separate a suite of trace organic contaminants (TOrcs) that are added to wastewater through human use. TOrcs that are unregulated for which there are potential consequences for ecosystems and human health from long-term exposures include pharmaceuticals, personal care products, endocrine disrupting compounds, and other household and personal use organics.

Over the last two decades, focus on the fates of these chemicals during treatment and, subsequently, after discharge to the environment, indicated that removal efficiencies of TOrcs are highly variable and marginally predictable based on TOrc physical and chemical properties and on wastewater treatment parameters. Activated sludge with nitrogen treatment and membrane bioreactor have been pointed out as the most efficient in-plant processes to partially removal TOrcs, but still some compounds survive in conventional treatment trains and are discharged in the secondary effluent (Miège et al. 2009). Advanced oxidation processes (AOPs), activated carbon adsorption and membrane separations are commonly used as effective tertiary treatments for the

destruction or separation of TOrCs, following after primary and secondary clarifier in the conventional treatment plant.

1.2 Advanced oxidation processes

Advanced oxidation processes (AOPs) take advantage of using reactive radicals, primarily but not exclusively hydroxyl radical, which is a powerful and unselective electrophile, to oxidize a wide range of organic contaminants (Glaze et al. 1987). They are categorized in various ways, but mainly depending on the source for the generation of OH radicals, such as photons (UV/H₂O₂, UV/O₃, etc.), chemical catalysis (Fenton, TiO₂/H₂O₂, etc.), electrons (electro-Fenton), ultrasound, and combination of different sources (photo-Fenton, photoelectron-Fenton etc.) (Oturán & Aaron 2014).

Depending on the properties of the waste stream to be treated, different AOPs can be selected to meet the treatment objectives. Moreira et al. (2016) have assessed the treatment efficiencies of six different AOPs to remove pharmaceuticals from municipal wastewater. They found electro-UV/H₂O₂ did not improve trimethoprim decay compared with UV/H₂O₂ because of low accumulation rate of H₂O₂ in electrochemical process, photoelectron-Fenton could be very efficient only at low pH because precipitated iron at neutral pH will screen the light. Tokumura et al. (2016) have compared the matrix effects on removal of pharmaceuticals by three different AOPs, photo-Fenton, TiO₂/UV and O₃/H₂O₂. Besides scavenging effect on OH radical, wastewater matrix inhibits photo-Fenton by light scattering, inhibits TiO₂/UV by light scattering and adsorption on catalytic site, inhibits O₃/H₂O₂ by decreasing mass transfer efficiency from gas phase to

liquid phase, but improves Fenton reaction in photo-Fenton by the additional iron ions present.

1.3 Hydrogen peroxide photolysis (UV/H₂O₂)

The combination of ultraviolet light with hydrogen peroxide (UV/H₂O₂) is a well-established technology and used in full-scale for more than a decade (Kruithof et al., 2007). To better understand UV/H₂O₂ advanced oxidation, many efforts have been made to simulate the process. Various models have been developed and common elements in these models include: (i) the kinetics of radical production from the direct photolysis of hydrogen peroxide, and hydroxyl radical scavenging by hydrogen peroxide and other radicals; (ii) reaction of hydroxyl radicals with the target compound and, although to a lesser extent, (iii) radical scavenging by reaction by-products and intermediates.

Among those first people who made effort to simulate the UV/H₂O₂ process, Glaze et al. (1995) proposed the kinetic model to predict the time-dependent concentration of a halogenated target based on the quasi-steady-state assumption (QSSA) of free radicals. His model contained the most important elementary reactions in hydrogen peroxide photolysis. Peroxide breaking down to hydroxyl radical after absorbing the photon (equation 1) initializes the system of radical reactions. Due to the low absorption coefficient of peroxide in UV range (18.7 M⁻¹cm⁻¹ at 254 nm), in order to be effective, relatively high concentrations of peroxide is used to absorb the maximum amount of light possible. However, excess peroxide slows down the process due to the scavenging effect of hydroxyl radicals (equation 2). Crittenden et al. (1999) modeled UV/H₂O₂ process without reliance on a quasi-steady-state assumption for radical concentrations. Their

work showed that the QSSA tends to under-predict hydroxyl radical concentrations in some cases and therefore the rates of target compound decomposition. Subsequently, the model of Song et al. (2008) accounted for time-dependent radical concentrations, pH changes due to product formation (CO₂ and low molecular weight organic acids), and especially radical scavenging by natural organic matter. More recent modeling efforts of UV/H₂O₂ oxidation have emphasized on the influence of intermediate compounds and by-products over target compound degradation.



Poor absorbance by hydrogen peroxide in the UV range contributes to energy demand in UV/H₂O₂ processes (Glaze et al. 1987). This inefficiency can be remedied by reflecting unabsorbed light into the reactive mixture, as suggested by Navntoft et al. (2008), who used an aluminum reflector in a batch reactor to enhance the efficiency of a solar disinfection process. Based on the light distribution model of Yang et al. (2005), aluminum shows good reflectivity in the UV range (40.0%), followed by stainless steel (28.0%) and copper (4.0%). These authors developed a kinetic model for TO₂C destruction in an annular reactor with a cylindrical reflector by considering the reflector as a second light source. More recently, Li et al. (2012) assessed the impact of UV light reflection on the fluence rate distribution in an annular reactor using a micro-fluorescent silica detector. Results showed that reflection efficiencies for aluminum foil, stainless steel, and black cloth were 80.5%, 26.1%, and 11.1%, respectively.

1.4 Sunlight-driven photolysis

Treatment wetlands have become an attractive option for the removal of TOrCs from municipal wastewater effluents due to their low energy requirements and operational costs (Jasper et al., 2013). As one of the most important processes in the wetland, sunlight photolysis is able to transform many wastewater-derived TOrCs (Andreozzi et al., 2003; Lin and Reinhard, 2005; Fono et al., 2006), via direct and indirect mechanisms. Direct photolysis occurs when a contaminant absorbs sunlight and undergoes a transformation reaction. In indirect photolysis, light energy can activate an intermediate compound(s) existing in effluent wastewater. The activated intermediate then can either react with TOrCs or with an additional intermediate such as molecular oxygen to produce a reactive intermediate which is capable of reacting with TOrCs. Indirect photolysis mechanisms have been studied for decades, and several different reactive intermediates have been proposed involved in TOrCs transformation. Those intermediates include active species from dissolved organic matter (DOM) (Canonica et al., 1995), singlet oxygen (Zepp et al., 1977), hydroxyl radical (Zepp et al., 1987), superoxide radical anion (Blough and Zepp, 1995) and inorganic acid radicals, such as carbonate, nitrate and sulfate radicals (Lam et al., 2003).

1.5 Fe-based photocatalysis

Fenton's reagent is a well-established mechanism using a mixture of H_2O_2 and Fe^{2+} to produce hydroxyl radicals (equation 3) (Fenton, 1894). Since the iron is regenerated from the Fenton-like reaction (equation 4), hydroxyl radicals can be formed continuously by the catalytic behavior of the $\text{Fe}^{3+}/\text{Fe}^{2+}$ couple. However, it has been reported that the Fenton-

like reaction is much slower than the Fenton's reaction (Brillas et al., 2009), which makes the reduction of Fe^{3+} to Fe^{2+} limit the overall rate of radical production.



By introducing UV light into Fenton system (photo-Fenton), hydrogen peroxide is decomposed into hydroxyl radicals (equation 1), in the meantime, Fe^{3+} hydroxy complexes are decomposed into Fe^{2+} and hydroxyl radical (equation 5). The photo-Fenton oxidation process significantly enhances the production efficiency of OH radical, not only because UV/ H_2O_2 and Fenton's reagent are combined, but also because photons assist in the reduction of Fe^{3+} into Fe^{2+} (Nadtochenko and Kiwi, 1998).



Based on the well-established mechanisms of UV/ H_2O_2 and Fenton's reagent, to better understand the photo-Fenton process, the transformation kinetics of Fe^{3+} hydroxy complexes by photolysis has received considerable attention. Machulek et al. (2009) have proposed a kinetic model to investigate the formation of Fe^{2+} during the photolysis of Fe^{3+} in the presence of sulfate and/or chloride ions. They have concluded that present sulfate ion inhibited the formation of Fe^{2+} by photolysis of Fe^{3+} to a greater extent than present chloride ion. Wang and Liu (2014) have developed a model to simulate the kinetic of Fe^{2+} oxidation in irradiated aqueous solution with initial Fe^{3+} present. They addressed the importance of oxidation of Fe^{2+} by the dissolved oxygen in aqueous phase. However, based on previous studies, further investigation is still needed to better understand the mechanisms of Fe^{3+} hydroxy complexes photolysis.

1.6 Research objectives

This dissertation has a general objective to investigate and quantify the mechanisms of different advanced oxidation processes, including UV/H₂O₂ AOP, sunlight photolysis and photo-Fenton AOP to eliminate TOrCs (*p*-cresol, EE₂, etc.), specifically addressing the effect of reaction by-products and water matrix on oxidation efficiencies.

In the UV/H₂O₂ oxidation process, *p*-cresol was selected as an example of a substituted phenolic compound. Specific objectives include: 1) proposing a complete mechanism of *p*-cresol oxidation by hydroxyl radicals, including reactions of intermediates with hydroxyl radicals; 2) developing a kinetic model to verify and predict the oxidation performance of parent compound and the evolution of intermediates in batch reactor; 3) adapting the kinetic model into flow-through reactor with reflective walls to demonstrate the enhancement of reactor performance by wall reflectivity.

In the system of effluent wastewater exposed under sunlight, investigate the contribution of different pathways during the attenuation of TOrCs, especially the ones contribute to estrogenic activity. Possible pathways include direct/indirect photolysis, biodegradation and adsorption. Indirect photolysis can be led by different photosensitizer, such as triplet state dissolve organic matters, singlet oxygen, hydroxyl radicals, superoxide radical anions, and/or inorganic acid radicals, such as carbonate, nitrate and sulfate radicals.

Another objective is using selective probe compounds and quenching agents to examine the role of all potential reactive species during indirect photolysis of TOrCs.

As one of the key elementary reactions in photo-Fenton oxidation process, Fe³⁺ hydroxy complexes photolysis assists the production of Fe³⁺ into Fe²⁺ to guarantee the high

production efficiency of hydroxyl radicals. The objective was using first principles mathematical model to quantify the evolution of Fe^{2+} concentration during exposing Fe^{3+} hydroxyl complexes solution at low pH ($\text{pH} \leq 3.0$) under UV_{254} lamp.

1.7 Dissertation format

The first study presented in this dissertation (Appendix A) describes the modeling of oxidation of phenolic compounds by hydrogen peroxide photolysis. In this work, a comprehensive kinetic model was developed to quantify the oxidation of *p*-cresol by $\text{UV}/\text{H}_2\text{O}_2$ AOP in a batch reactor. The kinetics of *p*-cresol decomposition, as well as the main reaction intermediate (*4*-methylcatechol), were successfully simulated throughout a wide range of operation conditions. My contributions to this paper included conducting all the experiments (except hydrogen peroxide photolysis and *p*-cresol direct photolysis) and analysis, performing and analyzing the simulations, production of all figures and tables and writing of the first draft of the manuscript. This study “Modeling the oxidation of phenolic compounds by hydrogen peroxide photolysis” has been published in *Chemosphere*.

The second study (Appendix B) presents the modeling of $\text{UV}/\text{H}_2\text{O}_2$ oxidation of phenolic compounds in a continuous-flow reactor with reflective walls. In this work, the kinetic model developed in Appendix A was adapted into a pilot-scale flow-through reactor with reflective walls. The model was manipulated to incorporate UV light reflection from the reactor walls. The hydrodynamics of the annular flow was considered in the model. The model accurately predicts the destruction of the target compound (*p*-cresol) in a wide range of experimental conditions. Experimental and theoretical results demonstrate that

the wall reflectivity significantly enhances the rate of conversion of the target. My contributions to this paper included conducting all the experiments and analysis, performing and analyzing the simulations, production of all figures and tables and writing of the first draft of the manuscript. This study “Modeling the UV/H₂O₂ oxidation of phenolic compounds in a continuous-flow reactor with reflective walls” has been submitted to Journal of Hazardous Materials.

The third study (Appendix C) focuses on examining the fate of a suite of TOrCs and estrogenic activity in water and sediments in an effluent-dependent stream in Tucson, Arizona. The results showed that some TOrCs, including contributors to estrogenic activity, were rapidly attenuated with the distance of travel in the river. Independent experiments, conducted by spiking EE₂ in wastewater effluent and exposing under sunlight, showed that attenuation of estrogenic compounds may be due in part to indirect photolysis caused by the formation of organic radicals from sunlight absorption. Taken together, evidence suggests that natural processes can attenuate at least some TOrCs, reducing the potential impacts to ecosystem and human health. My contributions to this paper included conducting independent experiments and partial analysis of independent experiments, and participation in one of the field sampling campaigns. This study “Fate of trace organics in a wastewater effluent dependent stream” has been published in Science of the Total Environment.

The fourth study (Appendix D) presents a kinetic model to simulate the kinetics of the photo-Fenton process. The model includes the photolysis of Fe³⁺ hydroxo complexes, the H₂O₂ photolysis mechanism, as well as Fenton mechanism. A good agreement was

achieved between experimental observation and model prediction initially, however, after few minutes, the predicted Fe^{2+} concentrations were much lower than observations. My contributions to this paper included conducting the experiments and analysis, performing the simulations when trace organic contaminant (*p*-cresol) is present. This study “Kinetic study of the photo-Fenton process” has been submitted to Chemosphere.

The fifth study (Appendix E) reviews and assesses the effectiveness of the TOrCs removal by different engineered and natural wastewater treatment processes, including UV photolysis (direct and indirect), sunlight photolysis, activated carbon adsorption and membrane separation (reverse osmosis/nanofiltration). In this work, fifty-five frequently encountered TOrCs were selected as target compounds. Based on their physicochemical properties, removal efficiencies of TOrCs were calculated under representative process conditions for each treatment process using simulation method in hand. Results lead to determine a high efficient treatment chain for each (type of) TOrCs. My contributions to this paper included: 1) collecting data, performing and analyzing the chemical structural simulation of TOrCs, and production of figures and tables in membrane separations section; 2) collecting data, performing and analyzing the simulation, and production of figures and tables in sunlight photolysis section. This study “Effectiveness of engineered and natural wastewater treatment processes for the removal of trace organics in water reuse” has been published in Journal of Environmental Engineering.

2 PRESENT STUDY

The complete methods, results, and conclusions of this study are presented in the papers appended to this dissertation. The following is a summary of the most important findings.

Appendix A: Modeling the oxidation of phenolic compounds by hydrogen peroxide photolysis

T. Zhang, L. Cheng, L. Ma, F. Meng, R. G. Arnold, A. E. Sáez, 2016. Modeling the oxidation of phenolic compounds by hydrogen peroxide photolysis. *Chemosphere*, 161, 349-357

Rojas et al. (2011) have proposed a kinetic model to simulate the oxidation of phenolic compound (*p*-cresol) by solar-catalyzed UV/H₂O₂. The model contains the kinetics of radical production from the direct photolysis of hydrogen peroxide, hydroxyl radical scavenging by hydrogen peroxide and other radicals and reaction of hydroxyl radicals with the target compound. The model of Rojas et al. (2011) successfully simulated the decomposition of *p*-cresol for a wide range of operating conditions under solar-catalyzed UV/H₂O₂ oxidation, however, overestimated destruction rate of *p*-cresol under the UV₂₅₄/H₂O₂ oxidation using low-pressure lamp as light source.

A full mechanism of *p*-cresol oxidation by hydroxyl radicals was proposed based on literature review. The first step is OH radical addition to the ring to form 4-methylcatechol. Compared with addition to the ring, reaction between OH radical and methyl group is negligible. Then 4-methylcatechol can be oxidized via two steps: the OH

radical attacks the ring forming a 4-methylcatechol semiquinone radical, after which the semiquinone radical converts to 4-methylbenzoquinone in the presence of molecular oxygen. Once 4-methylbenzoquinone is formed, ring tension and oxidizing agents force fission of the ring. The C-C bond in the ring between the carbons attached to oxygen atoms is cleaved, and 3-methyl-muconic acid is one of the fission products. Oxidation of 3-methyl-muconic acid involves the carbon double bonds. Because of the higher acidity of the α -hydrogen adjacent to the double bond, it can be easily abstracted by the OH radical. Low molecular weight organic acids such as lactic and oxalic acid are oxidation products. The abstraction of α -hydrogen next to a -COOH group by OH radical forms additional low-molecular-weight acids such as acetic and formic acids. Eventually, oxalic acid, acetic acid, and formic acid are oxidized by OH radicals to carbon dioxide.

Incorporating the full mechanism proposed for OH-induced oxidation of *p*-cresol with the model of Rojas et al. (2011), the kinetic model accurately predicted the decay curves for *p*-cresol in a series of experiments carried out at different initial concentrations of H₂O₂ and *p*-cresol. As the 1st-step reaction intermediate, 4-methylcatechol was considered to be consumed via direct photolysis and reaction with OH radical in the model. The production of 4-methylcatechol was measured in the experiments, there was good agreement between experimental observation of 4-methylcatechol concentration and model prediction. In addition, the model adequately predicted the trends in hydrogen peroxide consumption, pH drop and total organic carbon change in the solution. A significant drop in pH was observed in 3-h experiment, and the model concluded that the drop of pH was due to the formation of organic acids.

In conclusion, the success in the simulation of *p*-cresol destruction by hydrogen peroxide photolysis indicates that the full reaction mechanism needs to be considered to evaluate process performance. In particular, reaction intermediates, especially those formed before ring cleavage, play an important role in the quenching of hydroxyl radicals and, consequently, those compounds must be considered in kinetic models of AOP degradation of phenolic compounds.

Appendix B: Modeling the UV/H₂O₂ oxidation of phenolic compounds in a continuous-flow reactor with reflective walls

T. Zhang, R. G. Arnold, G. Diefenthal, A. E. Sáez, 2017. Modeling the UV/H₂O₂ oxidation of phenolic compounds in a continuous-flow reactor with reflective walls. *Journal of Hazardous Materials*, submitted.

(This paper has been submitted to “Journal of Hazardous Materials”)

In this work, a novel flow-through UV reactor equipped with a concentric lamp and a reflective pipe surface was used to investigate the destruction of *p*-cresol during hydrogen peroxide photolysis. Two UV lamps were used in the experiments. A 254-nm monochromatic lamp and a dichromatic lamp that emits light at 185 and 254 nm. The kinetic model developed in Appendix A was applied to simulate the oxidation process. Furthermore, the hydrodynamics of the annular flow and UV light reflection from the reactive walls are incorporated in the model.

Since all experiments were conducted in the laminar flow regime, the simulation results based on ideal plug flow assumption were corrected. The velocity profile in the annular region of the reactor for a given volumetric flow rate (Q , m³s⁻¹) was obtained by solving the Navier-Stokes equations. Residence time distribution functions ($E_{(t)}$) was generated numerically from the velocity profile as a function of volumetric flow rate. Then, the average residence time and the species concentrations at the reactor exit were corrected using residence time distribution functions.

In the model, the inside of the outer cylinder was held to be a perfect reflector of 254-nm light. Nevertheless, some of the reflected light was lost as it returned to the concentric lamp. To model this behavior, we introduced a parameter, β , that represented the fraction of reflected light that was lost at the point it reached the lamp.

Lamp fluence rates were determined by fitting the model to experiments using low transmittance solutions to eliminate the effect of the reflecting walls. Initial concentrations $[p\text{-cresol}]_0 = 400 \mu\text{M}$ and $[\text{H}_2\text{O}_2]_0 = 50 \text{ mM}$ yield transmittances lower than 5% for one light pass through the annulus, including reflection. The fluence rate of dichromatic lamp at UV₂₅₄ was initially determined by neglecting the effect of UV₁₈₅. And it was confirmed later that UV₁₈₅ is negligible with the presence of high concentration of hydrogen peroxide.

To verify the effectiveness of the reflective walls, a group of experiments using high transmittance solutions (> 90%) was conducted under monochromatic lamp.

Experimental were fitted by $\beta = 0.15$. The quantum yield of *p*-cresol at UV₂₅₄ was also calculated by fitting the kinetic model to experimental data using the quantified fluence rate of monochromatic lamp and light decay parameter.

The fluence rate of the dichromatic lamp at 185 nm is significant. This leads to produce hydroxyl radicals by the photolysis of water. The fluence rate of the dichromatic lamp at 185 nm was determined by fitting the kinetic model to the data representing *p*-cresol degradation at two initial concentrations.

The calibrated kinetic model was used to predict the degradation of *p*-cresol via hydrogen peroxide photolysis in the low pressure UV reactor under both lamps. Experiments were

designed to achieve a wide range of one-pass (lamp to wall) light transmittance (32.3% to 93.8%) at 254 nm based on changes in initial concentrations of *p*-cresol and H₂O₂. The kinetic model accurately simulates *p*-cresol degradation over the entire range of independent variables examined.

In conclusion, there are undoubtedly cases in which the application of a reflective coating on UV reactor walls can enhance AOP reactor performance or reduce reactor size/energy intensity necessary to satisfy treatment targets.

Appendix C: Fate of trace organics in a wastewater effluent dependent stream

B. Dong, A. Kahl, L. Cheng, H. Vo, S. Ruehl, T. Zhang, S. Snyder, A. E. Sáez, D.

Quanrud, R. G. Arnold, 2015. Fate of trace organics in a wastewater effluent dependent stream. *Science of the Total Environment*, 518-519, 479-490

This study examined the fate of a suite of TOrCs and estrogenic activity in water and sediments in an effluent-dependent stream in Tucson, Arizona. Sampling campaigns were performed during 2011 to 2013 along the Lower Santa Cruz River (SCR), where TOrCs and estrogenic activity were measured in aqueous (surface) and solid (riverbed sediment) phases.

In the aqueous samples, a suite of twelve dissolved TOrCs was measured over the same (37-km long) reach of the SCR during three sampling campaigns in 2011, while *p*-nonylphenol (NP) and *p*-octylphenol (OP) were measured separately during a February 2013 sampling event. Tonalide, fluoxetine, iopromide, sucralose, PFOS, NP, and OP were attenuated during surface transport along the 37-km studied reach of the river. Carbamazepine, DEET, sulfamethoxazole, TCEP, trimethoprim, and primidone were conserved. Candidate mechanisms for TOrCs attenuation in the river include biodegradation, photolysis, and sorption on bottom sediments or suspended solids. In the riverbed sediments samples, fourteen TOrCs were detected. Only five of the fourteen compounds found in sediments were also detected in the liquid-phase sampling campaign. Riverbed concentrations of TOrCs generally decreased with distance. Both NP and OP were present in water and sediments. The result suggested that sorption may play

an important role in the fate of alkylphenols in the river due to their relatively high hydrophobicity.

Estrogenic activity was measured in the SCR during sampling campaigns to indirectly establish probable attenuation mechanisms. The measured estrogenic activity in Roger Road Wastewater Reclamation Plant (RRWTP) effluent (starting point for sampling campaigns) was almost two orders of magnitude higher than levels that feminize continuously exposed fathead minnows (Lange et al., 2001). Just 1.50 km below the RRWTP outfall, estrogenic activity was ~20-25% of measured levels in the RRWTP effluent. Despite the rapid attenuation of estrogenic activity, measured values exceeded concentrations necessary to disrupt sexual differentiation and reproduction in continuously exposed organisms over a distance of ~ 10 km below the outfall. Beyond 11 km downstream from the RRWTP, estrogenic activity fell below the detection limit, estimated as $1.5 \times 10^{-13}\text{M}$ (equivalent concentration of EE₂). Extractable estrogenic activities in the top (0-2.5 cm) and deeper (10.2-12.7 cm) sediment strata were measured during each sampling campaign. The level of estrogenic activity in the top layer sediment at the sampling site 11 km downstream of the RRWTP outfall was ~5 times higher than the level in the lower sediment layer. At the extreme downstream sampling site (37 km below RRWTP), extractable estrogenic activity in the lower sediment layer was ~2 times that of the surface layer, indicating that estrogenic compounds were not degraded completely in the stream or, alternatively, that some estrogenic compounds adsorbed to sediments closer to the outfalls and were redistributed with distance and depth in river sediments during storm events.

To establish the role of sunlight photolysis on the attenuation of estrogenic compounds, independent experiments were conducted by exposing wastewater effluent and 0.32 nM EE₂ spiked wastewater effluent under sunlight. The estrogenic activities in both reactors decreased below detection limit after 2 h period of exposure, which indicated the attenuation of estrogenic compounds was due, at least in part, to indirect photolysis caused by formation of reactive species from sunlight absorption.

The results of this work show that some TOrCs, including biodegradable compounds and those that contribute to estrogenic activity, are rapidly attenuated with distance of travel in the Santa Cruz River. Independent experiments indicate that the attenuation of estrogenic compounds is due, at least in part, to indirect sunlight photolysis. TOrCs that survive percolation to ground water generally have in common low biodegradation probabilities and low octanol–water distribution ratios. The resuspension and transport of sediments play an important role in the fate of TOrCs in rivers impacted by wastewater treatment.

Appendix D: Kinetic study of the photo-Fenton process

L. Cheng, T. Zhang, R. G. Arnold, A. E. Sáez, 2017. Kinetic study of the photo-Fenton process. *Chemosphere*, submitted.

(This paper has been submitted to “Chemosphere”)

Rojas et al. (2010) proposed a kinetic model which can successfully simulate Fenton-like oxidation process. The kinetic model in Appendix A is able to predict the kinetics of hydrogen peroxide photolysis under UV₂₅₄. In this work, a kinetic model was proposed to anticipate the kinetics of photo-Fenton-like oxidation process. Accounting for Fenton-like reactions and direct photolysis of H₂O₂ formed by radical recombination, the model contains the photolysis of Fe³⁺ and Fe³⁺ hydroxo complexes which are able to decompose to Fe²⁺ and hydroxyl radicals under UV₂₅₄. The model was tested in a wide range of experimental conditions.

Firstly, the quantum yields of Fe³⁺ and Fe(OH)²⁺ were verified by adding excess *p*-cresol to quench OH radicals and then minimize the oxidation of Fe²⁺ to Fe³⁺. The experiments were conducted by exposing Fe(ClO₄)₃ solutions under UV₂₅₄ at pH 2.0 and 3.0. In relatively short period (30s), the accumulations of Fe²⁺ were well predicted by the kinetic model at both pHs, which confirmed the reported quantum yield values of Fe³⁺ and Fe(OH)²⁺ (Lee and Yoon, 2004). However, after 30s irradiation, a small deviation started between experimentally observed Fe²⁺ concentration and predicted one.

To better understand the kinetics of Fe³⁺ and Fe³⁺ hydroxo complexes photolysis, a series of experiments were conducted by exposing Fe(ClO₄)₃ solutions to UV light at different

pH (2.0 to 3.0) and different initial $\text{Fe}(\text{ClO}_4)_3$ concentrations (0.025 mM to 0.1 mM) in the absence of *p*-cresol. Higher Fe^{2+} accumulation rates were observed with higher $\text{Fe}(\text{ClO}_4)_3$ concentrations, as well as higher pH. The trends of accumulation rates of Fe^{2+} under either different pH or different initial $\text{Fe}(\text{ClO}_4)_3$ concentrations were predicted by the kinetic model; however, the model underestimated the conversion rate of Fe^{3+} to Fe^{2+} under all experimental conditions. The comparison of Fe^{2+} accumulation rates ($d\text{Fe}^{2+}/dt$) versus irradiation time between experimental observation and model prediction suggested that the failure of the model was due to inaccuracies at the start of the process. Based on the proposed mechanisms, six elementary reactions produce Fe^{2+} , and four oxidize Fe^{2+} . By comparing the contribution of each elementary reaction under the operation conditions, the formation of Fe^{2+} is dominated by Fe^{3+} and FeOH^{2+} photolysis and the consumption of Fe^{2+} is dominated by the reaction between Fe^{2+} and OH radicals. Therefore, the possible explanations for the discrepancies of model prediction include (i) something in the reactor quenches OH radicals at the start of the experiment, or/and (ii) Fe^{2+} was somehow “shielded”, inhibiting its oxidation by OH radicals. The kinetic model was further tested by conducting $\text{Fe}(\text{ClO}_4)_3$ photolysis experiments with various initial concentrations of H_2O_2 , and experiment of photolysis of 1:1 mixed $\text{Fe}^{2+}/\text{Fe}^{3+}$ solutions that were spiked with H_2O_2 twice at different times during the experiment. The model was able to anticipate trends of evolution of Fe^{2+} for the experiments with H_2O_2 present, but further evidence/improvement is still needed to fully describe the mechanism of $\text{Fe}(\text{ClO}_4)_3$ photolysis.

Appendix E: Effectiveness of engineered and natural wastewater treatment processes for the removal of trace organics in water reuse

L. Cheng, T. Zhang, H. Vo, D. Diaz, D. Quanrud, R. G. Arnold, A. E. Sáez, 2017.

Effectiveness of engineered and natural wastewater treatment processes for the removal of trace organics in water reuse. *Journal of Environmental Engineering*, 0733-9372.

In this work, the physicochemical and biological determinants of removal efficiencies in a variety of engineered and natural processes were explored for 55 frequently encountered trace organic compounds (TOrcs) in wastewater. Weak correlations between field observations and predicted TOrc biodegradabilities led to adoption of an empirical approach to prediction of compound removal during conventional wastewater treatment. The efficiencies of TOrc removals by UV photolysis (direct and indirect), activated carbon adsorption, membrane separation (reverse osmosis/nanofiltration) and sunlight photolysis were determined under representative process conditions.

Estimated times required for primary metabolic transformations for each TOrc on a semi-quantitative scale were predicted by BioWin4. Predicted transformation times were ranked and divided into five groups, ranging in duration from days to months for the 55 selected TOrcs. The wide range of biodegradability indices of the 55 TOrcs considered reflects the diversity present among their molecular structures. In particular, polycyclic aromatic hydrocarbons (PAHs) were less biodegradable than other groups. Predicted hormone biodegradabilities were generally lower than those of pesticides, herbicides and pharmaceuticals.

Direct UV₂₅₄ photolysis was calculated by applying literature reported quantum yield and molar absorptivity for each TOrC individually. Matrix effects (light shading effect only) were considered by comparing the calculation results using clean matrix (Milli-Q water) and wastewater effluent. The predicted results indicated that regardless of matrix, TOrCs removal rate by UV₂₅₄ photolysis directly depends on the product between quantum yield and molar absorptivity coefficient of the compound. Combining with hydrogen peroxide photolysis mechanism, the oxidation of TOrCs by UV/H₂O₂ AOP was predicted. With 5 ppm initial H₂O₂ concentration, all TOrCs were efficiently removed (> 80%, but mostly close to 100%) in clean water matrix with 10 nM initial concentration. In the wastewater effluent matrix, accounting for both shading effect and scavenging effect of OH radicals by matrix organics, TOrCs removal efficiencies were only marginally improved by the addition of H₂O₂ compared with direct photolysis.

The bed volumes fed (BVF) to breakthrough for 43 TOrCs with available Freundlich parameters and related physicochemical information were calculated using AdDesignSTM to investigate the treatment efficiency of carbon adsorption. The water matrices used were either natural organic matter (NOM) free water or Rhine River (Germany) water, which contains a significant anthropogenic input. In the presence of fouling by NOM, calculated BVFs ranged from approximately 10² to 10⁶. Values for diclofenac and caffeine were > 5 × 10⁶. Conversely, estriol was predicted to break through first at ~ 200 bed volumes. As expected, fouling of the activated carbon by NOM in the matrix inhibits TOrC separation, which was particularly noted for pesticides and herbicides. The pore

and surface diffusion model from AdDesignS™ reduces the Freundlich capacity parameter to reflect the fouling process.

In membrane separations, the TOrCs rejection at 50% NaCl rejection was determined from linear regression lines based on literature reported data of TOrC rejection vs. NaCl rejection. To determine whether rejection data were influenced by TOrC molecular dimensions or hydrophobicity, compound-specific rejections were examined as a function of $\log D_{ow}$, molecule length and thickness for each compound. Only TOrC thickness proved to be a reasonable predictor of compound removal. Specifically, molecules with thickness < 0.25 nm penetrate RO/NF membranes under conditions that result in 50% (and presumably higher) NaCl penetration, molecules with thicknesses > 0.3 nm are generally well removed ($> 75\%$) under the same conditions.

Direct sunlight photolysis of TOrCs was investigated and analyzed using the same approach as direct UV_{254} photolysis, but integrating the photolyzing effect from 300 nm to 400 nm wavelength. Uniform quantum efficiency was assumed in the whole range of wavelength. Shading effect of the effluent matrix was also calculated and compared to clean matrix. The predicted results showed acetaminophen, norfloxacin and sulfamethoxazole were exceptionally sensitive to sunlight.

The simulation results for each individual tertiary treatment process led to heuristic guidelines for the selection of sequenced treatment processes for TOrCs management. However, due to lack of good understanding of matrix effects as well as degradation mechanism of TOrCs during photon-driven tertiary treatment—e.g. UV-based advanced oxidation and sunlight photolysis, removals were simulated without considering the

potential impact of by-products and interactions among matrix organics with targets and by-products. Even under these conditions, the effects of radical scavenging and light shading by organic matrix compounds have an important impact on TOrC treatment. Quantification of matrix interferences both in terms of physical effects (such as light absorption) and chemical effects (degradation mechanisms, radical scavenging, production of reactive oxygen species) remains a challenging key point in the evaluation of treatment technologies.

3 CONCLUSIONS

Water reuse requires tertiary treatment processes, such as advanced oxidation processes, carbon adsorption or membrane separations to remove trace organic compounds that persist after conventional wastewater treatment. Mathematical assessment of individual tertiary treatment process using simulation tools indicates the treatment efficiency is sensitive to TOrC physicochemical properties and water matrix effects. The anticipated removal efficiency of TOrCs by individual treatment calculated based on compound physicochemical properties has led to heuristic guidelines for the selection of sequenced treatment processes for TOrCs management. However, matrix interferences and by-product effects (in AOPs) during tertiary treatment have to be addressed. Radical scavenging and light shading by organic matrix compounds, as well as radical scavenging by reaction intermediates diminish the removal efficiency of TOrCs during photocatalytic AOPs. On the other hand, reactive species formed after exposing the effluent organic matter to solar light sometimes assist the destruction of TOrCs. The organic matrix compounds may lead to fouling on membranes and activated carbon, which dramatically diminishes the performance of these processes on TOrCs removal.

In this study, three types of advanced oxidation processes, including UV/H₂O₂, sunlight photolysis and photo-Fenton were quantified to anticipate the fate of TOrCs, specifically addressing the significant effect of reaction by-products and effluent wastewater matrix on treatment efficiencies.

Kinetic model developed for the simulation of oxidation of phenolic compound by UV/H₂O₂ AOP in a batch reactor throughout a wide range of operation conditions proved

the important role of reaction by-products in hydroxyl radical quenching and light distribution. During the oxidation process, the reaction intermediates formed before ring cleavage were especially important, which indicated the by-products with a high reaction rate with hydroxyl radicals ($>10^9 \text{ M}^{-1} \text{ s}^{-1}$) have to be considered in the modeling of the oxidation process. The mechanism proposed for *p*-cresol oxidation by hydroxyl radicals also highlighted the importance of distinguishing the dominant reaction products on the success of the simulation. The same approach can be applied to develop the full mechanisms of the oxidation of other groups of contaminants by hydroxyl radicals.

Hydrogen peroxide is a poor UV absorber, which makes UV/H₂O₂ not a very energy efficient treatment process. A novel annular UV reactor with reflective walls to increase the UV path length, thus improving efficiency of light absorption, was studied. The UV/H₂O₂ kinetic model for phenolic compounds demonstrated that the reflective wall was significant in enhancing the conversion rate of the target. For the particular reactor tested, this study found that 15% of the reflected light was lost to the lamp. The effects of reactor configuration and lamp placement needs to be assessed in the future.

In the system of effluent wastewater exposed under sunlight, the results show that some TOxCs, especially those that contribute to estrogenic activity are rapidly attenuated during effluent transports along the river. Independent experiments demonstrated that the attenuation of estrogenic compounds was due, at least in part, to indirect photolysis caused by the formation of reactive species from sunlight absorption. The reactive species sensitized by effluent organic matter were investigated using selective probe compounds (furfuryl alcohol, trimethylphenol and *p*-cresol) and quenching agents

(isopropyl alcohol and sodium azide). The results indicated that singlet oxygen was responsible for essentially all observed transformations of TOrCs (results are not included in this work). Identification of photosensitizer(s) and functional wavelengths of sunlight needs to be investigated to better understand the full mechanism of sunlight-assist indirect photolysis.

The photo-Fenton oxidation process significantly enhances the production efficiency of OH radicals with respect to the original Fenton's process. The proposed kinetic model was used to describe the photolysis of Fe^{3+} hydroxo complexes then to simulate photo-Fenton AOP. The model was verified in the absence of trace organics. When Fenton's reagent dominated, the model was able to anticipate the evolution of iron species and the decomposition of H_2O_2 with initial Fe^{2+} and H_2O_2 present. But model failed when the photolysis of ferric hydroxo complexes dominated. Model sensitivity test indicated that the possible missing element could be (i) something unknown in the reactor quenched OH radicals at the start of the experiment, or/and (ii) Fe^{2+} was somehow "shielded" in the beginning of the process. Future investigations need to focus on these possible explanations.

APPENDIX A
MODELING THE OXIDATION OF PHENOLIC COMPOUNDS BY HYDROGEN
PEROXIDE PHOTOLYSIS

(published, Chemosphere, 161 (2016) 349-357)

Tianqi Zhang, Long Cheng, Lin Ma, Fanchao Meng, Robert G. Arnold, and A. Eduardo Sáez

Department of Chemical and Environmental Engineering, University of Arizona, Tucson,
Arizona 85721, United States

Abstract

Hydrogen peroxide UV photolysis is among the most widely used advanced oxidation processes (AOPs) for the destruction of trace organics in waters destined for reuse. Previous kinetic models of hydrogen peroxide photolysis focus on the dynamics of hydroxyl radical production and consumption, as well as the reaction of the target organic with hydroxyl radicals. However, the rate of target destruction may also be affected by radical scavenging by reaction products. In this work, we build a predictive kinetic model for the destruction of *p*-cresol by hydrogen peroxide photolysis based on a complete reaction mechanism that includes reactions of intermediates with hydroxyl radicals. The results show that development of a predictive kinetic model to evaluate process performance requires consideration of the complete reaction mechanism, including reactions of intermediates with hydroxyl radicals.

Keywords

Advanced oxidation processes; kinetic model; phenolic compounds; radical reactions

Introduction

Alkylphenol ethoxylates are non-ionic surfactants commonly used to formulate products such as detergents, paints, dispersing agents, wetting products, pesticides, and lubricants (Nagarnaik and Boulanger, 2011). These compounds are converted into alkylphenols in bioreactors used in wastewater treatment (Ahel *et al.*, 1996), leading to their presence in surface waters (Scullion *et al.*, 1996; Dong *et al.*, 2015), groundwater (Swartz *et al.*, 2006), municipal and industrial wastewater (Loyo-Rosales *et al.*, 2007), aquatic sediments and marine shellfish (Lye *et al.*, 1999). The most commonly detected metabolite, *p*-nonylphenol, induces breast tumor cell proliferation (Soto *et al.*, 1991) and is a recognized endocrine disrupter (Lee and Lee, 1996). Therefore, the fates of *p*-nonylphenol and other phenolic compounds during wastewater treatment and following the release of treated wastewater into the environment is of practical importance.

Advanced oxidation processes (AOPs) are effective treatments for phenolic compounds due to their high rates of reaction with hydroxyl radicals (second-order rate constants in the range 10^9 - 10^{10} M⁻¹s⁻¹; Buxton *et al.*, 1988). The UV photolysis of hydrogen peroxide (UV/H₂O₂) is among the most widely used AOPs in water treatment. Various models have been developed to simulate process kinetics. Common elements in these models include: (i) the kinetics of radical production from the direct photolysis of hydrogen peroxide, and hydroxyl radical scavenging by hydrogen peroxide and other radicals; (ii) reaction of hydroxyl radicals with the target compound and, although to a lesser extent, (iii) radical scavenging by reaction byproducts and intermediates (Lay, 1989; Glaze *et al.*,

1995; Liao and Gurol, 1995; Stefan *et al.*, 1996; Crittenden *et al.*, 1999; Murcia *et al.*, 2015; Rojas *et al.*, 2010, 2011).

The first step in the reaction mechanism for radical oxidation of phenolic compounds is OH addition to the ring (Wojnárovits *et al.*, 2002). The position of OH addition is controlled by substitutions on the ring, but *para*- and *ortho*-hydroxylation normally predominate due to the electrophilic nature of the hydroxyl radical (Omura and Matsuura, 1968; Matsuura and Omura, 1974). Further oxidation of the resulting dihydroxy compound occurs via abstraction of a hydrogen atom to form benzoquinones, after which the ring can be cleaved to yield aliphatic acids (Scheck and Frimmel, 1995).

Previous efforts on the kinetic modeling of the UV/H₂O₂ process generally include a complete description of the chemistry behind radical formation, but rarely consider reaction intermediate and by-products. Glaze *et al.* (1995) proposed a kinetic model containing the most important elements of UV/H₂O₂ photolysis to predict the time-dependent concentration of a halogenated target. They used a quasi-steady-state assumption (QSSA) to calculate the time-dependent concentrations of free radicals. Their model did not account for CO₂ evolution/pH change and neglected the role of all radical scavenging species except H₂O₂. Stefan *et al.* (1996) followed a similar approach, but assumed that the target compound (in their case acetone) was transformed to oxalic and formic acids and then to CO₂. Subsequently, Crittenden *et al.* (1999) modeled UV/H₂O₂ process without reliance on a quasi-steady-state assumption for radical concentrations. Their work showed that the QSSA tends to under-predict hydroxyl radical concentrations

in some cases and therefore the rates of target compound decomposition. Furthermore, their model included radical scavenging reactions.

The model of Song et al. (2008) accounted for time-dependent radical concentrations, pH changes due to product formation (CO₂ and low molecular weight acids), and radical scavenging by H₂O₂ and natural organic matter.

More recent modeling efforts of oxidation of phenolic compounds usually include a full formulation of the dynamics of radical formation, but very few or no details of the influence of intermediate compounds and by-products over target compound degradation.

De Luis et al. (2011) presented a model of phenol and cresol degradation during the UV/H₂O₂ process that considered possible reactions of the organic compounds with produced radicals, but without considering intermediate compounds and by-products. A similar approach was followed by Rojas et al. (2010, 2011) to model the UV/H₂O₂ and Fenton's reaction processes. Moreira et al. (2012) developed a phenomenological model to simulate the TiO₂ photocatalysis of phenol, which includes specific details about the reaction mechanism.

In this work, *p*-cresol was selected as an example of a substituted phenolic compound. Even though *p*-cresol itself is not a common trace organic in wastewater effluent, it has chemical structure and reactivity with hydroxyl radicals similar to *p*-nonylphenol, which is a common endocrine disrupter compound widely present in wastewater effluent. A mechanism for radical-dependent UV/photolysis was proposed and calibrated based on time-dependent measurements of *p*-cresol and a number of reaction products/intermediates in a batch reactor. The model accounts for changes in ionic

strength and pH due to reactant conversions. Reactor fluence rate and the *p*-cresol quantum yield during direct photolysis were considered in the kinetic model. The calibrated model was employed to predict the evolution of concentrations of *p*-cresol and reaction intermediates under various experimental conditions.

Materials and methods

Chemicals

All chemicals were obtained from commercial sources and used without further purification, including *p*-cresol (Acros, 99+%), 4-methylcatechol (Acros, 98%), hydrogen peroxide (Acros, 50 wt%), titanium sulfate (Pfaltz&Bauer, 30%), formate (Fluka, 1000 mg/L \pm 4 mg/L), acetate (Fluka, 1000 mg/L \pm 4 mg/L), oxalate (Fluka, 1000 mg/L \pm 4 mg/L), and TOC standard (Fluka, 50 mg/L \pm 2 mg/L). Methanol (Fisher Chemical, HPLC Grade) and acetonitrile (Fisher Chemical, HPLC Grade) were solvents for HPLC analyses. Milli-Q water (resistivity $\geq 18.0 \text{ m}\Omega \text{ cm}^{-1}$) was obtained from a Barnstead NANOpure II system. Glassware was washed and heated overnight at 550 °C prior to use.

Experimental procedure

All experiments were conducted in a cylindrical (14-cm diameter, 950-mL) glass batch reactor, equipped with low pressure (LP) UV lamp, UV fluence meter (Hamamatsu, H8025-254) and magnetic stirrer. Stock solutions of *p*-cresol were prepared one day before use. 4-Methylcatechol stock solutions were prepared a half hour before use in amber glass containers. The UV lamp (43-cm long) was turned on two hours before the experiments. The lamp position was 21 cm above the liquid level in the reactor. A quartz sleeve covered the lamp to cut-off wavelengths below 185 nm. Solution volume was 300

mL in all experiments (liquid depth was 1.95 cm). Experiments were initiated by exposing the reactor to UV light. Experiment duration depended on the initial *p*-cresol concentration but ranged from one to three hours. Samples were analyzed immediately after withdrawal. Dilution was frequently necessary to maintain concentrations within the recommended analytical range. Temperature was maintained at $T = 24.5 \pm 0.5$ °C. The trajectory of solution pH was determined in each experiment.

Analytics

The concentration of *p*-cresol was measured by fluorescence spectrometry (PerkinElmer LS 55). The inner filter effect (IFE) caused by light absorption and reabsorption of light-absorbing compounds was corrected mathematically, accounting for the absorption spectrum of the sample (MacDonald *et al.*, 1997). Solution spectra were measured using a UV-Vis spectrophotometer (Thermo Science, Genesys 10s). Even though the reaction intermediate 4-methylcatechol is produced in concentrations that are comparable in order of magnitude to *p*-cresol, independent measurements showed that its fluorescence intensities were negligible compared to those of *p*-cresol in the relevant range of wavelengths.

Analysis of primary intermediates, particularly 4-methylcatechol, was carried out by HPLC (Agilent Technologies, 1200 Series) with a Polar-RP, 80A column (15 cm × 4.6 mm × 4 μm) (Phenomenex) and UV/VIS detector at 280 nm. Elution solvents were 10% methanol in water (A) and acetonitrile (B), $Q = 0.4$ mL/min. The mobile phase initially consisted of 45% vol. B, linearly ramped to 65% vol. B at 15 min and then restored to the initial condition.

Formate, acetate and oxalate were measured via ion chromatography (Dionex, ICS-5000) equipped with an AS18 column (2×250 mm) (Dionex IonPacTM), an AG18 guard column (2×50 mm) (Dionex IonPacTM), and an AS-DV (Dionex) autosampler. Ions were detected by suppressed conductivity of the eluent using an ASRS-2mm self-regenerating suppressor (Dionex). The eluent (KOH solution; $Q = 0.4$ mL/min) was programmed as follows: 1 mM for 8 min, ramped (linearly) to 30 mM in 20 min, then immediately restored to 1 mM.

Hydrogen peroxide was measured using a modified peroxytitanic (colorimetric) method (Boltz and Holwell, 1978). Absorbance was measured spectrophotometrically (Thermo Science, Genesys 10s) at 407 nm. Samples were diluted to maintain absorbance values within linear limits. TOC was monitored using a Total Organic Carbon analyzer (Shimadzu, TOC-V_{CSH}).

Proposed mechanism

The proposed mechanism of *p*-cresol oxidation by hydroxyl radicals is shown in Figure 1. The first step is OH radical addition to the ring to form 4-methylcatechol (Matsuura and Omura, 1974; Olariu *et al.*, 2002). Two possible pathways (Omura and Matsuura, 1968; Scheck and Frimmel, 1995) are used to explain the hydroxylation. One is the attack of OH radical on the phenolic ring, resulting in the formation of a cyclohexadienyl radical, which is subsequently converted into 4-methylcatechol. The other involves abstraction of a hydrogen atom yielding a phenoxyl radical that can combine with a second OH radical. However, the hydrogen abstraction reaction of a methyl H atom (Wang *et al.*, 1998) is at least one order of magnitude slower than the formation of a cyclohexadienyl radical

(Sehested *et al.*, 1975; Wojnárovits *et al.*, 2002). Further hydroxylation may convert 4-methylcatechol; however, this reaction has negligible yield (Scheck and Frimmel, 1995). Oxidation of 4-methylcatechol to 4-methylbenzoquinone occurs in two steps: the OH radical attacks the ring forming a 4-methylcatechol semiquinone radical (Gohn and Getoff, 1977), after which the semiquinone radical converts to 4-methylbenzoquinone in the presence of molecular oxygen (Davies *et al.*, 1995). Once 4-methylbenzoquinone is formed, ring tension and oxidizing agents force fission of the ring. The C-C bond in the ring between the carbons attached to oxygen atoms is cleaved, and 3-methyl-muconic acid is one of the fission products (Pospisil *et al.*, 1957; Scheck and Frimmel, 1995). Oxidation of 3-methyl-muconic acid involves the carbon double bonds. Because of the higher acidity of the α -hydrogen adjacent to the double bond, it can be easily abstracted by the OH radical (Jin *et al.*, 2010; Huang *et al.*, 2011). Low molecular weight organic acids such as lactic and oxalic acid are oxidation products. The abstraction of α -hydrogen next to a -COOH group by OH radical forms additional low-molecular -weight acids such as acetic and formic acids (Boonrattanakij *et al.*, 2009). Eventually, oxalic acid, acetic acid and formic acid are oxidized by OH radicals to carbon dioxide (Getoff *et al.*, 1971; Leitner and Dore, 1997; Hart, 1951; Sun and Saeys, 2008).

Kinetic model

The proposed kinetic model for the oxidation of p-cresol during UV/H₂O₂ photolysis consists of 36 reactions (Table 1). The UV/H₂O₂ photolysis mechanism, including an initiation step that produces hydroxyl radical ($\cdot\text{OH}$) and propagation steps that scavenge $\cdot\text{OH}$ and produce other active radicals ($\text{O}_2^{\cdot-}$ and $\text{CO}_3^{\cdot-}$), is based on the work of Rojas *et*

al. (2010; 2011) and references therein. Since the reactor was open to the atmosphere, the initial carbon dioxide concentration was assumed to be at equilibrium with atmospheric carbon dioxide. The scavenging effect of inorganic carbon species, bicarbonate and carbonate ions was considered in the model, but calculations showed that their effect was negligible in the range of conditions of the experiments.

The rate of direct photolysis of H_2O_2 is given by

$$R_{R1} = -\Phi_{H_2O_2} f_{H_2O_2} I_0 e^{-2.303A_z} \quad (1)$$

where $\Phi_{H_2O_2}$ (Table 1) is the quantum yield for the photocatalytic decomposition of H_2O_2 , $f_{H_2O_2}$ is the fraction of total light absorbed by H_2O_2 , I_0 is the average fluence rate (in Einsteins per unit time and reactor volume) at the reactor surface and A_z is the total absorbance of the solution as function of depth. In the model, H_2O_2 , PC, 4MC and 4MB are the only important light-absorbing species at 254 nm. Therefore, A_z is given by

$$A_z = (\varepsilon_{H_2O_2}[H_2O_2] + \varepsilon_{PC}[PC] + \varepsilon_{4MC}[4MC] + \varepsilon_{4MB}[4MB])z \quad (2)$$

where $\varepsilon_{H_2O_2}$, ε_{PC} , ε_{4MC} (Table 1) and ε_{4MB} ($2100 \text{ M}^{-1}\text{cm}^{-1}$; Waite, 1976; Jongberg *et al.*, 2011) are molar extinction coefficients for hydrogen peroxide, *p*-cresol, 4-methylcatechol and 4-methylbenzoquinone at 254 nm, respectively, and z is the distance measured downward within the reactive mixture from the top surface. Note that

$$f_{H_2O_2} = \frac{\varepsilon_{H_2O_2} z [H_2O_2]}{A_z} \quad (3)$$

The volume averaging of equation (1) over the batch reactor is, after manipulations,

$$\langle R_{R1} \rangle = -\Phi_{H_2O_2} f_{H_2O_2} I_0 (1 - e^{-2.303A}) \quad (4)$$

where the angular brackets denote volume average, and $A = A_z$ ($z = l$), where l is the depth of the reacting mixture. Other direct photolysis reactions are treated in the same manner.

Radical reactions are generally second-order reactions. For example, the reaction rate for the consumption of *p*-cresol by OH radical is

$$R_{R23} = -k_{23}[PC][\cdot OH] \quad (5)$$

where k_{23} is the second-order rate constant of *p*-cresol reaction with $\cdot OH$ (Table 1).

Acid-base reactions are considered to be at equilibrium. The equilibrium equations are used to relate concentrations of the species involved. For example, for acetic acid,

$$[HA] = \frac{TOT_A \gamma_{\pm 1} [H^+]}{K_{36} + \gamma_{\pm 1} [H^+]} \quad (6)$$

$$\gamma_{\pm 1} [A^-] = \frac{TOT_A K_{36}}{K_{36} + \gamma_{\pm 1} [H^+]} \quad (7)$$

where $TOT_A = [HA] + [A^-]$, K_{36} is equilibrium constant of acetic acid dissociation and $\gamma_{\pm 1}$ is the activity coefficient, which is calculated from the Davies Equation.

Based on the mechanism proposed, the corresponding mole balances of H_2O_2 , *p*-cresol and 4-methylcatechol yield the following system of differential equations:

$$\begin{aligned} \frac{d[H_2O_2]}{dt} = & -\Phi_{H_2O_2} f_{H_2O_2} I_0 (1 - e^{-2.303A}) - k_2 [H_2O_2][\cdot OH] + k_8 [\cdot OH]^2 - \\ & k_{10} [H_2O_2] \gamma_{\pm 1} [O_2^{\cdot -}] + k_{13} [HO_2^{\cdot}]^2 - k_{14} [H_2O_2][HO_2^{\cdot}] - k_{15} [H_2O_2] \gamma_{\pm 1} [CO_3^{\cdot -}] - \\ & k_{18} [H_2O_2] + k_{18r} \gamma_{\pm 1} [HO_2^{\cdot -}] \gamma_{\pm 1} [H^+] \quad (8) \end{aligned}$$

$$\frac{d[PC]}{dt} = -\Phi_{PC} f_{PC} I_0 (1 - e^{-2.303A}) - k_{23} [PC][\cdot OH] \quad (9)$$

$$\frac{d[4MC]}{dt} = -\Phi_{4MC}f_{4MC}I_0(1 - e^{-2.303A}) + k_{23}[PC][\cdot OH] - k_{25}[4MC][\cdot OH] \quad (10)$$

$$[TOC] = [TOC]_0 - [CO_2] + [CO_2]_0 \quad (11)$$

where $[TOC]_0$ and $[CO_2]_0$ are initial TOC and CO_2 molar concentrations. More details of the model formulation, including mole balances of radicals ($\cdot OH$, $HO_2\cdot$, $O_2^{\cdot -}$ and $CO_3^{\cdot -}$) and reaction intermediates (4MB, 3MM, LA^- , OA^- , OA^{2-} , $OA^{\cdot -}$, AA, AA^- and FA^-), plus algebraic equations ($[H_2CO_3]$ as a function of $[TOTCO_3]$ and charge balance) are provided in the supporting information.

The fact that the reactor is well mixed implies that most species concentrations are uniform in the reactor. However, the relatively high reaction rates of radical species suggest that their concentrations are not necessarily uniform. For example, the OH radical production by reaction R1 (Table 1) is not uniform due to the attenuation of light with depth. In the model equations, radical concentrations are volume-averaged concentrations. The formulation is based on the assumption that kinetics that are not linear on radical concentrations (such as in radical/radical reactions like R8, Table 1) can be expressed in terms of volume-averaged radical concentrations. This approximation was explored in detail by Rojas *et al.* (2010).

The final system of equations was solved using the stiff-differential-equations solver ODE15s in MATLAB (based on Gear's method). The relative tolerance was 10^{-8} , whereas the absolute tolerances for concentrations of all species were set four orders of magnitude below their respective values.

Results and discussion

Actinometry. Hydrogen peroxide photolysis

The average fluence rate at the surface of the reactor was determined using H₂O₂ actinometry. Hydrogen peroxide direct decomposition experiments were conducted at various initial concentrations. The kinetic model was applied to calculate the reactor surface average fluence rate by fitting experimental data for H₂O₂ decay. Reactions 1-21 (Table 1) were used in the model formulation. A value of $I_0 = 0.85 \times 10^{-6} \text{Ein L}^{-1}\text{s}^{-1}$ was obtained (Figure 2), which was in agreement with the fluence rate measured by the fluence meter.

***p*-Cresol and 4-methylcatechol direct photolysis**

Quantum yields of *p*-cresol and 4-methylcatechol were determined from direct photolysis experiments for each compound separately. In the experiments, *p*-cresol or 4-methylcatechol solutions were exposed to UV light in the absence of H₂O₂. The quantum yield of each compound was calculated by fitting the kinetic model to data representing compound decay. The solution absorbance for all experiments was measured as a function of time to determine A_z (equation 2). This was necessary in direct photolysis experiments since data showed that the products of direct photolysis reaction also absorb 254-nm light. (2,2'-Dihydroxy-5,5'-dimethylbiphenyl, 4-methylcatechol and 2-hydroxy-4',5'-dimethyldiphenyl ether have been reported as products in the direct photolysis of *p*-cresol, Joschek and Miller, 1966.) Results are presented in Figure 3. To generate model predictions, we used the calculated fluence from the actinometry experiments (Figure 2) and fitted the quantum yields to experimental data.

Model predictions: *p*-cresol degradation

Figure 4 provides predicted and experimental decay curves for *p*-cresol in a series of experiments carried out at different initial concentrations of H₂O₂ and *p*-cresol. Model calculations include the fluence rate determined via actinometry and the quantum yields for *p*-cresol and 4-methylcatechol determined via direct photolysis. In all cases experimental results are accurately predicted by the model. Omitting OH radical scavenging by reaction intermediates significantly overestimates the destruction rate of *p*-cresol in most cases (dashed lines in Figure 4), which highlights the importance of incorporating the full mechanism in the kinetic model.

Calculations show that intermediates, especially those before ring cleavage (4-methylcatechol and 4-methylbenzoquinone) played an important role in hydroxyl radical quenching. There is no reported kinetic rate constant for the reaction of 4-methylbenzoquinone reaction with hydroxyl radical although Scheck and Frimmel (1995) reported that 1,2-benzoquinone was not detected during oxidation of phenol by the UV/H₂O₂ process because it is easily cleaved into aliphatic compounds. In this study, the rate constant for the reaction of 4-methylbenzoquinone with hydroxyl radical was held to be of the same magnitude as that of 4-methylcatechol, $k_{26} = 2.0 \times 10^{10} \text{ M}^{-1}\text{s}^{-1}$, near the diffusion limit. Model results were obtained with no additional fitted parameters; all other rate constants were obtained from preliminary experiments (i.e. actinometry and direct photolysis experiments) or published data (Table 1).

Molecular oxygen participates in several steps of the reaction mechanism—specifically, in the oxidation of 4-methylcatechol to 4-methylbenzoquinone (Davies *et al.*, 1995) and the oxidation of carbon double bonds (Jin *et al.*, 2010; Huang *et al.*, 2011). To test the

potential role of oxygen, we performed experiments with degassed solutions by bubbling argon into the solution before exposure to UV light. During the experiment, an argon atmosphere was maintained over the reactor to prevent oxygen diffusion into the reacting mixture. The results in terms of *p*-cresol concentration vs. time showed no appreciable difference relative to the original experiments, suggesting that dissolved oxygen is not important in *p*-cresol oxidation. Representative results are provided in the supporting information.

There are two possible pathways for the OH-induced oxidation of *p*-cresol to 4-methylcatechol (Omura and Matsuura, 1968; Scheck and Frimmel, 1995): the first involves the cyclohexadienyl radical formed due to OH radical attack that converts the *p*-cresol into dihydroxy compounds. In the second, the phenoxyl radical formed due to the abstraction of hydrogen atom subsequently combines with a second OH radical.

However, the second mechanism is dominant only when the OH-radical is present at high concentrations (Waters, 1964). In the kinetic model used here, only one OH radical is involved in the conversion of *p*-cresol to 4-methylcatechol, suggesting that the cyclohexadienyl pathway predominates.

The production of 4-methylcatechol was measured in the experiments (Figure 5). The reaction of *p*-cresol with OH radical was the only 4-methylcatechol source, but two sinks are considered in the kinetic model: direct photolysis and reaction with OH radical. Even though the rate constant for 4-methylcatechol reaction with OH radical is higher than that of *p*-cresol, 4-methylcatechol accumulates until most of the *p*-cresol is consumed. There was good agreement between data and predictions at low H₂O₂ concentrations (Figure

5a), but the model tends to underpredict concentrations of 4-methylcatechol at later times and higher measured concentrations (Figure 5b) while still trending correctly.

The evolutions of formic acid, acetic acid and oxalic acid concentrations are presented in Figure 6 for a representative experiment. (Results for *p*-cresol degradation in this experiment are in Figure 5b.) Although the α -hydrogens next to the carbon double bonds and carboxyl groups are more active under oxidizing conditions, there may be several ways in which to break down the aliphatic acid formed by the ring cleavage. Therefore, the final stages of the mechanism proposed (Figure 1) may lead to formation of other species. Figure 7 shows the trajectory of total carbon corresponding to measured concentrations of aliphatic acids along with model calculations for a representative experiment. Both model and data indicate that aliphatic acids accumulate throughout the experiment. By the end of the experiment (180 min), essentially all the *p*-cresol is destroyed (Figure 5b).

The concentrations of H₂O₂ and TOC, and pH were measured throughout the experiment and predicted using the kinetic model (Figures 8 to 10). Despite some differences, the model adequately predicts trends in H₂O₂ concentration (Figure 8) and pH (Figure 9). Previous studies have calculated pH changes during this type of experiment by assuming that the target organics are completely converted into carbon dioxide (Crittenden *et al.*, 1999, Rojas *et al.*, 2010). In our study, a significant drop in pH was observed in the 3-h experiment. However, the drop of pH was due to the formation of organic acids. The lack of CO₂ production (that is, complete mineralization of the target) is evident in the TOC

results (Figure 10) since TOC does not change appreciably during the experiments, as predicted by our model.

Model predictions: 4-methylcatechol degradation

Experiments were carried out with 4-methylcatechol as the initial substrate at different initial hydrogen peroxide concentrations. As anticipated, degradation rate was directly related to the initial hydrogen peroxide concentration within the range of experiments (Figure 11). Agreement between experimental data and model simulations is observed at 0.2 mM H₂O₂ but the model tends to over-estimate degradation rates at higher H₂O₂ concentrations.

Concluding remarks

A comprehensive kinetic model was developed to quantify the oxidation of *p*-cresol by UV/H₂O₂ AOP in a batch reactor. The model was based on known elementary chemical and photo-chemical reactions of the UV/H₂O₂ photolysis system, together with experimentally established direct photolysis reactions and proposed OH-radical reactions with intermediates. The kinetics of *p*-cresol decomposition, as well as the main reaction intermediate (4-methylcatechol) was successfully simulated throughout a wide range of operating conditions. The approach employed shows that the full reaction mechanism needs to be considered to evaluate process performance. In particular, reaction intermediates, especially those formed before ring cleavage, play an important role in the quenching of hydroxyl radicals and, consequently, those compounds must be considered in kinetic models of AOP degradation of phenolic compounds.

References

- Ahel, M., Schaffner, C., Giger, W., 1996. Behaviour of alkylphenol polyethoxylate surfactants in the aquatic environment - III. Occurrence and elimination of their persistent metabolites during infiltration of river water to groundwater. *Water Res.*, 30, 37-46.
- Benjamin, M. M., 2002. *Water Chemistry*. Waleland Press Inc., p 139.
- Bielski, B.H. J., Cabelli, D. E., Arudi, R. L., Ross, A. B., 1985. Reactivity of HO₂/O₂ radicals in aqueous solution. *J. Phys. Chem. Ref. Data*, 14, 1041-1100.
- Boltz, D., Holwell, J., 1978. *Colorimetric determination of nonmetals*. 2nd ed. John Wiley and Sons: New York.
- Boonrattanakij, N., Lu, M., Anotai, J., 2009. Kinetics and mechanism of 2,6-dimethylaniline degradation by hydroxyl radicals. *J. Hazard. Mater.*, 172, 952-957.
- Buxton, G. V., Greenstock, C. L., Helman W. P., Ross, A. B., 1988. Critical review of rate constants for reactions of hydrated electrons, hydrogen atoms and hydroxyl radicals ($\cdot\text{OH}/\text{O}^-$) in aqueous solution. *J. Phys. Chem. Ref. Data*, 17, 513-886.
- Crittenden, J. C., Hu, S., Hand, D. W., Green, S. A., 1999. A kinetic model for H₂O₂/UV process in a completely mixed batch reactor. *Wat. Res.*, 33, 2315-2328.
- Davies, M. S., Mile, B., Rowlands, C. C., 1995. Oxidation of 4-methylcatechol by dioxygen studies by ESR spectroscopy. The different regioselectivity of OH⁻ and MeO⁻ nucleophilic attack and kinetic deuterium isotope effects. *Magn. Reson. Chem.*, 33, 15-19.
- De Luis, A., Lombraña, J.I., Menendez, A., 2011. Modeling of the radicalary state in the H₂O₂/UV oxidation system to predict the degradation kinetics of phenolic mixture solutions. *AIChE J.*, 30, 196-207.
- Dong, B., Kahl, A., Cheng, L., Vo, H., Ruehl, S., Zhang, T., Snyder, S., Sáez, A.E., Quanrud, D., Arnold R.G., 2015. Fate of Trace Organics in a Wastewater Effluent Dependent Stream, *Sci. Total Environ.*, 518-519, 479-490.
- Eriksen, T. E., Lind, J., Merenyi, G., 1985. On the acid-base equilibrium of the carbonate radical. *Radiat. Phys. Chem.*, 26, 197-199.
- Ershov, B. G., Janata, E., Alam, M. S., Gordeev, A. V., 2008. Studies of the reaction of the hydroxyl radical with the oxalate ion in an acidic aqueous solution by pulse radiolysis. *Russ. Chem. Bull., Int. Ed.* 57, 1189.
- Getoff, N., Schworer, F., Markovie, V. M., Sehested, K., Nielsen, S. O. 1971. Pulse radiolysis of oxalic acid and oxalates. *J. Phys. Chem.*, 75, 749-755.
- Glaze, W. H., Lay, Y., Kang, J.-W., 1995. Advanced oxidation processes. A kinetic model for the oxidation of 1,2-dibromo-3-chloropropane in water by the combination of hydrogen peroxide and UV radiation. *Ind. Eng. Chem. Res.*, 34, 2314-2323.
- Greenwood, N. N., Earnshaw, A., 1997. *Chemistry of the Elements*, 2nd ed., Butterworth-Heinemann, p 310.

- Gohn, M., Getoff, N., 1977. Pulse radiolysis of 3,4-dihydroxytoluene. *J. Chem. Soc.*, 1207-1215.
- Hart, E. J., 1951. Mechanism of the γ -Ray induced oxidation of formic acid in aqueous solution. *J. Am. Chem. Soc.*, 73, 68-73.
- Holeman, J., Bjergbakke, E., Sehested, K., 1987. The importance of radical-radical reactions in pulse radiolysis of aqueous carbonate/bicarbonate. *Proc. Tihany Symp. Radiat. Chem.*, 1, 149-153.
- Housecroft, C. E., Sharpe, A. G., 2005. *Inorganic Chemistry*, 2nd ed., Prentice-Pearson-Hall, p 368.
- Huang, D., Zhang X., Chen, Z. M., Zhao, Y., Shen, X. L., 2011. The kinetics and mechanism of an aqueous phase isoprene reaction with hydroxyl radical. *Atoms. Chem. Phys.*, 11, 7399-7415.
- Jin, F., Zhong, H., Cao, J., Cao, J., Kawasaki, K., Kishita, A., Matsumoto, T., Tohji, K., Enomoto, H., 2010. Oxidation of unsaturated carboxylic acids under hydrothermal conditions. *Bioresour. Technol.*, 101, 7624-7634.
- Jongberg, S., Gislason, N. E., Lund, M. N., Skibsted, L. H., Waterhouse, A. L., 2011. Thiol-quinone adduct formation in myofibrillar proteins detected by LC-MS. *J. Agric. Food Chem.*, 59, 6900-6905.
- Joschek, H. I., Miller S. I., 1966. Photooxidation of phenol, cresols, and dihydroxybenzenes. *J. Am. Chem. Soc.*, 88(14), 3273-3281.
- Kang, N., Lee, D. S., Yoon, J., 2002. Kinetic modeling of Fenton oxidation of phenol and monochlorophenols. *Chemosphere*, 47, 915-924.
- Lay Y. S., 1989. Oxidation of 1,2-dibromo-3-chloropropane in groundwater using advanced oxidation processes. Ph.D. dissertation, University of California, Los Angeles.
- Lee, P.-C., Lee, W., 1996. In vivo estrogenic action of nonylphenol in immature female rats. *Bull. Environ. Contam. Toxicol.*, 57, 341-348.
- Leitner, N. K. V., Dore, M., 1997. Mechanism of the reaction between hydroxyl radicals and glycolic, glyoxylic, acetic and oxalic acids in aqueous solution: consequence on hydrogen peroxide consumption in the H_2O_2/UV and O_3/H_2O_2 systems. *Water Res.*, 31, 1383-1397.
- Liao, C.-H., Gurol, M., 1995. Chemical oxidation by photolytic decomposition of hydrogen peroxide. *Environ. Sci. Technol.*, 29, 3007-3014.
- Loyo-Rosales, J. E., Rice, C. P., Torrents, A., 2007. Fate of octyl- and nonylphenol ethoxylates and some carboxylated derivatives in three American wastewater treatment plants. *Environ. Sci. Technol.*, 41, 6815-6821.
- Lye, C. M., Frid, C. L. J., Gill, M. E., Cooper, D. W., Jones, D. M., 1999. Estrogenic alkylphenols in fish tissues, sediments, and waters from the U.K. Tyne and Tees Estuaries., 33, 1009-1014.

- MacDonald, B. C., Lvin, S. J., Patterson, H., 1997. Correction of fluorescence inner filter effects and the partitioning of pyrene to dissolved organic carbon. *Anal. Chim. Acta*, 338, 155-162.
- Matsuura, T., Omura, K., 1974. Photochemical hydroxylation of aromatic compounds. *Synthesis*, 173-184.
- Moreira, J., Serrano, B., Ortiz, A., de Lasa, H., 2012. A unified kinetic model for phenol photocatalytic degradation over TiO₂ photocatalysts. *Chem. Eng. Sci.*, 78, 186-203.
- Murcia, M. D., Vershinin, N. O., Briantceva, N., Gomez, M., Gomez, E., Cascales, E., Hidalgo, A. M., 2015. Development of a kinetic model for the UV/H₂O₂ photodegradation of 2,4-dichlorophenoxyacetic acid. *Chem. Eng. J.*, 266, 356-367.
- Nagarnaik, P. M., Boulanger, B., 2011. Advanced oxidation of alkylphenol ethoxylates in aqueous systems. *Chemosphere*, 85, 854-860.
- Neta, P., Huie, R. E., Ross, A. B., 1988. Rate constants for reactions of inorganic radicals in aqueous solution. *J. Phys. Chem. Ref. Data.*, 17, 1027-1284.
- Olariu, R. I., Klotz, B., Barnes, I., Becker, K. H., Mocanu, R., 2002. FT-IR study of the ring-retaining products from the reaction of OH radicals with phenol, *o*-, *m*-, and *p*-cresol. *Atmos. Environ.*, 36, 3685-3697.
- Omura, K., Matsuura, T., 1968. Photo-induced reactions-IX: The hydroxylation of phenols by the photo-decomposition of hydrogen peroxide in aqueous media. *Tetrahedron*, 24, 3475-3487.
- Perry, R., Green, D., Maloney, J., 1981. *Perry's Chemical Engineerings' Handbook*, 5th ed., McGraw-Hill, New York.
- Pospisil, J., Ettl, V., Skola, V., 1957. Pyrocatechol oxidation to muconic acid. *Chemicky Prumysl.*, 7, 244-248.
- Rojas, M. R., Perez, F., Whitley, D., Arnold, R. G., Sáea, A. E., 2010. Modeling of advanced oxidation of trace organic contaminants by hydrogen peroxide photolysis and Fenton's reaction. *Ind. Eng. Chem. Res.*, 49, 11331-11343.
- Rojas, M. R., Leung, C., Whitley, D., Zhu, Y., Arnold, R. G., Sáea, A. E., 2011. Advanced oxidation of trace organics in water by hydrogen peroxide solar photolysis. *Ind. Eng. Chem. Res.*, 50, 12479-12487.
- Scheck, C. K., Frimmel, F. H., 1995. Degradation of phenol and salicylic acid by ultraviolet radiation/ hydrogen peroxide/oxygen. *Wat. Res.*, 29, 2346-2352.
- Scullion, S. D., Clench, M. R., Cooke, M., Ashcroft, A. E., 1996. Determination of surfactants in surface water by solid-phase extraction, liquid chromatography and liquid chromatography-mass spectrometry. *J. Chromatogr., A* 733, 207-216.
- Sehested, K., Corflitzen, H., Christensen, H. C., Hart, E. J., 1975. Rates of reaction of O⁻, OH and H with methylated benzenes in aqueous solution. Optical spectra of radicals. *J. Phys. Chem.*, 79, 310-315.

- Soto, A. M., Justicia, H., Wray, J. W., Sonnenschein, C., 1991. *p*-Nonyl-phenol: An estrogenic xenobiotic released from “modified” polystyrene. *Environ. Health Perspect.*, 92, 167-173.
- Stefan, M. I., Hoy, A. R., Bolton, J. R., 1996. Kinetics and mechanism of the degradation and mineralization of acetone in dilute aqueous solution sensitized by the UV photolysis of hydrogen peroxide. *Environ. Sci. Technol.*, 30, 2382-2390.
- Song, W., Ravindran, V., Pirbazari, M., 2008. Process optimization using a kinetic model for the ultraviolet radiation-hydrogen peroxide decomposition of natural and synthetic organic compounds in groundwater. *Chem. Eng. Sci.*, 63, 3249-3270.
- Sun, W., Saeys, M., 2008. First principles study of the reaction of formic and acetic acids with hydroxyl radicals. *J. Phys. Chem. A*, 112, 6918-6928.
- Swartz, C. H., Reddy, S., Benotti, M. J., Yin, H., Barber, L. B., Brownawell, B. J., Rudel, R. A., 2006. Steroid estrogens, nonylphenol ethoxylate metabolites, and other wastewater contaminants in groundwater affected by a residential septic system on Cape Cod, MA. *Environ. Sci. Technol.*, 40, 4894-4902.
- Volman, D. H., Chen, J. C., 1959. The photochemical decomposition of hydrogen peroxide in aqueous solutions of allyl alcohol at 2537 Å. *J. Am. Chem. Soc.*, 81 (16) 4141-4144.
- Waite, J. H., 1976. Calculating extinction coefficients for enzymatically produced *o*-quinones. *Anal. Biochem.*, 75, 211-218.
- Wang, K., Hsieh, Y., Chen, L., 1998. The heterogeneous photocatalytic degradation, intermediates and mineralization for the aqueous solution of cresols and nitrophenols. *J. Hazard. Mater.*, 59, 251-260.
- Waters, W. A., 1964. Mechanism of oxidation of organic compounds. Methuen, p 132.
- Weinstein, J., Bielski, B. H. J., 1979. Kinetics of the interaction of perhydroxyl and superoxide radicals with hydrogen peroxide. The Haber-Weiss reaction. *J. Am. Chem. Soc.*, 101, 58-62.
- Wojnárovits, L., Foldiak, G., D’angelantonio, M., Emmi, S. S., 2002. Mechanism of OH radical-induced oxidation of *p*-cresol to *p*-methylphenolxyl radical. *Res. Chem. Intermed.*, 28, 373-386.

Table 1. Kinetic and equilibrium parameters used in the model. Acronyms are defined in Figure 1. Quantum yield (Φ) and molar extinction coefficients (ϵ) are reported for photolysis reactions, kinetic rate constants (k) are reported for relevant reactions, and equilibrium constants (K) are reported for reactions assumed to reach equilibrium instantaneously in the reaction mixture.

	Reaction	Parameters	Reference
R1	$\text{H}_2\text{O}_2 + h\nu \rightarrow 2 \cdot\text{OH}$	$\epsilon_1 = 18.7 \text{ M}^{-1}\text{cm}^{-1}$ $\Phi_1 = 0.5 \text{ mol/Ein}$	Volman and Chen (1959)
R2	$\cdot\text{OH} + \text{H}_2\text{O}_2 \rightarrow \text{O}_2^{\cdot-} + \text{H}_2\text{O} + \text{H}^+$	$k_2 = 2.7 \times 10^7 \text{ M}^{-1}\text{s}^{-1}$	Buxton et al. (1988)
R3	$\cdot\text{OH} + \text{HO}_2^- \rightarrow \text{O}_2^{\cdot-} + \text{H}_2\text{O}$	$k_3 = 7.5 \times 10^9 \text{ M}^{-1}\text{s}^{-1}$	Buxton et al. (1988)
R4	$\cdot\text{OH} + \text{HCO}_3^- \rightarrow \text{CO}_3^{\cdot-} + \text{H}_2\text{O}$	$k_4 = 8.5 \times 10^6 \text{ M}^{-1}\text{s}^{-1}$	Buxton et al. (1988)
R5	$\cdot\text{OH} + \text{CO}_3^{2-} \rightarrow \text{CO}_3^{\cdot-} + \text{OH}^-$	$k_5 = 3.9 \times 10^8 \text{ M}^{-1}\text{s}^{-1}$	Buxton et al. (1988)
R6	$\cdot\text{OH} + \text{HO}_2^{\cdot} \rightarrow \text{O}_2 + \text{H}_2\text{O}$	$k_6 = 6.6 \times 10^9 \text{ M}^{-1}\text{s}^{-1}$	Buxton et al. (1988)
R7	$\cdot\text{OH} + \text{O}_2^{\cdot-} \rightarrow \text{O}_2 + \text{OH}^-$	$k_7 = 8.0 \times 10^9 \text{ M}^{-1}\text{s}^{-1}$	Buxton et al. (1988)
R8	$\cdot\text{OH} + \cdot\text{OH} \rightarrow \text{H}_2\text{O}_2$	$k_8 = 5.5 \times 10^9 \text{ M}^{-1}\text{s}^{-1}$	Buxton et al. (1988)
R9	$\cdot\text{OH} + \text{CO}_3^{\cdot-} \rightarrow \text{products}$	$k_9 = 3.0 \times 10^9 \text{ M}^{-1}\text{s}^{-1}$	Holcman et al. (1987)
R10	$\text{O}_2^{\cdot-} + \text{H}_2\text{O}_2 \rightarrow \cdot\text{OH} + \text{O}_2 + \text{OH}^-$	$k_{10} = 0.13 \text{ M}^{-1}\text{s}^{-1}$	Bielski et al. (1985)
R11	$\text{O}_2^{\cdot-} + \text{CO}_3^{\cdot-} \rightarrow \text{O}_2 + \text{CO}_3^{2-}$	$k_{11} = 6.5 \times 10^8 \text{ M}^{-1}\text{s}^{-1}$	Eriksen et al. (1985)
R12	$\text{O}_2^{\cdot-} + \text{HO}_2^{\cdot} \rightarrow \text{HO}_2^- + \text{O}_2$	$k_{12} = 9.7 \times 10^7 \text{ M}^{-1}\text{s}^{-1}$	Benon et al. (1985)
R13	$\text{HO}_2^{\cdot} + \text{HO}_2^{\cdot} \rightarrow \text{H}_2\text{O}_2 + \text{O}_2$	$k_{13} = 8.6 \times 10^5 \text{ M}^{-1}\text{s}^{-1}$	Weinstein and Bielski (1979)
R14	$\text{HO}_2^{\cdot} + \text{H}_2\text{O}_2 \rightarrow \cdot\text{OH} + \text{O}_2 + \text{H}_2\text{O}$	$k_{14} = 3.7 \text{ M}^{-1}\text{s}^{-1}$	Bielski et al. (1985)
R15	$\text{CO}_3^{\cdot-} + \text{H}_2\text{O}_2 \rightarrow \text{HCO}_3^- + \text{O}_2^{\cdot-} + \text{H}^+$	$k_{15} = 8.0 \times 10^5 \text{ M}^{-1}\text{s}^{-1}$	Neta et al. (1988)
R16	$\text{CO}_3^{\cdot-} + \text{HO}_2^- \rightarrow \text{HCO}_3^- + \text{O}_2^{\cdot-}$	$k_{16} = 3.0 \times 10^7 \text{ M}^{-1}\text{s}^{-1}$	Neta et al. (1988)
R17	$\text{CO}_3^{\cdot-} + \text{CO}_3^{\cdot-} \rightarrow 2\text{CO}_3^{2-}$	$k_{17} = 2.0 \times 10^7 \text{ M}^{-1}\text{s}^{-1}$	Neta et al. (1988)
R18	$\text{H}_2\text{O}_2 \leftrightarrow \text{HO}_2^- + \text{H}^+$	$k_{18} = 2.51 \times 10^{-2} \text{ s}^{-1}$ $k_{18r} = 1 \times 10^{10} \text{ M}^{-1}\text{s}^{-1}$	Perry et al. (1981)
R19	$\text{HO}_2^{\cdot} \leftrightarrow \text{O}_2^{\cdot-} + \text{H}^+$	$k_{19} = 1.58 \times 10^5 \text{ s}^{-1}$ $k_{19r} = 1 \times 10^{10} \text{ M}^{-1}\text{s}^{-1}$	Perry et al. (1981)
R20	$\text{CO}_2(\text{aq}) + \text{H}_2\text{O} \leftrightarrow \text{H}_2\text{CO}_3$	$k_{20} = 0.039 \text{ s}^{-1}$ $k_{20r} = 23 \text{ s}^{-1}$	Housecroft and Sharpe (2005)
R21	$\text{H}_2\text{CO}_3 \leftrightarrow \text{HCO}_3^- + \text{H}^+$	$k_{21} = 1.25 \times 10^7 \text{ s}^{-1}$ $k_{21r} = 5 \times 10^{10} \text{ M}^{-1}\text{s}^{-1}$	Greenwood and Earnshaw (1997)
R22	$\text{PC} + h\nu \rightarrow \text{products}$	$\epsilon_{22} = 340 \text{ M}^{-1}\text{cm}^{-1}$ $\Phi_{22} = 0.034 \text{ mol/Ein}$	This work
R23	$\text{PC} + \cdot\text{OH} \rightarrow 4\text{MC}$	$k_{23} = 1.2 \times 10^{10} \text{ M}^{-1}\text{s}^{-1}$	Buxton et al. (1988)
R24	$4\text{MC} + h\nu \rightarrow \text{products}$	$\epsilon_{24} = 310 \text{ M}^{-1}\text{cm}^{-1}$ $\Phi_{24} = 0.007 \text{ mol/Ein}$	This work
R25	$4\text{MC} + \cdot\text{OH} \rightarrow 4\text{MB}$	$k_{25} = 1.6 \times 10^{10} \text{ M}^{-1}\text{s}^{-1}$	Gohn and Getoff (1977)
R26	$4\text{MB} + \cdot\text{OH} \rightarrow 3\text{MM}^-$	$k_{26} = 2.0 \times 10^{10} \text{ M}^{-1}\text{s}^{-1}$	This work

R27	$3\text{MM}^- + \cdot\text{OH} \rightarrow \text{L}^- + 2 \text{Ox}^- (\text{Ox}^{2-})$	$k_{27} = 5.0 \times 10^8 \text{ M}^{-1}\text{s}^{-1}$	Kang et al. (2002)
R28	$\text{L}^- + \cdot\text{OH} \rightarrow \text{HA} (\text{A}^-) + \text{CO}_2 + \text{H}_2\text{O}$	$k_{28} = 3.0 \times 10^8 \text{ M}^{-1}\text{s}^{-1}$	Buxton et al. (1988)
R29	$\text{Ox}^- + \cdot\text{OH} \rightarrow \text{Ox}^- + \text{H}_2\text{O}$	$k_{29} = 4.7 \times 10^7 \text{ M}^{-1}\text{s}^{-1}$	Buxton et al. (1988)
R30	$\text{Ox}^{2-} + \cdot\text{OH} \rightarrow \text{Ox}^- + \text{OH}^-$	$k_{30} = 7.7 \times 10^6 \text{ M}^{-1}\text{s}^{-1}$	Buxton et al. (1988)
R31	$\text{Ox}^- + \text{Ox}^- \rightarrow \text{Ox}^- (\text{Ox}^{2-}) + 2 \text{CO}_2$	$k_{31} = 5.0 \times 10^8 \text{ M}^{-1}\text{s}^{-1}$	Ershov et al. (2008)
R32	$\text{HA} + \cdot\text{OH} \rightarrow \text{F}^- + \text{CO}_2 + \text{H}_2\text{O}$	$k_{32} = 1.23 \times 10^8 \text{ M}^{-1}\text{s}^{-1}$	Sun and Saeys (2008)
R33	$\text{A}^- + \cdot\text{OH} \rightarrow \text{F}^- + \text{CO}_2 + \text{OH}^-$	$k_{33} = 8.5 \times 10^7 \text{ M}^{-1}\text{s}^{-1}$	Buxton et al. (1988)
R34	$\text{F}^- + \cdot\text{OH} \rightarrow \text{CO}_2 + \text{H}_2\text{O}$	$k_{34} = 9.77 \times 10^7 \text{ M}^{-1}\text{s}^{-1}$	Sun and Saeys (2008)
E35	$\text{Ox}^- \leftrightarrow \text{Ox}^{2-} + \text{H}^+$	$K_{35} = 6.31 \times 10^{-5} \text{ M}$	Benjamin (2002)
E36	$\text{HA} \leftrightarrow \text{A}^- + \text{H}^+$	$K_{36} = 1.74 \times 10^{-5} \text{ M}$	Benjamin (2002)
E37	$\text{HCO}_3^- \leftrightarrow \text{CO}_3^{2-} + \text{H}^+$	$K_{37} = 4.48 \times 10^{-11} \text{ M}$	Benjamin (2002)

Figure captions

Figure 1. Proposed mechanism of *p*-cresol oxidation by hydroxyl radicals.

Figure 2. Decomposition of hydrogen peroxide in Milli-Q water in the batch reactor. Solid lines: model predictions obtained by fitting the model to decay curves using the fluence rate as adjustable parameter.

Figure 3. Decomposition of (a) *p*-cresol, and (b) 4-methylcatechol in aqueous solution by (LP)UV direct photolysis. Solid lines: model predictions obtained from a fit of model results to decay curves using the respective quantum yield as adjustable parameter. (a) $[PC]_0 = 0.438$ mM, (b) $[4MC]_0 = 0.103$ mM.

Figure 4. Degradation of *p*-cresol in aqueous solution by UV/H₂O₂ advanced oxidation as a function of initial H₂O₂ concentrations (a), and initial *p*-cresol concentrations (b). Solid lines: full model predictions using the proposed mechanism; dashed lines: model calculations neglecting reactions of intermediates. (a) $[PC]_0 = 0.1$ mM, (b) $[H_2O_2]_0 = 1$ mM.

Figure 5. Degradation of *p*-cresol in aqueous solution by UV/H₂O₂ advanced oxidation. Evolution of 4-methylcatechol concentration with time. Solid lines: model predictions. $[PC]_0 = 0.5$ mM, (a) $[H_2O_2]_0 = 1$ mM, (b) $[H_2O_2]_0 = 5$ mM.

Figure 6. Evolution of formic acid, acetic acid and oxalic acid concentrations with time. $[PC]_0 = 0.5$ mM, $[H_2O_2]_0 = 5$ mM.

Figure 7. Evolution of aliphatic reaction intermediates concentration with time. Solid line: model prediction. $[PC]_0 = 0.5$ mM, $[H_2O_2]_0 = 5$ mM. Abbreviations in Figure 1.

Figure 8. Evolution of H₂O₂ concentration with time. Solid line: model prediction. $[PC]_0 = 0.5$ mM, $[H_2O_2]_0 = 5$ mM.

Figure 9. Evolution of pH with time. Solid line: model prediction. $[PC]_0 = 0.5$ mM, $[H_2O_2]_0 = 5$ mM.

Figure 10. Evolution of TOC with time. Solid line: model prediction. $[PC]_0 = 0.5$ mM, $[H_2O_2]_0 = 5$ mM.

Figure 11. Degradation of 4-methylcatechol in aqueous solution by UV/H₂O₂ advanced oxidation as a function of initial H₂O₂ concentrations. Solid lines: model predictions. $[4MC]_0 = 0.1$ mM.

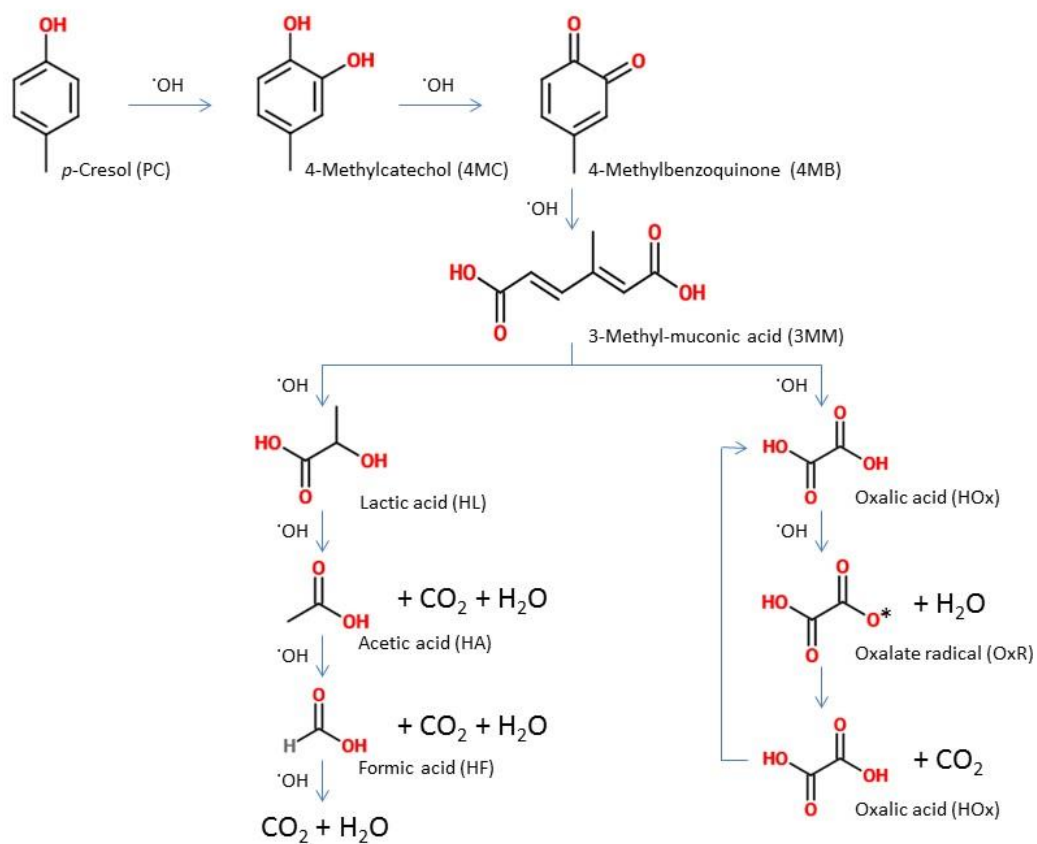


Figure 1. Proposed mechanism of *p*-cresol oxidation by hydroxyl radicals (see text for description).

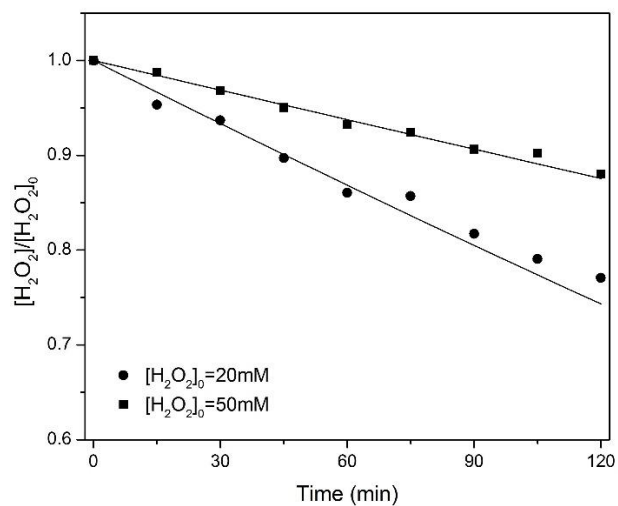


Figure 2. Decomposition of hydrogen peroxide in Milli-Q water in the batch reactor. Solid lines: model predictions obtained by fitting the model to decay curves using the fluence rate as adjustable parameter.

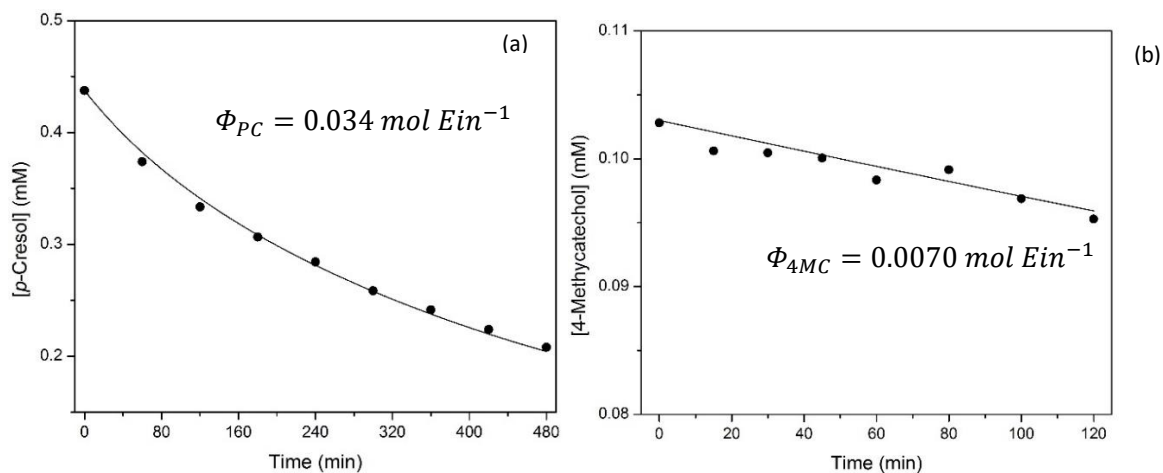


Figure 3. Decomposition of (a) p-cresol, and (b) 4-methylcatechol in aqueous solution by (LP)UV direct photolysis. Solid lines: model predictions obtained from a fit of model results to decay curves using the respective quantum yield as adjustable parameter. (a) $[PC]_0 = 0.438 \text{ mM}$, (b) $[4MC]_0 = 0.103 \text{ mM}$.

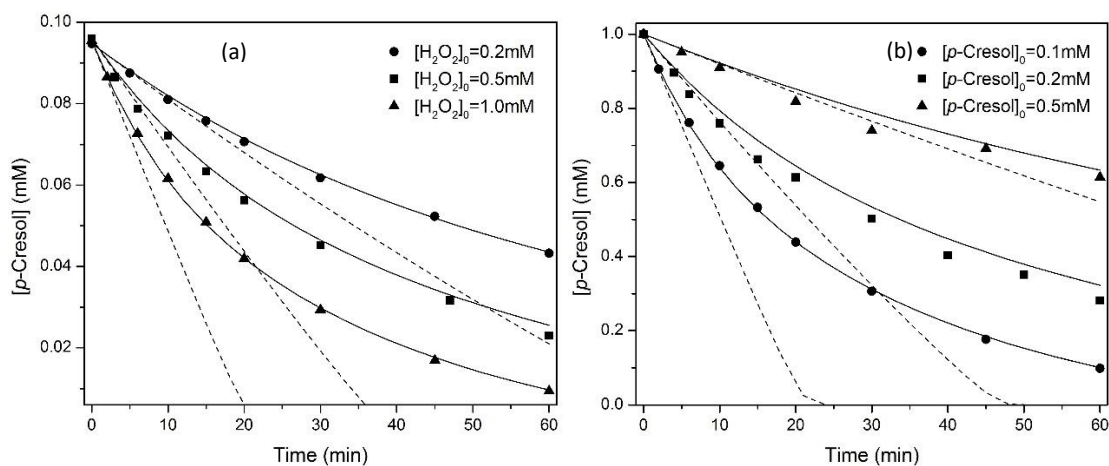


Figure 4. Degradation of p-cresol in aqueous solution by UV/ H_2O_2 advanced oxidation as a function of initial H_2O_2 concentrations (a), and initial p-cresol concentrations (b). Solid lines: full model predictions using the proposed mechanism; dashed lines: model calculations neglecting reactions of intermediates. (a) $[PC]_0 = 0.1 \text{ mM}$, (b) $[H_2O_2]_0 = 1 \text{ mM}$.

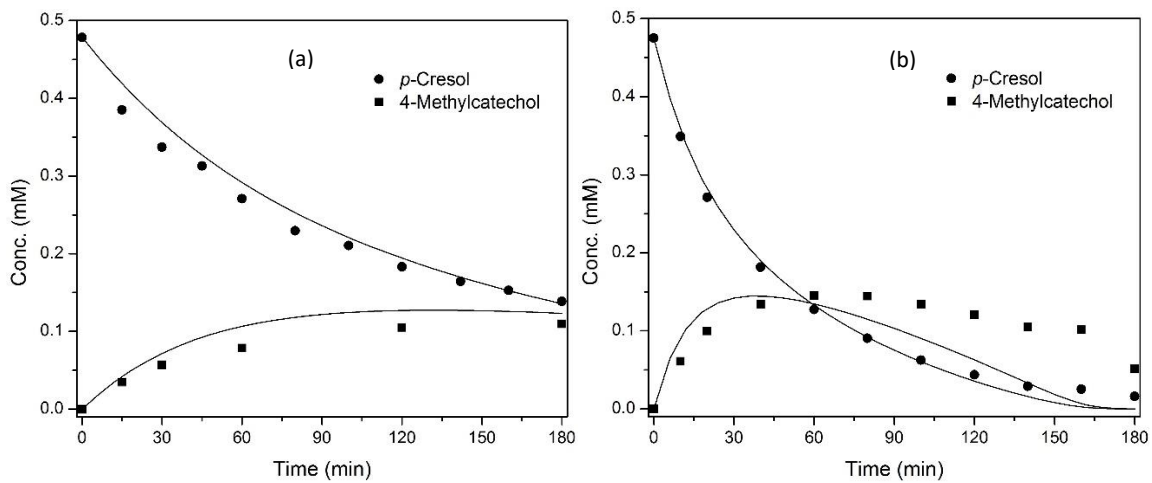


Figure 5. Degradation of *p*-cresol in aqueous solution by UV/H₂O₂ advanced oxidation. Evolution of 4-methylcatechol concentration with time. Solid lines: model predictions. [PC]₀ = 0.5 mM, (a) [H₂O₂]₀ = 1 mM, (b) [H₂O₂]₀ = 5 mM.

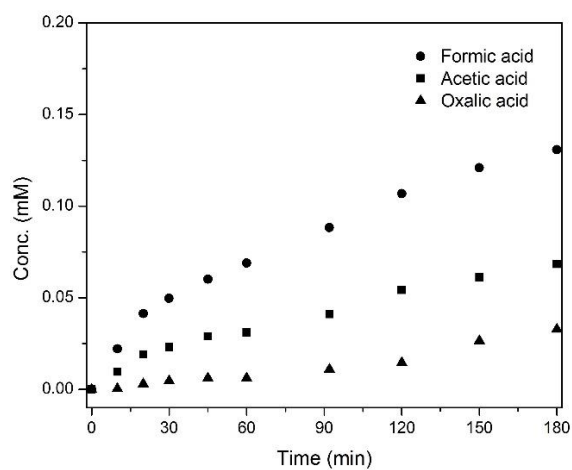


Figure 6. Evolution of formic acid, acetic acid and oxalic acid concentrations with time.
[PC]₀ = 0.5 mM, [H₂O₂]₀ = 5 mM.

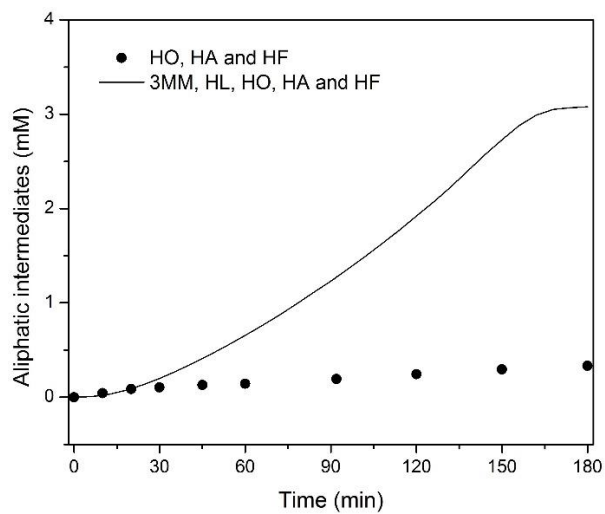


Figure 7. Evolution of aliphatic reaction intermediates concentration with time. Solid line: model prediction. $[PC]_0 = 0.5$ mM, $[H_2O_2]_0 = 5$ mM. Abbreviations in Figure 1.

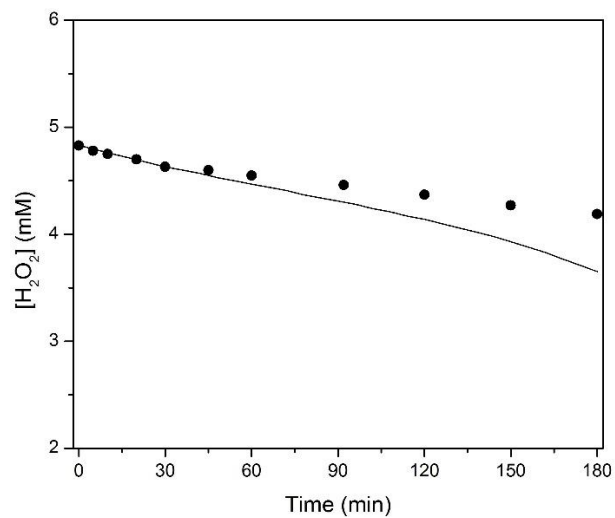


Figure 8. Evolution of H_2O_2 concentration with time. Solid line: model prediction. $[PC]_0 = 0.5$ mM, $[H_2O_2]_0 = 5$ mM.

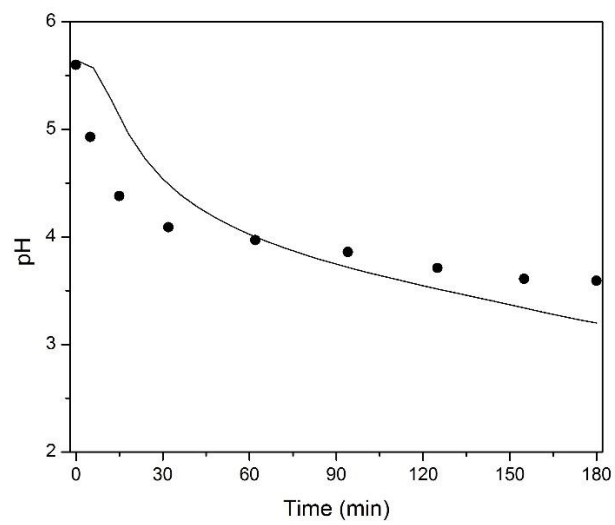


Figure 9. Evolution of pH with time. Solid line: model prediction. $[\text{PC}]_0 = 0.5 \text{ mM}$, $[\text{H}_2\text{O}_2]_0 = 5 \text{ mM}$.

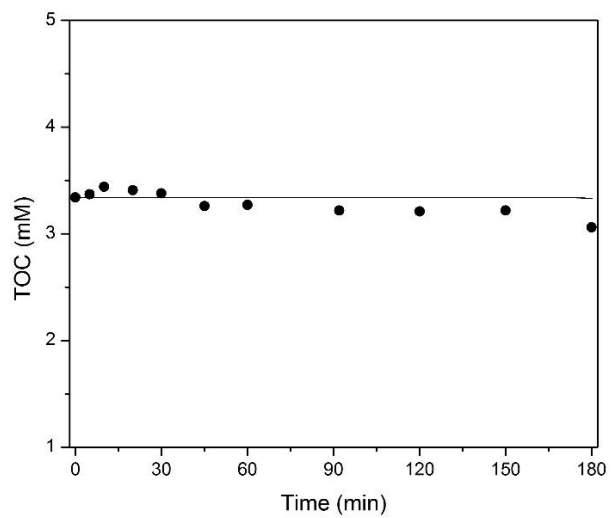


Figure 10. Evolution of TOC with time. Solid line: model prediction. $[\text{PC}]_0 = 0.5 \text{ mM}$, $[\text{H}_2\text{O}_2]_0 = 5 \text{ mM}$.

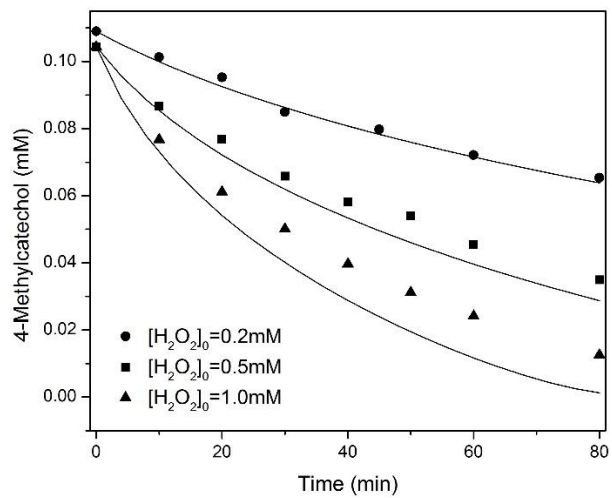


Figure 11. Degradation of 4-methylcatechol in aqueous solution by UV/H₂O₂ advanced oxidation as a function of initial H₂O₂ concentrations. Solid lines: model predictions. [4MC]₀ = 0.1 mM.

APPENDIX B**MODELING THE UV/H₂O₂ OXIDATION OF PHENOLIC COMPOUNDS IN A
CONTINUOUS-FLOW REACTOR WITH REFLECTIVE WALLS**

(submitted, Journal of Hazardous Materials)

Tianqi Zhang,^a Robert G. Arnold,^a George Diefenthal,^b A. Eduardo Sáez^a

a Department of Chemical and Environmental Engineering, University of Arizona,

Tucson AZ 85721

b Neotech Aqua Solutions, Inc., 3853 Calle Fortunada, Suite B San Diego, CA 92123

Abstract

Continuous-flow advanced oxidation processes (AOPs) are commonly used for the destruction of persistent trace organics that survive conventional wastewater treatment processes. The UV/H₂O₂ process is applied to large-scale operations using tubular reactors that contain one or more UV lamps. A common configuration consists of a single concentric lamp located at the center of a pipe. In this work, a novel flow-through UV reactor with a concentric lamp and a reflective surface is used to investigate the destruction of *p*-cresol, chosen as representative of phenolic trace organics in wastewater. A kinetic/transport model was developed to simulate the process. The model includes elementary reactions of the UV/H₂O₂ system; direct UV photolysis of the target; and reactions of hydroxyl radical with the target, H₂O₂ and reaction intermediates. The model incorporates UV light reflection from the reactor walls, as well as the hydrodynamics of the annular flow. The model accurately predicts the destruction of the target compound (*p*-cresol) in a wide range of experimental conditions. Experimental and theoretical results demonstrate that the wall reflectivity significantly enhances the rate of conversion of the target.

Keywords: UV/H₂O₂ advanced oxidation; kinetic model; continuous flow reactor.

Introduction

The occurrence and fate of trace organic compounds (TOrcs) in the aquatic environment are important issues in environmental chemistry [1,2]. Advanced oxidation processes (AOPs) can be used to remove a wide range of TOrcs by means of reactive species among which hydroxyl radical is prevalent [3,4]. The UV photolysis of hydrogen peroxide (UV/H₂O₂) produces hydroxyl radicals and is a well-established AOP technology used in full-scale treatment of wastewater effluents.

Understanding of the UV/H₂O₂ AOP process is based on simulation of physicochemical aspects of the process. Glaze et al. [5] proposed a kinetic model to predict the time-dependent concentration of a halogenated organic target during UV/H₂O₂ photolysis, including elementary reactions of hydrogen peroxide photolysis. The model employed a quasi-steady-state approximation (QSSA) to calculate the concentration of hydroxyl radicals. This approach was followed in various subsequent simulation efforts. Crittenden et al. [6] generalized the kinetic model by omitting the QSSA, which allowed for simulations under a wide range of experimental conditions. The same approach was followed by Rojas et al. [7,8], whose models predicted organic target conversions in batch reactors exposed to 254 nm UV light and solar light.

More recent UV/H₂O₂ process models include consideration of hydroxyl radical scavenging by compounds in complex water matrices and by organic intermediates produced from the oxidation of the parent target. In our previous work [9], we proposed a complete mechanism for the destruction of *p*-cresol by the UV/H₂O₂ process. A kinetic model was developed to simulate the process in a batch reactor. Model calculations

indicated that hydroxyl radical quenching by reaction intermediates produced during the oxidation of *p*-cresol must be accounted for to predict *p*-cresol degradation accurately. Poor absorbance by hydrogen peroxide in the UV range contributes to energy demand in UV/H₂O₂ processes. In poor light-absorbing matrices, a significant portion of the energy is wasted. This inefficiency can be remedied by reflecting unabsorbed light into the reactive mixture, as suggested by Navntoft et al. [10], who used an aluminum reflector in a batch reactor to enhance the efficiency of a solar disinfection process. Based on the light distribution model of Yang et al. [11], aluminum shows good reflectivity in the UV range (40.0%), followed by stainless steel (28.0%) and copper (4.0%). These authors developed a kinetic model for TOrC destruction in an annular reactor with a cylindrical reflector by considering the reflector as a second light source. More recently, Li et al. [12] assessed the impact of UV light reflection on the fluence rate distribution in an annular reactor using a micro-fluorescent silica detector. Results showed that reflection efficiencies for aluminum foil, stainless steel, and black cloth were 80.5%, 26.1%, and 11.1%, respectively.

In this work we use a flow-through UV reactor with a concentric light source and UV reflecting surface for *p*-cresol removal. A kinetic model for the oxidation of *p*-cresol by hydrogen peroxide photolysis developed previously [9] was modified to account for annular flow hydrodynamics, surface light reflection and the full mechanism of *p*-cresol oxidation by hydroxyl radicals.

Materials and methods

Experimental

Chemicals were used as obtained from the original sources: *p*-cresol (Acros, 99+%), hydrogen peroxide (Acros, 50 wt%), isopropyl alcohol (OmniSolv, >99.99%) and titanium sulfate (Pfaltz&Bauer, 30%). Milli-Q water (resistivity $\geq 18.0 \text{ m}\Omega \text{ cm}^{-1}$) was produced in a Barnstead NANOpure II system. Stock solutions of *p*-cresol were prepared one day before use. All glassware was thoroughly washed and baked overnight at 550 °C before use.

The reactor (Figure 1) was supplied by Neotech. It consists of a 4.1-cm i.d., 50.0-cm long stainless steel cylinder, a low-pressure amalgam UV lamp located concentrically in the barrel, a control box with electrical panel, and a UV monitor attached to the outer cylinder. The reflecting surface has a high reflection efficiency, up to 99% in the UV range $\geq 185 \text{ nm}$. The lamp is enclosed by a cylindrical quartz sleeve that is transparent to UV light with wavelengths $\geq 185 \text{ nm}$. The external diameter of the sleeve is 2.54 cm. The total available volume of the annular region of the reactor is 375 mL. The solution to be treated is supplied to the reactor by a centrifugal pump (Dayton, 4JMV2) from a glass feed tank (90 L). Flow rates are measured by a rotameter (Bule-White, F-400) at the downstream end of the reactor. Two UV lamps were used in the experiments. A 254-nm monochromatic lamp and a dichromatic lamp that emits light at 185 and 254 nm.

The solutions to be treated were prepared immediately before the experiments by diluting a concentrated *p*-cresol stock solution in 50 L Milli-Q water in the feed tank. Hydrogen peroxide was added to specified concentrations at the start of the experiment. The lamp

was turned on 20 minutes before the pump was started to allow it to reach stable operation. Samples were collected from the reactor outlet at various flow rates. To ensure that measurements represent steady conditions, samples were taken after ten residence times. The reactor was flushed with 200 L deionized water and 50 L Milli-Q water before and after every experiment.

The *p*-cresol concentration was measured using a fluorescence spectrometer (PerkinElmer LS 55). Light absorption by the solution (inner filtering) was taken into account to correct the fluorescent signal using previous models [13]. UV spectra were determined by a UV-Vis spectrophotometer (Thermo Science, Genesys 10s). Hydrogen peroxide concentrations were determined using the peroxytitanic (colorimetric) method [14].

Reactor model

The mechanism for the degradation of *p*-cresol by hydroxyl radicals (Figure 1s in supporting information) during UV₂₅₄/H₂O₂ photolysis was developed previously [9]. It includes chemical and photochemical reactions of the UV₂₅₄/H₂O₂ system, the direct photolysis of *p*-cresol, and reactions of hydroxyl radicals with byproducts and intermediates (Table 1s in supporting information).

Absent reflection, the fluence rate (expressed as light intensity per unit time and reactor volume) that reaches the outer surface of the reactor is given by the Beer-Lambert law,

$$I_l = I_0 e^{-\alpha l} \quad (1)$$

where I_0 (Ein/s m³) is the fluence rate at 254 nm emitted by the lamp per unit reactor volume, $\alpha = -2.303A$, in which A (m⁻¹) is the absorbance of the solution, $A = \sum \epsilon_i c_i$,

where ε_i ($\text{m}^{-1}\text{M}^{-1}$) is the extinction coefficient of species i at 254 nm and c_i (M) is its concentration, and l (m) is the distance from the lamp sleeve surface to the inside of the outer cylinder.

Among the species in the reaction mechanism (Table 1s), only H_2O_2 , p -cresol, 4-methylcatechol and 4-methylbenzoquinone absorb light at 254 nm. The absorbed fluence rate during the first light pass is given by

$$I_{Abs_1} = I_0(1 - e^{-\alpha l}) \quad (2)$$

The inside of the outer cylinder is held to be a perfect reflector of 254-nm light.

Nevertheless, some of the reflected light is lost as it returns to the concentric lamp. To model this behavior, we introduce a parameter, β , that represents the fraction of reflected light that is lost at the point it reaches the lamp. Extension of the Beer-Lambert law to multiple reflections (representing consecutive reflections until all light is absorbed by the solution or lost to the lamp assuming a loss fraction β for each light pass) leads to the following expression

$$I_{Abs} = \frac{I_0(1 - e^{-2\alpha l})}{1 - (1 - \beta)e^{-2\alpha l}} \quad (3)$$

The rate of direct photolysis for light-absorbing species at 254 nm can be calculated from this absorbed fluence. For example, for H_2O_2 , the rate is

$$R_{R_1} = -\Phi_1 f_{\text{H}_2\text{O}_2} I_0 \frac{1 - e^{-2\alpha l}}{1 - (1 - \beta)e^{-2\alpha l}} \quad (4)$$

where R_1 refers to the direct photolysis of H_2O_2 (reaction R_1 in Table 1s), Φ_1 is the quantum yield for that reaction, and $f_{\text{H}_2\text{O}_2}$ is the fraction of the total absorbed light that is absorbed by H_2O_2 .

The lamp's quartz sleeve allows 185-nm light to penetrate the reactor when employing the dichromatic lamp. Thus the photolysis of water at this wavelength [15] was considered in the use of the model to simulate results obtained with the dichromatic lamp. Calculations showed that nearly all the 185-nm light was absorbed by water during the first light pass from the lamp to the outer surface, so the effect of wall reflectivity in this case was neglected. The rate of direct photolysis of H₂O under 185-nm light is given by

$$R_{R_{37}} = -\Phi_{37}I_{185nm}(1 - e^{-\alpha_1 l}) \quad (5)$$

where Φ_{37} (reaction 37, Table 1s) is the quantum yield for the photocatalytic decomposition of H₂O, I_{185nm} is the fluence rate of the dichromatic lamp at 185 nm, and $\alpha_1 = -2.303A_{37}$, in which A_{37} is the absorption coefficient of water at 185 nm in the reactor (light absorption by other species at this wavelength was negligible.)

Radical reactions included in the model are generally second-order reactions. Acid-base reactions are considered to be at equilibrium under the operating conditions. Reactions involving carbon dioxide are included, since the solutions used were initially at equilibrium with atmospheric CO₂, and mineralization of the target led to the production of CO₂. Activity coefficients were calculated using the Davies equation to account for ionic strength effects.

The set of mole balances for the full reaction mechanism are presented in the supplementary information. Mole balances for H₂O₂, OH radical and *p*-cresol (PC) based on the proposed mechanism follow:

$$\begin{aligned} \frac{d[H_2O_2]}{dt} = & -\Phi_1 f_{H_2O_2} I_0 \frac{1-e^{-2\alpha l}}{1-(1-\beta)e^{-2\alpha l}} - k_2[H_2O_2][\cdot OH] + k_8[\cdot OH]^2 - \\ & k_{10}[H_2O_2]\gamma_{\pm 1}[O_2^-] + k_{13}[HO_2^-]^2 - k_{14}[H_2O_2][HO_2^-] - k_{15}[H_2O_2]\gamma_{\pm 1}[CO_3^-] - \\ & k_{18}[H_2O_2] + k_{18r}\gamma_{\pm 1}[HO_2^-]\gamma_{\pm 1}[H^+] \end{aligned} \quad (6)$$

$$\begin{aligned} \frac{d[\cdot OH]}{dt} = & 2\Phi_1 f_{H_2O_2} I_0 \frac{1-e^{-2\alpha l}}{1-(1-\beta)e^{-2\alpha l}} + \Phi_{37} I_{185nm} (1 - e^{-\alpha_1 l}) - k_2[H_2O_2][\cdot OH] - \\ & k_3\gamma_{\pm 1}[HO_2^-][\cdot OH] - k_4\gamma_{\pm 1}[HCO_3^-][\cdot OH] - k_5\gamma_{\pm 2}[CO_3^{2-}][\cdot OH] - k_6[HO_2^-][\cdot OH] - \\ & k_7\gamma_{\pm 1}[O_2^-][\cdot OH] - 2k_8[\cdot OH]^2 - k_9\gamma_{\pm 1}[CO_3^-][\cdot OH] + k_{10}[H_2O_2]\gamma_{\pm 1}[O_2^-] + \\ & k_{14}[H_2O_2][HO_2^-] - k_{23}[PC][\cdot OH] - k_{25}[4MC][\cdot OH] - 2k_{26}[4MB][\cdot OH] - \\ & 4k_{27}\gamma_{\pm 1}[3MM^-][\cdot OH] - k_{28}\gamma_{\pm 1}[L^-][\cdot OH] - k_{29}\gamma_{\pm 1}[Ox^-][\cdot OH] - \\ & k_{30}\gamma_{\pm 2}[Ox^{2-}][\cdot OH] - k_{32}[HA][\cdot OH] - k_{33}\gamma_{\pm 1}[A^-][\cdot OH] - k_{34}\gamma_{\pm 1}[F^-][\cdot OH] \end{aligned} \quad (7)$$

$$\frac{d[PC]}{dt} = -\Phi_{22} f_{PC} I_0 \frac{1-e^{-2\alpha l}}{1-(1-\beta)e^{-2\alpha l}} - k_{23}[PC][\cdot OH] \quad (8)$$

where t (s) is residence time and $\gamma_{\pm j}$ is the activity coefficient for the ionic species with charge j .

The resulting system of algebraic/differential equations was solved in MATLAB (R2016a) using the stiff differential equation solver ODE15s. The absolute tolerances for concentrations of all species were set four orders of magnitude below their respective values.

The mole balances shown above apply directly to a plug-flow reactor. However, all experiments were conducted in the laminar flow regime in the continuous flow reactor.

The velocity profile in the annular region of the reactor for a given volumetric flow rate was obtained from the solution of the Navier-Stokes equations. Residence time

distribution functions ($E_{(t)}$) were generated from the velocity profile as a function of volumetric flow rate (Fig. 2s).

The average residence time (t_R) is calculated from the residence time distribution as follows

$$t_R = \int_0^{\infty} E_{(t)} t dt \quad (9)$$

Species concentrations at the reactor exit are calculated from

$$c_{(t_R)} = \int_0^{\infty} E_{(t)} c_{(t)} dt \quad (10)$$

where $c_{(t)}$ is the outlet species concentration in plug flow, which is calculated from the kinetic model presented above.

Results and discussion

Actinometry at 254 nm

Lamp fluence rates were determined by fitting the model to experiments using low transmittance solutions to eliminate the effect of the reflecting walls. Initial concentrations $[p\text{-cresol}]_0 = 400 \mu\text{M}$ and $[\text{H}_2\text{O}_2]_0 = 50 \text{ mM}$ yield transmittances lower than 5% for one light pass through the annulus. For the dichromatic lamp, water photolysis was considered. Results for the two lamps are shown in Figure 2.

Direct photolysis in monochromatic light

Since the quantum yield of hydrogen peroxide is known, direct photolysis experiments with high transmittance were conducted to determine the effectiveness of the reflecting surfaces. In these experiments, the light decay parameter β was determined by fitting the data to the UV/H₂O₂ model without organic target present. The experiments were conducted at two different initial hydrogen peroxide concentrations, 0.5 mM and 1 mM,

which had transmittances of 98.4% and 96.7%, respectively, for one pass through the annular region. Results are presented in Figure 3. The fitted parameter was $\beta = 0.15$, which indicates that 15% of the light reflected by the outer surface is lost to the lamp in each reflection.

After determining the monochromatic lamp fluence rate and the light decay parameter, direct photolysis experiments were performed with *p*-cresol to determine its quantum yield. Solutions with initial *p*-cresol concentrations of 20 and 100 μM were exposed to light from the monochromatic light in the absence of H_2O_2 . The quantum yield of *p*-cresol was determined by fitting the kinetic model to the experimental data (Figure 4).

Dichromatic light experiments

The fluence rate of the dichromatic lamp at 185 nm is significant in the sense that it leads to an appreciable degree of water photolysis. The hydroxyl radicals produced contribute to the observed rate of *p*-cresol disappearance. The role of the hydroxyl radicals produced by water photolysis was probed by adding excess isopropyl alcohol (a hydroxyl radical scavenger) to the solution to eliminate the radical contribution to *p*-cresol conversion (results in Figure 5). Reaction rate constants for hydroxyl radicals with isopropyl alcohol and *p*-cresol are 1.9×10^9 and $1.2 \times 10^{10} \text{ M}^{-1}\text{s}^{-1}$ [16], respectively, so that an isopropyl alcohol concentration 1000 \times that of *p*-cresol was sufficient to scavenge all the hydroxyl radicals. Decreased *p*-cresol degradation in the presence of isopropanol (Figure 5) indicates that water photolysis contributes significantly to target transformation and must be considered in the kinetic model for the dichromatic lamp.

The fluence rate of the dichromatic lamp at 185 nm was determined by fitting the kinetic model to data of *p*-cresol degradation at two initial concentrations (Figure 6). It is important to note that > 90% of 185-nm light is absorbed in one pass because of the relatively high absorbance of water at that wavelength. Thus, effects of reflections were disregarded at that wavelength. The direct photolysis of *p*-cresol at 185-nm light was also neglected in the application of the model, since water absorbs most of the light. A value of $I_{185nm} = 2 \times 10^{-6} \text{Ein L}^{-1}\text{s}^{-1}$ was obtained, which is more than 10× lower than the fluence rate at 254 nm ($6.5 \times 10^{-5} \text{Ein L}^{-1}\text{s}^{-1}$).

The effect of 185-nm light on hydrogen peroxide decomposition was also examined using the kinetic model. Model calculations include the fluence rate at 254 nm determined via actinometry and the fluence rate at 185 nm determined above. Good agreement is apparent between simulations and experimental data (Figure 7). Omission of hydroxyl radical production from water photolysis causes the model to underestimate the decomposition rate of hydrogen peroxide.

Model predictions: significance of reflection

The calibrated kinetic model was used to predict the degradation of *p*-cresol via hydrogen peroxide photolysis in the low pressure UV reactor. Comparison with experimental data (Figures 8 and 9) provide model validation. Both lamps were used for this work.

Experiments were designed to achieve a wide range of one-pass (lamp to wall) light transmittance (32.3% to 93.8%) at 254 nm based on changes in initial concentrations of *p*-cresol and H₂O₂. The kinetic model accurately simulates *p*-cresol degradation over the entire range of independent variables examined.

The results clearly illustrate the impact of the reflective surface. The dashed lines in each figure are predictions of reactor performance with a zero reflectance wall. As expected, the degree to which reflection improves reactor performance increases as the one-pass transmittance of the original solution increases.

Concluding remarks

The oxidation of *p*-cresol by the UV/H₂O₂ process in an annular flow-through reactor has been represented by a kinetic model, which includes reactions of the UV/H₂O₂ photolysis system and a full mechanism for hydroxyl-radical-dependent transformation of *p*-cresol. The effects of light reflection from the reactor wall, loss of a fraction of light that is returned to the UV lamp after reflection and fluid dispersion under laminar flow conditions are represented in the model. Under high-transmittance conditions, reactor performance is significantly enhanced by reactor wall reflectance. There are undoubtedly cases in which the application of reflective coatings on UV reactor walls can enhance AOP reactor performance or reduce reactor size/energy intensity necessary to satisfy treatment constraints.

Acknowledgments

The authors would like to thank Dr. Long Cheng for helping install the equipment. This work was supported in part by USGS through the 104b grant program.

References

- [1] A. Pal, K.Y.H. Gin, A.Y.C. Lin, M. Reinhard, Impacts of emerging organic contaminants on freshwater resources: Review of recent occurrences, sources, fate and effects, *Sci. Total Environ.* 408 (2010) 6062–6069.
- [2] Y. Luo, W. Guo, H.H. Ngo, L.D. Nghiem, F.I. Hai, J. Zhang, S. Liang, X.C. Wang, A review on the occurrence of micropollutants in the aquatic environment and their fate and removal during wastewater treatment, *Sci. Total Environ.* 473–474 (2014) 619–641.
- [3] M. Klavarioti, D. Mantzavinos, D. Kassinou, Removal of residual pharmaceuticals from aqueous systems by advanced oxidation processes, *Environ. Int.* 35 (2009) 402–417.
- [4] J.C. Kruithof, P.C. Kamp, B.J. Martijn, UV/H₂O₂ treatment: A practical solution for organic contaminant control and primary disinfection, *Ozone-Science Eng.* 29 (2007) 273–280.
- [5] W.H. Glaze, Y. Lay, J.-W. Kang, Advanced Oxidation Processes. A Kinetic Model for the Oxidation Hydrogen Peroxide and U V Radiation, *Ind. Eng. Chem. Res.* 37 (1995) 2314–2323.
- [6] J.C. Crittenden, S. Hu, D.W. Hand, S.A. Green, A kinetic model for H₂O₂/UV process in a completely mixed batch reactor, *Water Res.* 33 (1999) 2315–2328.
- [7] M.R. Rojas, F. Pérez, D. Whitley, R.G. Arnold, A.E. Sáez, Modeling of advanced oxidation of trace organic contaminants by hydrogen peroxide photolysis and fentons reaction, *Ind. Eng. Chem. Res.* 49 (2010) 11331–11343.
- [8] M.R. Rojas, C. Leung, D. Whitley, Y. Zhu, R.G. Arnold, A.E. Sáez, Advanced oxidation of trace organics in water by hydrogen peroxide solar photolysis, *Ind. Eng. Chem. Res.* 50 (2011) 12479–12487.
- [9] T. Zhang, L. Cheng, L. Ma, F. Meng, R.G. Arnold, A.E. Sáez, Modeling the oxidation of phenolic compounds by hydrogen peroxide photolysis, *Chemosphere.* 161 (2016) 349–357.
- [10] C. Navntoft, E. Ubomba-Jaswa, K.G. McGuigan, P. Fernández-Ibáñez, Effectiveness of solar disinfection using batch reactors with non-imaging aluminium reflectors under real conditions: Natural well-water and solar light, *J. Photochem. Photobiol. B Biol.* 93 (2008) 155–161.
- [11] Q. Yang, S.O. Pehkonen, M.B. Ray, Light distribution model for an annular reactor with a cylindrical reflector, *Ind. Eng. Chem. Res.* 44 (2005) 3471–3479.
- [12] M. Li, Z. Qiang, J.R. Bolton, W. Ben, Impact of reflection on the fluence rate

distribution in a UV reactor with various inner walls as measured using a micro-fluorescent silica detector, *Water Res.* 46 (2012) 3595–3602.

- [13] B.C. MacDonald, S.J. Lvin, H. Patterson, Correction of fluorescence inner filter effects and the partitioning of pyrene to dissolved organic carbon, *Anal. Chim. Acta.* 338 (1997) 155–162.
- [14] D.F. Boltz, *Colorimetric determination of nonmetals*, 2nd editio, John Wiley and Sons Inc., 1978.
- [15] J.H. Barrett, Jack; Baxendale, The photolysis of liquid water, *Trans. Faraday Soc.* 56 (1960) 37–43.
- [16] G. V Buxton, C.L. Greenstock, W.P. Helman, A.B. Ross, Critical Review of rate constants for reactions of hydrated electrons, hydrogen atoms and hydroxyl radicals in aqueous solution, *J. Phys. Chem. Ref. Data.* 17 (1988) 513.

Figure captions

Fig. 1. Flow-through UV reactor (Neotech)

Fig. 2. Degradation of *p*-cresol via UV/H₂O₂ advanced oxidation as a function of the mean reactor residence time for (a) UV₂₅₄ monochromatic lamp, and (b) dichromatic lamp. Solid lines: model predictions obtained by fitting the model to decay curves using the fluence rate at 254 nm as an adjustable parameter (fitted values shown). Dashed line in (b) include effect of 185-nm irradiation. Initial conditions: [*p*-Cresol]₀ = 400 μM, [H₂O₂]₀ = 50 mM.

Fig. 3. UV decomposition of hydrogen peroxide as a function of average residence time in the continuous flow reactor with monochromatic lamp. Solid lines: model predictions obtained by fitting the model to the data with the adjustable parameter, $\beta = 0.15$.

Fig. 4. Degradation of *p*-cresol by direct photolysis using the monochromatic lamp. Solid lines: model predictions obtained by fitting the model to the data shown using *p*-cresol quantum yield (fitted value shown) as adjustable parameter.

Fig. 5. Degradation of *p*-cresol as a function of residence time in the dichromatic lamp in the absence and presence of isopropyl alcohol. The concentration of isopropyl alcohol employed (20 mM) ensures that it completely quenches hydroxyl radicals in the reactor.

Fig. 6. Degradation of *p*-cresol using the dichromatic lamp as a function of residence time and initial *p*-cresol concentration. Solid lines: model predictions obtained by fitting the kinetic model using the fluence rate at 185 nm as adjustable parameter. Dashed lines: model calculations neglecting the hydroxyl radicals generated by water photolysis at 185 nm.

Fig. 7. Decomposition of hydrogen peroxide as a function of residence time in experiments with the dichromatic lamp. Solid lines: model predictions considering both direct photolysis of H₂O₂ by UV₂₅₄ and reaction with hydroxyl radicals generated by water photolysis at 185 nm. Dashed lines: model calculations neglecting water photolysis.

Fig. 8. Degradation of *p*-cresol by UV/H₂O₂ advanced oxidation as a function of residence time and initial concentrations of *p*-cresol and H₂O₂ using the monochromatic lamp. Solid lines: model predictions. Dashed lines: model calculations neglecting surface reflection. The transmittance of the initial solution for the path length between the lamp and reactor wall is shown.

Fig. 9. Degradation of *p*-cresol by UV/H₂O₂ advanced oxidation as a function of residence time and initial concentrations of *p*-cresol and H₂O₂ using the dichromatic lamp. Solid lines: model predictions. Dashed lines: model calculations neglecting surface reflection. The transmittance of the initial solution for the path length between the lamp reactor wall is shown.

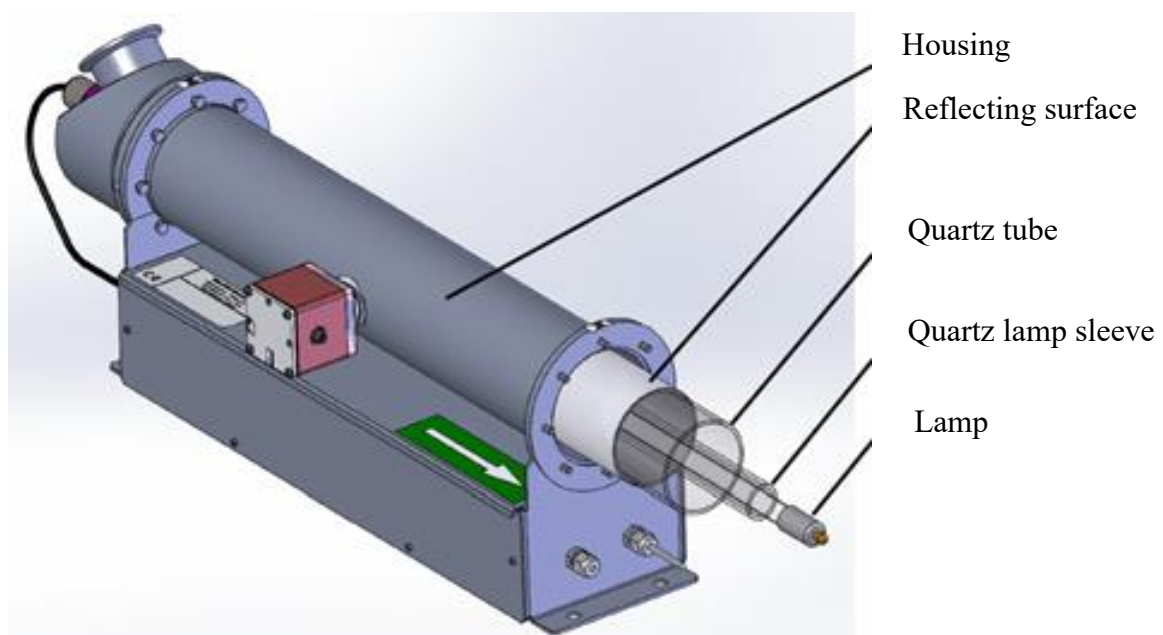


Fig. 1. Flow-through UV reactor (Neotech)

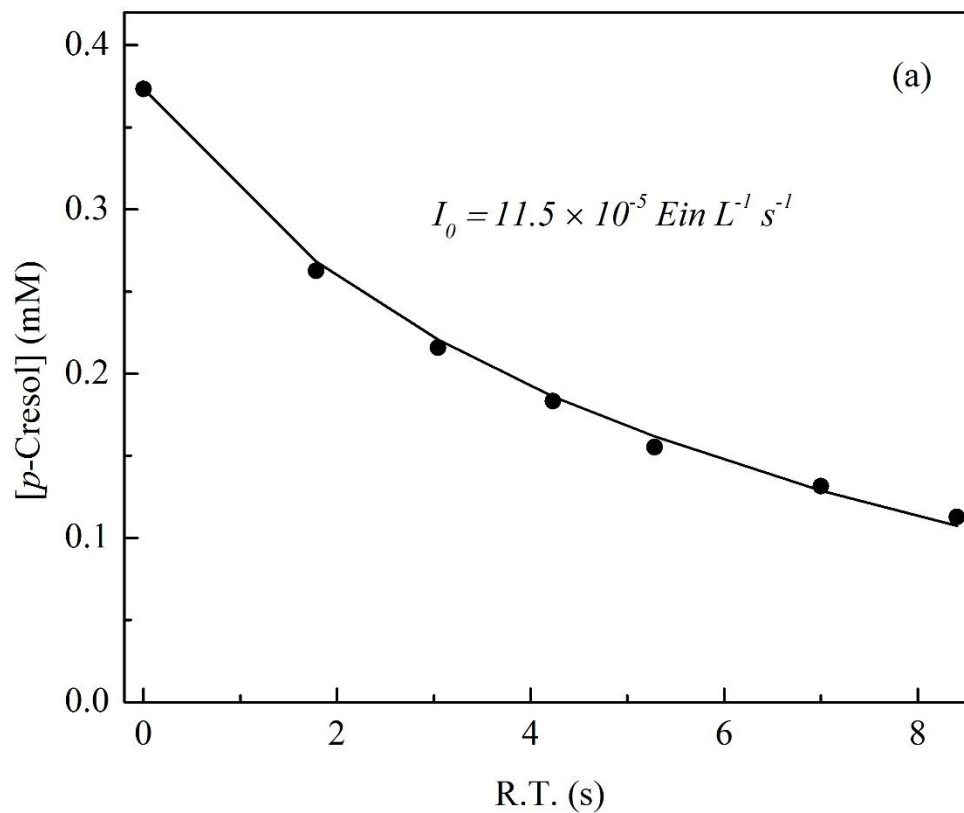


Fig. 2. Degradation of *p*-cresol via UV/H₂O₂ advanced oxidation as a function of the mean reactor residence time for (a) UV₂₅₄ monochromatic lamp, and (b) dichromatic lamp. Solid lines: model predictions obtained by fitting the model to decay curves using the fluence rate at 254 nm as an adjustable parameter (fitted values shown). Dashed line in (b) include effect of 185-nm irradiation. Initial conditions: [p-Cresol]₀ = 400 μM, [H₂O₂]₀ = 50 mM.

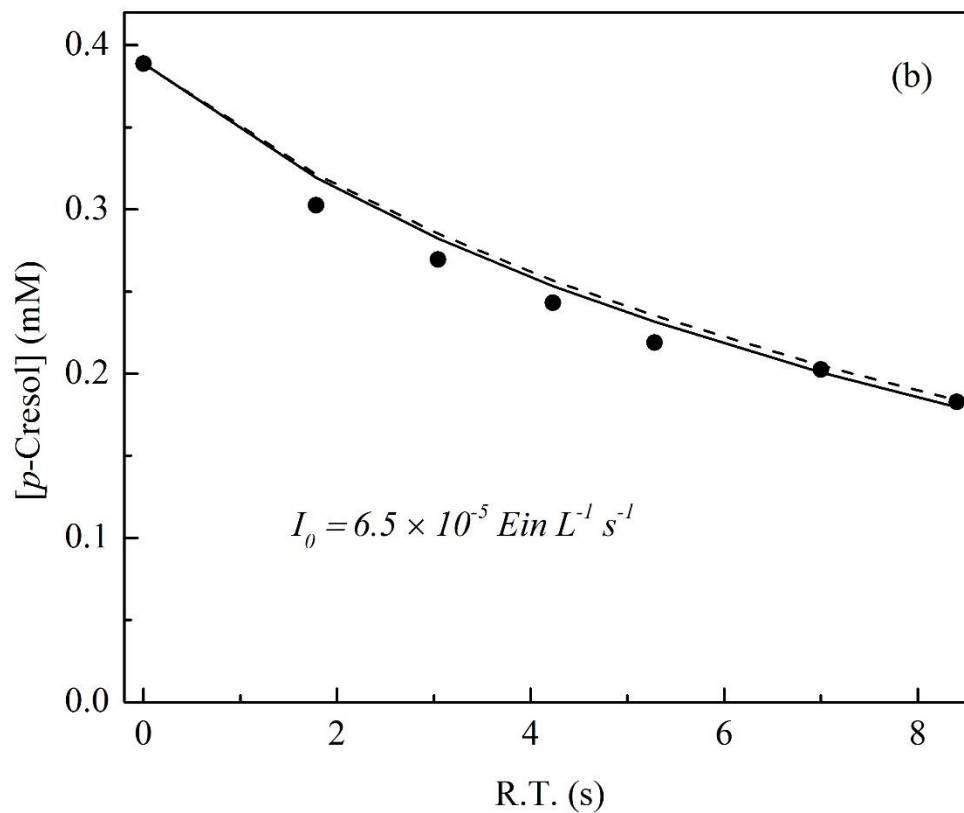


Fig. 2. Degradation of *p*-cresol via UV/H₂O₂ advanced oxidation as a function of the mean reactor residence time for (a) UV₂₅₄ monochromatic lamp, and (b) dichromatic lamp. Solid lines: model predictions obtained by fitting the model to decay curves using the fluence rate at 254 nm as an adjustable parameter (fitted values shown). Dashed line in (b) include effect of 185-nm irradiation. Initial conditions: [p-Cresol]₀ = 400 μM, [H₂O₂]₀ = 50 mM.

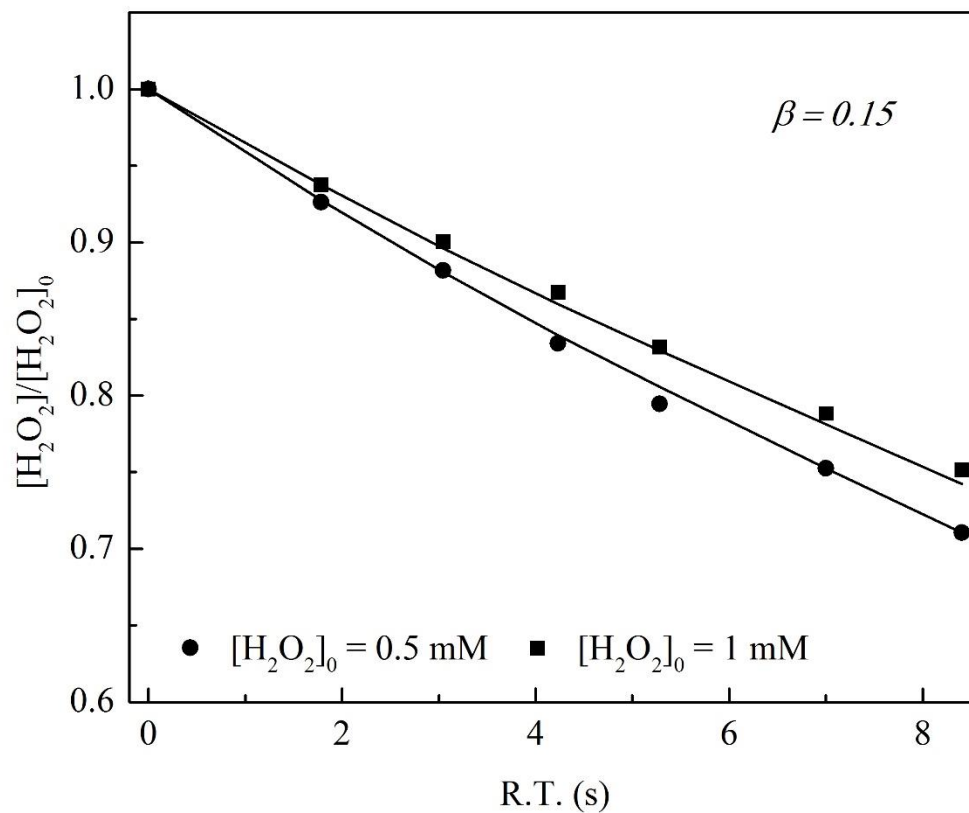


Fig. 3. UV decomposition of hydrogen peroxide as a function of average residence time in the continuous flow reactor with monochromatic lamp. Solid lines: model predictions obtained by fitting the model to the data with the adjustable parameter, $\beta = 0.15$.

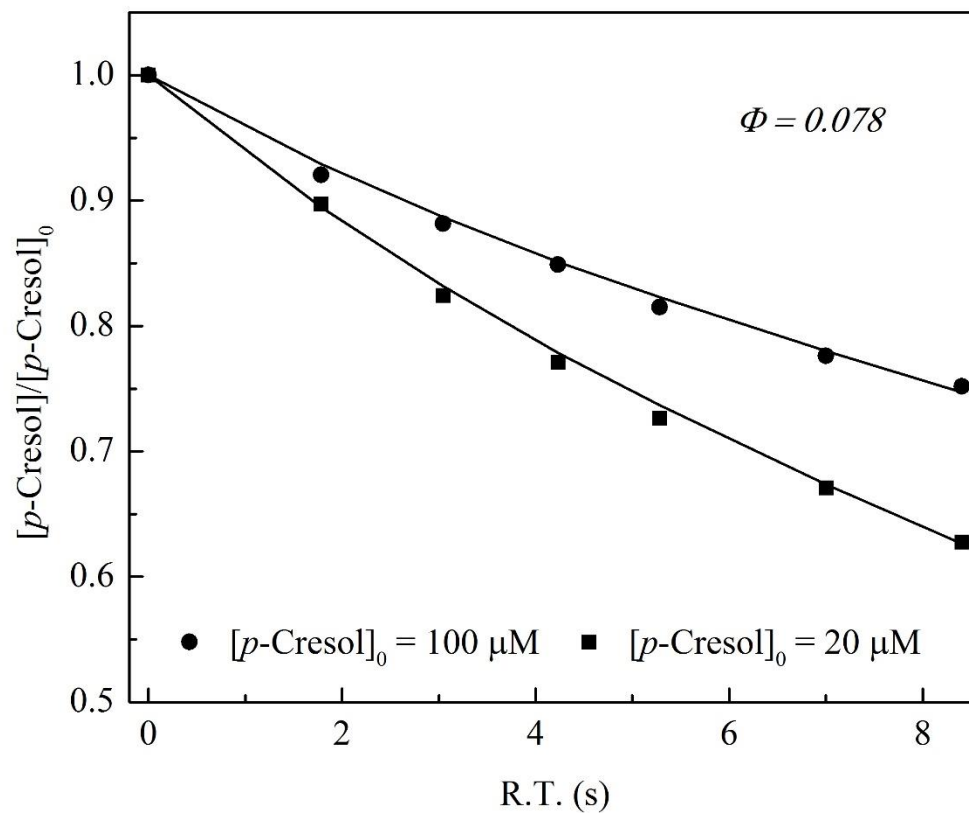


Fig. 4. Degradation of *p*-cresol by direct photolysis using the monochromatic lamp. Solid lines: model predictions obtained by fitting the model to the data shown using *p*-cresol quantum yield (fitted value shown) as adjustable parameter.

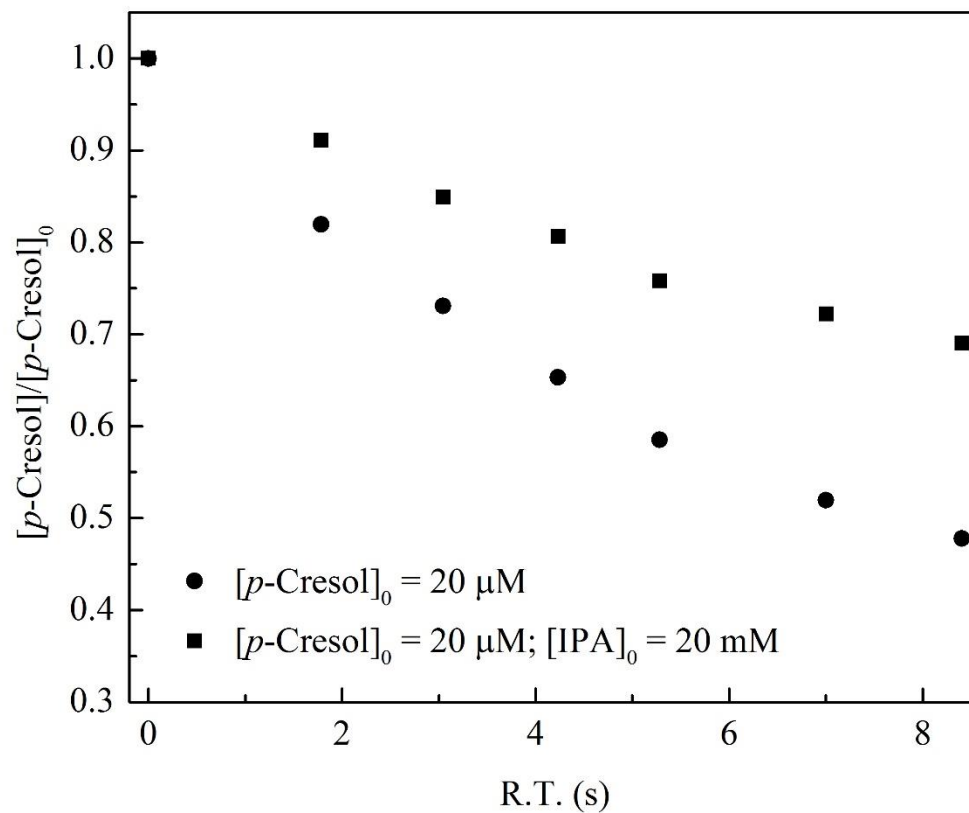


Fig. 5. Degradation of *p*-cresol as a function of residence time in the dichromatic lamp in the absence and presence of isopropyl alcohol. The concentration of isopropyl alcohol employed (20 mM) ensures that it completely quenches hydroxyl radicals in the reactor.

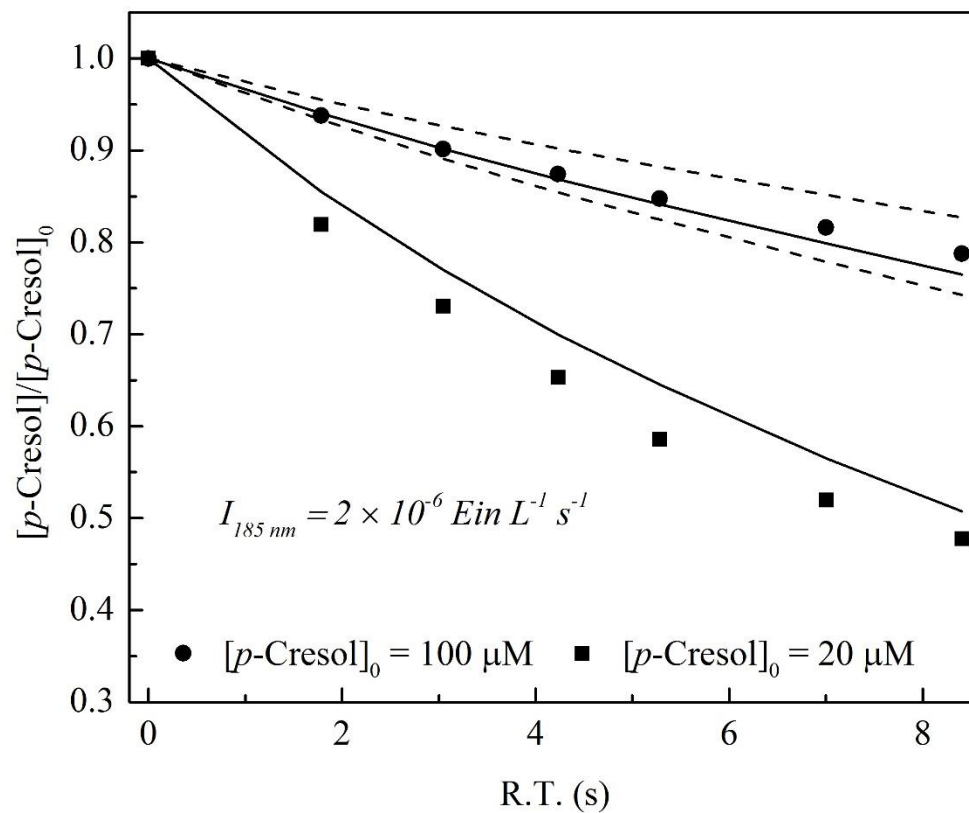


Fig. 6. Degradation of *p*-cresol using the dichromatic lamp as a function of residence time and initial *p*-cresol concentration. Solid lines: model predictions obtained by fitting the kinetic model using the fluence rate at 185 nm as adjustable parameter. Dashed lines: model calculations neglecting the hydroxyl radicals generated by water photolysis at 185 nm.

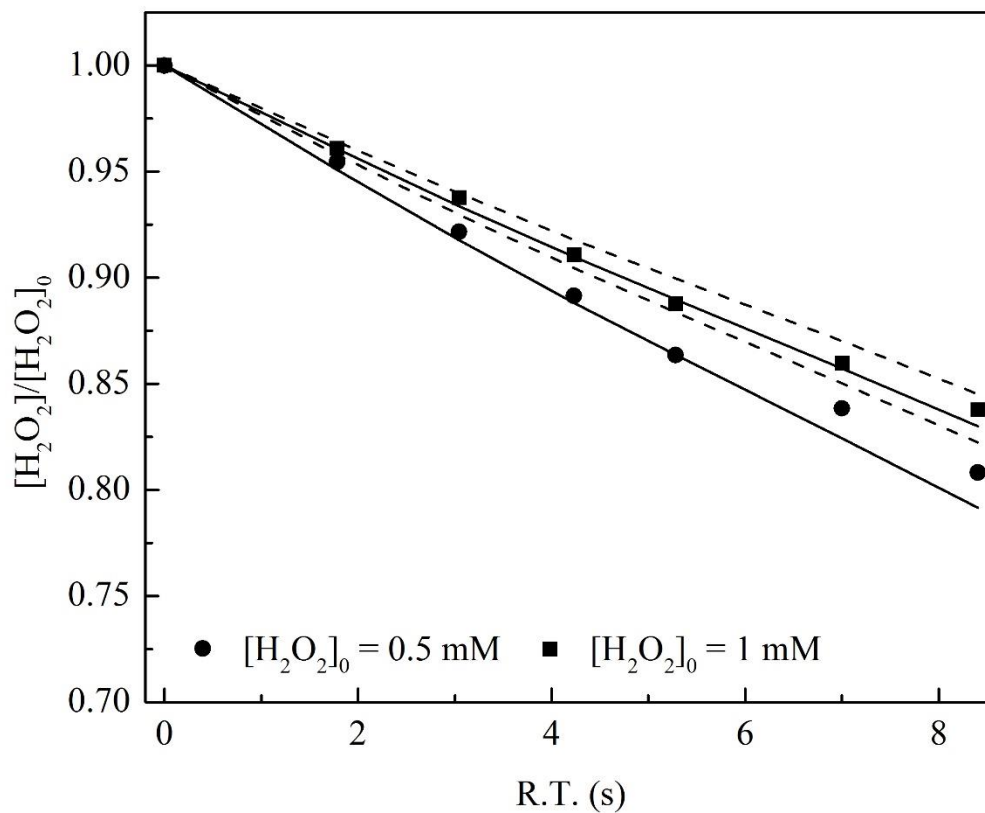


Fig. 7. Decomposition of hydrogen peroxide as a function of residence time in experiments with the dichromatic lamp. Solid lines: model predictions considering both direct photolysis of H_2O_2 by UV_{254} and reaction with hydroxyl radicals generated by water photolysis at 185 nm. Dashed lines: model calculations neglecting water photolysis.

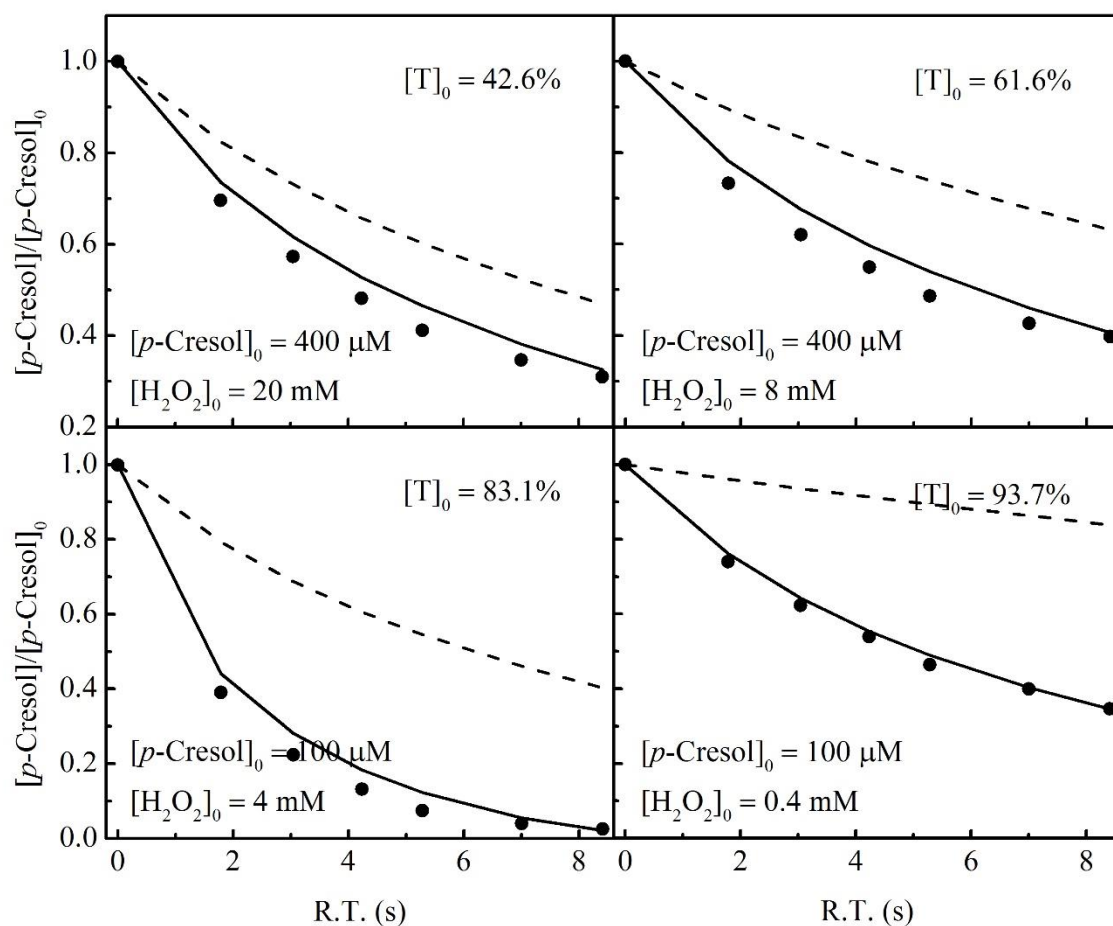


Fig. 8. Degradation of *p*-cresol by UV/H₂O₂ advanced oxidation as a function of residence time and initial concentrations of *p*-cresol and H₂O₂ using the monochromatic lamp. Solid lines: model predictions. Dashed lines: model calculations neglecting surface reflection. The transmittance of the initial solution for the path length between the lamp and reactor wall is shown.

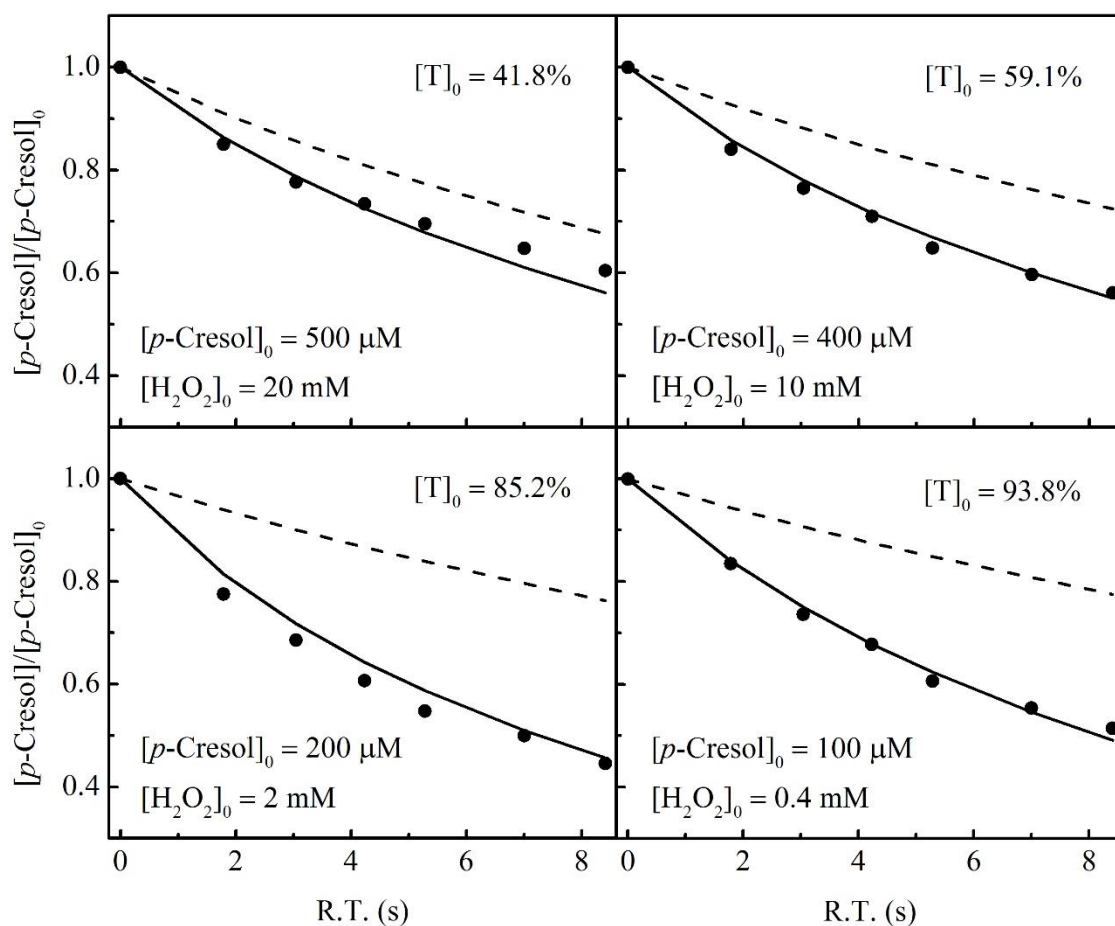


Fig. 9. Degradation of *p*-cresol by UV/H₂O₂ advanced oxidation as a function of residence time and initial concentrations of *p*-cresol and H₂O₂ using the dichromatic lamp. Solid lines: model predictions. Dashed lines: model calculations neglecting surface reflection. The transmittance of the initial solution for the path length between the lamp reactor wall is shown.

APPENDIX C

**FATE OF TRACE ORGANICS IN A WASTEWATER EFFLUENT DEPENDENT
STREAM**

Bingfeng Dong,^a Alandra Kahl,^b Long Cheng,^a Hao Vo,^a Stephanie Ruehl,^a Tianqi
Zhang,^a
Shane Snyder,^a A. Eduardo Sáez,^a David Quanrud^{c*} and Robert G. Arnold^a

^aDepartment of Chemical and Environmental Engineering, The University of Arizona,
Tucson, AZ 85721

^bPenn State Greater Allegheny, Pennsylvania State University, McKeesport, PA 15132

^cSchool of Natural Resources and the Environment, The University of Arizona, Tucson,
AZ 85721

*Corresponding author at: School of Natural Resources and the Environment, University
of Arizona, AZ 85721, USA. Tel: +1 520 621 8591; fax: +1 520 621 8801. Email
address: quanrud@email.arizona.edu (D. Quanrud)

Abstract

Trace organic compounds (TOrcs) in municipal wastewater effluent that is discharged to streams are of potential concern to ecosystem and human health. This study examined the fate of a suite of TOrcs and estrogenic activity in water and sediments in an effluent-dependent stream in Tucson, Arizona. Sampling campaigns were performed during 2011 to 2013 along the Lower Santa Cruz River, where TOrcs and estrogenic activity were measured in aqueous (river) and solid (riverbed sediment) phases. Some TOrcs, including contributors to estrogenic activity, were rapidly attenuated with distance and time of travel in the river. Those TOrcs that survived percolation to ground water have in common low biodegradation probabilities and low octanol-water distribution ratios. Independent experiments showed that attenuation of estrogenic compounds may be due in part to indirect photolysis caused by formation of organic radicals from sunlight absorption. Hydrophobic TOrcs may accumulate in riverbed sediments during dry weather periods; riverbed sediment quality is periodically improved through storm-related scouring during periods of heavy rainfall and runoff. Taken together, evidence suggests that natural processes can attenuate at least some TOrcs, reducing potential impacts to ecosystem and human health.

Keywords: trace organic compounds; estrogenic activity; solar photolysis; effluent dependent stream.

Introduction

For more than thirty years, it has been known that pharmaceuticals, personal care products and other trace organic contaminants (TOrcs) survive conventional wastewater treatment and persist in the environment to varying degrees (Richardson and Bowron, 1985; Ahel et al., 1994a; Kolpin et al., 2002). More than any other group of trace organics in municipal wastewater, endocrine disrupting compounds (EDCs) have attracted the attention of health professionals and the public (Heberer, 2002; Teske and Arnold, 2008; Sumpter and Jobling, 2013). These compounds interfere with normal endocrine function by blocking signaling/response (antagonists) or stimulating inappropriate activity (agonists). Chemicals present in municipal wastewater that promote estrogenic response include natural steroidal estrogens such as estrone (E_1), 17β -estradiol (E_2) and estriol (E_3), and anthropogenic mimics such as 17α -ethinylestradiol (EE_2) and alkylphenols (APs) (Routledge and Sumpter, 1996; Teske and Arnold, 2008). All these compounds share similar chemical structure: presence of phenolic rings, similar molecular weight, and mild to high hydrophobicity.

Early evidence of endocrine disrupting activity in treated wastewater arose from elevated incidence of intersex characteristics (compromised gonadal growth, spermatogenesis, sperm motility, and fertilization success) among male fish in rivers of the United Kingdom (Purdom et al., 1994; Jobling et al., 1998). E_2 and EE_2 elicit physiological changes in continuously exposed organisms at levels that are routinely measured in conventionally treated municipal wastewater effluent (Sanchez et al., 2011). Factors that influence the removal of EDCs and other TOrcs during wastewater treatment have been

widely studied. Simulations of conventional treatment have not, however, been entirely successful in predicting chemical-specific removal efficiencies during municipal wastewater treatment (Rojas et al., 2010).

Gross et al. (2004) studied the fates of TOrCs in an effluent dominated stream and wetland in southern California, measuring attenuations of ibuprofen, gemfibrozil and chlorinated tris-propylphosphates as well as the conversion of alkylphenol polyethoxylates to APs. Fono et al. (2006) measured the attenuations of ethylenediaminetetraacetate (EDTA), gemfibrozil, ibuprofen, metoprolol, naproxen, and total adsorbable organic iodide in the Trinity River, an effluent dominated stream in Texas. Although the iodated compounds were conserved, others decreased in concentration by 60-90% during two weeks of travel over 500 km. In a more recent Arizona survey, Chiu and Westerhoff (2010) found that surface water concentrations of sucralose, sulfamethoxazole, acetaminophen, cotinine, dilantin, caffeine, DEET and oxybenzone exhibited seasonal trends. Oxybenzone and sucralose concentrations were generally higher in summer months due to increased recreational use of surface water resources.

Candidate mechanisms for the attenuation of trace organics during in-stream transport include biodegradation, photolysis and adsorption on riverbed sediments (Barber et al., 2013; Hanamoto et al., 2013; Writer et al., 2013). Conditional rate constants representing relative compound biodegradability have been based on either direct measurement (Salveson et al., 2010) or moiety-specific contributions to biological transformation rates (ASTreat 1.0, a windows based computer model designed by Procter and Gamble

Company, 1999). The contribution of removal on organic solids should be directly related to compound hydrophobicity, as reflected by octanol/water partitioning (K_{ow} or D_{ow}) (Ying et al., 2002; Snyder et al., 2003). It is expected that, other factors being equal, compound hydrophobicity would lead to accumulation in river sediments due to both sedimentation and the retention of contaminants during infiltration. Direct and indirect photolysis also contribute to in-stream compound disappearance (Watts and Linden, 2008; Wols and Hofman-Caris, 2012). Direct photolysis occurs when a compound undergoes transformation as a result of light absorption. This is envisioned as a two-step process in which the absorption of light energy promotes the compound to an excited state, after which either chemical transformation occurs or the excited compound devolves to its original ground state. Indirect photolysis is initiated through light absorption by other chemicals, leading to production of reactive intermediates such as hydroxyl or organic radicals that react chemically with the target compound (Wols and Hofman-Caris, 2012).

The Santa Cruz River (SCR) is an effluent dependent stream in Tucson, Arizona (Figure 1). Prior to 2014, the Pima County Regional Wastewater Reclamation Department's (PCRWRD) two major wastewater treatment plants discharging to the SCR were the Roger Road wastewater treatment plant (RRWTP; trickling filter) and the Ina Road Water Pollution Control Facility (IRWPCF; activated sludge). Due to a mandate by the State of Arizona requiring nutrient removal, in February 2014 the RRWTP was decommissioned and replaced by the Agua Nueva Water Reclamation Facility (WRF) and the IRWPCF was similarly upgraded and renamed the Tres Rios WRF. This study

was conducted prior to the new WRFs going online. Together, the two upgraded WRFs discharge ~50,000 AFY (acre-feet per year) (6.17×10^7 m³/year) of municipal wastewater effluent to the SCR. Galyean (1996) estimated that about 90% of the treated wastewater effluent discharged to the SCR infiltrates within a 25-mile (40 km) length downstream from the RRWTP. With the improved effluent quality discharged to the SCR since early 2014, it is anticipated that infiltration rates in the riverbed will increase and the length of the wetted reach will decrease relative to the period prior to February 2014. In a 1999-2000 nationwide survey of United States surface waters, the US Geological Survey measured some of the highest in-stream concentrations of trace organics at a sampling point in the lower SCR, several miles downstream from the IRWPCF outfall (Kolpin et al., 2002). The rainfall pattern in southern Arizona typically includes brief periods of heavy precipitation in the summer months (the Sonoran monsoon) that motivate equally brief periods of high stream flow (Figure S1). It has been shown that these events tend to scour sediments in the SCR, redistributing deposits that accumulate over the remainder of the year (Lacher, 1996). It is expected that high flow conditions in the river will produce discontinuities in time-dependent sediment concentrations of trace organic contaminants, although this has not been confirmed via direct measurement.

In this work, concentrations of TO_rCs of wastewater origin and estrogenic activity were measured in SCR surface waters, groundwater samples obtained from monitoring wells proximate to the SCR, and riverbed sediments. The monitoring program and supplementary controlled experiments using local effluent were designed to test hypotheses regarding mechanisms of stream purification. The work is timely in light of

process improvements recently completed at the Agua Nueva WRF and Tres Rios WRF and consequent improvements in both effluent and environmental quality. The data provide a baseline against which the effects of process improvements can be measured.

Our hypotheses related to natural stream purification mechanisms follow:

1. Biodegradable TOrCs, including those that contribute to estrogenic activity, are rapidly attenuated with distance and time of travel in the SCR. It is noted that dilution is not a candidate mechanism for contaminant attenuation, since the SCR is effluent dependent except during infrequent periods of rainfall/runoff.
2. The primary mechanisms of TOrC attenuation in the river are related to physical/chemical properties of the contaminants including biodegradability, hydrophobicity and susceptibility to indirect or direct photolysis.
3. Riverbed sediments are a sink for TOrCs during dry weather periods and are periodically scoured from the bottom during storm-related periods of high water flow.

Materials and methods

Chemicals and reagents

All TOrCs measured in this work (Table 1) were reagent grade or better and used as obtained. Bisphenol A and tris (2-chloroethyl) phosphate (TCEP) were from TCI America (Portland, OR). N,N-diethyl-meta-toluamide (DEET), ibuprofen, triclosan and perfluorooctanesulfonic acid (PFOS) were from Alfa Aesar (Lancashire, UK). Iopromide was from USP (Rockville, MD). Tonalide was purchased from Toronto Research Chemicals (Toronto, Canada). Sucralose was from AK Scientific (Union City, CA). Perfluorohexadecanoic acid (PFHxDA) was from Matrix Scientific (Columbia, SC) and

meprobamate was from Cerilliant (Round Rock, TX). The rest of the compounds were acquired from Sigma-Aldrich (St. Louis, MO). Compounds were selected based on their presence in conventionally treated wastewater effluent in previous studies and the existence of sufficiently sensitive analytical methods. Together, they provide a broad range of physical/biochemical characteristics, allowing us to investigate hypothesized cause-effect relationships governing contaminant fates in surface waters.

Isotopically labeled internal standards were from three sources. $^{13}\text{C}_4$ -PFOA, $^{13}\text{C}_4$ -PFOS, $^{13}\text{C}_2$ -PFHxDA, $^{13}\text{C}_4$ -PFBA were from Wellington Laboratories (Ontario, Canada). $^{13}\text{C}_6$ -diclofenac, primidone-d₅, Ibuprofen-d₃, sulfamethoxazole-d₄, triclosan-d₃ and iopromide-d₃ were from Toronto Research Chemicals (Toronto, Canada). Gemfibrozil-d₆, 4-nonylphenol-d₄, estrone-d₄, DEET-d₇, carbamazepine-d₁₀ and bisphenol A-d₁₆ were from C/D/N Isotopes (Quebec, Canada).

Stock solutions of target analytes and internal standards were prepared in 50 v% water/methanol. Calibration and fortification solutions were prepared by successive dilution of stocks to 10 µg/L in methanol. Liquid chromatography solvents were of the highest purity available. Methanol, acetonitrile and formic acid were purchased from EMD Chemicals (Gibbstown, NJ). Methyl *tert*-butyl ether (MTBE) and ammonium hydroxide were from Fisher Scientific (Pittsburgh, PA). LCMS reagent water was obtained from J.T. Baker (Center Valley, PA).

Sample collection and preparation

Sample collection vessels and all glassware were cleaned with methanol and rinsed three times with ultrapure water, then heated in Thermolyne 6000 Muffle Furnace (Dubuque,

IA) at 550 °C for 5 h prior to use. In spring and summer 2011, surface water and groundwater sampling was performed three times at twelve locations along the 37-km study reach (Figure 1). Groundwater samples near the river were obtained from a series of eleven monitoring wells owned by the PCRWRD.

Liquid samples were filtered through 0.7 µm glass fiber filters (Pall Corporation, Fort Washington, NY) before deuterated internal standards were added. Samples were then extracted using Oasis HLB SPE cartridges (Waters, Milford, MA). HLB sorbents were first conditioned by stepwise addition of 5 mL of methanol, 5 mL of MTBE and 5 mL of water. A half gram of EDTA was dissolved in 1 L of each water sample before it was loaded onto the SPE sorbent at 10 mL/min using a Dionex™ AutoTrace™ 280 Solid-Phase Extraction (SPE) instrument (Thermo Scientific, Pittsburgh, PA). Following the sorption step, sorbents/adsorbates were dried under nitrogen gas for 40 min before they were sequentially eluted with 3 mL of methanol, 3 mL of 5% NH₄OH in MeOH, 3 mL of acetonitrile and 3 mL of MTBE. The combined eluents were evaporated to about 50 µL and re-dissolved in 1 mL of 50% water/methanol for liquid chromatography tandem mass spectrometric (LC/MS) analysis.

In 2012-2013, surface water and riverbed sediment samples were collected four times at five SCR locations (Figure 1). Locations were chosen based on ease of access, position in the river (0-37 km extending northwest from the RRWTP outfall) and presence of representative riverbed sediments. The river was dry upstream of the RRWTP outfall, except during storm runoff episodes. At each sampling point, 4-L surface water samples were collected. The monitoring program was designed to provide samples before (June

22, 2012), during (July 18, 2012) and after (October 13, 2012) the summer precipitation period (July-September—Sonoran monsoon). A fourth set of samples was collected after a winter rainfall event (February 3, 2013). At each sampling site/time, one riverbed surface sediment sample and one sediment core samples (5 cm in diameter) were collected. These were subsequently used to produce sediment samples, hereinafter referred to as surface sediment (0-2.5 cm) and bottom core sediment (10.2-12.7 cm). Surface sediment samples were obtained using a clean stainless steel trowel. Core samples were collected using a purpose-built stainless steel core sampler (Rickly Hydrological Co., Columbus, OH; model 603-004) that was driven into the riverbed and then withdrawn. Cores were retained in the sampler during withdrawal by a core catcher mechanism. Sediment cores and samples were transferred to muffled glass jars, stored at 4 °C and extracted on the day after collection.

Two liters of each surface water sample were filtered through a 0.7 µm Whatman GF/F glass fiber filter (GE Healthcare). The pre-weighed filters and non-filterable solids were dried for 48 h at 60 °C and reweighed to establish suspended solids concentrations before organics in the suspended solid of river samples were extracted via microwave-assisted extraction (MAE) using a Microwave Accelerated Reaction System (MARS, CEM Corporation, Glendale, CA) (Lopez-Avila et al., 1994; Sparr Eskilsson and Björklund, 2000; Sanchez-Prado et al., 2010). For suspended solids, the whole dried portion retained on the glass fiber filter was used. For riverbed sediment extractions, about 3 g of dried sediment were used. The samples were conditioned overnight in 15 mL methanol in Teflon microwave vessels ahead of MAE extractions (70 °C for 60 min). Extracts were

poured off and saved, after which vessels and residual sediments were rinsed twice with 5 mL methanol. The pooled extracts were then dried under a gentle stream of N₂ gas before residual organics were re-dissolved in 1 mL methanol. In order to clean the extracts, the methanol containing extracted organics was diluted to 250 mL with nanopure water before the mixture was slowly passed under vacuum through 47 mm Empore™ Extraction Disks (octadecylsilane, 3M, Eagan, Minnesota). Retained organics were separated by sequential elution in a stepwise methanol gradient using 15 mL washes consisting of 20%, 50%, 80% and 100% (v/v) methanol in water. Half of each eluent mixture was added to a single 40-mL glass vial and stored at 4 °C for further processing. The other half was dried under nitrogen and redissolved in nanopure water for analysis of estrogenic activity. To eliminate bacterial contamination, samples for measurement of estrogenic activity were autoclaved at 121 °C for 10 min prior to analysis (Littlehat, 2007).

Yeast estrogen screen (YES) bioassay method

The YES bioassay, based on that of Routledge and Sumpter (1996), was used to measure estrogenic activity in sample extracts. The test organism was a recombinant strain of *Saccharomyces cerevisiae* in which the DNA sequence of the human estrogen receptor (hER- α) was integrated into the yeast genome. The yeast strain also contains expression plasmids carrying estrogen-responsive sequences (EREs) controlling transcription of the reporter gene *lacZ* (encoding β -galactosidase). In the presence of estrogen, β -galactosidase is synthesized in the cells. Its activity is measured colorimetrically. Sample extracts were serially diluted across 96-well micro-titer plates (Corning Costar®),

Corning, NY). In positive controls, refreshed cells were added to serial dilutions of standard hormone (EE₂) preparations. Cell suspensions were incubated for 24 h at 32 °C in the presence of either the prepared extracts or known concentrations of EE₂ for growth and hormone-dependent gene expression. After that, 50 µL of cycloheximide (4 mg/mL)/CPRG (chlorophenol red β-D-galactopyranoside, 0.4 mg/mL) solution was added to each test well. Following an additional incubation for 24 h at 32 °C, color was measured: $A_{570} - R \times A_{630}$, using a UV-VIS micro-plate reader (Bio-tek Instruments, Winooski, VT), where A is absorbance at the indicated wavelength (nm), and R is the ratio of optical densities at 570 nm and 630 nm in negative controls. Color was converted to total sample estrogenic activity using results of the contemporary positive control. To compare standards and samples from one event to another, data were normalized as follows

$$\% \text{ relative estrogenic activity} = \frac{A_{\text{sample}} - A_{\text{background}}}{A_{\text{maximum}} - A_{\text{background}}} \times 100\%$$

In the equation, A_{maximum} and $A_{\text{background}}$ are the maximum and the negative control absorbances at 570 nm for the standard curve (EE₂ solution), and A_{sample} is the absorbance of the sample. The percent relative estrogenic activity for the sample was the estrogenic activity indicated relative to the standard curve run along with the data set. That is, the range of response observed in the standard was used to normalize the data from the sample.

A practical quantification limit (PQL) for the assays was arbitrarily adopted as the EC₂₀ value for EE₂ divided by the highest sample concentration factor tested in the YES procedure (normally 400). Below the PQL was a method detection limit (MDL). The

MDL was the EE_2 concentration that produced a test response equal to 3 times the standard deviation in $(A_{570}-R \times A_{630})$ in hormone-free (blank) test wells, divided by the highest concentration factor tested.

Gas chromatography–mass spectroscopy

An Agilent 6890 gas chromatograph and Agilent 5973 mass-selective detector were used for GC-MS analyses of nonylphenol (NP) and octylphenol (OP). Compounds were separated on a fused silica column (HP5-MS, 30 m \times 0.25 mm i.d., 0.25 μ m film thickness, Agilent, Santa Clara, CA). The oven temperature program used was: 1 min at 90 °C, ramp at 15 °C min^{-1} to 220 °C, hold for 2 min, ramp at 15 °C min^{-1} to 240 °C, followed by 10 °C min^{-1} to 280 °C. Helium was the carrier gas at a constant flow rate of 1 mL min^{-1} . The inlet, transfer line and ion source were at 250, 280 and 230 °C, respectively. Sample injection (1 μ L) was in splitless mode. The mass detector was operated in the electron ionization mode using selected ion monitoring (SIM) method. Quantification ions were as follows: m/z 135 for NP and m/z 107 for OP. The limit of detection (LOD) and limit of quantification (LOQ) were defined as three times and ten times the signal-to-noise ratio (Komori et al., 2004).

Liquid chromatography–mass spectrometry

An Agilent 1290 Infinity LC System and Agilent 6460 Triple Quadrupole LC/MS system with both positive and negative electrospray ionization were used for analyses of other trace organic contaminants. Multiple-reaction monitoring mode was used for fragmentation data, monitoring both quantifiers (highest response product ion) and qualifiers (next highest product ion) for each compound measured. Calibration curves

contained at least five points, with $R^2 > 0.99$ for linear fits. LOD and LOQ were defined the same as in the GC-MS analytical work. When surrogate (isotope) recovery was less than 5%, concentrations were flagged as non-detectable due to disappearance during extraction.

Photodegradation of estrogenic activity in secondary effluent

Milli-Q water (18 M Ω) was prepared using a Millipore water purification system (Billerica, MA). Secondary effluent from the RRWTP was spiked with EE₂ (0.32 nM). Irradiation experiments were done in direct sunlight in cloud-free weather. Five glass photoreactors, containing 600 mL Milli-Q water or secondary effluent plus EE₂ were set up in parallel and sacrificed at 0, 0.5, 1, 2 and 4 h for analysis via excitation-emission matrix (EEM) fluorescence spectroscopy and the YES bioassay (estrogenic activity). Dark controls were set up and sacrificed after four hours for the same set of measurements.

Fluorescence of secondary effluent samples was characterized by a PerkinElmer LS 55 fluorescence spectrophotometer (Walham, MA). The inner filter effect (IFE) caused by light absorption and reabsorption of emitted light by light-absorbing compounds was corrected by a mathematical model that takes into account the absorption spectrum of the sample (MacDonald et al., 1997). A Thermo Scientific Genesys 10s UV-Vis spectrophotometer was employed to obtain the absorption spectra of test samples. EEM fluorescence data obtained from the fluorescence spectrophotometer corresponded to scan ranges of emission and excitation wavelengths of 280 to 400 nm. Scan speed was 600 nm/min.

Results and discussion

Trace organics attenuation in the Santa Cruz River

A suite of twelve dissolved TOrCs (Table 1) were measured over the same (37-km long) reach of the SCR during three sampling campaigns in 2011, while *p*-nonylphenol (NP) and *p*-octylphenol (OP) were measured separately during a February 2013 sampling event.

For the sampling campaigns in 2011, the twelve TOrCs measured were detected in the effluents of both the RRWTP and IRWPCF and at all twelve sampling points along the 37-km study reach of the Santa Cruz River. A complete set of results from these three sampling periods is provided in Table S1. TOrCs present at the highest concentrations were sucralose, sulfamethoxazole, trimethoprim and DEET. Of these compounds, DEET, trimethoprim, and iopromide were substantially higher in effluent from the RRWTP than in the IRWPCF effluent, whereas the reverse was true for primidone and fluoxetine.

Since IRWPCF is located about 7.5 km downstream of the RRWTP, and the contribution of TOrCs from the IRWPCF secondary effluent to the SCR may be significant, only the distributions of contaminant concentrations between the IRWPCF and the end of our survey area (37 km downstream of the RRWTP) were representative of attenuation.

Profiles of TOrC concentration with distance downstream from the IRWPCF (Figures 2a and 2b) indicate that tonalide, fluoxetine, iopromide, sucralose (not shown) and PFOS were attenuated during surface transport along the 37-km studied reach of the river.

Carbamazepine, DEET, sulfamethoxazole, TCEP, trimethoprim and primidone were conserved.

Concentrations of NP and OP in the SCR were measured during the February 2013 sampling event. In filtered river samples, NP concentrations ranged from 244-484 ng/L (Figure 2c), which were smaller than the concentration of NP in the river at N. Cortaro Road (location in Figure 1) reported by Kolpin et al. (2002). OP concentrations spanned the range 8.6-101 ng/L, although only one stream sample was above 50 ng/L. This was within the range of results of Kolpin et al. (2002). Profiles of NP and OP concentration versus distance downstream followed the same trends, first decreasing below the RRWTP and then fluctuating modestly with distance in the stream reach immediately below the IRWPCF outfall. The data are consistent with the hypothesis that are in-stream conversion of alkylphenol polyethoxylates and carboxylates (APnEOs and APnECs) to the more stable AP forms, as observed by others (Ahel et al., 1994b; Gross et al., 2004). Concentrations of NP were about 10-fold greater than OP in all river water samples, probably due to the widespread use of nonylphenol ethoxylates (NPnEOs) in industrial, agricultural, and domestic applications (Giger et al., 1984). Although in-stream loss was not observed here, previous work has shown that NP biodegrades under aerobic conditions during wastewater treatment and in receiving waters (Soares et al., 2008). Attenuation and persistence trends in the position-dependent TOrCs concentrations were examined using linear regression analysis. Examples are provided in Figure 2, and results are summarized in Table 2. The measured values decreased significantly with distance ($p \leq 0.05$) for five of the twelve compounds (Table 2). Candidate mechanisms for TOrC attenuation in the river include biodegradation, photolysis and sorption on bottom sediments or suspended solids. Since none of the TOrCs monitored was volatile (i.e., all

had air-water partition coefficients $K_{AW} < 10^{-5}$, Table 1), and each survived conventional wastewater treatment, volatilization was neglected as a mechanism for in-stream attenuation.

Stepwise (backward) multiple linear regression was applied to analyze relationships between three independent variables ($\log D_{ow}$, P_B and k_{OH}) and attenuation of the trace organics in the river (dependent variable). Attenuation was represented by the normalized slope of compound concentration versus travel distance ($\Delta B_0/C_0$), where B_0 is the slope of the concentration vs. distance profile (Table 2) and C_0 is concentration in the river sample just beyond the IRWPCF outfall. Results (Table 3) indicate that the three independent variables, alone or together, do not account for a significant fraction of the observed compound-dependent attenuation in the Santa Cruz River, at least within the context of the linear model, and suggest that the responsible mechanism lies outside those proposed.

In-stream attenuation of estrogenic activity

Estrogenic activity was measured in the SCR during each of four sampling campaigns (2012-2013) to indirectly establish probable attenuation mechanisms (Figure 3a). The measured estrogenic activity in the RRWTP effluent (0 km point in Figure 3a) was almost two orders of magnitude higher than levels that feminize continuously exposed fathead minnows (*Pimephales promelas*) (Lange et al., 2001). Just 1.50 km below the RRWTP outfall, estrogenic activity was ~20-25% of measured levels in the RRWTP effluent. Travel time from the RRWTP outfall to that point is estimated at one hour. Despite the rapid attenuation of estrogenic activity, measured values exceeded

concentrations necessary to disrupt sexual differentiation and reproduction in continuously exposed organisms over a distance of ~10 km below the outfall. Total estrogenic activity in the SCR did not increase at the IRWRCF outfall located about 7.7 km below the RRWTP (Figure 3a). Beyond 11 km downstream from the RRWTP, estrogenic activity fell below the detection limit, estimated as 1.5×10^{-13} M (equivalent concentration of EE₂). Log D_{ow} values for estrogenic compounds in wastewater lie in the range 3-6 (e.g. EE₂, OP and NP, Table 1), suggesting that attenuation of their aqueous-phase concentrations is due in part to sorptive partitioning on organic-rich solids (Lee and Liu, 2002; Drewes et al., 2005). However, the contribution of estrogenic activity in extracts derived from in-stream suspended solids was < 20% of total estrogenic activity in all SCR samples and usually much less (Figure 3b), perhaps due to low residual suspended solids concentrations in plant effluents. Consequently, it is unlikely that sorption/sedimentation is a major contributor to loss of estrogenic activity with travel distance in the SCR.

As indicated previously, NP and OP concentrations in the river decreased much more slowly than total estrogenic activity. Furthermore, representative factors for converting NP and OP concentrations to equivalent concentrations of EE₂ are 7.0×10^{-5} and 3.3×10^{-6} , respectively (Routledge and Sumpter, 1996). Thus, in samples taken close to the treatment plants, it is unlikely that NP and OP contributed significantly to total sample estrogenic activity (Table 4).

Phototransformation effects

To investigate the role of photolysis in attenuating estrogenic activity in the SCR, batch reactors containing either wastewater effluent from the RRWTP or Milli-Q water were spiked with 0.32 nM EE₂ and exposed to sunlight on the University of Arizona campus for a period of four hours (10 am to 2 pm) on cloudless days. A dark control was maintained over the same period, and a second control consisted of wastewater effluent without supplementary EE₂. Samples were withdrawn for separation and measurement of liquid phase estrogenic activity at the start of the experiment and after 0.5, 1.0, 2.0 and 4.0 h of exposure. In addition, fluorescence excitation-emission matrix (EEM) measurements were carried out on each sample. Preliminary tests designed to measure recovery of estrogenic activity from wastewater effluent spiked with EE₂ showed that the extraction procedure recovered essentially all of the spiked EE₂ plus the contribution from estrogenic TOxCs originally present in the effluent. Ground level spectral irradiance data during the solar irradiation experiments were obtained from SMARTS (Simple Model of the Atmospheric Radiative Transfer of Sunshine), a spectral irradiance simulation program that requires geographical information and atmospheric conditions for the experiment site and date (Gueymard, 1995; Kaskaoutis and Kambezidis, 2008). Atmospheric conditions were obtained from satellite data (OMI/Aura and MODIS) provided by Giovanni, a NASA database (Gueymard, 2004). On the dates of the experiments (June 20, July 29 and August 13, 2013), the noontime ground level global spectral irradiances were indistinguishable (Figure 4).

In both the unspiked wastewater effluent control and the reactor containing effluent plus 0.32 nM EE₂, total estrogenic activity decreased below the method detection limit during the 4-hour period of solar light exposure (Figure 5). Profiles of fractional removal versus time in spiked and unspiked effluent were similar: calculated half-lives for liquid-phase estrogenic activity in the reactors were about 0.75 h. Estrogenic activity was essentially unchanged, however, in dark controls and in Milli-Q water containing EE₂ that was exposed to sunlight. The latter result shows that direct photolysis of estrogenic compounds is not an important mechanism for attenuation of estrogenic activity under most environmental conditions, including those encountered in the SCR. The decrease in estrogenic activity in the spiked and unspiked effluent samples exposed to solar light suggests that indirect photolysis is the responsible mechanism may motivate the attenuation of estrogenic activity with distance in the SCR. Indirect photolysis depends on the excitation of chromophores in the water sample. Subsequent dark reactions can produce a variety of organic radicals and hydrogen peroxide (e.g. Jasper and Sedlak, 2013). Photolytic pathways leading to production of hydroxyl radicals can also begin with sunlight irradiance of aqueous-phase nitrate and nitrite ions and various iron complexes (Blough and Zepp, 1995). A number of previous investigators have established the importance of dissolved organics in wastewater in similar photolytic reactions (Lin and Reinhard, 2005; Leech et al., 2009; Hanamoto et al., 2013). The resistance of estrogenic activity to attack via direct photolysis may be due to lack of light absorbance by the steroidal hormones at $\lambda > 310$ nm. Most energy in the solar spectrum is

focused in the visible and infrared ranges ($\lambda > 380$ nm; Figure 4) (Rosenfeldt and Linden, 2004).

The effect of effluent dissolved organic matter in sunlight-activated photolytic reactions is apparent in fluorescence EEM measurements (Figure 6a). EEM peaks in the RRWTP effluent sample have been assigned to humic-acid-like (upper peak) and fulvic-acid-like (lower peak) substances (Chen et al., 2003). Attenuation of these peaks over the four-hour period of experimentation is apparent in the exposed reactors but not in the dark control (Figure 6b). These results indicate that these fluorescent compounds are transformed during the 4-h period of exposure, making them candidate sources of organic radicals for the indirect photolysis of TOxCs. Additional study is warranted to confirm the role of indirect photolysis as a fate mechanism.

Trace organics in monitoring wells along the SCR

Twelve groundwater monitoring wells along the SCR (Figure 1) were sampled during three campaigns in 2011. Eight of the twelve target TOxCs (compounds listed in Table 2, excluding NP and OP) were detected in well water (Table 5). The compounds not detected in the monitoring wells were DEET, TCEP, fluoxetine, and trimethoprim. There were substantial well-specific differences in TOxC concentrations, with the highest levels generally in wells SC-3, SC-5, and SC-7. Quanrud et al. (2004) found that samples from SC-3 and SC-5 contained a substantially higher fraction of water derived from the infiltration of wastewater effluent than did other monitoring wells along the SCR. TOxC concentrations in the wells were generally at least an order of magnitude lower than respective aqueous-phase concentrations in SCR samples, and sulfamethoxazole and

iopromide were about two orders of magnitude lower. Candidate mechanisms for compound attenuations include biodegradation, sorption and/or dilution with native ground water. Exceptions included PFOS, PFOA, sucralose and carbamazepine, which were present at similar or higher concentrations in the wells than in river samples and suggested that dilution was not responsible when attenuation was observed. These four persistent TOrCs have in common relatively low biodegradation probabilities and low log D_{ow} values (Table 1).

Trace organics in riverbed sediments

TOrCs were measured in riverbed sediments during the February 2013 sampling event. Among the forty trace organic analytes (all the compounds in Table 1 except EE_2), fourteen (Table 6) were detected in sediment extracts. A number of those detected are hydrophobic and poorly biodegraded (Table 1).

Carbamazepine was observed to persist in the liquid-phase in the SCR, consistent with studies done in other rivers, (Tixier et al., 2003; Yamamoto et al., 2009). TCP is structurally similar to TCEP, which was observed to persist in liquid phase samples in our study and elsewhere (Fries and Puttmann, 2001; Yoon et al., 2010). The log D_{ow} of TCP indicates that it is hydrophobic as well, so this is not surprising to see it consistently appearing in the sediment samples along the SCR.

Only five of the fourteen compounds found in sediments were also detected in the liquid-phase sampling campaign. Sediment concentrations of four out of those five decreased with distance in the river (Figure 7); NP was the lone exception. Of the same five

compounds in river water samples, only the rate of decrease of PFOS with distance was statistically significant ($p < 0.05$ – Table 2).

Both NP and OP are present in water and sediments. Concentrations of NP (85-254 ng/g) and OP (2.8-9.6 ng/g) in the surface sediment layer (0-2.5 cm) were comparable to levels in the sediments of other effluent-dependent streams (Isobe et al., 2001; Liu et al., 2004). The results suggest that sorption may play an important role in the fate of alkylphenols in the river due to their relatively high hydrophobicity (Isobe et al., 2001). Biodegradation of their parent compounds, APnEOs, may have contributed to NP and OP concentrations in sediment samples (Ahel et al., 1994a).

After NP, caffeine was the most abundant TOrC among those measured in SCR sediments (Table 6). BPA, PFOS and PFDA were present at values near their respective detection limits. Riverbed concentrations of TOrCs generally decreased with distance.

Estrogenic activity in riverbed sediments

Extractable estrogenic activities in the top (0-2.5 cm) and deeper (10.2-12.7 cm) sediment strata were measured during each sampling campaign in 2012 and 2013. Values were generally higher before (June) than immediately after (July) the intense summer rainfall period (Figure 8). The data suggest that intense rainfall/runoff events are capable of attenuating sediment estrogenic levels throughout the sediment strata tested, probably through sediment scour and redeposition (Williams et al. 1999). Lacher (1996) observed a general improvement in channel infiltration capacity following high flows in early March in the SCR. During the summer months, there was a general increase followed by a progressive reduction in the infiltration capacity of the streambed, as indicated by the

length of the wetted reach of the streambed during dry weather flows. Storm flows scoured the upstream portion of the study reach and exhibited depositional behavior in the downstream end of the reach. Seasonal changes in sediment estrogenic activity may have a similar explanation.

Prior to the rainy season, the level of estrogenic activity in the top layer sediment at the sampling site 11 km downstream of the RRWTP outfall was ~5x times higher than the level in the lower sediment layer (Figure 8). At the extreme downstream sampling site (37 km below RRWTP), extractable estrogenic activity in the lower sediment layer was ~2x that of the surface layer, indicating that estrogenic compounds are not degraded completely in the stream or, alternatively, that some estrogenic compounds adsorb to sediments closer to the outfalls and are redistributed with distance and depth in river sediments during storm events.

Conclusions

The results presented show that some TOrCs, including those that contribute to estrogenic activity, are rapidly attenuated with distance and time of travel in the Santa Cruz River. Independent experiments indicate that the attenuation of estrogenic compounds may be due, at least in part, to indirect photolysis caused by formation of organic radicals from sunlight absorption. Those TOrCs that survived percolation to ground water have in common low biodegradation probabilities and low octanol-water distribution ratios. Evidence is presented that suggests that riverbed sediment quality, in terms of concentrations of hydrophobic TOrCs, is periodically improved through storm-related scouring during periods of heavy rainfall and runoff. The sum of natural

attenuation processes occurring during river transport in the Santa Cruz River, an effluent-dependent stream, and during percolation to local ground water, substantially reduce the concentrations of some if not many TOrCs, providing potential benefit to the local ecosystem and human health of downstream communities that may utilize that water.

Acknowledgment

This work was supported by the University of Arizona Water, Environmental and Energy Solutions initiative co-managed by the Water Sustainability Program, Institute of the Environment, and Renewable Energy Network. The authors also wish to acknowledge funding from the National Institutes for Water Resources. Thanks to Darryl Jones and Andrew Keller for sampling and experimental support. Thanks also to Rob Speir, Jason Grodman, and Mike Silva from Pima County Regional Wastewater Reclamation Department for assistance in collection of groundwater samples.

References

- Ahel, M., Giger, W., and Koch, M. (1994a). Behaviour of alkylphenol polyethoxylate surfactants in the aquatic environment—I. Occurrence and transformation in sewage treatment. *Water Research*, 28(5), 1131-1142.
- Ahel, M., Giger, W., and Schaffner, C. (1994b). Behaviour of alkylphenol polyethoxylate surfactants in the aquatic environment—II. Occurrence and transformation in rivers. *Water Research*, 28(5), 1143-1152.
- Barber, L. B., Keefe, S. H., Brown, G. K., Furlong, E. T., Gray, J. L., Kolpin, D. W., Meyer, M. T., Sandstrom, M. W., and Zaugg, S. D. (2013). Persistence and Potential Effects of Complex Organic Contaminant Mixtures in Wastewater-Impacted Streams. *Environmental Science & Technology*, 47(5), 2177-2188.
- Blough, N., and Zepp, R. (1995). Reactive Oxygen Species in Natural Waters. In C. Foote, J. Valentine, A. Greenberg and J. Liebman (Eds.), *Active Oxygen in Chemistry* (Vol. 2, pp. 280-333): Springer Netherlands.
- Chen, W., Westerhoff, P., Leenheer, J. A., and Booksh, K. (2003). Fluorescence Excitation–Emission Matrix Regional Integration to Quantify Spectra for Dissolved Organic Matter. *Environmental Science & Technology*, 37(24), 5701-5710.
- Chiu, C., and Westerhoff, P. K. (2010). Trace Organics in Arizona Surface and Wastewaters *Contaminants of Emerging Concern in the Environment: Ecological and Human Health Considerations* (Vol. 1048, pp. 81-117): American Chemical Society.
- Dodd, M. C., Kohler, H.-P. E., and von Gunten, U. (2009). Oxidation of Antibacterial Compounds by Ozone and Hydroxyl Radical: Elimination of Biological Activity during Aqueous Ozonation Processes. *Environmental Science & Technology*, 43(7), 2498-2504.
- Drewes, J. E., Hemming, J., Ladenburger, S. J., Schauer, J., and Sonzogni, W. (2005). An Assessment of Endocrine Disrupting Activity Changes during Wastewater Treatment through the Use of Bioassays and Chemical Measurements. *Water Environment Research*, 77(1), 12-23.
- Fono, L. J., Kolodziej, E. P., and Sedlak, D. L. (2006). Attenuation of Wastewater-Derived Contaminants in an Effluent-Dominated River. *Environmental Science & Technology*, 40(23), 7257-7262.
- Fries, E., and Puttmann, W. (2001). Occurrence of organophosphate esters in surface water and ground water in Germany. *Journal of Environmental Monitoring*, 3(6), 621-626.
- Galyean, K. C. (1996). *Infiltration of Wastewater Effluent in the Santa Cruz River Channel, Pima County, Arizona*: US Department of the Interior, US Geological Survey.

- Giger, W., Brunner, P., and Schaffner, C. (1984). 4-Nonylphenol in sewage sludge: accumulation of toxic metabolites from nonionic surfactants. *Science*, 225(4662), 623-625.
- Gross, B., Montgomery-Brown, J., Naumann, A., and Reinhard, M. (2004). Occurrence and fate of pharmaceuticals and alkylphenol ethoxylate metabolites in an effluent-dominated river and wetland. *Environmental Toxicology and Chemistry*, 23(9), 2074-2083.
- Gueymard, C. (1995). Simple model of the atmospheric radiative transfer of sunshine (SMARTS2): algorithms and performance assessment. *Florida: Solar Energy Center*.
- Gueymard, C. A. (2004). The sun's total and spectral irradiance for solar energy applications and solar radiation models. *Solar Energy*, 76(4), 423-453.
- Hanamoto, S., Nakada, N., Yamashita, N., and Tanaka, H. (2013). Modeling the Photochemical Attenuation of Down-the-Drain Chemicals during River Transport by Stochastic Methods and Field Measurements of Pharmaceuticals and Personal Care Products. *Environmental Science & Technology*, 47(23), 13571-13577.
- Heberer, T. (2002). Occurrence, fate, and removal of pharmaceutical residues in the aquatic environment: a review of recent research data. *Toxicology Letters*, 131(1-2), 5-17.
- Hyunwoong, P. (2010). Photolysis of aqueous perfluorooctanoate and perfluorooctane sulfonate. *Rev. Roum. Chim*, 55(10), 611-619.
- Isobe, T., Nishiyama, H., Nakashima, A., and Takada, H. (2001). Distribution and Behavior of Nonylphenol, Octylphenol, and Nonylphenol Monoethoxylate in Tokyo Metropolitan Area: Their Association with Aquatic Particles and Sedimentary Distributions. *Environmental Science & Technology*, 35(6), 1041-1049.
- Jasper, J. T., and Sedlak, D. L. (2013). Phototransformation of Wastewater-Derived Trace Organic Contaminants in Open-Water Unit Process Treatment Wetlands. *Environmental Science & Technology*, 47(19), 10781-10790.
- Jobling, S., Nolan, M., Tyler, C. R., Brighty, G., and Sumpter, J. P. (1998). Widespread Sexual Disruption in Wild Fish. *Environmental Science & Technology*, 32(17), 2498-2506.
- Kaskaoutis, D. G., and Kambezidis, H. D. (2008). The role of aerosol models of the SMARTS code in predicting the spectral direct-beam irradiance in an urban area. *Renewable Energy*, 33(7), 1532-1543.
- Kolpin, D. W., Furlong, E. T., Meyer, M. T., Thurman, E. M., Zaugg, S. D., Barber, L. B., and Buxton, H. T. (2002). Pharmaceuticals, Hormones, and Other Organic Wastewater Contaminants in U.S. Streams, 1999-2000: A National Reconnaissance. *Environmental Science & Technology*, 36(6), 1202-1211.

- Komori, K., Tanaka, H., Okayasu, Y., Yasojima, M., and Sato, C. (2004). Analysis and occurrence of estrogen in wastewater in Japan. *Water Sci Technol*, 50(15499675), 93-9100.
- Lacher, L. J. (1996). Recharge characteristics of an effluent dominated stream near Tucson, Arizona. PhD dissertation. The University of Arizona.
- Lam, M. W., Young, C. J., and Mabury, S. A. (2004). Aqueous Photochemical Reaction Kinetics and Transformations of Fluoxetine. *Environmental Science & Technology*, 39(2), 513-522.
- Lange, R., Hutchinson, T. H., Croudace, C. P., Siegmund, F., Schweinfurth, H., Hampe, P., Panter, G. H., and Sumpter, J. P. (2001). Effects of the synthetic estrogen 17 alpha-ethinylestradiol on the life-cycle of the fathead minnow (*Pimephales promelas*). *Environ Toxicol Chem*, 20(11392131), 1216-1227.
- Lee, H. B., and Liu, D. (2002). Degradation of 17 β -Estradiol and its Metabolites by Sewage Bacteria. *Water, Air, and Soil Pollution*, 134(1-4), 351-366.
- Leech, D. M., Snyder, M. T., and Wetzel, R. G. (2009). Natural organic matter and sunlight accelerate the degradation of 17 β -estradiol in water. *Science of The Total Environment*, 407(6), 2087-2092.
- Lin, A. Y.-C., and Reinhard, M. (2005). Photodegradation of common environmental pharmaceuticals and estrogens in river water. *Environmental Toxicology and Chemistry*, 24(6), 1303-1309.
- Littlehat, P. (2007). *Thyromimetic and proteomic analysis of secondary wastewater effluent*. (Ph.D. 3284339), The University of Arizona, United States -- Arizona.
- Liu, R., Zhou, J. L., and Wilding, A. (2004). Microwave-assisted extraction followed by gas chromatography–mass spectrometry for the determination of endocrine disrupting chemicals in river sediments. *Journal of Chromatography A*, 1038(1–2), 19-26.
- Lopez-Avila, V., Young, R., and Beckert, W. F. (1994). Microwave-Assisted Extraction of Organic Compounds from Standard Reference Soils and Sediments. *Analytical Chemistry*, 66(7), 1097-1106.
- MacDonald, B. C., Lvin, S. J., and Patterson, H. (1997). Correction of fluorescence inner filter effects and the partitioning of pyrene to dissolved organic carbon. *Analytica Chimica Acta*, 338(1–2), 155-162.
- Machairas, A. (2004). *The UV/H₂O₂ advanced oxidation process in UV disinfection units: removal of selected phosphate esters by hydroxyl radical*. Citeseer.
- Ning, B., Graham, N. J. D., and Zhang, Y. (2007). Degradation of octylphenol and nonylphenol by ozone – Part II: Indirect reaction. *Chemosphere*, 68(6), 1173-1179.

- Purdom, C. E., Hardiman, P. A., Bye, V. V. J., Eno, N. C., Tyler, C. R., and Sumpter, J. P. (1994). Estrogenic Effects of Effluents from Sewage Treatment Works. *Chemistry and Ecology*, 8(4), 275-285.
- Quanrud, D. M., Quast, K., Conroy, O., Karpiscak, M. M., Gerba, C. P., Lansey, K. E., Ela, W. P., and Arnold, R. G. (2004). Estrogenic Activity and Volume Fraction of Waste Water Origin in Monitoring Wells Along the Santa Cruz River, Arizona. *Ground Water Monitoring & Remediation*, 24(2), 86-93.
- Razavi, B., Song, W., Cooper, W. J., Greaves, J., and Jeong, J. (2009). Free-Radical-Induced Oxidative and Reductive Degradation of Fibrate Pharmaceuticals: Kinetic Studies and Degradation Mechanisms. *The Journal of Physical Chemistry A*, 113(7), 1287-1294.
- Richardson, M. L., and Bowron, J. M. (1985). The fate of pharmaceutical chemicals in the aquatic environment. *Journal of Pharmacy and Pharmacology*, 37(1), 1-12.
- Rojas, M. R., Pérez, F., Whitley, D., Arnold, R. G., and Sáez, A. E. (2010). Modeling of Advanced Oxidation of Trace Organic Contaminants by Hydrogen Peroxide Photolysis and Fenton's Reaction. *Industrial & Engineering Chemistry Research*, 49(22), 11331-11343.
- Rosenfeldt, E. J., and Linden, K. G. (2004). Degradation of Endocrine Disrupting Chemicals Bisphenol A, Ethinyl Estradiol, and Estradiol during UV Photolysis and Advanced Oxidation Processes. *Environmental Science & Technology*, 38(20), 5476-5483.
- Routledge, E. J., and Sumpter, J. P. (1996). Estrogenic activity of surfactants and some of their degradation products assessed using a recombinant yeast screen. *Environmental Toxicology and Chemistry*, 15(3), 241-248.
- Salveson, A., Brown, J., Zhou, Z., and Lopez, J. L. (2010). Monitoring for Microconstituents in an Advanced Wastewater Treatment (AWT) Facility and Modeling Discharge of Reclaimed Water to Surface Canals for Indirect Potable Use. *Water Reuse Foundation*.
- Sanchez-Prado, L., Garcia-Jares, C., and Llompart, M. (2010). Microwave-assisted extraction: Application to the determination of emerging pollutants in solid samples. *Journal of Chromatography A*, 1217(16), 2390-2414.
- Sanchez, W., Sremski, W., Piccini, B., Palluel, O., Maillot-Maréchal, E., Betoulle, S., Jaffal, A., Ait-Aïssa, S., Brion, F., Thybaud, E., Hinfrey, N., and Porcher, J.-M. (2011). Adverse effects in wild fish living downstream from pharmaceutical manufacture discharges. *Environment International*, 37(8), 1342-1348.
- Snyder, S. A., Westerhoff, P., Yoon, Y., and Sedlak, D. L. (2003). Pharmaceuticals, Personal Care Products, and Endocrine Disruptors in Water: Implications for the Water Industry. *Environmental Engineering Science*, 20(5), 449-469.

- Soares, A., Guieysse, B., Jefferson, B., Cartmell, E., and Lester, J. N. (2008). Nonylphenol in the environment: a critical review on occurrence, fate, toxicity and treatment in wastewaters. *Environ Int*, 34(18282600), 1033-1049.
- Song, W., Cooper, W. J., Mezyk, S. P., Greaves, J., and Peake, B. M. (2008). Free Radical Destruction of β -Blockers in Aqueous Solution. *Environmental Science & Technology*, 42(4), 1256-1261.
- Sparr Eskilsson, C., and Björklund, E. (2000). Analytical-scale microwave-assisted extraction. *Journal of Chromatography A*, 902(1), 227-250.
- Sumpter, J. P., and Jobling, S. (2013). The occurrence, causes, and consequences of estrogens in the aquatic environment. *Environmental Toxicology and Chemistry*, 32(2), 249-251.
- Teske, S. S., and Arnold, R. G. (2008). Removal of natural and xeno-estrogens during conventional wastewater treatment. *Reviews in Environmental Science and Bio/Technology*, 7(2), 107-124.
- Tixier, C., Singer, H. P., Oellers, S., and Müller, S. R. (2003). Occurrence and Fate of Carbamazepine, Clofibrilic Acid, Diclofenac, Ibuprofen, Ketoprofen, and Naproxen in Surface Waters. *Environmental Science & Technology*, 37(6), 1061-1068.
- Toth, J. E., Rickman, K. A., Venter, A. R., Kiddle, J. J., and Mezyk, S. P. (2012). Reaction Kinetics and Efficiencies for the Hydroxyl and Sulfate Radical Based Oxidation of Artificial Sweeteners in Water. *The Journal of Physical Chemistry A*, 116(40), 9819-9824.
- Ward, C. P. (2010). *Direct and Indirect Photochemical Degradation of Two Polycyclic Musk Fragrances and Two Polycyclic Aromatic Hydrocarbons in Natural Waters*. The Ohio State University.
- Watts, M. J., and Linden, K. G. (2008). Photooxidation and subsequent biodegradability of recalcitrant tri-alkyl phosphates TCEP and TBP in water. *Water Research*, 42(20), 4949-4954.
- Williams, R. J., Jürgens, M. D., and Johnson, A. C. (1999). Initial predictions of the concentrations and distribution of 17 β -oestradiol, oestrone and ethinyl oestradiol in 3 English rivers. *Water Research*, 33(7), 1663-1671.
- Wols, B. A., and Hofman-Caris, C. H. M. (2012). Review of photochemical reaction constants of organic micropollutants required for UV advanced oxidation processes in water. *Water Research*, 46(9), 2815-2827.
- Writer, J. H., Antweiler, R. C., Ferrer, I., Ryan, J. N., and Thurman, E. M. (2013). In-Stream Attenuation of Neuro-Active Pharmaceuticals and Their Metabolites. *Environmental Science & Technology*, 47(17), 9781-9790.
- Yamamoto, H., Nakamura, Y., Moriguchi, S., Nakamura, Y., Honda, Y., Tamura, I., Hirata, Y., Hayashi, A., and Sekizawa, J. (2009). Persistence and partitioning of

eight selected pharmaceuticals in the aquatic environment: Laboratory photolysis, biodegradation, and sorption experiments. *Water Research*, 43(2), 351-362.

Ying, G.-G., Kookana, R. S., and Ru, Y.-J. (2002). Occurrence and fate of hormone steroids in the environment. *Environment International*, 28(6), 545-551.

Yoon, Y., Ryu, J., Oh, J., Choi, B.-G., and Snyder, S. A. (2010). Occurrence of endocrine disrupting compounds, pharmaceuticals, and personal care products in the Han River (Seoul, South Korea). *Science of The Total Environment*, 408(3), 636-643.

Table 1. Relevant physical/chemical properties for TORCs measured in the Santa Cruz River water during the sampling campaigns in 2011 (in boldface) and in riverbed sediments. EE2 was not measured directly, but used as a reference for quantification of estrogenic activity.

Compound	Usage	Log D _{ow} at pH=7 ^[a]	k _{OH} (10 ⁹ M ⁻¹ s ⁻¹)	P _B ^[b]	Log K _{AW} ^[c]	Monitoring event ^[d]
17 α -Ethinylestradiol (EE2)	Estrogen	4.11	10.3 \pm 0.7 ^[e]	0.0354	-9.489	
4-nonylphenol	Derived from detergents	6.14	11.0 \pm 0.2 ^[f]	0.5086	-2.857	LS
4-octylphenol	Derived from detergents	5.63	14.0 \pm 0.2 ^[f]	0.5025	-3.735	LS
Atenolol	b-blocker	-2.09	7.10 ^[g]	0.2349	-16.252	S
Atrazine	Herbicide	2.64	2.30 \pm 0.14 ^[e]	0	-7.016	S
Benzophenone	Photo initiator	3.21	NA	-0.0737	-4.101	S
Benzotriazole	Drug precursor	1.42	NA	0.3935	-5.221	S
Bisphenol A	Plasticizer	3.64	8.00 \pm 3.11 ^[e]	0.1559	-9.427	S
Carbamazepine	Anticonvulsant	1.89	8.02 \pm 1.90 ^[e]	0.0364	-8.355	LWS
Caffeine	Stimulant	-0.63	6.40 \pm 0.71 ^[e]	0.0521	-8.835	S
DEET	Insect repellent	2.42	5 ^[g]	0.4437	-6.07	LWS

Dexamethasone	Anti-inflammatory and immune- suppressant	2.03	NA	0.0015	-5.534	LWS
Diclofenac	Nonsteroidal anti- inflammatory drug (NSAID)	1.77	8.38±1.24 ^[e]	0.0029	-9.714	S
Diltiazem	Calcium channel blockers	2.98	NA	0.0267	-14.453	S
Diphenhydramine	Antihistamine	1.25	5.42 ^[e]	0.0313	-6.82	S
Fluoxetine	Anti-depressant	1.15	9.60±0.80 ^[h]	0	-5.439	LWS
Gemfibrozil	Blood lipid regulator	2.07	10.0±0.60 ^[i]	0.6123	-6.313	S
Ibuprofen	Nonsteroidal anti- inflammatory drug (NSAID)	0.94	7.04±0.52 ^[e]	0.1521	-5.207	S
Meprobamate	Anxiolytic	0.7	NA	0.314	-8.121	S

Naproxen	Nonsteroidal anti-inflammatory drug (NSAID)	0.73	8.61 ^[e]	0.3447	-7.858	S
Norgestrel	Hormonal contraceptives	3.37	NA	0.0469	-7.502	S
PFBS	Surfactant	-1.81	NA	0	-3.23	S
PFDA	Surfactant	4.15	NA	0	2.011	S
PFDoA	Surfactant	5.61	NA	0	3.452	S
PFOA	Surfactant	2.69	0.01 ^[j]	0	0.57	LWS
PFOS	Surfactant	1.01	0.01 ^[j]	0	-0.347	LWS
PFHxDA	Surfactant	8.53	NA	0	6.334	S
Prednisone	Immunosuppressant	1.57	NA	0.1452	-7.937	S
Primidone	Anticonvulsant	0.83	6.70 ^[e]	0.4211	-8.101	LWS
Propylparaben	Preservative	2.88	NA	0.8344	-6.584	S
Simazine	Herbicide	2.28	2.90±0.28 ^[e]	0	-7.414	S
Sucralose	Artificial sweetener	0.23	1.50±0.10 ^[k]	0.004	-16.787	LWS
Sulfamethoxazole	Antibiotic	-0.22	5.82±1.99 ^[e]	0.006	-10.408	LWS
Testosterone	Steroid hormone	3.18	NA	0.1514	-6.841	S

Triclocarban	Antibiotic	6.07	NA	0.0017	-8.733	S
Triclosan	Antibiotic	5.28	5.40 ^[l]	0.0187	-6.69	S
Trimethoprim	Antibiotic	0.27	6.30±0.85 ^[e]	0.0172	-12.01	LWS
TCEP	Flame retardant	-5.91	2.00 ^[m]	0.0193	-3.871	LWS
T CPP	Flame retardant	2.53	27.1 ^[m]	0.0013	-5.613	S
Tonalide	Aromatic musk	5.06	4.72 ^[n]	0.0737	-2.245	LW
Iopromide	Contrast medium	-2.66	3.30 ^[e]	0	-26.388	LW

Log D_{OW}: n-octanol–water distribution ratio at pH 7; k_{OH}: second-order reaction rate constant between compound and hydroxyl radical; P_B: Probability of biodegradation; K_{AW}: air-water partition coefficient;

^[a] Data directly obtained from SciFinder

^[b] Calculated by Biowin6 (MITI Non-Linear Model). US EPA; Estimation Program Interface (EPI) Suite. Ver. 4.1.

^[c] Calculated by KOAWIN. US EPA; Estimation Program Interface (EPI) Suite. Ver. 4.1.

^[d] Monitoring event: indicates sampling events in which the compound was measured: W- monitoring well, L- river liquid, S - sediment. For example, for NP, LS means that it was measured in liquid and sediment but not in well sampling.

^[e] (Wols and Hofman-Caris, 2012)

^[f] (Ning et al., 2007)

^[g] (Song et al., 2008)

^[h] (Lam et al., 2004)

^[i] (Razavi et al., 2009)

^[j] (Hyunwoong, 2010)

^[k] (Toth et al., 2012)

^[l] (Dodd et al., 2009)

^[m] (Machairas, 2004)

^[n] (Ward, 2010)

Table 2. Results of simple linear regression analysis ($C=B_0x+B_1$, where C is concentration and x is distance from the IRWPCF outfall) in the Santa Cruz River liquid samples.

Compound	B₀ (ng/ L km)	B₁ (ng/L)	R²	p (significance)
Carbamazepine	0.610	280.8	0.077	0.437
DEET^[a]	4.780	352.5	0.533	0.016
Sulfamethoxazole	7.629	879.6	0.175	0.229
TCEP	0.897	275.6	0.171	0.236
Tonalide^[a]	-0.523	24.03	0.789	0.001
Fluoxetine^[a]	-1.123	36.38	0.901	<0.0005
Trimethoprim	-1.961	184.1	0.248	0.143
Primidone	-0.194	179.6	0.011	0.777
Iopromide^[a]	-1.001	70.30	0.451	0.033
Sucralose^[a]	-94.15	6321	0.580	0.010
PFOS^[a]	-1.145	41.84	0.468	0.029
PFOA	-0.123	11.88	0.062	0.448
4-<i>n</i>-Nonylphenol	-1.009	362.5	0.020	0.859
4-Octylphenol	0.532	18.17	0.244	0.506

^[a] Compound attenuation was statistically significant ($p \leq 0.05$)

Table 3. Sequential multiple linear regression results (see text for explanation) for correlation between the normalized attenuation slope ($-B_0/C_0$) in river water samples and the indicated compound properties. B represents the fitted coefficient of proportionality with respect to each listed independent variable. The standardized coefficients represent the change (in number of standard deviations) of the dependent variable induced by a change of one standard deviation of the corresponding dependent variable.

Model		Correlation Coefficients		Standardized	Significance (p)
		B	Std. Error	Coefficients β	
1	(Constant)	9.463	6.420		0.171
	Log Dow	1.415	1.475	0.274	0.360
	P _B	-0.330	0.115	-0.844	0.017
	k _{OH} (M ⁻¹ s ⁻¹)	0.720	1.191	0.160	0.559
2	(Constant)	12.234	4.364		0.017
	Log Dow	1.586	1.406	0.307	0.283
	P _B	-0.309	0.106	-0.791	0.014
3	(Constant)	12.401	4.411		0.016
	P _B	-0.242	0.089	-0.618	0.019

Table 4. Contributions of NP and OP to the total estrogenic activity in the liquid river samples. Calculations are based on the relative estrogenic activities of single estrogens in the YES test (Routledge and Sumpter, 1996), and an additive model for total estrogenic activity. See Figure 1 for sampling locations.

Sampling point	Distance from RRWTP outfall (km)	Total estrogenic activity (M)	NP equivalent activity (M)	Percent NP for estrogenic activity	OP equivalent activity (M)	Percent OP for estrogenic activity
RRWTP effluent	0	7.51×10^{-11}	3.05×10^{-13}	0.41%	3.57×10^{-15}	0.048%
El Camino del Cerro	1.5	1.05×10^{-10}	2.21×10^{-13}	0.21%	5.08×10^{-16}	0.005%
N Silverbell Rd	7.2	2.67×10^{-12}	3.22×10^{-13}	12.1%	7.89×10^{-16}	0.296%
N Cortaro Rd	11.1	5.33×10^{-12}	2.82×10^{-13}	5.3%	3.03×10^{-16}	0.057%
Heritage Park Dr	26.9	1.33×10^{-11}	4.39×10^{-13}	3.3%	1.59×10^{-15}	0.120%
N Trico Rd	35.7	4.44×10^{-12}	2.23×10^{-13}	5.0%	8.75×10^{-16}	0.197%

Table 5. Concentrations of TOrCs (ng/L) in Santa Cruz River monitoring wells. See Figure 1 for well locations.

Sampling point	Distance from RRWTP (km)	Depth of Screened Interval (m)	Carbamazepine	Sulfamethoxazole	Primidone	Iopromide	Sucralose	PFOS	PFOA	Tonalide
SC-1	0.8	33.5 - 45.7	191.2 ± 3.5	7.9 ± 0.1	134.4 ± 2.9	<MRL	307.8 ± 5.4	13.2 ± 0.1	9.5 ± 0.6	5.9 ± 0.5
SC-2	3.7	29.0 - 41.1	268.5 ± 55.3	15.2 ± 6.6	142.3 ± 10.4	1.4 ± 1.3	322.1 ± 160.8	55.1 ± 4.5	12.6 ± 5.9	18.4 ± 4.8
SC-3	8.4	27.4 - 39.6	369.1 ± 110.3	260.8 ± 81.1	184.9 ± 0.4	22.7 ± 4.1	1180.4 ± 158.8	20.5 ± 0.7	7.9 ± 3.3	109.0 ± 61.9
SC-5	13.1	32.0 - 50.3	312.0 ± 96.4	55.0 ± 43.6	172.4 ± 33.5	2.0 ± 0.5	3470.2 ± 1014.7	34.2 ± 5.7	10.6 ± 2.7	18.4 ± 19.2
SC-6	14.8	35.1 - 56.4	374.5 ± 2.6	31.0 ± 1.5	227.8 ± 3.0	<MRL	609.0 ± 17.3	40.2 ± 0.4	17.8 ± 0.7	71.6 ± 6.8
SC-7	18.0	42.7 - 61.0	259.2 ± 57.2	62.1 ± 1.0	193.4 ± 4.0	1.4 ± 0.3	1808.9 ± 57.5	49.3 ± 7.5	12.3 ± 9.4	92.4 ± 29.8
SC-8	20.0	61.0 - 91.4	202.4 ± 0.6	13.2 ± 2.3	59.5 ± 2.8	<MRL	109.4 ± 21.7	65.7 ± 2.1	14.8 ± 0.3	1.8 ± 0.3
SC-9	25.6	88.4 - 115.8	7.5 ± 0.4	9.0 ± 1.9	9.2 ± 0.1	<MRL	94.7 ± 31.4	8.9 ± 1.3	2.5 ± 0.3	4.9 ± 0.1
SC-10	27.2	91.4 - 112.8	12.3 ± 0.2	6.4 ± 0.1	12.4 ± 0.9	<MRL	71.0 ± 1.2	8.3 ± 0.6	2.5 ± 0.1	8.0 ± 3.4
SC-11	32.7	57.6 - 100.3	196.0 ± 6.3	12.8 ± 0.9	74.2 ± 1.9	<MRL	379.9 ± 23.6	47.3 ± 1.7	10.9 ± 0.3	12.4 ± 0.9
SC-12	35.7	70.1 - 94.5	329.6 ± 3.1	50.0 ± 28.5	43.3 ± 0.7	<MRL	179.1 ± 47.0	79.7 ± 4.1	13.9 ± 0.1	1.1 ± 0.5

Values represent averages plus/minus one standard deviation.

<MRL means less than method reporting limit, a value that is arbitrarily set at 9 times the signal-to-noise ratio.

Table 6. Concentrations of TOrCs in the Lower Santa Cruz River sediments (ng/g dry weight) for the six locations sampled in February 2013. See Table 4 for downstream distances of sampling points.

Analyte	RRWTP	El	N. Silverbell	N. Cortaro	Heritage Park	N. Trico
		Camino del Cerro	Rd	Rd	Dr	Rd
Nonylphenol	101.46	85.55	110.3	117.73	254.1	148.12
Octylphenol	9.64	8.05	3.01	3.16	5.43	2.77
Caffeine	67.6	19.5	16	5.87	7.5	4.54
Trimethoprim	0.52	0.72	0.53	0.26	0.36	0.31
Carbamazepine	0.39	0.11	0.39	0.02	0.02	0.02
TCPP	2.83	2.73	2.75	1.63	1.38	1.3
Benzophenone	4.51	23.2	10.3	12.5	5.29	3.89
Benzotriazole	0.24	3.39	0.08	0.18	0.33	0.2
Diclofenac	0.56	<MRL	0.26	0.16	<MRL	0.16
Bisphenol A	0.24	1.25	1.13	0.7	0.17	0.42
PFDA	0.19	0.08	0.08	<MRL	0.06	0.07
PFOS	0.89	0.16	0.11	0.1	0.05	0.11
Triclocarban	3.72	2.41	0.92	1	0.54	1
Triclosan	3.68	2.73	0.57	1.49	<MRL	0.62

<MRL means less than method reporting limit, a value that is arbitrarily set at 9 times the signal-to-noise ratio.

Figure captions

Figure 1. Wastewater treatment facilities and sampling sites along the Santa Cruz River in Tucson, AZ. Red dots: major water reclamation facilities; black stars: sampling sites in the 2011 campaign (groundwater wells); green dots: sampling sites in the 2012-13 campaigns. Relative distances for all sampling points are reported in Tables 4 and 5. In February 2014, the Roger Road wastewater treatment plant (RRWTP) was replaced by the Agua Nueva Water Reclamation Facility (WRF); and the Ina Road Water Pollution Control Facility (IRWPCF) was similarly upgraded and renamed Tres Rios WRF.

Figure 2. In-stream TO₁₄C concentration versus distance traversed in the Santa Cruz River downstream from the RRWTP. Solid lines are linear fits of the data downstream of the IRWPCF. Regression data are shown in Table 2: (a) tonalide and fluoxetine; (b) iopromide and PFOS; (c) p-nonylphenol and p-octylphenol.

Figure 3. (a) aqueous-phase and (b) suspended solid estrogenic activity as a function of position in the lower Santa Cruz River. Dates shown are those of sample collection. Suspended solids were isolated from river water samples by filtering through 0.7 μm Whatman GF/F glass fiber filters.

Figure 4. Global spectral irradiance for the Tucson area for the dates of sunlight photolysis experiments.

Figure 5. Estrogenic activity changes in RRWTP secondary effluent during sunlight photolysis experiments. Results are shown for original samples and samples spiked with 0.32 nM EE₂.

Figure 6. (a) Fluorescence Excitation–Emission Matrix (EEM) test results for the RRWTP secondary effluent spiked with EE₂; color contour values represent light intensity (arbitrary units). (b) The humic (top) and fulvic (bottom) peaks of the EEM contours were attenuated after four hours in sunlight but not in the dark (EE₂ does not contribute significantly to the high intensity regions in the EEM maps). I represents fluorescence intensity, obtained by integrating the EEM contours over a region of 5 nm around the maximum intensity point of the specified peaks; I₀ is the initial fluorescence intensity of the peak.

Figure 7. Observed trace organic concentrations in SCR sediments vs. distance in the February 2013 sampling event. Concentrations are in ng of compound per g of dry sediment. Measurements correspond to surface sediment samples from the riverbed (0-2.5 cm depth).

Figure 8. Estrogenic activities as a function of position and time in riverbed sediment samples taken from the Santa Cruz River: (a) top layer sediment (top 2.5 cm); (b) lower layer sediment (10.2-12.7 cm depth).

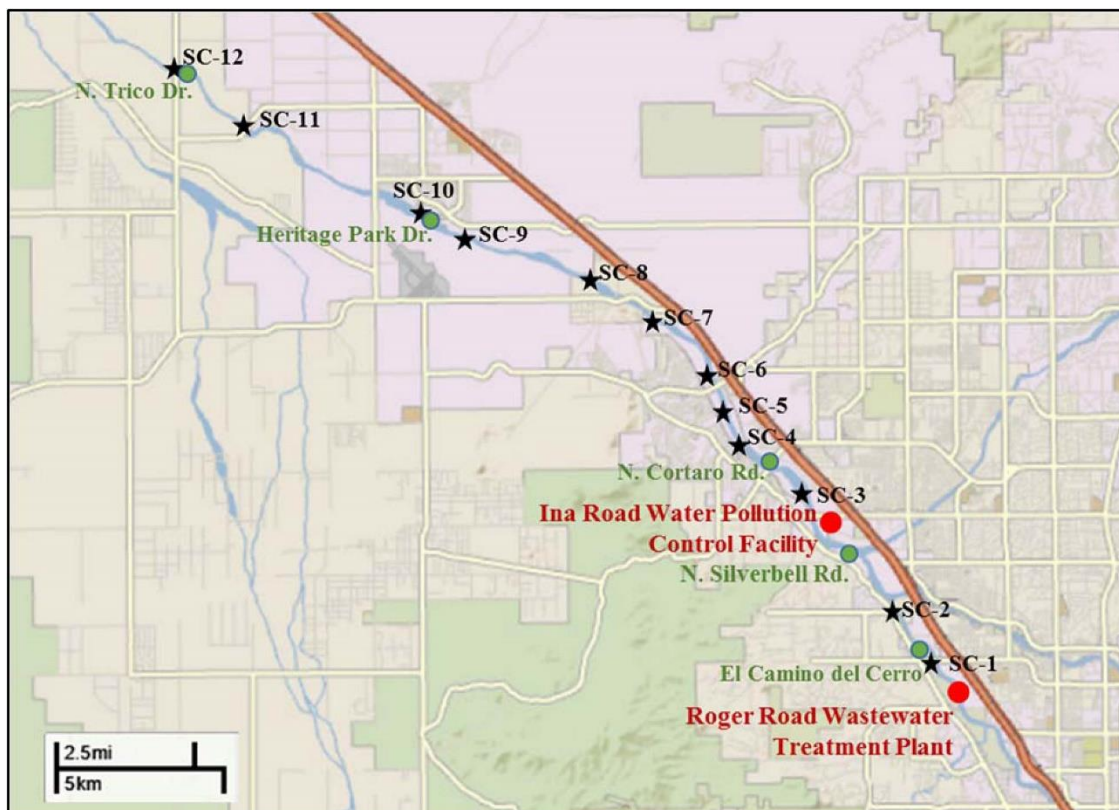


Figure 2. Wastewater treatment facilities and sampling sites along the Santa Cruz River in Tucson, AZ. Red dots: major water reclamation facilities; black stars: sampling sites in the 2011 campaign (groundwater wells); green dots: sampling sites in the 2012-13 campaigns. Relative distances for all sampling points are reported in Tables 4 and 5. In February 2014, the Roger Road wastewater treatment plant (RRWTP) was replaced by the Agua Nueva Water Reclamation Facility (WRF); and the Ina Road Water Pollution Control Facility (IRWPCF) was similarly upgraded and renamed Tres Rios WRF.

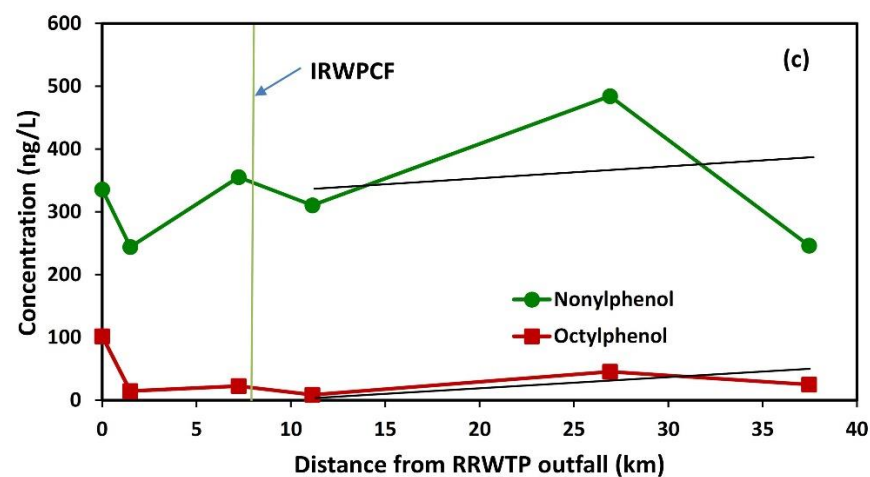
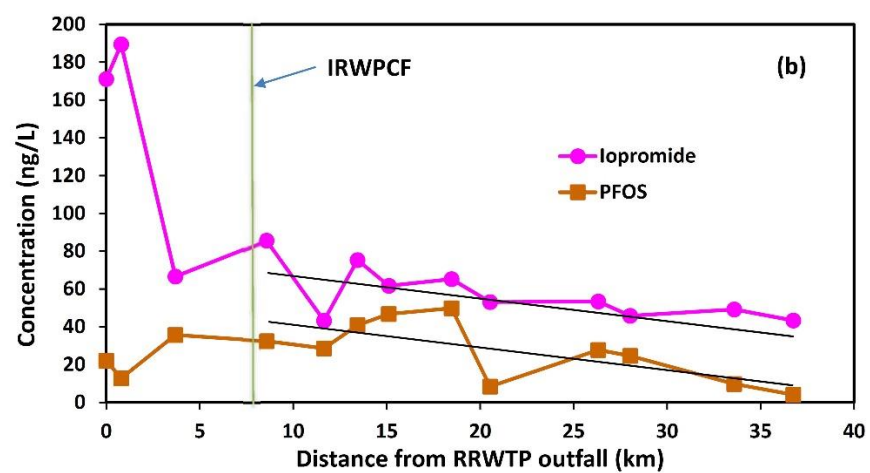
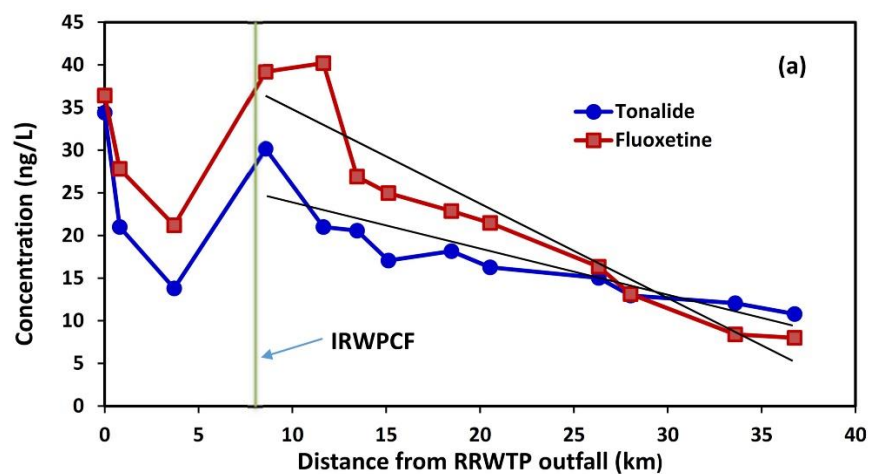


Figure 2. In-stream TOrC concentration versus distance traversed in the Santa Cruz River downstream from the RRWTP. Solid lines are linear fits of the data downstream of the IRWPCF. Regression data are shown in Table 2: (a) tonalide and fluoxetine; (b) iopromide and PFOS; (c) p-nonylphenol and p-octylphenol.

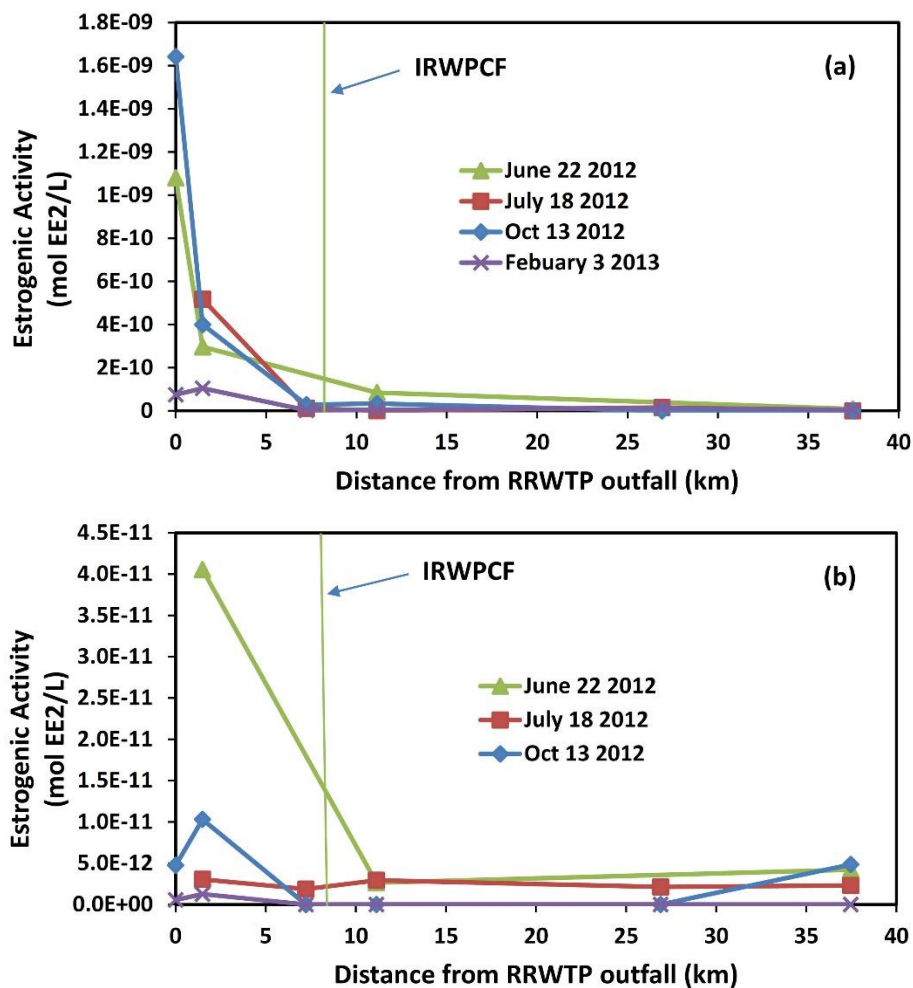


Figure 3. (a) aqueous-phase and (b) suspended solid estrogenic activity as a function of position in the lower Santa Cruz River. Dates shown are those of sample collection. Suspended solids were isolated from river water samples by filtering through 0.7 μm Whatman GF/F glass fiber filters.

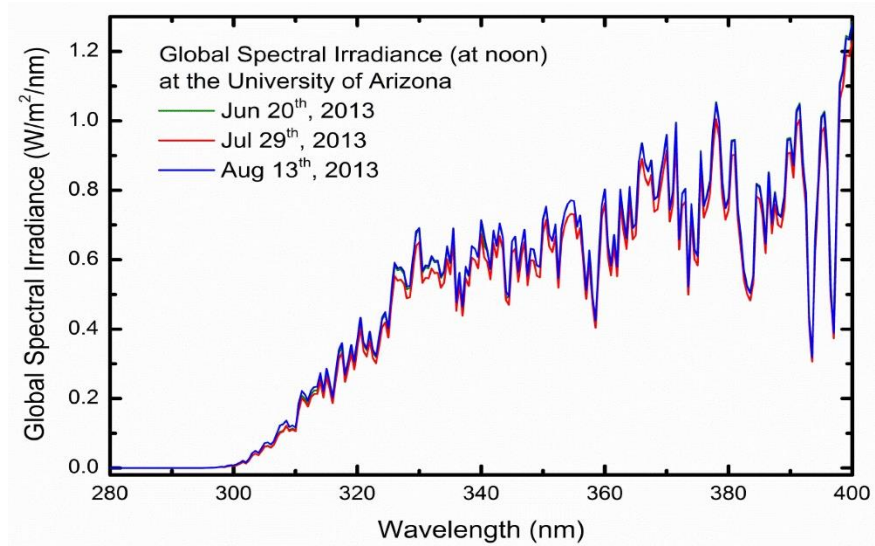


Figure 4. Global spectral irradiance for the Tucson area for the dates of sunlight photolysis experiments.

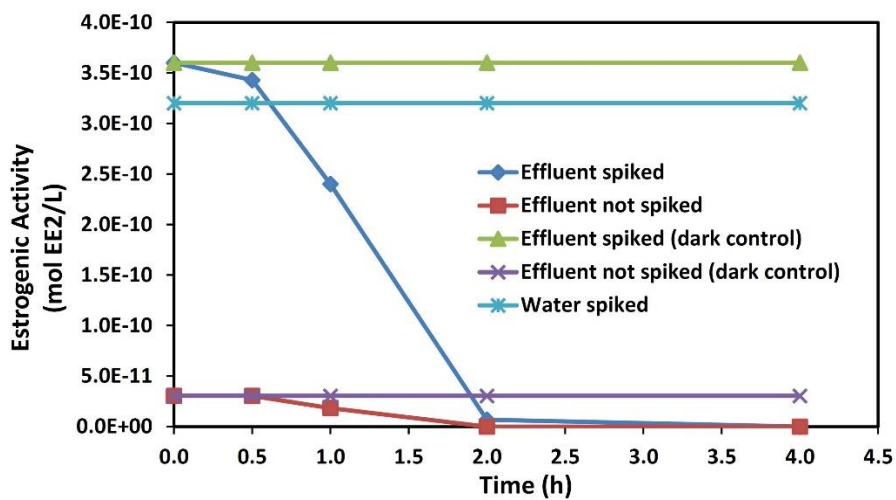


Figure 5. Estrogenic activity changes in RRWTP secondary effluent during sunlight photolysis experiments. Results are shown for original samples and samples spiked with 0.32 nM EE₂.

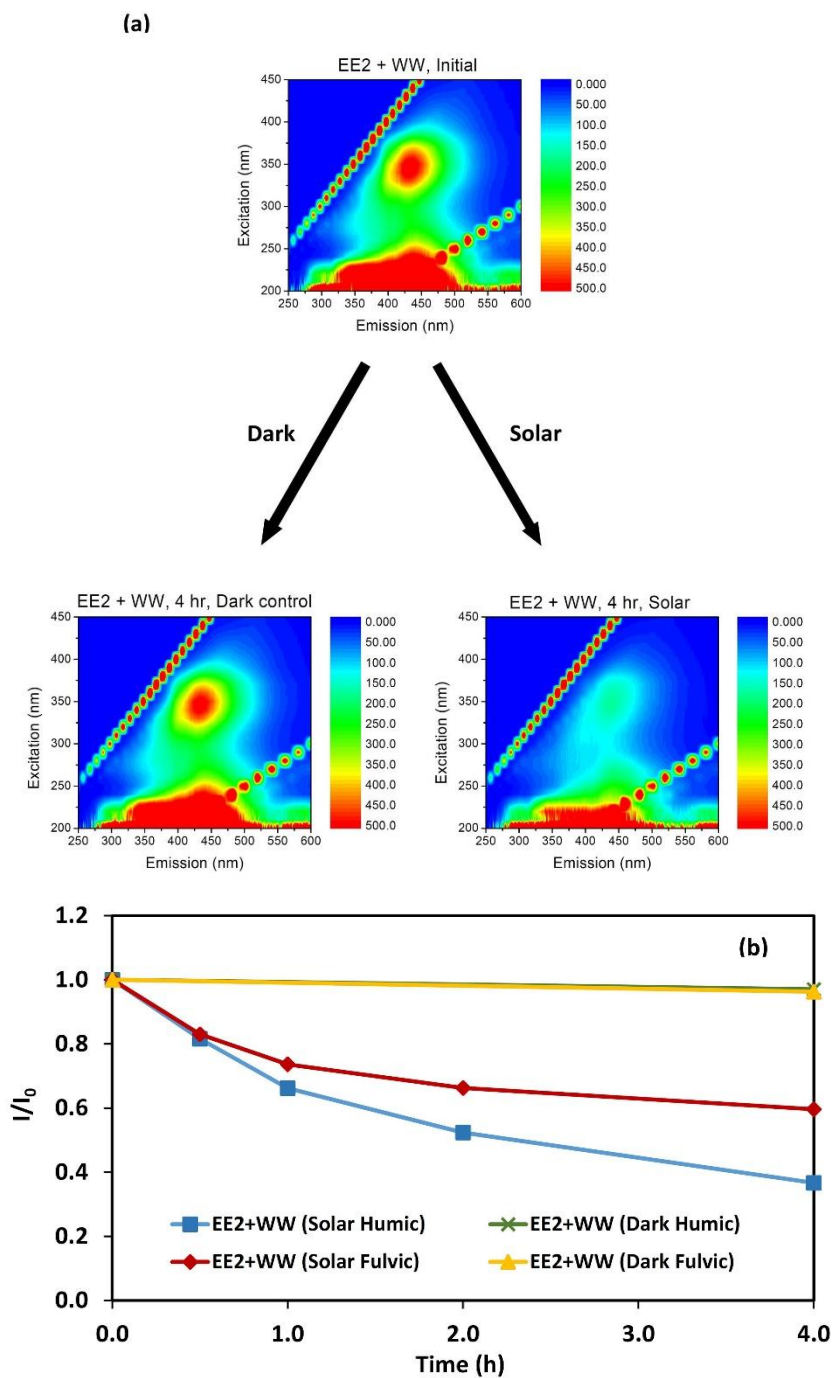


Figure 6. (a) Fluorescence Excitation–Emission Matrix (EEM) test results for the RRWTP secondary effluent spiked with EE₂; color contour values represent light intensity (arbitrary units). (b) The humic (top) and fulvic (bottom) peaks of the EEM contours were attenuated after

four hours in sunlight but not in the dark (EE_2 does not contribute significantly to the high intensity regions in the EEM maps). I represents fluorescence intensity, obtained by integrating the EEM contours over a region of 5 nm around the maximum intensity point of the specified peaks; I_0 is the initial fluorescence intensity of the peak.

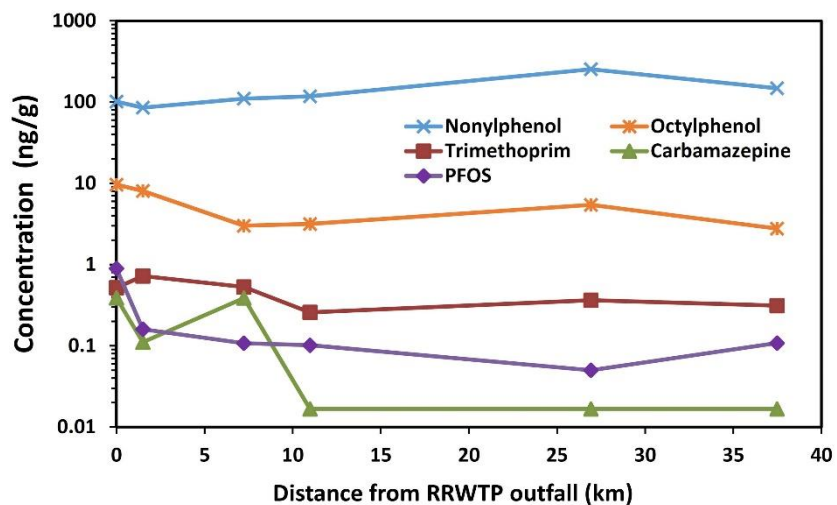


Figure 7. Observed trace organic concentrations in SCR sediments vs. distance in the February 2013 sampling event. Concentrations are in ng of compound per g of dry sediment. Measurements correspond to surface sediment samples from the riverbed (0-2.5 cm depth).

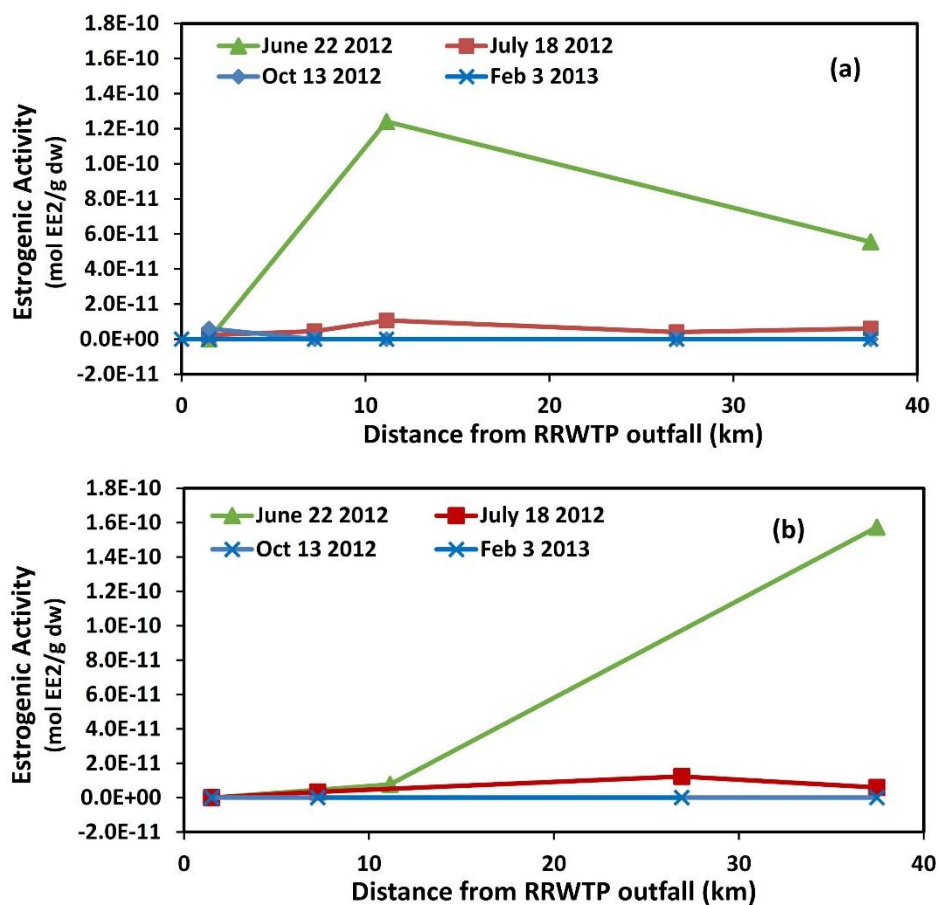


Figure 8. Estrogenic activities as a function of position and time in riverbed sediment samples taken from the Santa Cruz River: (a) top layer sediment (top 2.5 cm); (b) lower layer sediment (10.2-12.7 cm depth).

APPENDIX D**KINETIC STUDY OF THE PHOTO-FENTON PROCESS**

(submitted, Chemosphere)

Long Cheng, Tianqi Zhang, Robert G. Arnold, A. Eduardo Sáez*

Department of Chemical and Environmental Engineering, The University of Arizona, Tucson,
AZ 85721.

Corresponding author: A. Eduardo Sáez, esaez@email.arizona.edu, (520) 621-5369

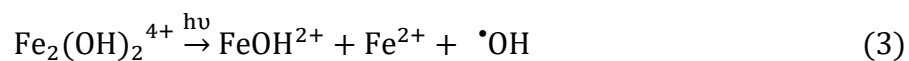
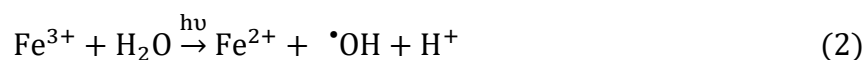
Abstract

A kinetic model in which aquahydroxo complexes of Fe^{3+} and their hydrolysis products are disproportionated to Fe^{2+} and hydroxyl radicals in ultraviolet light is proposed and tested experimentally. The model accounts for Fenton-like reactions and direct photolysis of H_2O_2 formed by radical recombination. Iron speciation and photochemical parameters, including the molar absorptivities of light-absorbing species and the quantum yields of Fe^{3+} and FeOH^{2+} hydrolysis (hydroxyl radical production/photon absorption) were experimentally validated. However, the predicted, time-dependent Fe^{2+} concentrations during Fe(III)/UV photolysis were much lower than measured. Potential explanations include overestimation of Fe^{2+} oxidation by hydroxyl radicals. When UV irradiation was discontinued, both measured and simulated Fe^{2+} levels decreased immediately as a consequence of reaction with residual H_2O_2 . Simulated Fe^{2+} trajectories were accurate when hydrogen peroxide was initially present at sufficiently high concentrations—so that Fenton's reactions overwhelmed the photolytic pathways. The kinetic model also accurately predicts the trajectory of Fe^{2+} when the initial concentration of ferrous iron is large. The nature of elements missing from the proposed model that would account for residual deficiencies is discussed.

Keywords: advanced oxidation; photolysis; ferric hydroxo complexes; hydroxyl radical; mechanism.

Introduction

Photolytic disproportionation reactions involving aqua-Fe(III) complexes have received considerable attention as means for generating hydroxyl radicals (reactions 1-3) (Baxendale and Magee 1955; Adamson et al. 1962; Langford and Carey 1975; Pozdnyakov et al. 2000). The ability of hydroxyl radicals to destroy trace organic compounds in water, treated wastewater and industrial waste is widely appreciated (e.g. Rosario-Ortiz et al. 2010; Matilainen and Sillanpää 2010; Rodríguez et al. 2012; Prieto-Rodríguez et al. 2013; Pešoutová et al. 2014). Once formed, the recombination of hydroxyl radicals to form hydrogen peroxide (reaction 4) is inevitable, providing all the elements of the proposed photo-Fenton mechanism (Faust and Hoigné 1990; Zepp et al. 1992; Kim and Vogelpohl 1998). These works frequently used $\cdot\text{OH}$ scavengers in short term irradiation experiments to avoid oxidation of Fe^{2+} by $\cdot\text{OH}$ and simplify the reaction mechanism while establishing reaction quantum yields (e.g. Logan 1990; Kawaguchi and Inagaki 1993; Benkelberg and Warneck 1995; Nadochenko and Kiwi 1998; Joseph et al. 2001; Rodríguez et al. 2002; Lee and Yoon 2004a, 2004b). In those cases, the full range of reactions that determine the trajectory of Fe^{2+} concentration was not observed.



The environmental relevance of these reactions arises from the non-specific reactions of hydroxyl and other inorganic radicals with dissolved organic compounds, including a variety of trace organics of anthropogenic origin that routinely survive municipal wastewater treatment processes (e.g. Andreozzi et al. 2006; Rodríguez et al. 2007; Jin et al. 2014; Spasiano et al. 2014).

Photo-Fenton nomenclature covers treatment strategies based on the addition of iron and peroxide under ultraviolet irradiation, taking advantage of both aqua-Fe(III) species photolysis and iron cycling via reaction with peroxide to produce hydroxyl radicals (e.g. Kavitha and Palanivelu 2004; Badawy et al. 2006; Shemer et al. 2006; Méndez-Arriaga et al. 2010). The advantage of photo-Fenton processes is generally kinetic since hydroxyl radicals are produced via aqua-Fe(III) and H_2O_2 photolyses as well as the reaction of Fe^{2+} with supplemental H_2O_2 . The kinetics and mechanism of photo-Fenton processes are less established than those of Fenton reactions and Fe(III) photolysis alone despite successful studies by Einschlag et al. (2013) and others. Successful simulation of photo-Fenton processes under natural conditions necessarily involves pathways critical to both Fenton's mechanism, and aqua-Fe(III) photolysis, hydroxyl radical quenching by H_2O_2 and perhaps other radical interactions leading the formation of nitrate and sulfate radicals.

A kinetic model for photolysis of ferric-hydroxo, -sulfate and -chloride complexes under black light was proposed and validated by Machulek et al. (2009). Their model, which consists of (i) photolyses of FeOH^{2+} , $\text{Fe}(\text{OH})_2$, FeCl^{2+} and FeSO_4^+ and (ii) a Fenton-like mechanism in the presence of sulfate and chloride in acidic solutions, fit experimental data for Fe(II) formation

under various conditions satisfactorily. Another Fe(III)/UV photolysis kinetic model was established and tested by Wang and Liu (2014). Besides integrating photolysis of FeOH^{2+} with Fenton-like systems, those authors also considered the photochemical oxidation of Fe^{2+} by dissolved oxygen.

Here we propose and evaluate a kinetic model combining the photolysis of aqua-Fe(III) species with Fenton's reactions. The model is supported by bench-scale measurements under controlled conditions. Work is restricted, for example to irradiance at 254 nm, and iron is provided as ferric perchlorate ($\text{Fe}(\text{ClO}_4)_3$), since the perchlorate anion is viewed as chemically inert under these circumstances.

Materials and methods

Chemicals

All chemicals were reagent grade and used without further purification, including iron (III) perchlorate hydrate ($\text{Fe}(\text{ClO}_4)_3 \cdot x\text{H}_2\text{O}$, Aldrich, crystalline, low chloride), iron (II) perchlorate hydrate ($\text{Fe}(\text{ClO}_4)_2 \cdot x\text{H}_2\text{O}$, Aldrich, 98%), perchloric acid (HClO_4 , Ricca Chemical, 2.00 N aqueous), sodium perchlorate (NaClO_4 , Sigma-Aldrich, $\geq 98.0\%$ ACS grade), hydroxylamine hydrochloride (Sigma-Aldrich, ReagentPlus[®], 99%), 1,10-phenanthroline monohydrate (Fluka, for the spectrophotometric determination of Fe(II)) Pd, V ($\geq 99.0\%$), ammonium acetate ($\text{NH}_4\text{CH}_3\text{CO}_2$, Sigma-Aldrich, BioXtra, $\geq 98\%$), glacial acetic acid (Fisher, Certified ACS), *p*-cresol (Acros, 99+%), hydrogen peroxide (H_2O_2 , Fisher Scientific, 30% ACS grade), titanium (IV) sulfate (Pfaltz&Bauer, 30%) and nitric acid in water (Acros, 68-70% ACS grade). Milli-Q

water (resistivity ≥ 18.0 m Ω -cm; Barnstead NANOpure II system) was used in solution preparations.

Solution preparation

All iron solutions were prepared immediately before the experiments as follows: (1) Fe(III) and Fe(II) stock solutions were prepared by dissolving ferric and ferrous salts into a few milliliters of Milli-Q water-diluted HClO₄ solution (0.1 N); (2) after measuring the iron content of stock solutions (described later), appropriate volumes of the Fe(III) and Fe(II) (if needed) stock solutions were added to the reactor to reach the desired total volume and iron concentrations; (3) 2.0 N HClO₄ was added to adjust pH; and (4) NaClO₄ salt was added to achieve 0.1 M ionic strength. In experiments where *p*-cresol was utilized as a \cdot OH scavenger, a freshly prepared 50 mM *p*-cresol aqueous solution was added to make the initial concentration of *p*-cresol 100 μ M. After preparation, solutions were stirred for 15 minutes before UV irradiation began. For photo-Fenton experiments, H₂O₂ was introduced immediately following exposure to light unless otherwise indicated.

Experimental setup and procedure

A STER-L-RAY[®] low-pressure UV ($\lambda = 254$ nm) lamp (G10T5 1/2L, ozone free) was used for irradiation in this study. A cylindrical glass batch reactor (14-cm inner diameter, 300 mL volume with 2-cm light path length) with continuous agitation using a HI 190M-1 magnetic mini-stirrer (Hanna Instruments) and 6 \times 25 mm PTFE magnetic stir bar was employed. The reactor was set on an optical table 20 cm below the low-pressure UV lamp (Figure 1). At this distance, the

average intensity at the fluid surface was $780 \mu\text{W}/\text{cm}^2$ —measured using a UV Power Meter (Model C8026, Hamamatsu Photonics K.K.) with 254 nm sensor (Model H8025-254).

During the experiments, 1-mL samples were periodically withdrawn for iron analysis. Samples were also taken for determinations of *p*-cresol and H_2O_2 . All samples were analyzed immediately after collection. The reactor temperature was maintained at 25 °C, and solution pH was continuously monitored (VWR, SP70P).

All glassware was washed with 1% nitric acid aqueous solution first, then rinsed 3 to 5 times with Milli-Q water, and baked overnight at 550 °C using a Thermolyne 6000 Muffle Furnace (Dubuque, IA). Quartz cuvettes (Perkin Elmer, Quartz SUPRASIL Macro) used in fluorescence and UV/Vis spectroscopic analyses were pre-soaked in 3% nitric acid/water before use.

Analytical

The *o*-phenanthroline colorimetric method (Tamura et al. 1974) was used to measure Fe(II) and Fe(III) ($[\text{Fe(III)}] = [\text{Fe}]_{\text{tot}} - [\text{Fe(II)}]$). During the experiments, 1-mL samples were added to 20-mL borosilicate glass scintillation vials containing 2.5-mL Milli-Q water, 1-mL ammonium acetate buffer solution (250 g $\text{NH}_4\text{CH}_3\text{CO}_2$ dissolved in 150-mL Milli-Q water plus 700-mL glacial acetic acid) and 0.5-mL phenanthroline solution (100 mg 1,10-phenanthroline monohydrate solids dissolved in 100-mL Milli-Q water) for Fe(II) analysis. Absorbance of the assay mixture was measured by a Thermo Scientific Genesys 10s UV-Vis spectrophotometer at 510 nm ($\epsilon = 11,000 \text{ M}_{\text{Fe(II)}}^{-1}\text{cm}^{-1}$). Next, 0.1-mL of concentrated hydroxylamine hydrochloride solution (200 g/L) was spiked into the assay mixture to reduce all Fe(III) to Fe(II) before the absorbance of the assay mixture was again measured (same method) to obtain the total iron

concentration (i.e.— $[\text{Fe(II)}] = [\text{Fe}]_{\text{tot}}$ in this case). Iron absorption spectra from 200 to 380 nm were determined using the same UV-Vis spectrophotometer.

p-Cresol was analyzed using a PerkinElmer LS 55 fluorescence spectrophotometer equipped with a pulsed xenon lamp to reduce the photobleaching effect. The inner filter effect (IFE) caused by incident light absorption and reabsorption of fluorescence was corrected by a mathematical model (MacDonald et al. 1997) that takes into account the sample absorption spectrum. Sample spectra were obtained by UV-Vis spectrophotometry. All fluorescence intensities (arbitrary unit, AU) were corrected by the IFE model before data analysis.

H_2O_2 concentrations were determined using the titanium sulfate colorimetric method (Boltz and Holwell 1978), which has a detection range from 1.5×10^{-6} to 10^{-1} M, using assay dilution factors ranging from 0.98 to 0.007. Absorbance of the complex formed from the reaction between H_2O_2 and titanium sulfate was measured using the UV-Vis spectrophotometer at 407 nm ($\epsilon = 730 \text{ M}_{\text{H}_2\text{O}_2}^{-1} \text{ cm}^{-1}$).

Modeling

Kinetic model

Reactions that comprise the kinetic model, rate constants for all elementary reactions and equilibrium constants for reversible reactions are provided in Table 1. The kinetic model accounts for: (1) photolysis of Fe^{3+} , $\text{Fe}(\text{OH})^{2+}$, and H_2O_2 ; (2) Fenton-like reactions—i.e. $\text{Fe(III)}/\text{H}_2\text{O}_2$ and related reactions; and (3) reactions of *p*-cresol and its oxidation by-products with $\cdot\text{OH}$.

The initial step of this system was used to study the photolysis of Fe^{3+} and $\text{Fe}(\text{OH})^{2+}$ alone (P1 and P2 in Table 1). The rate of reduction of Fe(III) via photolysis is given by

$$\frac{d[\text{Fe(III)}]_{\text{photo}}}{dt} = -(\Phi_{\text{Fe}}f_{\text{Fe}} + \Phi_{\text{FeOH}}f_{\text{FeOH}})I_0(1 - 10^{-\text{Abs}_{254}}) \quad \text{Eq (1)}$$

Φ_{Fe} and Φ_{FeOH} are quantum yields (hydroxyl radical production/photon absorption, mol/Ein) for the hydrolytic disproportionation of Fe^{3+} and $\text{Fe}(\text{OH})^{2+}$ at 254 nm, respectively; I_0 is the average UV₂₅₄ fluence rate ($\text{EinL}^{-1}\text{s}^{-1}$); f_{Fe} and f_{FeOH} are the fractions of light absorbed by Fe^{3+} and FeOH^{2+} and Abs_{254} is the total solution absorbance at 254 nm.

The UV₂₅₄ fluence rate is calculated from

$$I_0 = \frac{A_R \lambda E}{V_R h c N_a} \quad \text{Eq (2)}$$

where A_R and V_R are reactor surface area (m^2) and volume (L), λ is incident light wavelength (m), E is incident light intensity (W/m^2), h is Planck's constant ($\text{kg}\cdot\text{m}^2\cdot\text{s}^{-1}/\text{photon}$), c is speed of light (m/s) and N_a is Avogadro constant (photons/Ein).

Fractions of light absorbed by the Fe^{3+} and FeOH^{2+} are

$$f_{\text{Fe}} = \frac{\varepsilon_{\text{Fe}}[\text{Fe}^{3+}]\ell}{\text{Abs}_{254}} \quad \text{Eq (3)}$$

$$f_{\text{FeOH}} = \frac{\varepsilon_{\text{FeOH}}[\text{FeOH}^{2+}]\ell}{\text{Abs}_{254}} \quad \text{Eq (4)}$$

where ε_{Fe} and $\varepsilon_{\text{FeOH}}$ are molar absorptivities ($\text{M}^{-1}\text{cm}^{-1}$) of Fe^{3+} and $\text{Fe}(\text{OH})^{2+}$ at 254 nm, respectively, and ℓ is the UV path length (cm). The total solution absorbance is then

$$\text{Abs}_{254} = \sum \varepsilon_i [i] \ell \quad \text{Eq (5)}$$

ε_i is the total molar absorptivity ($\text{M}^{-1}\text{cm}^{-1}$) at 254 nm including light absorption by Fe^{3+} , FeOH^{2+} , $\text{Fe}(\text{OH})_2^+$, $\text{Fe}_2(\text{OH})_2^{4+}$, $\text{Fe}(\text{HO}_2)^{2+}$, $\text{Fe}(\text{OH})(\text{HO}_2)^+$, Fe^{2+} , Na^+ , ClO_4^- , H_2O_2 , *p*-cresol or $\cdot\text{OH}$ oxidation by-products of *p*-cresol (i.e.—4MC and 4MB). Except for ε_{4MC} ($310 \text{ M}^{-1}\text{cm}^{-1}$; Zhang et al. 2016), ε_{4MB} ($2100 \text{ M}^{-1}\text{cm}^{-1}$; Waite 1976; Jongberg et al. 2011) and ε_{IPOH} ($0.003 \text{ M}^{-1}\text{cm}^{-1}$; this study), molar extinction coefficients are as provided in supporting informations.

Once $\cdot\text{OH}$ is produced, H_2O_2 will be formed from radical-radical extinction (R15), which has a reported rate constant of $5.2 \times 10^9 \text{ M}^{-1}\text{s}^{-1}$. The in this way, the production of hydrogen peroxide converts the Fe(III) photolysis process initially present to a photo-Fenton process, although the concentrations of H_2O_2 are expected to remain low throughout. The overall process becomes a combination of three coincident $\cdot\text{OH}$ generation mechanisms: Fe(III) photolysis, H_2O_2 photolysis and Fenton-like radical generation. The Fenton-like mechanism, which was studied by De Laat and Gallard (1999), was used in this study. In a subset of the experiments conducted here, *p*-cresol was used as a radical scavenger. In those cases, the mechanism of *p*-cresol oxidation by $\cdot\text{OH}$ (Zhang et al. 2016) was integrated into the kinetic model.

According to the mechanism provided in Table 1, rate equations for Fe(III) species, Fe^{2+} (at the pH of this study, $[\text{Fe}^{2+}] = [\text{Fe}(\text{II})]$), H_2O_2 , *p*-cresol and $\cdot\text{OH}$ can be expressed in terms of the following set of differential equations:

$$\begin{aligned} \frac{d[\text{H}_2\text{O}_2]}{dt} = & -\Phi_{\text{H}_2\text{O}_2} f_{\text{H}_2\text{O}_2} I_0 (1 - 10^{-\text{Abs}_{254}}) - k_3 [\text{H}_2\text{O}_2] [\text{Fe}^{2+}] - k_5 [\text{H}_2\text{O}_2] [\cdot\text{OH}] \\ & + k_{11} [\text{HO}_2\cdot] [\text{HO}_2\cdot] + k_{12} [\text{O}_2^{\cdot-}] [\text{HO}_2\cdot] + k_{15} [\cdot\text{OH}] [\cdot\text{OH}] \end{aligned} \quad \text{Eq (6)}$$

$$\frac{d[\cdot\text{OH}]}{dt} = (2\Phi_{\text{H}_2\text{O}_2} f_{\text{H}_2\text{O}_2} + \Phi_{\text{Fe}} f_{\text{Fe}} + \Phi_{\text{FeOH}} f_{\text{FeOH}}) I_0 (1 - 10^{-\text{Abs}_{254}})$$

$$\begin{aligned}
& +k_3[\text{Fe}^{2+}][\text{H}_2\text{O}_2] - k_4[\cdot\text{OH}][\text{Fe}^{2+}] - k_5[\cdot\text{OH}][\text{H}_2\text{O}_2] - k_{13}[\cdot\text{OH}][\text{HO}_2\cdot] \\
& -k_{14}[\cdot\text{OH}][\text{O}_2^{\cdot-}] - 2k_{15}[\cdot\text{OH}][\cdot\text{OH}] - k_{16}[\cdot\text{OH}][p\text{-cresol}] \\
& -k_{17}[4\text{MC}][\cdot\text{OH}] - 2k_{18}[4\text{MB}][\cdot\text{OH}] - 4k_{19}\gamma_{\pm 1}[3\text{MM}^-][\cdot\text{OH}] \\
& -k_{20}\gamma_{\pm 1}[\text{L}^-][\cdot\text{OH}] - k_{21}\gamma_{\pm 1}[\text{Ox}^-][\cdot\text{OH}] - k_{22}\gamma_{\pm 2}[\text{Ox}^{2-}][\cdot\text{OH}] \\
& -k_{24}[\text{HA}][\cdot\text{OH}] - k_{25}\gamma_{\pm 1}[\text{A}^-][\cdot\text{OH}] - k_{26}\gamma_{\pm 1}[\text{F}^-][\cdot\text{OH}] \\
& -k_{27a/b}[\cdot\text{OH}][\text{IPOH}]
\end{aligned} \tag{Eq (7)}$$

$$\begin{aligned}
\frac{d[\text{Fe}^{2+}]}{dt} &= (\Phi_{\text{Fe}}f_{\text{Fe}} + \Phi_{\text{FeOH}}f_{\text{FeOH}})I_0(1 - 10^{-\text{Abs}_{254}}) + k_1[\text{Fe}(\text{HO}_2)^{2+}] \\
& +k_2[\text{Fe}(\text{OH})(\text{HO}_2)^+] - k_3[\text{Fe}^{2+}][\text{H}_2\text{O}_2] - k_4[\text{Fe}^{2+}][\cdot\text{OH}] \\
& -k_6[\text{Fe}^{2+}][\text{HO}_2\cdot] - k_7[\text{Fe}^{2+}][\text{O}_2^{\cdot-}] + k_8[\text{HO}_2\cdot][\text{Fe}(\text{III})] \\
& +k_9[\text{O}_2^{\cdot-}][\text{Fe}(\text{III})]
\end{aligned} \tag{Eq (8)}$$

$$\frac{d[\text{Fe}(\text{III})]_{\text{tot}}}{dt} = -\frac{d[\text{Fe}^{2+}]}{dt} \tag{Eq (9)}$$

$$\frac{d[p\text{-cresol}]}{dt} = -\Phi_{p\text{-cresol}}f_{p\text{-cresol}}I_0(1 - 10^{-\text{Abs}_{254}}) - k_{16}[p\text{-cresol}][\cdot\text{OH}] \tag{Eq (10)}$$

where

$$[\text{Fe}(\text{III})]_{\text{tot}} = [\text{Fe}(\text{III})] + [\text{Fe}(\text{HO}_2)^{2+}] + [\text{Fe}(\text{OH})(\text{HO}_2)^+] \tag{Eq (11)}$$

$$[\text{Fe}(\text{III})] = [\text{Fe}^{3+}] + [\text{Fe}(\text{OH})^{2+}] + [\text{Fe}(\text{OH})_2^+] + 2[\text{Fe}_2(\text{OH})_2^{4+}] \tag{Eq (12)}$$

$$\gamma_{\pm 1} = 10^{-0.51 \times (\pm 1)^2 \left(\frac{\sqrt{\text{ionic strength}}}{1 + \sqrt{\text{ionic strength}}} - 0.2 \times \text{ionic strength} \right)} \tag{Eq (13)}$$

and

$$[\text{Fe}(\text{OH})^{2+}] = \frac{K_1[\text{Fe}^{3+}]}{[\text{H}^+]} \tag{Eq (14)}$$

$$[\text{Fe}(\text{OH})_2^+] = \frac{K_2[\text{Fe}^{3+}]}{[\text{H}^+]^2} \quad \text{Eq (15)}$$

$$[\text{Fe}_2(\text{OH})_2^{4+}] = \frac{K_3[\text{Fe}^{3+}]^2}{[\text{H}^+]^2} \quad \text{Eq (16)}$$

$$[\text{Fe}(\text{HO}_2)^{2+}] = \frac{K_4[\text{Fe}^{3+}][\text{H}_2\text{O}_2]}{[\text{H}^+]} \quad \text{Eq (17)}$$

$$[\text{Fe}(\text{OH})(\text{HO}_2)^+] = \frac{K_5[\text{Fe}(\text{OH})^{2+}][\text{H}_2\text{O}_2]}{[\text{H}^+]} = \frac{K_1 K_5 [\text{Fe}^{3+}]^2 [\text{H}_2\text{O}_2]}{[\text{H}^+]^2} \quad \text{Eq (18)}$$

$$[\text{H}^+] = \frac{\{\text{H}^+\}}{\gamma_{\pm 1}} = \frac{10^{-\text{pH}}}{\gamma_{\pm 1}} \quad \text{Eq (19)}$$

Reaction rate expressions for other radicals and *p*-cresol $\cdot\text{OH}$ oxidation by-products are available in the supplementary data. The resultant set of simultaneous, ordinary differential equations/algebraic equations was solved using the MATLAB (R2016a) ode15s solver.

Prediction of iron speciation

At a given pH, H_2O_2 concentration, total iron and Fe(II) contents, the composition of an iron solution with 0.1 M ionic strength can be computed by solving equations Eq (20) - (22) for the three unknowns: $[\text{Fe}^{3+}]$, $[\text{ClO}_4^-]$ and $[\text{Na}^+]$. These equations are based on the iron mass balance, charge balance and solution ionic strength. They were solved using MATLAB (R2016a) fsolve.

$$[\text{Fe}]_{\text{tot}} = [\text{Fe}^{3+}] + [\text{Fe}(\text{OH})^{2+}] + [\text{Fe}(\text{OH})_2^+] + 2[\text{Fe}_2(\text{OH})_2^{4+}] \\ + [\text{Fe}(\text{HO}_2)^{2+}] + [\text{Fe}(\text{OH})(\text{HO}_2)^+] + [\text{Fe}^{2+}] \quad \text{Eq (20)}$$

$$[\text{OH}^-] + [\text{ClO}_4^-] = 3[\text{Fe}^{3+}] + 2[\text{Fe}(\text{OH})^{2+}] + [\text{Fe}(\text{OH})_2^+] + 4[\text{Fe}_2(\text{OH})_2^{4+}] \\ + 2[\text{Fe}(\text{HO}_2)^{2+}] + [\text{Fe}(\text{OH})(\text{HO}_2)^+] + 2[\text{Fe}^{2+}] + [\text{Na}^+] + [\text{H}^+] \quad \text{Eq(21)}$$

$$\begin{aligned}
\text{Ionic strength} = & 0.5(16[\text{Fe}_2(\text{OH})_2^{4+}] + 9[\text{Fe}^{3+}] + 4([\text{Fe}(\text{OH})^{2+}] + [\text{Fe}(\text{HO}_2)^{2+}] \\
& + [\text{Fe}^{2+}]) + [\text{Fe}(\text{OH})_2^+] + [\text{Fe}(\text{OH})(\text{HO}_2)^+] + [\text{Na}^+] + [\text{H}^+] \\
& + [\text{OH}^-] + [\text{ClO}_4^-])
\end{aligned} \tag{Eq (22)}$$

The resultant pH-dependent mole fractions of primary Fe(III) species for the case in which $[\text{Fe(III)}] = 0.1 \text{ mM}$ and ionic strength is 0.1 M are as shown (Figure 2).

Absorption spectrum calculation

Using the calculated solution composition shown above, total absorption spectra from 200 to 380 nm were calculated using following equation:

$$\text{Abs}_\lambda = \sum \varepsilon_{i-\lambda} [i] \tag{Eq (23)}$$

where $\varepsilon_{i-\lambda}$ is molar absorptivity ($\text{M}^{-1}\text{cm}^{-1}$) at wavelength λ of species i , including Fe^{3+} , FeOH^{2+} , $\text{Fe}(\text{OH})_2^+$, $\text{Fe}_2(\text{OH})_2^{4+}$, $\text{Fe}(\text{HO}_2)^{2+}$, $\text{Fe}(\text{OH})(\text{HO}_2)^+$, Fe^{2+} , Na^+ , ClO_4^- and H_2O .

Results and discussion

In principle, the kinetic model for the photo-Fenton system should also be able to predict reactor performance for the following special cases: (i) iron solution with H_2O_2 without irradiation, i.e. Fenton-like system and (ii) H_2O_2 aqueous solution without iron, with irradiation, i.e. H_2O_2 direct UV_{254} photolysis. Before engaging in these experiments, the accuracies of iron species equilibria and light extinction parameters for individual species were confirmed by comparing experimentally determined absorption spectra of $\text{Fe}(\text{ClO}_4)_3$ solutions with spectra predicted using equations Eq (20) - (23) (Figure 3).

Results of both Fenton-like and H₂O₂ direct UV₂₅₄ photolysis experiments are well predicted by the kinetic model (Figure 4), illustrating the ability of the model to simulate the iron photolysis process once relevant photochemical constants, i.e.—quantum yields of Fe³⁺ and FeOH²⁺ and molar absorptivities of light absorbing compounds—are determined.

Good agreement between measured and calculated spectra of iron solutions under these conditions supports the validity of solution speciation calculations, as well as the molar absorptivity data for light absorbing species, both of which are key components of the general kinetic model.

The second step of the investigation was to verify the quantum yields of Fe³⁺ and Fe(OH)²⁺. *p*-Cresol, whose reaction with hydroxyl radical has a rate constant of $1.2 \times 10^{10} \text{ M}^{-1} \text{ s}^{-1}$, was used to quench $\cdot\text{OH}$, minimizing the oxidation of Fe(II) to Fe(III). Excess *p*-cresol (100 μM initially) was maintained throughout the 90-second irradiation experiments so that $k_{16}[p\text{-cresol}][\cdot\text{OH}] \gg k_4[\text{Fe}^{2+}][\cdot\text{OH}]$. To generate significant spread in resultant trajectories of free ferrous ion, Fe(ClO₄)₃ solutions at pH 2 and 3 were irradiated with UV light. Results are summarized in Figure 5a. Data for control experiments without *p*-cresol as well as absence of irradiation are shown in Figure 5b.

Fe(II) accumulation in the first 30 seconds of the experiment was well predicted by the kinetic model at both pHs, which confirms the reported values of Φ_{Fe} and Φ_{FeOH} from Lee and Yoon (2004a). The formation rates of Fe(II) from Fe³⁺ and FeOH²⁺ photolysis were $5.24 \times 10^{-8} \text{ M/s}$ and $1.20 \times 10^{-7} \text{ M/s}$ at pH 2 and pH 3, respectively (Eq 1). Assuming that these rates remained essentially constant and ignoring other reactions, development of Fe(II) after 30 seconds at pH 2

and pH 3 would be 1.6 μM and 3.6 μM . This approximation provides the same result as the kinetic model (Figure 5a). In other words, with the $\cdot\text{OH}$ scavenger present, the evolution of Fe(II) was due exclusively to Fe^{3+} and FeOH^{2+} photolysis. Absent *p*-cresol, however, the Fe(II) concentration grew more slowly, especially after 30 seconds (Figure 5b). When the UV source was eliminated, the Fe(II) concentration stopped increasing immediately and decreased slightly during the next five seconds.

After about 30 seconds of irradiation, a small deviation between data and simulation is apparent (Figure 5a). Even after 90 seconds of the experiment, however, $k_{16}[\textit{p}\text{-cresol}] \gg k_4[\text{Fe}^{2+}]$, noting that the Fe(II) concentration was about 9 μM (data at pH 3). It is unlikely that the concentration of *p*-cresol was much affected during that period. Thus the deceleration of Fe(II) accumulation cannot be explained by our current kinetic model. Potential explanations for the discrepancy lie in (i) the reoxidation of Fe(II) by reactive intermediates other than hydroxyl radical, e.g., H_2O_2 developed through a mechanism that was not including in our model or (ii) an unanticipated reaction involving reactive intermediate(s) derived from the oxidation of *p*-cresol by $\cdot\text{OH}$.

In order to explore Fe(II) behavior over a long time scale in the presence of excess *p*-cresol, an 8-hr irradiation study including a light-out test at $t = 405$ min was carried out. Per Figure 6, Fe(II) accumulated rapidly during the first 10 minutes, and this fast growth is well represented by the model. Beyond $t \approx 15$ min, however, the measure accumulation of Fe(II) lagged behind simulation results significantly, so that Fe(II) reached a maximum at $t = 210$ min $[\text{Fe(II)}]/[\text{Fe}]_{\text{tot}} \approx 0.7$ ratio and declined thereafter, presumably due to the gradual disappearance of the $\cdot\text{OH}$

scavenger ($[p\text{-cresol}] < 10 \mu\text{M}$). The model, however, quickly reached steady state with $[\text{Fe(II)}]/[\text{Fe}]_{\text{tot}} \approx 1.0$ at $t = 90 \text{ min}$.

The rapid decomposition of *p*-cresol in the first 60 minutes is due to the fast reaction between *p*-cresol and the $\cdot\text{OH}$ generated from Fe(III) photolysis, which essentially eliminated the reaction of $\cdot\text{OH}$ with Fe^{2+} . A concentration of $6 \mu\text{M}$ of H_2O_2 was measured when the lamp was turned off at $t = 405 \text{ min}$, which is much higher than the predicted level (10^{-14} M). As a consequence, the Fe(II) level dropped from $50 \mu\text{M}$ to $40 \mu\text{M}$ over the next few minutes. That change was well predicted by the model (black solid line).

In total, results shown to this point indicate that the kinetic model developed here can predict the behavior of: (1) the UV/ H_2O_2 process, (2) the Fenton's reaction process, (3) the direct photolysis of *p*-cresol and H_2O_2 , and (4) Fe(III) photolysis at relatively short times (Figure 5). However, when the model is applied to Fe(III) photolysis in long-term experiments (Figure 7), large discrepancies arise.

Model deficiencies are even more apparent in long term photolysis experiments/simulations (Figure 7). Under all experimental conditions, Fe(II) accumulated far more rapidly than predicted during the first few minutes of the experiment. The rate of increase of Fe(II) concentration decreased continuously over the hour-long experiments but remained positive throughout. Two trends are clear from the results shown: (1) At constant pH, observed rates of Fe(II) accumulation are directly related to initial Fe(III) concentrations and (2) at the same initial Fe(III) concentration, higher solution pH favors the accumulation of Fe(II). Both observations are subjectively consistent with the kinetic model proposed. Nevertheless, the most obvious

result of the long-term experiments is the underprediction of time-dependent Fe(II) concentrations by the model. Measured absorption spectra in samples taken during these experiments were in excellent agreement with spectra predicted on the basis of measured Fe(II) concentrations and Fe(III) species calculated on the basis of total iron and pH measurements (Figure 8)—eliminating the possibility of analytical error in the measurement of iron forms. By employing OriginPro 2016 (v. 9.3.2), a trendline was fitted (using B-spline connection fitting) to the experimental data on Fe(II) vs. time for the experiment with $[\text{Fe}]_{\text{tot}} = [\text{Fe(III)}]_0 = 0.1 \text{ mM}$ at $\text{pH} = 3$, in order to yield a continuous smooth curve of the overall accumulation rate of Fe(II) as a function of irradiation time. Results are presented in Figure 9.

Per Figure 9, the initial accumulation rate of Fe(II), which is determined by Eq (1) in model calculations, is the same for both curves. However, the model predicts a decrease in the net rate of iron reduction from 10^{-7} M/s to 10^{-9} M/s within in the first minute of the experiment, while the observed accumulation rate decreased much more slowly. After the first few minutes, both model and data follow similar trends (i.e., the fractional difference between observed and measured rates of Fe(II) accumulation remain essentially constant). The failure of the model to reproduce the long-term experiments is apparently due to inaccuracies at the start of the process. Based on the proposed reaction mechanism (Table 1), six elementary reactions (P1, P2, R1, R2, R8 and R9) produce Fe(II), and four (R3, R4, R6 and R7) oxidize Fe(II). The (predicted) individual contribution of each elementary reaction to the net rate of Fe(II) accumulation over the hour-long experiments was as shown (Figure 10). Initial conditions for the exercise were as follows: $[\text{Fe}]_{\text{tot}} = [\text{Fe(III)}]_0 = 0.1 \text{ mM}$ at $\text{pH} = 3$.

The predicted rate of formation of Fe(II) is dominated by Fe^{3+} and FeOH^{2+} photolysis throughout the experiment period. This is logical since Fe(II) remains a small fraction of total iron in the simulations. The predicted rate of Fe(II) oxidation is dominated by the reaction between Fe^{2+} and $\cdot\text{OH}$. Since the photochemical properties of Fe^{3+} and FeOH^{2+} have been validated, it is likely that the kinetic model overestimates the oxidation rate of Fe(II) by $\cdot\text{OH}$ in the first minute, suggesting that hydroxyl radical does not increase as rapidly as predicted by the model or that the reaction of Fe(II) with hydroxyl radical is much slower than was originally estimated. Possibilities include that either (i) something in the reactor quenches $\cdot\text{OH}$ at the start of the experiment, or (ii) Fe(II) was somehow “shielded”, inhibiting oxidation of Fe(II) by $\cdot\text{OH}$. Results generated in the presence of excess *p*-cresol (Figure 5b) clearly show that the fault in the model does not lie on the photolysis (generation) side of the Fe(II) production equation (Eq 1).

Underestimation of Fe(II) accumulation during Fe(III) photolysis was noted previously. Wang and Liu (2014) fitted experimental data under conditions similar to this work by decreasing the reaction rate constant for the oxidation of Fe^{2+} by hydroxyl radical from $3.2 \times 10^8 \text{ M}^{-1}\text{s}^{-1}$ to $3.47 \times 10^6 \text{ M}^{-1}\text{s}^{-1}$. This is not supported by the work of Stuglik and Zagórski (1981), who established the higher rate constant (used here) by pulse radiolysis. The higher value is similar to that of Jayson et al. (1972) ($2.3 \times 10^8 \text{ M}^{-1}\text{s}^{-1}$) estimated using the same method.

The kinetic model developed here accurately predicts rates of decomposition of H_2O_2 in the Fenton system (Figure 4a) and the H_2O_2 UV photolysis system (Figure 4b). In addition, the simulated destructions of trace organics using the two systems are accurate, suggesting that

hydroxyl radical concentrations derived from the model are also accurate (Rojas et al. 2010; 2011). The model fails, however, to predict iron behavior during Fe(III) photolysis.

To further diagnose the problem, we carried out additional Fe(III) photolysis experiments, increasing the initial concentration of H₂O₂ in a series of steps. This was designed to gradually shift the process from a predominantly photolytic system to a predominantly Fenton-driven system (Figure 11). Deviation between experimental and predicted Fe(II) concentration profiles was much reduced at higher initial H₂O₂ concentrations. The data show that Fe(II) is initially generated faster in the reactor with 50 μM H₂O₂ compared to the H₂O₂-free control. This is due to ·OH quenching by H₂O₂, which encourages Fe(II) to accumulate. However, the rate of increase of Fe(II) concentration becomes slower in the reactors with 1.0 and 12 mM H₂O₂ (initial concentrations) presumably because Fe(II) formed is reoxidized to Fe(III) by H₂O₂, particularly in the first 5 minutes of the experiment. The trajectory of Fe(II) concentration in the reactor with 12 mM H₂O₂ exhibited three stages: (1) 0 – 5 minutes, fast buildup, (2) 5 – 30 minutes, slow and steady accumulation, and (3) 30 – 60 minutes, steadily increasing rate of accumulation (Figure 11a). Interestingly, all three phases were predicted by the model. In addition, roughly 80% H₂O₂ loss was measured in each experiment, regardless of initial peroxide dose (Figure 11b). Except for the H₂O₂-free experiments, the evolution of Fe(II) is well represented by the model during the first 5 minutes. However, in the [H₂O₂]₀ = 50 μM experiment, the predicted Fe(II) concentration reached a steady, maximum after five minutes that was not observed among the measured values. Predicted Fe(II) concentrations for the reactor with 1 mM H₂O₂ matched experimental results for the first 30 minutes before approaching a steady maximum that, again, was not observed in the

data. The model accurately predicted the Fe(II) concentration throughout the 60-minute experiment at the highest initial H₂O₂ dose provided (12 mM).

To further explore inadequacies of the proposed iron conversion mechanism, experiments and simulations were carried out for Fenton and photo-Fenton systems starting with iron present as Fe(II) (Figure 12). Absent irradiation (i.e.—Fenton system), the Fe(II) concentration dropped > 50% during the first 5 seconds of the experiment and another 25% (based on initial concentration) during the next 45 seconds. With irradiation, oxidation of Fe(II) was even faster. The model accurately predicted the decrease in Fe(II) during the Fenton experiment. Model results were unchanged by UV irradiance, whereas UV light accelerated the observed conversion of Fe(II) in the photo-Fenton experiment.

The kinetic model was also tested for an photo-Fenton experiment that started with a Fe(II)/Fe(III) that was roughly equal to 1.0 and pH₀ = 3.0. The solution was UV irradiated for 30 minutes before 25 μM H₂O₂ was spiked into the reactor. A second identical peroxide spike was added at 75 minutes total irradiation time. Fe(II) and H₂O₂ were monitored semi-continuously. The Fe(II) level was stable throughout the first 30 minutes of the experiment (Figure 13). Following the first addition of H₂O₂, Fe(II) was oxidized from 57 μM to 20 μM within 20 minutes, stabilizing around 19 μM as peroxide was exhausted. The Fe(II) concentration decreased further, to 12 μM, and again leveled off after exhaustion of the second H₂O₂ spike. Observed characteristics in the trajectories of both Fe(II) and H₂O₂ concentrations were well described by the kinetic model.

Conclusions

An Fe(III) UV₂₅₄ photolysis kinetic model that combines the Fenton-like mechanism with photolysis of Fe³⁺, FeOH²⁺ and H₂O₂ was capable of simulating the time-dependent concentrations of iron species and peroxide during direct photolysis of iron species or H₂O₂ by UV₂₅₄. The model accurately described solute trajectories during Fenton-like reactions. Iron speciation, Fe(III) equilibrium constants, and molar absorptivity of light absorbing compounds were validated using spectrophotometric data and published Fe(III) spectra. The validities of reported quantum yields (Φ_{Fe} and Φ_{FeOH}) were verified via irradiation experiments using excess *p*-cresol as [•]OH scavenger.

The model failed, however, to correctly represent the trajectory of iron reduction in Once Fe(ClO₄)₃ solutions under UV₂₅₄ irradiation. Although model and experiment were initially in agreement, after a few minutes predicted Fe²⁺ concentrations were much lower than observations. The source of these discrepancies remains unresolved. Modeling suggests that absent addition of a hydroxide radical scavenger such as *p*-cresol, rates of iron reduction and oxidation should come into balance after a few minutes. At that point, reductions are dominated by the photolysis of Fe(III)-hydroxo species, and the major pathway for Fe(II) oxidation is the reaction of Fe²⁺ with [•]OH. Overestimation of Fe²⁺ oxidation by [•]OH could arise from either (i) production of an unidentified species that reacts with hydroxyl radicals or (ii) Fe(II) was somehow “shielded” from reaction with [•]OH in the first few minutes of the process.

Simulations were accurate when Fe(II) and H₂O₂ were both initially present in the reactor (photo-Fenton model) at relatively high concentrations and when both Fe(III) and Fe(II) were initially provided at high concentrations (photolysis model).

References

- Adamson, M. G., Baulch, D. L., and Dainton, F. S. (1962). "Use of iron-59 to measure the primary quantum yield of the reaction $\text{Fe}^{3+}_{\text{aq}} \xrightarrow{h\nu/2537} \text{Fe}^{2+} + \text{H}^+ + \text{OH}^-$." *Trans. Faraday Soc.*, 58, 1388-1393.
- Andreozzi, R., Canterino, M., and Marotta, R. (2006). "Fe(III) homogeneous photocatalysis for the removal of 1,2-dichlorobenzene in aqueous solution by means UV lamp and solar light." *Water Res.*, 40(20), 3785-3792.
- Badawy, M. I., Ghaly, M. Y., and Gad-Allah, T. A. (2006). "Advanced oxidation processes for the removal of organophosphorus pesticides from wastewater." *Desalination*, 194(1-3), 166-175.
- Baxendale, J. H., and Magee, J. (1955). "The photochemical oxidation of benzene in aqueous solution by ferric ion." *Trans. Faraday Soc.*, 51, 205-213.
- Baxendale, J. H., and Wilson, J. A. (1957). "The photolysis of hydrogen peroxide at high light intensities." *Trans. Faraday Soc.*, 53, 344-356.
- Benjamin, M. M. (2002). *Water Chemistry*, Waveland Press Inc., Long Grove.
- Benkelberg, H., and Warneck, P. (1995). "Photodecomposition of iron(III) hydroxo and sulfato complexes in aqueous solution: wavelength dependence of OH and SO_4^- quantum yields." *J. Phys. Chem.*, 99(14), 5214-5221.
- Boltz, D., and Holwell, J. (1978). *Colorimetric Determination of Nonmetals, 2nd Edition*, John Wiley and Sons, New York.
- Buxton, G. V., Greenstock, C. L., Helman, W. P., and Ross, A. B. (1988). "Critical review of rate constants for reactions of hydrated electrons, hydrogen atoms and hydroxyl radicals ($\cdot\text{OH}/\cdot\text{O}^-$) in aqueous solution." *J. Phys. Chem. Ref. Data*, 17(2), 513-886.
- De Laat, J., and Gallard, H. (1999). "Catalytic decomposition of hydrogen peroxide by Fe(III) in homogeneous aqueous solution: mechanism and kinetic modeling." *Environ. Sci. Technol.*, 33(16), 2726-2732.
- Einschlag, F. S. G., Braun, A. M., and Oliveros, E. (2013). "Fundamentals and Applications of the Photo-Fenton Process to Water Treatment." *Environmental Photochemistry Part III*, D. W. Bahnemann, and P. K. J. Robertson, eds., Springer, Berlin, 301-342.
- Ershov, B. G., Janata, E., Alam, M. S., and Gordeeva, A. V. (2008). "Studies of the reaction of the hydroxyl radical with the oxalate ion in an acidic aqueous solution by pulse radiolysis." *Russ. Chem. Bull. Int. Ed.*, 57(6), 1187-1189.
- Faust, B. C., and Hoigné, J. (1990). "Photolysis of Fe(III)-hydroxyl complexes as sources of OH radicals in clouds, fog and rain." *Atmos. Environ.*, 24A(1), 79-89.
- Gallard, H., De Laat, J., and Legube, B. (1999). "Spectrophotometric study of the formation of iron(III)-hydroperoxy complexes in homogeneous aqueous solutions." *Water Res.*, 33(13), 2929-

2936.

Gohn, M., and Getoff, N. (1977). "Pulse radiolysis of 3,4-dihydroxytoluene." *J. Chem. Soc., Faraday Trans. 1*, 73, 1207-1215.

Jayson, G. G., Parsons, B. J., and Swallow, A. J. (1972). "Oxidation of ferrous ions by hydroxyl radicals." *J. Chem. Soc., Faraday Trans. 1*, 68(0), 2053-2058.

Jin, L., Zhang, P., Shao, T., and Zhao, S. (2014). "Ferric ion mediated photodecomposition of aqueous perfluorooctane sulfonate (PFOS) under UV irradiation and its mechanism." *J. Hazard. Mater.*, 271, 9-15.

Jongberg, S., Gislason, N. E., Lund, M. N., Skibsted, L. H., and Waterhouse, A. L. (2011). "Thiol-quinone adduct formation in myofibrillar proteins detected by LC-MS." *J. Agric. Food. Chem.*, 59(13), 6900-6905.

Joseph, J. M., Varghese, R., and Aravindakumar, C. T. (2001). "Photoproduction of hydroxyl radicals from Fe(III)-hydroxy complex: a quantitative assessment." *J. Photochem. Photobiol., A*, 146, 67-73

Kang, N., Lee, D. S., and Yoon, J. (2002). "Kinetic modeling of Fenton oxidation of phenol and monochlorophenols." *Chemosphere*, 47, 915-924.

Kavitha, V., and Palanivelu, K. (2004). "The role of ferrous ion in Fenton and photo-Fenton processes for the degradation of phenol." *Chemosphere*, 55(9), 1235-1243.

Kawaguchi, H., and Inagaki, A. (1993). "Photochemical generation rates of hydroxyl radical in aqueous solutions containing Fe(III)-hydroxy complex." *Chemosphere*, 27(12), 2381-2387.

Kim, S., and Vogelpohl, A. (1998). "Degradation of organic pollutants by the photo-Fenton-process." *Chem. Eng. Technol.*, 21(2), 187-191.

Knight, R. J., and Sylva, R. N. (1975). "Spectrophotometric investigation of iron(III) hydrolysis in light and heavy water at 25°C." *J. Inorg. Nucl. Chem.*, 37, 779-783.

Langford, C. H., and Carey, J. H. (1975). "The charge transfer photochemistry of the hexaquoiron(III) ion, the chloropentaaquoiron(III) ion, and the p-dihydroxo dimer explored with tert-butyl alcohol scavenging." *Can. J. Chem.*, 53(16), 2430-2435.

Lee, C., and Yoon, J. (2004a). "Determination of quantum yields for the photolysis of Fe(III)-hydroxo complexes in aqueous solution using a novel kinetic method." *Chemosphere*, 57(10), 1449-1458.

Lee, C., and Yoon, J. (2004b). "Temperature dependence of hydroxyl radical formation in the hv/Fe³⁺/H₂O₂ and Fe³⁺/H₂O₂ systems." *Chemosphere*, 56(10), 923-934.

Logan, S. R. (1990). "Effects of temperature and wavelength on the primary process in the photo-oxidation of Iron(II) ion." *J. Chem. Soc., Faraday Trans.*, 86(4), 615-617.

MacDonald, B. C., Lvin, S. J., and Patterson, H. (1997). "Correction of fluorescence inner filter

- effects and the partitioning of pyrene to dissolved organic carbon.” *Anal. Chim. Acta*, 338, 155-162.
- Machulek, A., Jr., Moraes, J. E., Okano, L. T., Silverio, C. A., and Quina, F. H. (2009). “Photolysis of ferric ions in the presence of sulfate or chloride ions: implications for the photo-Fenton process.” *Photochem Photobiol Sci*, 8(7), 985-991.
- Matilainen, A., and Sillanpää, M. (2010). “Removal of natural organic matter from drinking water by advanced oxidation processes.” *Chemosphere*, 80(4), 351-365.
- Méndez-Arriaga, F., Esplugas, S., and Gimenez, J. (2010). “Degradation of the emerging contaminant ibuprofen in water by photo-Fenton.” *Water Res.*, 44(2), 589-595.
- Nadtochenko, V. A., and Kiwi, J. (1998). “Photolysis of FeOH_2^+ and FeCl_2^+ in aqueous solution. Photodissociation kinetics and quantum yields.” *Inorg. Chem.*, 37, 5233-5238.
- Pešoutová, R., Stritesky, L., and Hlavinek, P. (2014). “A pilot scale comparison of advanced oxidation processes for estrogenic hormone removal from municipal wastewater effluent.” *Water Sci Technol*, 70(1), 70-75.
- Pozdnyakov, I. P., Glebov, E. M., Plyusnin, V. F., Grivin, V. P., Ivanov, Y. V., Vorobyev, D. Y., and Bazhin, N. M. (2000). “Mechanism of $\text{Fe}(\text{OH})_2^+(\text{aq})$ photolysis in aqueous solution.” *Pure Appl. Chem.*, 72(11), 2187-2197.
- Prieto-Rodríguez, L., Oller, I., Klammerth, N., Aguera, A., Rodríguez, E. M., and Malato, S. (2013). “Application of solar AOPs and ozonation for elimination of micropollutants in municipal wastewater treatment plant effluents.” *Water Res.*, 47(4), 1521-1528.
- Rodríguez, E., Mimbbrero, M., Masa, F. J., and Beltran, F. J. (2007). “Homogeneous iron-catalyzed photochemical degradation of muconic acid in water.” *Water Res.*, 41(6), 1325-1333.
- Rodríguez, E. M., Fernandez, G., Alvarez, P. M., and Beltran, F. J. (2012). “ TiO_2 and Fe (III) photocatalytic ozonation processes of a mixture of emergent contaminants of water.” *Water Res.*, 46(1), 152-166.
- Rodríguez, M., Abderrazik, N. B., Contreras, S., Chamarro, E., Gimenez, J., and Esplugas, S. (2002). “Iron(III) photooxidation of organic compounds in aqueous solutions.” *Appl. Catal., B*, 37(2002), 131-137.
- Rojas, M. R., Leung, C., Whitley, D., Zhu, Y., Arnold, R. G., and Sáez, A. E. (2011). “Advanced oxidation of trace organics in water by hydrogen peroxide solar photolysis.” *Ind. Eng. Chem. Res.*, 50(22), 12479-12487.
- Rojas, M. R., Pérez, F., Whitley, D., Arnold, R. G., and Sáez, A. E. (2010). “Modeling of advanced oxidation of trace organic contaminants by hydrogen peroxide photolysis and Fenton's reaction.” *Ind. Eng. Chem. Res.*, 49(22), 11331-11343.
- Rosario-Ortiz, F. L., Wert, E. C., and Snyder, S. A. (2010). “Evaluation of $\text{UV}/\text{H}_2\text{O}_2$ treatment for the oxidation of pharmaceuticals in wastewater.” *Water Res.*, 44(5), 1440-1448.

- Shemer, H., Kunukcu, Y. K., and Linden, K. G. (2006). "Degradation of the pharmaceutical metronidazole via UV, Fenton and photo-Fenton processes." *Chemosphere*, 63(2), 269-276.
- Sun, W., and Saeys, M. (2008). "First principles study of the reaction of formic and acetic acids with hydroxyl radicals." *J. Phys. Chem. A*, 112(30), 6918-6928.
- Spasiano, D., Marotta, R., Gargano, I., Somma, I. D., Vitiello, G., D'Errico, G., and Andreozzi, R. (2014). "Kinetic modeling of partial oxidation of benzyl alcohol in water by means of Fe(III)/O₂/UV-solar simulated process." *Chemical Engineering Journal*, 249, 130-142.
- Stuglik, Z., and Zagórski, Z. P. (1981). "Pulse radiolysis of neutral iron(II) solutions: oxidation of ferrous ions by OH radicals." *Radiat. Phys. Chem.*, 17(4), 229-233.
- Tamura, H., Goto, K., Yotsuyanagi, T., and Nagayama, M. (1974). "Spectrophotometric determination of iron(II) with 1,10-phenanthroline in the presence of large amounts of iron(III)." *Talanta*, 21(4), 314-318.
- Waite, J. H. (1976). "Calculating extinction coefficients for enzymatically produced o-quinones." *Anal. Biochem.*, 75, 211-218.
- Wang, Z., and Liu, J. (2014). "New insight into photochemical oxidation of Fe(II): The roles of Fe(III) and reactive oxygen species." *Catalysis Today*, 224, 244-250.
- Zepp, R. G., Faust, B. C., and Hoigné, J. (1992). "Hydroxyl radical formation in aqueous reactions (pH 3-8) of iron(II) with hydrogen peroxide: the photo-Fenton reaction." *Environ. Sci. Technol.*, 26(2), 313-319.
- Zhang, T., Cheng, L., Ma, L., Meng, F., Arnold, R. G., and Saez, A. E. (2016). "Modeling the oxidation of phenolic compounds by hydrogen peroxide photolysis." *Chemosphere*, 161, 349-357.

Table 1. Summary of reaction rate and equilibrium constants for kinetic modeling of Fe(III) photolysis at 25 °C.

ID	Reactions	Rate constants	Reference
E1	$\text{Fe}^{3+} + \text{H}_2\text{O} \leftrightarrow \text{FeOH}^{2+} + \text{H}^+$	$K_1 = 2.9 \times 10^{-3} \text{ M}$	De Laat and Gallard 1999
E2	$\text{Fe}^{3+} + 2\text{H}_2\text{O} \leftrightarrow \text{Fe(OH)}_2^+ + 2\text{H}^+$	$K_2 = 7.62 \times 10^{-7} \text{ M}^2$	De Laat and Gallard 1999
E3	$2\text{Fe}^{3+} + 2\text{H}_2\text{O} \leftrightarrow \text{Fe}_2(\text{OH})_2^{4+} + 2\text{H}^+$	$K_3 = 0.8 \times 10^{-3} \text{ M}$	De Laat and Gallard 1999
E4	$\text{Fe}^{3+} + \text{H}_2\text{O}_2 \leftrightarrow \text{Fe}(\text{HO}_2)^{2+} + \text{H}^+$	$K_4 = 3.1 \times 10^{-3}$	De Laat and Gallard 1999
E5	$\text{FeOH}^{2+} + \text{H}_2\text{O}_2 \leftrightarrow \text{Fe(OH)(HO}_2)^+ + \text{H}^+$	$K_5 = 2.0 \times 10^{-4}$	De Laat and Gallard 1999
P1	$\text{Fe}^{3+} + \text{H}_2\text{O} + h\nu \rightarrow \text{Fe}^{2+} + \cdot\text{OH} + \text{H}^+$	$\Phi_{\text{Fe}} = 0.046 \text{ mol/Ein}$	Lee and Yoon 2004a
P2	$\text{FeOH}^{2+} + h\nu \rightarrow \text{Fe}^{2+} + \cdot\text{OH}$	$\Phi_{\text{FeOH}} = 0.69 \text{ mol/Ein}$	Lee and Yoon 2004a
P3	$\text{H}_2\text{O}_2 + h\nu \rightarrow \cdot\text{OH} + \cdot\text{OH}$	$\Phi_{\text{H}_2\text{O}_2} = 0.50 \text{ mol/Ein}$	Baxendale and Wilson 1957
R1	$\text{Fe}(\text{HO}_2)^{2+} \rightarrow \text{Fe}^{2+} + \text{HO}_2\cdot$	$k_1 = 2.7 \times 10^{-3} \text{ s}^{-1}$	De Laat and Gallard 1999
R2	$\text{Fe(OH)(HO}_2)^+ \rightarrow \text{Fe}^{2+} + \text{HO}_2\cdot + \text{OH}^-$	$k_2 = 2.7 \times 10^{-3} \text{ s}^{-1}$	De Laat and Gallard 1999
R3	$\text{Fe}^{2+} + \text{H}_2\text{O}_2 \rightarrow \text{Fe}^{3+} + \cdot\text{OH} + \text{OH}^-$	$k_3 = 6.3 \times 10^1 \text{ M}^{-1}\text{s}^{-1}$	De Laat and Gallard 1999
R4	$\text{Fe}^{2+} + \cdot\text{OH} \rightarrow \text{Fe}^{3+} + \text{OH}^-$	$k_4 = 3.2 \times 10^8 \text{ M}^{-1}\text{s}^{-1}$	De Laat and Gallard 1999
R5	$\cdot\text{OH} + \text{H}_2\text{O}_2 \rightarrow \text{HO}_2\cdot + \text{H}_2\text{O}$	$k_5 = 3.3 \times 10^7 \text{ M}^{-1}\text{s}^{-1}$	De Laat and Gallard 1999
R6	$\text{Fe}^{2+} + \text{HO}_2\cdot \rightarrow \text{Fe}(\text{HO}_2)^{2+}$	$k_6 = 1.2 \times 10^6 \text{ M}^{-1}\text{s}^{-1}$	De Laat and Gallard 1999
R7	$\text{Fe}^{2+} + \text{O}_2^{\cdot-} + \text{H}^+ \rightarrow \text{Fe}(\text{HO}_2)^{2+}$	$k_7 = 1.0 \times 10^7 \text{ M}^{-1}\text{s}^{-1}$	De Laat and Gallard 1999
R8	$\text{Fe(III)} + \text{HO}_2\cdot \rightarrow \text{Fe}^{2+} + \text{O}_2 + \text{H}^+$	$k_8 < 2.0 \times 10^3 \text{ M}^{-1}\text{s}^{-1}$	De Laat and Gallard 1999
R9	$\text{Fe(III)} + \text{O}_2^{\cdot-} \rightarrow \text{Fe}^{2+} + \text{O}_2$	$k_9 = 5.0 \times 10^7 \text{ M}^{-1}\text{s}^{-1}$	De Laat and Gallard 1999
R10	$\text{HO}_2\cdot \rightarrow \text{O}_2^{\cdot-} + \text{H}^+$	$k_{10} = 1.58 \times 10^5 \text{ s}^{-1}$	De Laat and Gallard 1999
R10r	$\text{O}_2^{\cdot-} + \text{H}^+ \rightarrow \text{HO}_2\cdot$	$k_{10r} = 1.0 \times 10^{10} \text{ M}^{-1}\text{s}^{-1}$	De Laat and Gallard 1999
R11	$\text{HO}_2\cdot + \text{HO}_2\cdot \rightarrow \text{H}_2\text{O}_2 + \text{O}_2$	$k_{11} = 8.3 \times 10^5 \text{ M}^{-1}\text{s}^{-1}$	De Laat and Gallard 1999
R12	$\text{HO}_2\cdot + \text{O}_2^{\cdot-} + \text{H}_2\text{O} \rightarrow \text{H}_2\text{O}_2 + \text{O}_2 + \text{OH}^-$	$k_{12} = 9.7 \times 10^7 \text{ M}^{-1}\text{s}^{-1}$	De Laat and Gallard 1999
R13	$\cdot\text{OH} + \text{HO}_2\cdot \rightarrow \text{H}_2\text{O} + \text{O}_2$	$k_{13} = 0.71 \times 10^{10} \text{ M}^{-1}\text{s}^{-1}$	De Laat and Gallard 1999
R14	$\cdot\text{OH} + \text{O}_2^{\cdot-} \rightarrow \text{OH}^- + \text{O}_2$	$k_{14} = 1.01 \times 10^{10} \text{ M}^{-1}\text{s}^{-1}$	De Laat and Gallard 1999
R15	$\cdot\text{OH} + \cdot\text{OH} \rightarrow \text{H}_2\text{O}_2$	$k_{15} = 5.2 \times 10^9 \text{ M}^{-1}\text{s}^{-1}$	De Laat and Gallard 1999
P4	$p\text{-cresol} + h\nu \rightarrow \text{products}$	$\Phi_{\text{PC}} = 0.034 \text{ mol/Ein}$	Zhang et al. 2016
R16	$\cdot\text{OH} + p\text{-cresol} \rightarrow 4\text{MC}$	$k_{16} = 1.2 \times 10^{10} \text{ M}^{-1}\text{s}^{-1}$	Buxton et al. 1988
P5	$4\text{MC} + h\nu \rightarrow \text{products}$	$\epsilon_{4\text{MC}} = 310 \text{ M}^{-1}\text{cm}^{-1}$ $\Phi_{\text{PC}} = 0.007 \text{ mol/Ein}$	Zhang et al. 2016
R17	$\cdot\text{OH} + 4\text{MC} \rightarrow 4\text{MB}$	$k_{17} = 1.6 \times 10^{10} \text{ M}^{-1}\text{s}^{-1}$	Gohn and Getoff 1977

Table 1. (Continued)

ID	Reactions	Rate constants	Reference
R18	$\cdot\text{OH} + 4\text{MB} \rightarrow 3\text{MM}^-$	$k_{18} = 2.0 \times 10^{10} \text{ M}^{-1}\text{s}^{-1}$	Zhang et al. 2016
R19	$\cdot\text{OH} + 3\text{MM}^- \rightarrow \text{L}^- + 2\text{Ox}^- (\text{Ox}^{2-})$	$k_{19} = 5.0 \times 10^8 \text{ M}^{-1}\text{s}^{-1}$	Kang et al. 2002
R20	$\cdot\text{OH} + \text{L}^- \rightarrow \text{HA} (\text{A}^-) + \text{CO}_2 + \text{H}_2\text{O}$	$k_{20} = 3.0 \times 10^8 \text{ M}^{-1}\text{s}^{-1}$	Buxton et al. 1988
R21	$\cdot\text{OH} + \text{Ox}^- \rightarrow \text{Ox}^{\cdot-} + \text{H}_2\text{O}$	$k_{21} = 4.7 \times 10^7 \text{ M}^{-1}\text{s}^{-1}$	Buxton et al. 1988
R22	$\cdot\text{OH} + \text{Ox}^{2-} \rightarrow \text{Ox}^{\cdot-} + \text{OH}^-$	$k_{22} = 7.7 \times 10^6 \text{ M}^{-1}\text{s}^{-1}$	Buxton et al. 1988
R23	$\text{Ox}^{\cdot-} + \text{Ox}^{\cdot-} \rightarrow \text{Ox}^- (\text{Ox}^{2-}) + 2\text{CO}_2$	$k_{23} = 5.0 \times 10^8 \text{ M}^{-1}\text{s}^{-1}$	Ershov et al. 2008
R24	$\cdot\text{OH} + \text{HA} \rightarrow \text{F}^- + \text{CO}_2 + \text{H}_2\text{O}$	$k_{24} = 1.23 \times 10^8 \text{ M}^{-1}\text{s}^{-1}$	Sun and Saeys 2008
R25	$\cdot\text{OH} + \text{A}^- \rightarrow \text{F}^- + \text{CO}_2 + \text{OH}^-$	$k_{25} = 8.5 \times 10^7 \text{ M}^{-1}\text{s}^{-1}$	Buxton et al. 1988
R26	$\cdot\text{OH} + \text{F}^- \rightarrow \text{CO}_2 + \text{H}_2\text{O}$	$k_{26} = 9.77 \times 10^7 \text{ M}^{-1}\text{s}^{-1}$	Sun and Saeys 2008
E6	$\text{Ox}^- \leftrightarrow \text{Ox}^{2-} + \text{H}^+$	$K_6 = 1.78 \times 10^{-4} \text{ M}$	Benjamin 2002
E7	$\text{HA} \leftrightarrow \text{A}^- + \text{H}^+$	$K_7 = 2.92 \times 10^{-5} \text{ M}$	Benjamin 2002
R27a	$\cdot\text{OH} + \text{IPOH} \rightarrow \text{IPOH}^{\cdot}$	$k_{27a} = 1.2 \times 10^{10} \text{ M}^{-1}\text{s}^{-1}$	Buxton et al. 1988
R27b	$\cdot\text{OH} + \text{IPOH} \rightarrow \text{HO}_2^{\cdot} + \text{Acetone}$	$k_{27b} = 1.2 \times 10^{10} \text{ M}^{-1}\text{s}^{-1}$	Wang and Liu 2014

Note: 4MC = 4-methylcatechol, 4MB = 4-methylbenzoquinone, 3MM⁻ = deprotonated 3-methyl-muconic acid, L⁻ = lactate ion, Ox⁻ (Ox²⁻) = hydrogen oxalate ion (oxalate ion), HA (A⁻) = acetic acid (acetate ion), Ox^{·-} = oxalate radical, F⁻ = formate ion. IPOH[·] = isopropanol radical.

All equilibrium constants are conditional equilibrium constants at ionic strength = 0.1 M.

Reversible reactions (E1 to E7) are assumed to reach equilibrium instantaneously.

Figure captions

Figure 1. Front view (top) and top view (bottom) of irradiation experiments setup used in this study (not to scale).

Figure 2. Computed molar fractions of individual iron species as functions of pH. Iron was added as $\text{Fe}(\text{ClO}_4)_3$ with $[\text{Fe}(\text{III})] = 0.1 \text{ mM}$ and ionic strength = 0.1 M.

Figure 3. Absorption spectra of $\text{Fe}(\text{ClO}_4)_3$ solutions with (a) $[\text{Fe}(\text{III})] = 0.1 \text{ mM}$ at different pH values and (b) different $\text{Fe}(\text{III})$ content at pH 3. Solid lines represent model predictions.

Figure 4. Time-dependent H_2O_2 concentrations for (a) $\text{Fe}(\text{ClO}_4)_3$ solutions with $[\text{Fe}(\text{III})]_0 = 0.1 \text{ mM}$ at pH values from 2.1-3.0 without UV_{254} irradiation and (b) different H_2O_2 aqueous solutions with UV_{254} irradiation (pH = 5.6) and without iron. Solid lines represent kinetic simulations.

Figure 5. Time-dependent $\text{Fe}(\text{II})$ trajectories in $\text{Fe}(\text{ClO}_4)_3$ solutions with $[\text{Fe}]_{\text{tot}} = [\text{Fe}(\text{III})]_0 = 0.1 \text{ mM}$ at (a) pH = 2 and 3 with *p*-cresol present and (b) pH = 3 with and without *p*-cresol, including a lamp out test (without *p*-cresol). Solid lines represent kinetic model predictions. For experiments with *p*-cresol, $[\text{p-cresol}]_0 = 100 \text{ }\mu\text{M}$. The insert shows the measured (circles) and predicted (solid line) fractional *p*-cresol residuals in the reactor at pH = 3.

Figure 6. *p*-Cresol and $\text{Fe}(\text{II})$ concentrations as functions of irradiation time in $\text{Fe}(\text{ClO}_4)_3$ solution with $[\text{Fe}(\text{III})]_0 = 0.1 \text{ mM}$, $[\text{p-cresol}]_0 = 100 \text{ }\mu\text{M}$ at pH 2.4. Blue (*p*-cresol) and red ($\text{Fe}(\text{II})$) solid lines represent simulations. The black solid line represents the predicted result based on the measured $\text{Fe}(\text{II})$ and H_2O_2 concentrations when the lamp was turned off at $t = 405 \text{ min}$.

Figure 7. $\text{Fe}(\text{II})$ vs. time in $\text{Fe}(\text{ClO}_4)_3$ solutions with (a) $[\text{Fe}(\text{III})]_0 = 0.1 \text{ mM}$ at different pH values and (b) different initial $\text{Fe}(\text{III})$ concentrations at pH 3 under UV_{254} irradiation. Solid lines represent kinetic model predictions.

Figure 8. Comparison of measured (red circles) and predicted (solid lines) spectra in long term photolysis experiments after (a) 0, (b) 5, (c) 20 and (d) 60 minutes. Initial experimental conditions were as indicated in Figure 7: $[\text{Fe}]_{\text{tot}} = [\text{Fe}(\text{III})]_0 = 0.1 \text{ mM}$ at pH = 3.

Figure 9. Overall $\text{Fe}(\text{II})$ accumulation rates obtained from the kinetic model and experimental data versus irradiation time for the experiment with $[\text{Fe}]_{\text{tot}} = [\text{Fe}(\text{III})]_0 = 0.1 \text{ mM}$ at pH = 3. The inset illustrates the trendline fitted to experimental data.

Figure 10. Contributions of elementary reactions (Table 1) to the production (a) and consumption (b) of $\text{Fe}(\text{II})$ as a function of time during the photolysis of $\text{Fe}(\text{III})$ -hydroxo species. $[\text{Fe}]_{\text{tot}} = [\text{Fe}(\text{III})]_0 = 0.1 \text{ mM}$ at pH = 3.

Figure 11. Measured and predicted $\text{Fe}(\text{II})$ concentrations (left) and H_2O_2 (right) vs. irradiation time in $\text{Fe}(\text{ClO}_4)_3$ solutions $[\text{Fe}]_{\text{tot}} = [\text{Fe}(\text{III})]_0 = 0.1 \text{ mM}$ and pH = 3 under UV_{254} irradiation with different initial H_2O_2 concentrations: 0 mM (∇), 0.05 mM (Δ), 1 mM (\circ) and 12 mM (\square).

Figure 12. Measured and predicted Fe(II) concentration versus time for Fenton and photo-Fenton experiments with $[\text{Fe}]_{\text{tot}} = [\text{Fe(II)}]_0 = 1.9 \text{ mM}$, $[\text{H}_2\text{O}_2]_0 = 1 \text{ mM}$ at $\text{pH} = 2.4$.

Figure 13. Comparison between experimental (open circles) and predicted (solid lines) Fe(II) and H_2O_2 concentrations during the photo-Fenton oxidation of Fe(II). Experimental conditions: $[\text{Fe}]_{\text{tot}} = 0.108 \text{ mM}$, $[\text{Fe(II)}]_0 = 57 \text{ }\mu\text{M}$, $\text{pH} = 3$. The reactor was spiked with $25 \text{ }\mu\text{M}$ H_2O_2 at $t = 30$ and 75 mins.

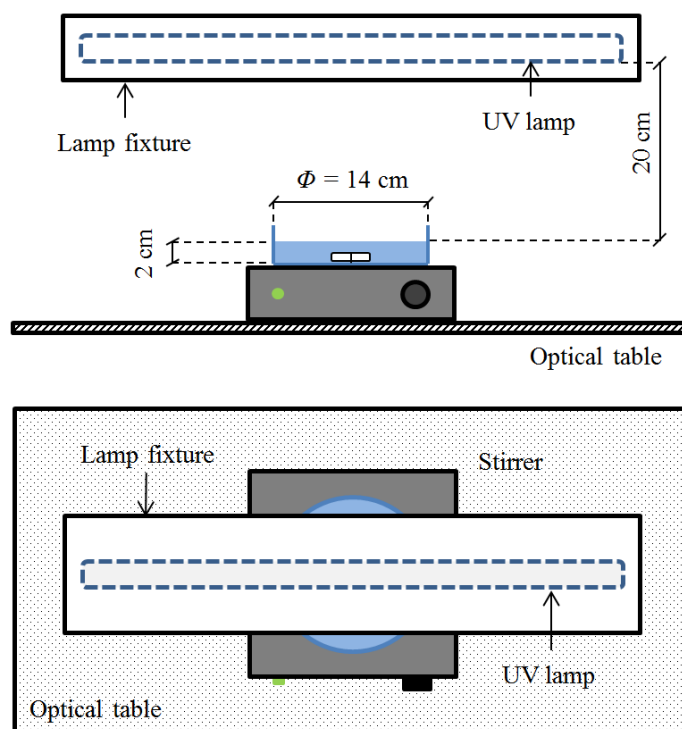


Figure 1. Front view (top) and top view (bottom) of irradiation experiments setup used in this study (not to scale).

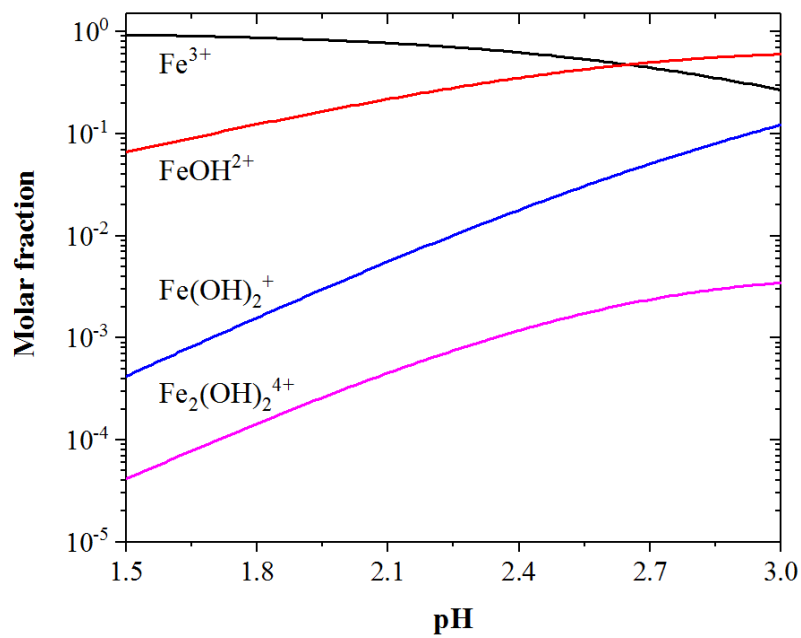


Figure 2. Computed molar fractions of individual iron species as functions of pH. Iron was added as $\text{Fe}(\text{ClO}_4)_3$ with $[\text{Fe}(\text{III})] = 0.1 \text{ mM}$ and ionic strength = 0.1 M.

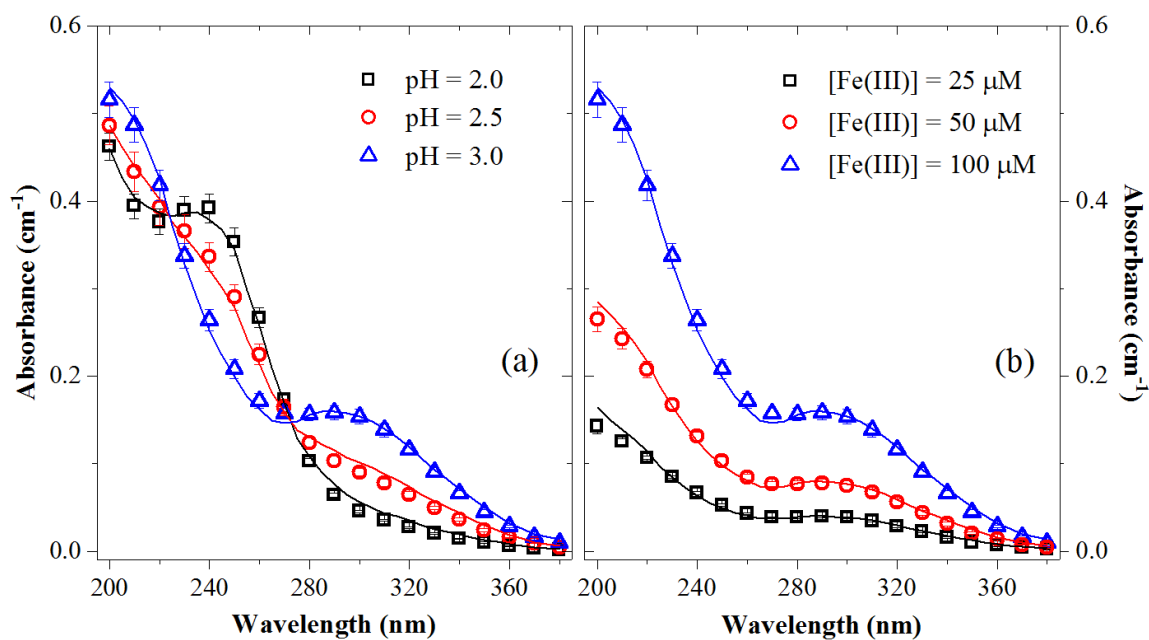


Figure 3. Absorption spectra of $\text{Fe}(\text{ClO}_4)_3$ solutions with (a) $[\text{Fe}(\text{III})] = 0.1 \text{ mM}$ at different pH values and (b) different $\text{Fe}(\text{III})$ content at pH 3. Solid lines represent model predictions.

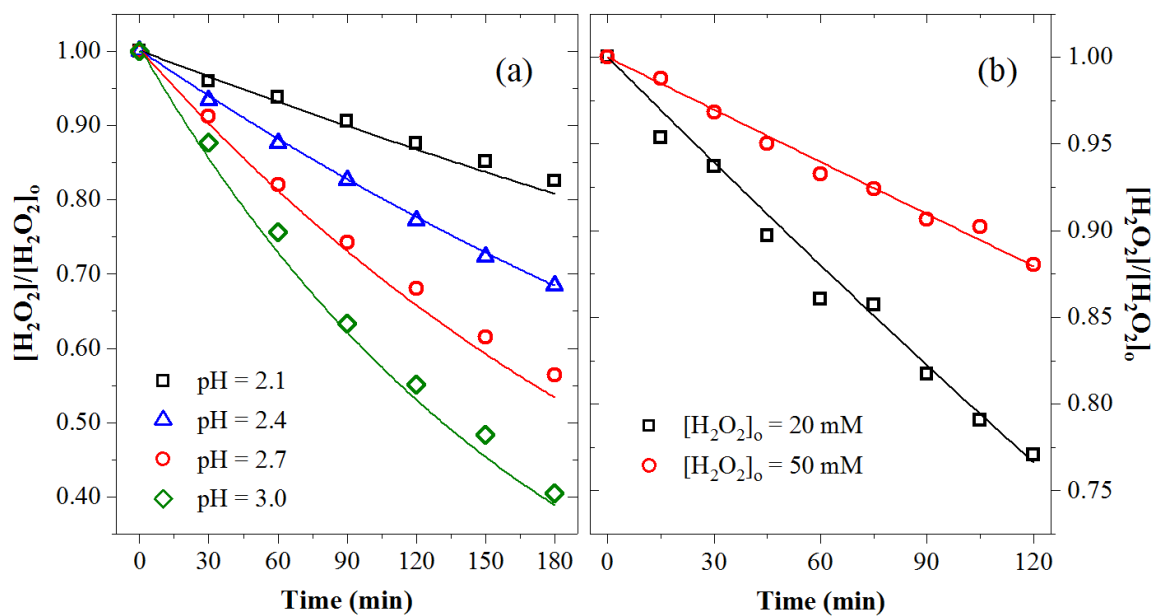


Figure 4. Time-dependent H₂O₂ concentrations for (a) Fe(ClO₄)₃ solutions with [Fe(III)]₀ = 0.1 mM at pH values from 2.1-3.0 without UV₂₅₄ irradiation and (b) different H₂O₂ aqueous solutions with UV₂₅₄ irradiation (pH = 5.6) and without iron. Solid lines represent kinetic simulations.

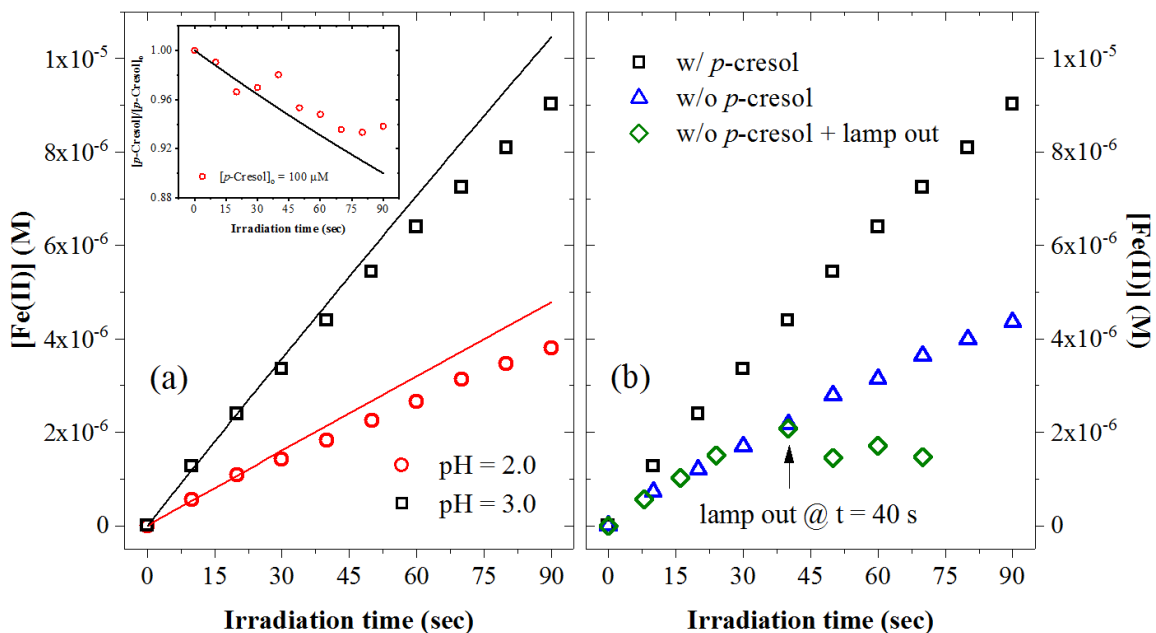


Figure 5. Time-dependent Fe(II) trajectories in $\text{Fe}(\text{ClO}_4)_3$ solutions with $[\text{Fe}]_{\text{tot}} = [\text{Fe}(\text{III})]_0 = 0.1$ mM at (a) pH = 2 and 3 with *p*-cresol present and (b) pH = 3 with and without *p*-cresol, including a lamp out test (without *p*-cresol). Solid lines represent kinetic model predictions. For experiments with *p*-cresol, $[p\text{-cresol}]_0 = 100 \mu\text{M}$. The insert shows the measured (circles) and predicted (solid line) fractional *p*-cresol residuals in the reactor at pH = 3.

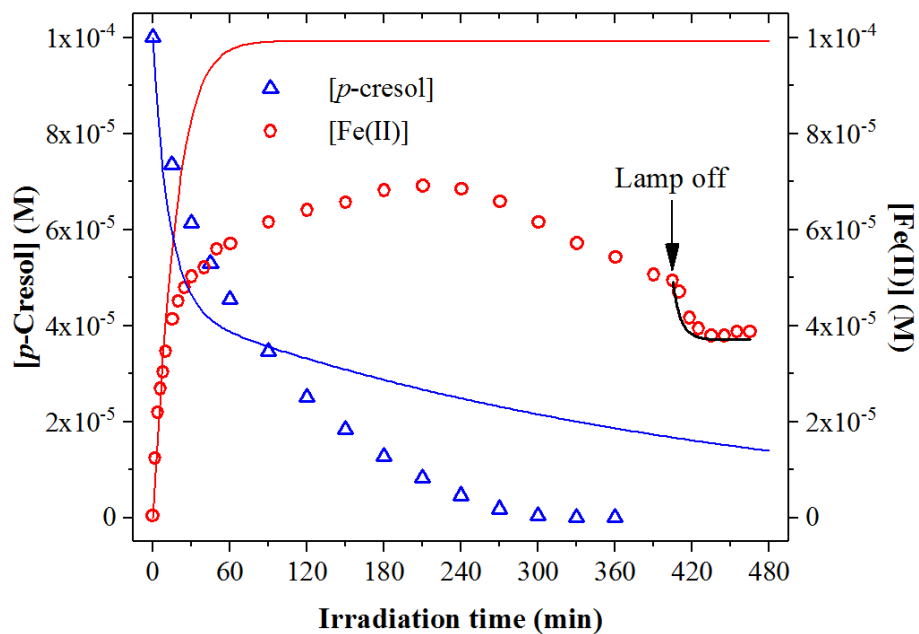


Figure 6. *p*-Cresol and Fe(II) concentrations as functions of irradiation time in $\text{Fe}(\text{ClO}_4)_3$ solution with $[\text{Fe}(\text{III})]_0 = 0.1 \text{ mM}$, $[\textit{p}\text{-cresol}]_0 = 100 \text{ }\mu\text{M}$ at pH 2.4. Blue (*p*-cresol) and red (Fe(II)) solid lines represent simulations. The black solid line represents the predicted result based on the measured Fe(II) and H_2O_2 concentrations when the lamp was turned off at $t = 405 \text{ min}$.

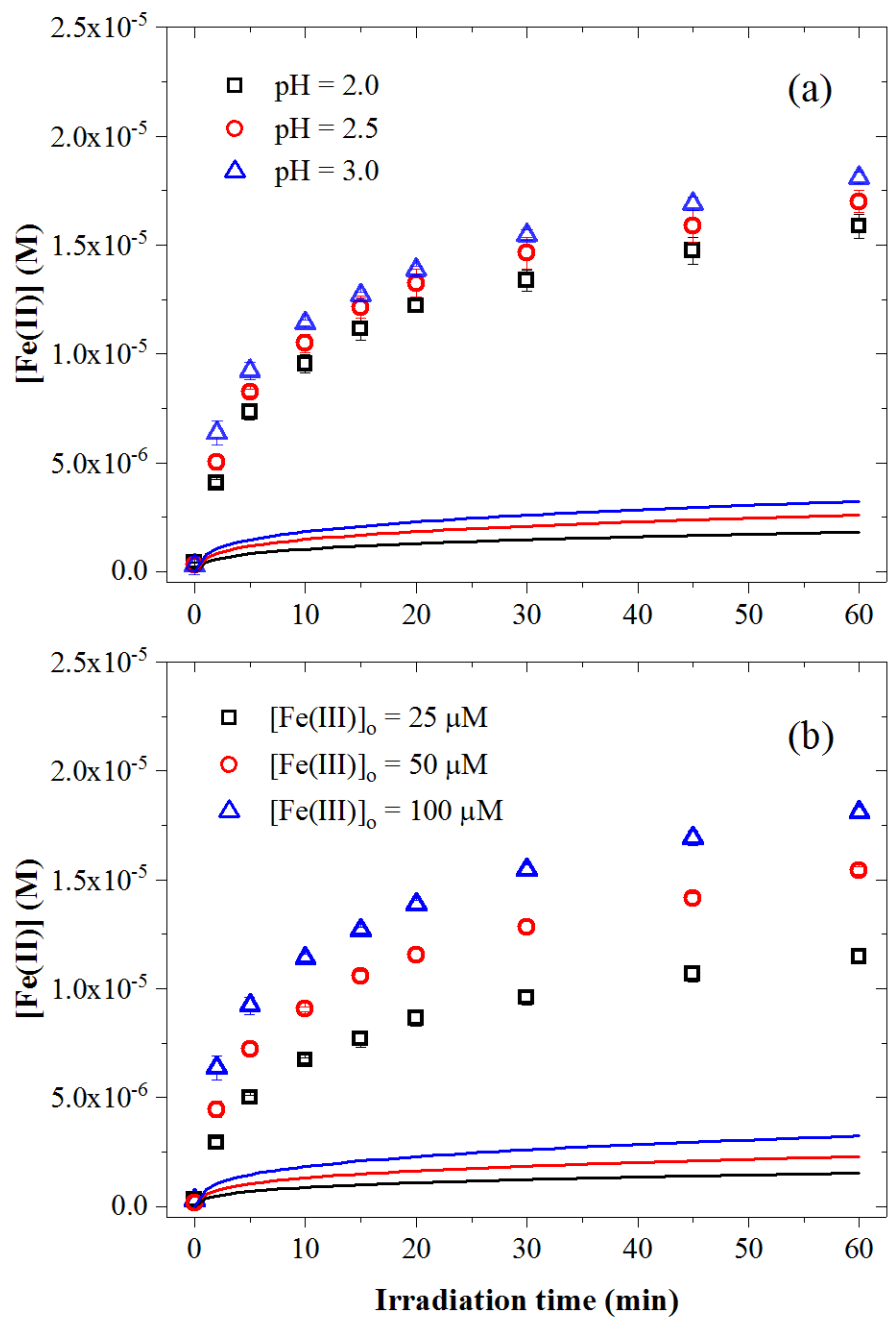


Figure 7. Fe(II) vs. time in $\text{Fe}(\text{ClO}_4)_3$ solutions with (a) $[\text{Fe(III)}]_0 = 0.1 \text{ mM}$ at different pH values and (b) different initial Fe(III) concentrations at pH 3 under UV₂₅₄ irradiation. Solid lines represent kinetic model predictions.

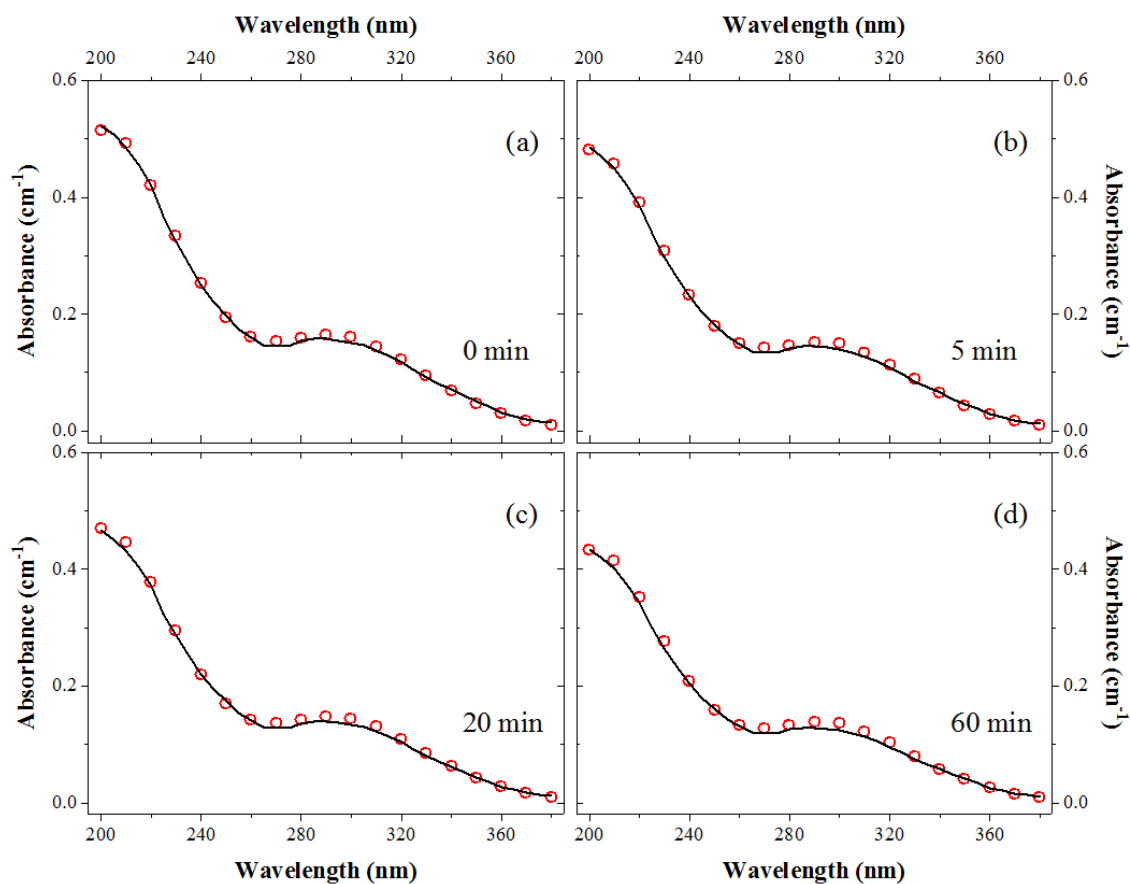


Figure 8. Comparison of measured (red circles) and predicted (solid lines) spectra in long term photolysis experiments after (a) 0, (b) 5, (c) 20 and (d) 60 minutes. Initial experimental conditions were as indicated in Figure 7: $[\text{Fe}]_{\text{tot}} = [\text{Fe(III)}]_0 = 0.1 \text{ mM}$ at $\text{pH} = 3$.

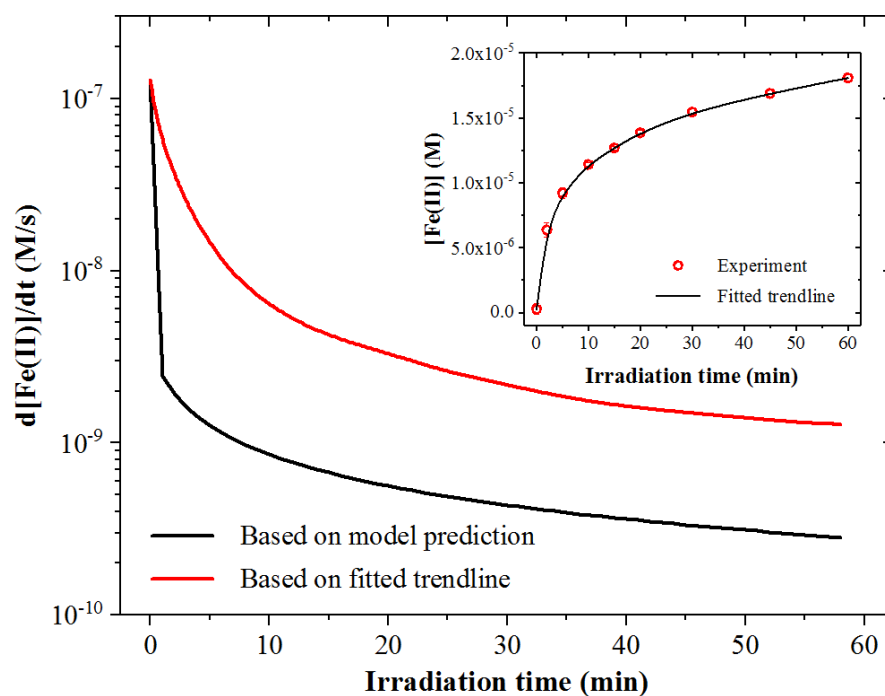


Figure 9. Overall Fe(II) accumulation rates obtained from the kinetic model and experimental data versus irradiation time for the experiment with $[\text{Fe}]_{\text{tot}} = [\text{Fe(III)}]_0 = 0.1$ mM at pH = 3. The inset illustrates the trendline fitted to experimental data.

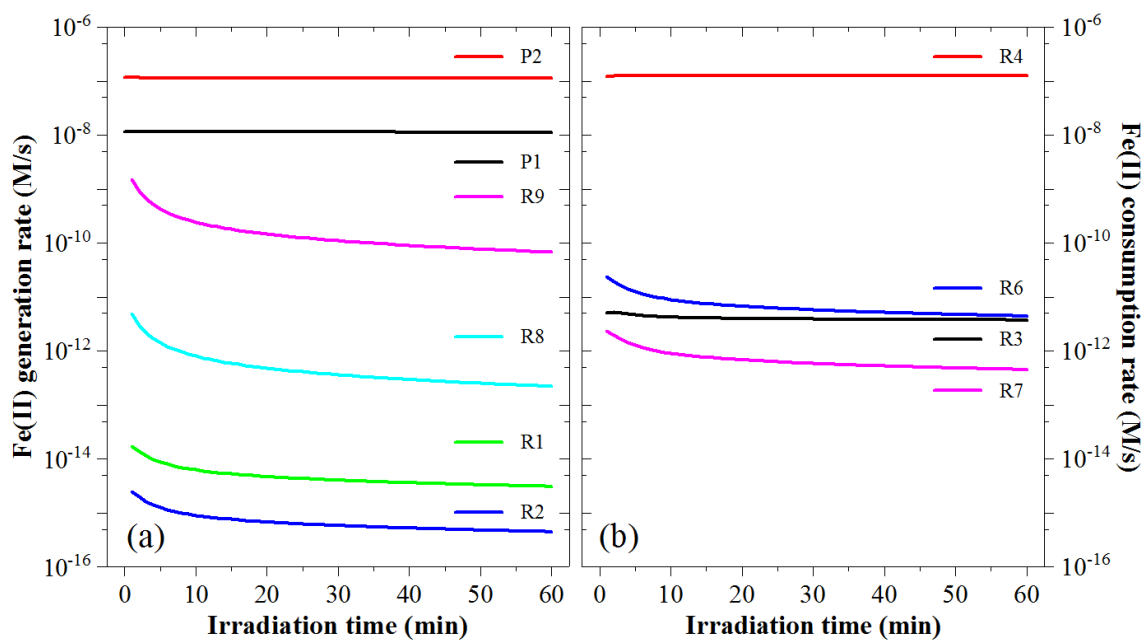


Figure 10. Contributions of elementary reactions (Table 1) to the production (a) and consumption (b) of Fe(II) as a function of time during the photolysis of Fe(III)-hydroxo species. $[\text{Fe}]_{\text{tot}} = [\text{Fe(III)}]_0 = 0.1 \text{ mM}$ at $\text{pH} = 3$.

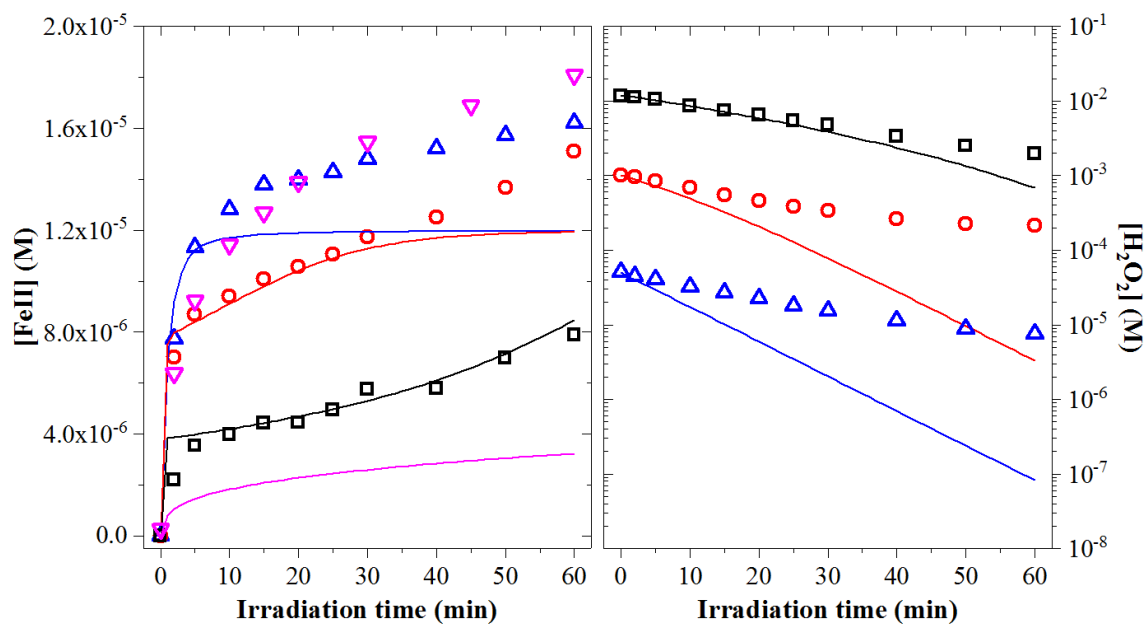


Figure 11. Measured and predicted Fe(II) concentrations (left) and H_2O_2 (right) vs. irradiation time in $Fe(ClO_4)_3$ solutions $[Fe]_{tot} = [Fe(III)]_0 = 0.1$ mM and pH = 3 under UV_{254} irradiation with different initial H_2O_2 concentrations: 0 mM (∇), 0.05 mM (Δ), 1 mM (o) and 12 mM (□).

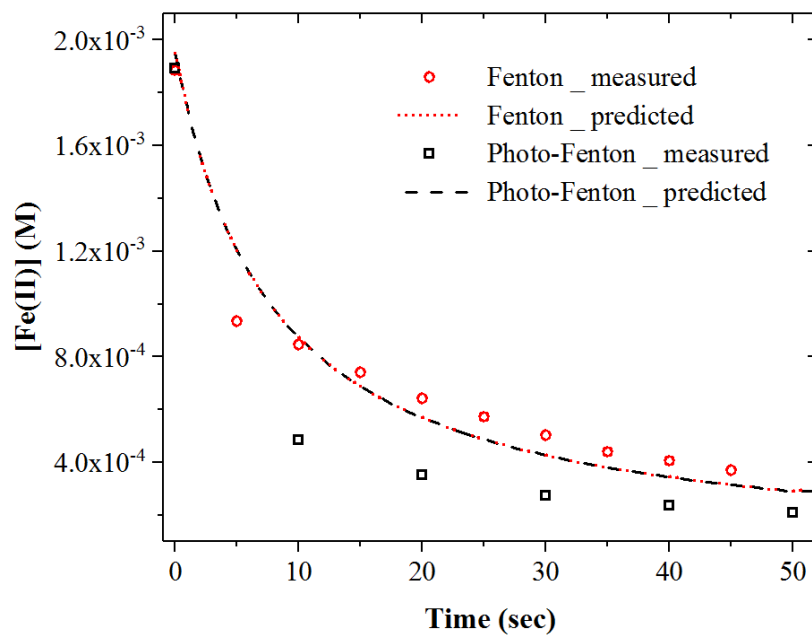


Figure 12. Measured and predicted Fe(II) concentration versus time for Fenton and photo-Fenton experiments with $[\text{Fe}]_{\text{tot}} = [\text{Fe(II)}]_0 = 1.9 \text{ mM}$, $[\text{H}_2\text{O}_2]_0 = 1 \text{ mM}$ at $\text{pH} = 2.4$.

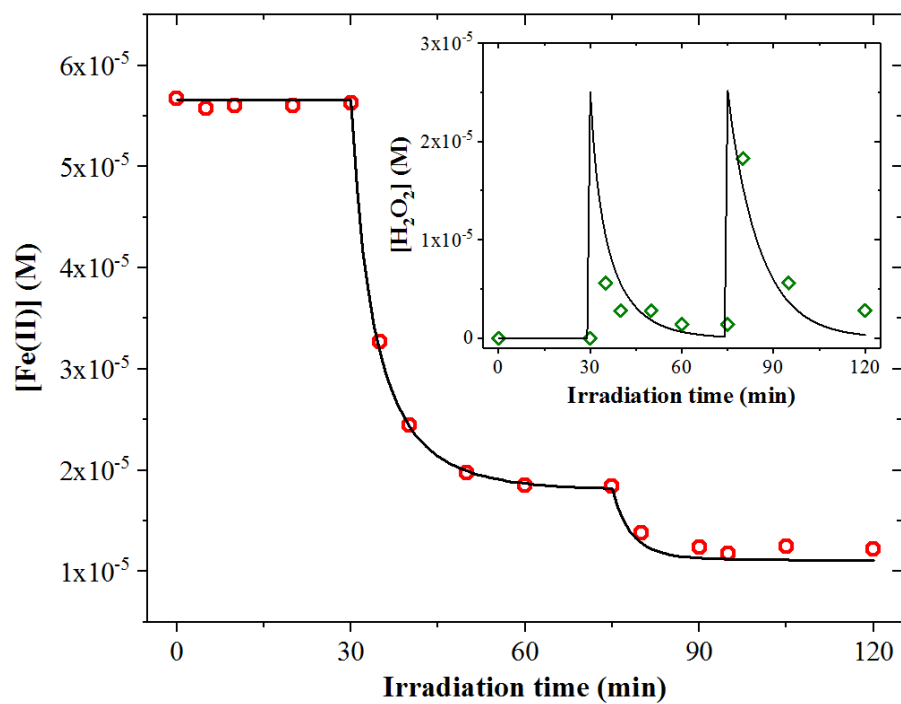


Figure 13. Comparison between experimental (open circles) and predicted (solid lines) Fe(II) and H₂O₂ concentrations during the photo-Fenton oxidation of Fe(II). Experimental conditions: $[\text{Fe}]_{\text{tot}} = 0.108 \text{ mM}$, $[\text{Fe(II)}]_0 = 57 \text{ }\mu\text{M}$, $\text{pH} = 3$. The reactor was spiked with $25 \text{ }\mu\text{M}$ H₂O₂ at $t = 30$ and 75 mins.

APPENDIX E**EFFECTIVENESS OF ENGINEERED AND NATURAL WASTEWATER TREATMENT
PROCESSES FOR THE REMOVAL OF TRACE ORGANICS IN WATER REUSE**

Long Cheng,¹ Tianqi Zhang,² Hao Vo,³ Daniel Diaz,⁴ David Quanrud,⁵ Robert G. Arnold,⁶ and
A. Eduardo Sáez⁷

¹Ph.D. Candidate, Department of Chemical and Environmental Engineering, The University of
Arizona, Tucson, AZ 85721.

²Ph.D. Candidate, Department of Chemical and Environmental Engineering, The University of
Arizona, Tucson, AZ 85721.

³Ph.D. Student, Department of Chemical and Environmental Engineering, The University of
Arizona, Tucson, AZ 85721.

⁴Undergraduate Student, Department of Chemical and Environmental Engineering, The
University of Arizona, Tucson, AZ 85721.

⁵Associate Research Scientist, School of Natural Resources and the Environment, The University
of Arizona, Tucson, AZ 85721.

⁶Professor, Department of Chemical and Environmental Engineering, The University of Arizona,
Tucson, AZ 85721.

⁷Professor, Department of Chemical and Environmental Engineering, The University of Arizona,
Tucson, AZ 85721 (corresponding author). Email: esaez@email.arizona.edu

Abstract

The physicochemical and biological determinants of removal efficiencies in a variety of engineered and natural processes were explored for 55 frequently encountered trace organic compounds (TOrcs) in wastewater. Weak correlations between field observations and predicted TOrc biodegradabilities led to adoption of an empirical approach to prediction of compound removal during conventional wastewater treatment. The efficiencies of TOrc removals by UV photolysis (direct and indirect), activated carbon adsorption, membrane separation (reverse osmosis/nanofiltration) and sunlight photolysis were determined under representative process conditions. Results led to heuristic guidelines for the selection of sequenced treatment processes for TOrc management. Process- and compound-specific treatment efficiencies were sensitive to TOrc physicochemical properties and matrix effects.

Keywords: Trace organic compounds; Tertiary wastewater treatment; Advanced oxidation process; Photolysis; Biotransformation

Introduction

Population growth and drought have produced unprecedented stress on regional water resources, especially in arid and semi-arid regions. Potable reuse of treated wastewater is a potential remedy but is impeded in part by the persistence of trace organics in conventionally treated wastewaters. A number of such compounds are poorly attenuated during conventional wastewater treatment (Jones et al. 2005; Miège et al. 2009; U.S. Environmental Protection Agency (EPA) 2009; 2010), so that a combination of conventional and advanced processes is necessary to restore water to potable quality.

Grady (1990) provided a pragmatic approach to rational, engineered biotransformations of xenobiotic organic compounds during conventional wastewater treatment. The article highlighted the difficulties inherent in simulating diverse, mixed-culture treatment of trace organics in the presence of a primary substrate. Citing extant kinetic and reactor performance data, Grady suggested a pathway for closing related gaps in process design and operation.

Grady emphasized the roles of available tools in reactor engineering, such as manipulation of solids and hydraulic retention times under aerobic, anaerobic and anoxic conditions, acknowledging that development of relationships between operational parameters and attenuation of trace organics remained a work in progress. Missing, at least in part, were databases necessary to determine intrinsic kinetic parameters, positive and negative interactions among substrates during biological treatment and the potential importance of non-biological removal mechanisms (volatilization and adsorption).

To simplify the problem, Grady suggested that all wastewater substrates could be lumped into three components—biogenic, toxic and individual target compounds. Targets were selected based on persistence and toxicity. To be useful, each compartment must be measurable—e.g., biogenic organics as total organic carbon—highlighting the importance of advanced analytical chemistry. Absent simplifications of this nature, successful process simulation was unlikely or impossible. Instead, Grady used Monod kinetics and its several rational extensions, accounting for observable positive (co-metabolic) and negative (toxicity) biochemical interactions. Grady laid out the limitations and strengths of the Andrews equation, for example, in process simulations, identifying information necessary to simulate the biodegradation of xenobiotic contaminants during conventional wastewater treatment and also proposing a reasonable set of steps to acquire missing data.

Grady's article covered many cases in which multiple xenobiotic compounds were simultaneously present—the rule in municipal wastewater treatment. The main conclusion was that in most engineering applications, transformations of multiple xenobiotic compounds could be treated independently, using a single-substrate kinetic approach. Grady was among those early to recognize that removal efficiency of xenobiotic compounds in continuous culture can be greatly enhanced by the presence of multiple biogenic compounds through co-metabolism. A simplification was recommended for dealing with microbial community complexity and substrate specificity in mixed cultures. Grady reasoned that the fraction of cells degrading each target xenobiotic compound was proportional to the compound's contribution to chemical oxygen demand. Under those conditions, the total biomass could be separated into the fraction

that degrades the target compound and the fraction that degrades everything else. Grady also identified the tools necessary to anticipate the fates of xenobiotic compounds in complex media, accounting for inter-phase partitioning, specific biotransformation rates and biomass. These included structure/activity relationships in various reactor configurations—e.g., activated sludge, trickling filters. Grady suggested that life scientists and environmental engineers should collaborate to establish the potential and role of biotechnology in protection of environmental and human health, accelerating the development of knowledge regarding the fates of xenobiotic contaminants during municipal wastewater treatment and following their discharge into the environment.

A relative few works so usefully stimulate broad-scale thinking relative to substantial environmental engineering problems as Grady's 1990 article. It was a departure point for much of the engineering effort aimed at treatment of trace organic contaminants in wastewater—an area that has gained attention with progress in analytical chemistry and toxicology.

The requirement for at least secondary treatment remains a foundation of municipal wastewater treatment. Unfortunately, conventional wastewater treatment is only partially successful in removing trace organics, including those that affect environmental and human health. At the same time, stress on existing water resources necessitates consideration of waters of initially low quality in water resources planning—to the point at which direct potable reuse of treated wastewater is sometimes considered seriously. Persistent trace organics impede such plans. There are neither universally accepted standards of treatment for many such compounds nor levels of exposure that are recognized as safe (Maruya et al. 2014).

The term trace organic compounds (TOrcs) is used to represent pharmaceuticals and personal care products (PPCPs), endocrine disrupting compounds (EDCs), disinfection by-products (DBPs), flame retardants, insecticides and herbicides and an assortment of additional organic compounds that are recognizable in water at sub-part-per-billion (ppb) levels. Public interest in TOrcs was enormously stimulated by Colburn et al. (1996), who informed on the potential threats to human health from man-made chemicals in water. In an unprecedented survey, Kolpin et al. (2002) reported the concentrations of 95 TOrcs in 139 U.S. surface waters. More than 85% of the 95 analytes were present at one or more sites. The influence of that study on the trajectory of environmental science is well illustrated by the frequency with which it has been cited—a total of 3911 times by July 2016, according to Web of Science. More recently, Lapworth et al. (2012) and Sui et al. (2015) reviewed presence of TOrcs in ground waters. Although many of the TOrcs in these surveys pose no recognizable human or ecological health risk, some cause physiological changes in exposed organisms at the concentrations encountered (Purdom et al. 1994; Sumpter 1995; Kidd et al. 2007).

There has been considerable recent effort to establish the fate of TOrcs during municipal wastewater treatment (e.g. Jones et al. 2007; Daughton and Ternes 1999; Urase and Kikuta 2005; Rojas et al. 2013). Eighty-eight studies involving almost 600 treatment systems carried out during 2003-2008 were summarized by the U.S. EPA (2010) to consolidate a database for more than 200 TOrcs. That work provides an accessible tool with which to anticipate TOrc removals by various treatment processes in different water matrices. Mean removal efficiencies and relative standard deviations during secondary treatment were summarized for 184 TOrcs as

functions of temperature, solids retention time (SRT) and hydraulic retention time (HRT) by Miège et al. (2009). Compounds that were, on average, efficiently removed (> 90%) included the natural estrogens, 17 β -estradiol and estriol, propranolol, salicylic acid, and paracetamol, among others. On the other hand, atenolol, carbamazepine and metoprolol exhibited poor removal efficiencies (< 10%). Up to 40% of observed (average) TOrC removals occurred during primary treatment, and 50-90% of the overall reduction was a consequence of activated sludge treatment, although the contributions of solid-phase partitioning and biotransformation were not separated. Process-dependent removals of 42 prominent TOrCs including PPCPs, alkylphenols, pesticides and plasticizers during conventional wastewater treatment were statistically analyzed by Rojas et al. (2013). Hydrophobicity and biodegradability (as quantified by BioWin models and laboratory-scale experiments) were, as expected, the most important compound properties affecting TOrC removal efficiencies. Similar to the observations of Miège et al. (2009), hormones such as testosterone and estrogens were good targets for conventional processes, with removal efficiencies typically greater than 75%. Carbamazepine and perfluorinated compounds (PFOA and PFOS), however, were exceptionally resistant to conventional treatment. The great variation in reported removals of individual antibiotics suggests that treatment efficiencies for these compounds are sensitive to operating conditions. Unfortunately, the lack of supporting information tends to obscure cause-effect relationships among compound characteristics, process parameters and removal efficiencies.

In this work, we explore the physicochemical and biological determinants of TOrC removal efficiencies in a variety of engineered and natural processes. Specific objectives are to: (i)

examine currently available methods for predicting TOrC biodegradation during conventional treatment; (ii) test potential relationships among biodegradability, compound hydrophobicity and the kinetics of specific physicochemical transformation processes, such as oxidation by hydroxyl radicals ($^{\bullet}\text{OH}$) and photolysis; and (iii) examine the utility of physicochemical processes as bases for tertiary treatment of TOrCs. This information can lead to heuristic guidelines for process selection. The treatment processes considered include (i) biodegradation, (ii) chemical transformations (direct and indirect photolysis, advanced oxidation), and (iii) separation processes (reverse osmosis (RO)/nanofiltration (NF) and activated carbon adsorption).

Methods

TOrC selection criteria

Candidate TOrCs included PPCPs, hormones and hormone mimics, herbicides and insecticides, polycyclic aromatic hydrocarbons (PAHs), plasticizers, alkylphenols and other trace contaminants that are commonly encountered in municipal wastewater. A set of 55 TOrCs was selected that (i) differ in terms of their susceptibility to removal during conventional secondary wastewater treatment (Miège et al. 2009; Rojas et al. 2013), (ii) are detected with >20 % frequency in surface and ground waters that are influenced by the discharge of treated wastewater (Kolpin et al. 2002; Sui et al. 2015), and (iii) have been the subject of widespread interest in previous studies (Comerton et al. 2008; Rivas et al. 2011; Wols and Hofman-Caris 2012). Compound-specific characteristics are presented in Table 1.

Physicochemical properties

In addition to Estimation Programs Interface (EPI) Suite™ (v4.11) from U.S. EPA (2016) and PhysChem Module in ACD/Labs Percepta Platform, over 140 literature sources were reviewed for relevant data. The resultant database covers (i) basic information such as molecular weight, octanol/water partition coefficient (K_{ow}) and pKa values; (ii) photochemical parameters such as molar absorptivity and quantum yields; (iii) $^{\bullet}OH$ reaction rate constants; (iv) physical parameters such as molar volume, water solubility and Freundlich constants; and (v) 3-D molecular structure and molecule dimensions (theoretical molecular length and thickness). The K_{ow} information was obtained from the EPI Suite™ database unless otherwise indicated. Estimated pKa values were taken from 11 different sources (Table 1). The pH-dependent octanol-water distribution coefficient (D_{ow}) was calculated at pH 7 using:

$$D_{ow} = K_{ow} \frac{1 + 10^{-pKa}}{1 + 10^{pH-pKa}} \quad \text{Eq (1)}$$

Photochemical parameters are listed in Table 2. When multiple values were reported, means and standard deviations are provided. Table 3 contains a summary of parameters required by Adsorption Design Software (AdDesignS™), which was utilized to compare carbon adsorption capabilities for selected TOrCs. Unless stated otherwise, molar volumes were estimated using PhysChem Module, and boiling points were predicted using EPI Suite™. Water solubilities and vapor pressures are from EPI Suite™. Freundlich isotherm parameters are from various literature sources.

Three-dimensional molecular structures were created and optimized using the software package Materials Studio 4.0. Theoretical molecular length was defined as the maximum distance between any two atoms in a single compound. Molecular thickness was calculated as the maximum distance between any two atoms in the compound on planes perpendicular to the direction of theoretical molecular length. Examples of the data are shown in Table 4 and Figures S1 to S10. These geometrical parameters were used to correlate membrane rejections for each compound.

Biodegradability predictions

BioWin is a user-friendly, fragment-based, quantitative structure-activity relationship (QSAR) program embedded in the EPI SuiteTM (v4.11) that can be used to assess biological wastewater treatment. The software requires the CAS # or details of compound structure.

There are seven BioWin versions, numbered 1-7. BioWin1 and BioWin2 estimate the probability of rapid biodegradation using multiple linear and nonlinear regression models, respectively, that were developed using a training set assembled by Syracuse Research Corporation (Howard et al. 1987; Howard et al. 1992; Boethling et al. 1994). BioWin3 and BioWin4 are based on a training set from 17 experts, who were surveyed to predict the times required for both ultimate (complete mineralization) and primary (initial step) biodegradation of chemicals on a semi-quantitative scale (Boethling et al. 1989, 1994). Developers employed 36 substructures and compound molecular weight as the 37 independent variables to estimate regression coefficients for the first four BioWin models (BioWin1 to BioWin4) (Boethling et al. 1994). BioWin5 and BioWin6 also employ multiple linear and nonlinear regression methods to estimate the chemical-specific

probability of passing the ready biodegradation test from the Japanese Ministry of International Trade and Industry (MITI). The method uses 43 independent variables (42 substructures and compound molecular weight) as the basis of the regression equations (Tunkel et al. 2000). The first six BioWin models were developed to predict biodegradability under aerobic conditions. The most recently developed model, BioWin7, estimates the probability of compound degradation under anaerobic (methanogenic) conditions (Meylan et al. 2007). Features of the seven BioWin models are summarized in Table 5.

The first six versions of BioWin were compared in terms of predictive accuracy (Tunkel et al. 2000; Boethling et al. 2003; Posthumus et al. 2005) and reviewed from a user's perspective (Rücker et al. 2012). Model performances were measured against validation sets from a database consisting of biodegradation results from 305 pre-manufacture notices (i.e., chemicals not yet in commerce that are subject to testing requirements under the Toxic Substances Control Act.) BioWin3 to BioWin6 were generally more accurate than BioWin1 and BioWin2 in terms of biodegradability (Boethling et al. 2003). BioWin4 predictions correlated well with observed removals of PPCPs during aerobic biological secondary treatment (Blair et al. 2013). On that basis, the semi-quantitative output of BioWin4 (v4.10) was used to estimate TOrC biodegradability here.

UV₂₅₄ photolysis

Photolytic processes employing monochromatic UV light (254 nm) are used in water treatment for disinfection or, in combination with hydrogen peroxide (H₂O₂), for advanced oxidation treatment. Some TOrCs are degraded by direct exposure to UV light (direct photolysis) or are

destroyed by radicals and/or other active chemical species generated by UV irradiation of other compounds (indirect photolysis). Direct photolysis is envisioned as a two-step process in which the absorption of light energy promotes the compound to an excited state, after which either chemical transformation occurs or the excited compound devolves to its original ground state. Indirect photolysis is initiated through light absorption by other chemicals, leading to production of reactive intermediates such as reactive oxygen species (ROS) or photo-excited dissolved organic matter (DOM) that reacts chemically with the target compound (Schwarzenbach et al. 2003).

Direct and indirect photolysis of TOrCs in either pure water or in a representative wastewater secondary effluent were simulated for a model system consisting of a plug flow reactor (PFR) (cylindrical with concentrically-centered UV lamp, 140 cm length, 14 cm barrel inner diameter and 4 cm lamp sleeve outside diameter – light path length 5 cm – with 20 L chamber volume) that was equipped with a low pressure UV lamp with total irradiance of $1.0 \times 10^{-5} \text{ EinL}^{-1}\text{s}^{-1}$. Flow rate was selected to yield 30 s of residence time. For UV/H₂O₂ simulations, the H₂O₂ reactor influent concentration was 5 ppm (0.15 mM).

For the representative secondary effluent used in simulations, an equivalent background compound (EBC) was used to approximate effluent organic matter (EfOM). Per methods outlined by Rosario-Ortiz et al. (2008), the initial concentration of EBC was set as $6.67 \times 10^{-4} \text{ M}_c$ (molarity of EBC based on moles of carbon) assuming that the dissolved organic carbon (DOC) of the effluent matrix is 8 ppm, with a molar absorptivity of $240 \text{ M}_c^{-1}\text{cm}^{-1}$. Matrix absorbance

was 0.16 cm^{-1} at 254 nm. The second-order kinetic rate constant for reaction of EBC with $^*\text{OH}$ was assumed to be $k_{\text{EBC-}^*\text{OH}} = 8.6 \times 10^8 \text{ M}_c^{-1}\text{s}^{-1}$.

The rate of decomposition of a TOrC via direct photolysis under UV-254 light in the absence of other reactions in a well-mixed batch reactor is given by

$$\frac{d[\text{TOrC}]}{dt} = -\Phi_{\text{TOrC-254}} I_0 f (1 - 10^{-\text{Abs}_{254}}) \quad \text{Eq (2)}$$

where t is time,

$$f = \frac{\epsilon_{\text{TOrC-254}} [\text{TOrC}]}{\epsilon_{\text{TOrC-254}} [\text{TOrC}] + \epsilon_{\text{EBC-254}} [\text{EBC}]_c} \quad \text{Eq (3)}$$

is the fraction of light absorbed by the TOrC, and the total solution absorbance is

$$\text{Abs}_{254} = (\epsilon_{\text{TOrC-254}} [\text{TOrC}] + \epsilon_{\text{EBC-254}} [\text{EBC}]_c) \ell \quad \text{Eq (4)}$$

where $\Phi_{\text{TOrC-254}}$ is the TOrC quantum yield (mol/Ein) at 254 nm, I_0 is the incident light intensity from the reactor lamp ($\text{EinL}^{-1}\text{s}^{-1}$), $\epsilon_{\text{TOrC-254}}$ and $\epsilon_{\text{EBC-254}}$ are the molar absorptivities ($\text{M}^{-1}\text{cm}^{-1}$ and $\text{M}_c^{-1}\text{cm}^{-1}$) of the target and EBC at 254 nm, respectively, and ℓ is the UV path length (cm). In pure water, $[\text{EBC}] = 0 \text{ M}_c$. Quantum yields and extinction coefficients for the TOrCs studied here are presented in Table S1.

Eq. 2 is also applicable to a plug-flow reactor, with time being equivalent to residence time at points along the reactor.

When H_2O_2 is present, the attenuation of TOrCs involves both direct and indirect photolysis. In this case, indirect photolysis was assumed to be due to the production of $^*\text{OH}$ from H_2O_2 photolysis only. Under these conditions, the rate of disappearance of the TOrC is given by

$$\frac{d[\text{TOrC}]}{dt} = -\Phi_{\text{TOrC-254}} I_0 f (1 - 10^{-\text{Abs}_{254}}) - k_{\text{TOrC-}^*\text{OH}} [^*\text{OH}][\text{TOrC}] \quad \text{Eq (5)}$$

where

$$f = \frac{\varepsilon_{\text{TOrC-254}} [\text{TOrC}]}{\varepsilon_{\text{TOrC-254}} [\text{TOrC}] + \varepsilon_{\text{H}_2\text{O}_2-254} [\text{H}_2\text{O}_2] + \varepsilon_{\text{EBC-254}} [\text{EBC}]_c} \quad \text{Eq (6)}$$

and

$$\text{Abs}_{254} = (\varepsilon_{\text{TOrC-254}} [\text{TOrC}] + \varepsilon_{\text{H}_2\text{O}_2-254} [\text{H}_2\text{O}_2] + \varepsilon_{\text{EBC-254}} [\text{EBC}]_c) \ell \quad \text{Eq (7)}$$

In Eq 5, $k_{\text{TOrC-}^*\text{OH}}$ is the second-order reaction rate constant ($\text{M}^{-1}\text{s}^{-1}$) for the reaction of $^*\text{OH}$ with the TOrC and $\varepsilon_{\text{H}_2\text{O}_2-254}$ is the molar absorptivity ($\text{M}^{-1}\text{cm}^{-1}$) of H_2O_2 at 254 nm. A complete mechanism for the UV/ H_2O_2 -based advanced oxidation process (AOP) is provided (Table 6). In reaction simulations, initial concentrations of all TOrCs were arbitrarily set at 10 nM, equivalent to the low ppb range, since molecular weights of the selected compounds are essentially all > 100 g/mol (phenol, 94.11 g/mol being the lone exception). Concentrations of most TOrCs in treated effluent and surface waters range from non-detectable to a few ppb (Kolpin et al. 2002; Miège et al. 2009). A model based on Eq (5) and mole balances for all reactive species (Table 6) was developed in MATLAB (R2012b). The system of ordinary differential equations (ODEs)/algebraic equations was solved using the MATLAB ode15s solver.

Activated carbon adsorption

The software AdDesignSTM from the Environmental Technologies Design Options Tool (ETDOT10) package developed by Michigan Technological University was used to predict TOrC removals by activated carbon treatment. AdDesignSTM provides three separate adsorption model scenarios: (i) equilibrium column model (ECM), (ii) constant pattern homogeneous

surface diffusion model (CPHSDM), and (iii) pore and surface diffusion model (PSDM), to simulate gas- and liquid-phase adsorption in fixed bed adsorbers. The PSDM, a dynamic fixed bed model considering external and intraparticle mass transfer resistance, was used in this study to evaluate adsorption performance with and without fouling of activated carbon by organic matter. Convective mass transfer coefficients, and pore and surface diffusion coefficients of TOrCs required by the PSDM were estimated by AdDesignS™. Adsorption simulations were performed for solutions involving single TOrCs at initial concentrations of 10 nM in either organic free water—i.e. without fouling, or Rhine river (Germany) water with anthropogenic input, as specified for “Fouling of GAC” options of the program. Adsorber characteristics and operating conditions were arbitrarily set at 2.0 m length, 3.66 m diameter, 8500 kg total mass of carbon, and 1.89 m³/min liquid flow rate, to represent a full-scale activated carbon process. In addition, the empty bed contact time (EBCT) was set to 11 minutes; 0.40 g/mL was the bed density, and 25 °C was the water temperature at 1 atm pressure. Spherical particles of Calgon F400 (12 × 40) activated carbon were selected as adsorbent. Adsorption isotherm parameters for the TOrCs studied here are presented in Table S3. Results of the simulation include bed volumes fed to breakthrough (BVF), volume treated per mass of adsorbent (VTM, m³/kg), length of the mass transfer zone (MTZ, cm) and breakthrough time. BVF was chosen to represent the chemical-specific propensity for adsorptive removal. Breakthrough was defined as the point where the exit concentration reached 5% of the inlet concentration.

Membrane separations

Published data were used to examine the compound-specific separation efficiencies achievable through RO and NF. TOrC rejection data reported without corresponding sodium chloride (NaCl) rejections were excluded. Simultaneous TOrC and NaCl rejections were obtained from the literature for 20 compounds (≥ 5 data points were required for inclusion in the dataset). Linear regression of data representing TOrC rejection versus NaCl rejection was carried out using Microsoft Excel 2010. Detailed information is provided in the supplementary information (Figs. S11-S15 and Table S4). TOrC rejection at 50% NaCl rejection was then determined from regression lines specific to each TOrC, and values were compared to key physicochemical properties, including molecule length and thickness and $\log D_{ow}$, to explore mechanism-based explanations for membrane removal efficiencies.

Sunlight photolysis

Treated wastewater is often discharged to waters exposed to sunlight, where direct and indirect photolysis may contribute to compound disappearance (Fono et al. 2006; Jasper and Sedlak 2013). In those situations, both natural organic matter (NOM) and effluent organic matter (EfOM) may act as photo-sensitizers for indirect photolytic reactions (Lee et al. 2013, Zhang et al. 2014, Dong et al. 2015). In addition, both NOM and EfOM contribute to light absorption, which reduces the light available for TOrC and H_2O_2 absorption (shading effect). TOrC transformations during solar irradiation with and without matrix shading were simulated in the following conditions: an open-top well-mixed cylindrical batch reactor (2 m^2 top surface area and 1 m^3 volume) with 0.5-m light path length containing individual TOrCs in either pure water

or secondary effluent from the Tres Rios Wastewater Reclamation Facility (TRWRF) in Tucson, AZ. Samples were exposed to sunlight over an eight-hour period from 8 am to 4 pm.

Instantaneous rates of TOrC transformation by direct photolysis in sunlight at UVA wavelengths are given by (Rojas et al. 2011)

$$\frac{d[\text{TOrC}]}{dt} = -C(t)\Phi_{\text{TOrC-sunlight}} \int_{300}^{400} I_{\lambda} f_{\lambda} (1 - 10^{-\text{Abs}_{\lambda}}) d\lambda \quad \text{Eq (8)}$$

where

$$f_{\lambda} = \frac{\epsilon_{\text{TOrC-}\lambda}[\text{TOrC}]\ell}{\epsilon_{\text{TOrC-}\lambda}[\text{TOrC}]\ell + \text{Abs}_{\text{matrix-}\lambda}} \quad \text{Eq (9)}$$

and

$$\text{Abs}_{\lambda} = \epsilon_{\text{TOrC-}\lambda}[\text{TOrC}]\ell + \text{Abs}_{\text{matrix-}\lambda} \quad \text{Eq (10)}$$

In addition, $\Phi_{\text{TOrC-sunlight}}$ is the average sunlight quantum yield (mol/Ein) for the TOrC modeled in the wavelength range 300 to 400 nm, I_{λ} is the noon-time ground level global spectral irradiance ($\text{EinL}^{-1}\text{s}^{-1}\text{nm}^{-1}$) at wavelength λ , $\epsilon_{\text{TOrC-}\lambda}$ is the spectral molar absorptivity ($\text{M}^{-1}\text{cm}^{-1}$) of the TOrC at wavelength λ , $\text{Abs}_{\text{matrix-}\lambda}$ is the water matrix absorbance at λ based on a 0.5-m light path, Abs_{λ} is the total solution absorbance at λ , and ℓ is the light path length (cm). The function $C(t)$ represents the light intensity at time t as a fraction of the light intensity at noon. The ground level global spectral irradiance in Tucson, AZ, on June 12, 2015 (from 8 am to 4 pm, local time) was obtained from the Simple Model of the Atmospheric Radiative Transfer of Sunshine (SMARTS, 2.9.5 PC package from National Renewable Energy Laboratory) and used in all computations. The function $C(t)$ is a second-order polynomial obtained by fitting the SMARTS-calculated spectral irradiance. Details of the calculation method were provided by Rojas et al.

(2011). In pure water, $\text{Abs}_{\text{matrix}-\lambda}$ is zero throughout the wavelength interval 300-400 nm while $\text{Abs}_{\text{matrix}-\lambda}$ is obtained from a secondary effluent sample collected from the TRWRF. Detailed information about sunlight spectral irradiance, $\epsilon_{\text{TOrC}-\lambda}$, $\text{Abs}_{\text{matrix}-\lambda}$ as well as the effluent quality is given in the supplemental materials (Fig. S16 and Table S5). Attenuation was predicted for each TOrC individually using an initial TOrC concentration of 10 nM and fluid matrices consisting of either pure water or wastewater effluent. Model outputs are the fractional removals of individual TOrCs by direct photolysis. Quantum yields for the TOrCs studies are presented in Table S2.

Statistical analysis

The Spearman's rank correlation method (Myers and Well 2003) was employed for analysis of potential relationships between process efficiencies and compound-specific physicochemical properties. The Spearman coefficient ρ (ranging from -1 to +1) is a monotonic, non-linear measure of strength of relationship between rank orders of two variables. Values of +1 and -1 indicate perfect correspondence (direct and inverse) between the ordered values of those variables. Value near 0 suggests that there is no relationship.

Results and discussion

The results represent efforts to anticipate individual TOrC removals during unit processes that are specific to conventional and advanced municipal wastewater treatment. Advanced treatment processes include those that are commonly relied upon to protect human health when potable reuse of treated wastewater is contemplated—i.e., direct photolysis, UV/H₂O₂ advanced oxidation, carbon adsorption and RO or NF. Photolysis of TOrCs in sunlight is also considered as a means to further purify treated water following discharge to natural waters. In most of these

areas, simulations are supported by empirical data necessary for model calibration/verification. In a few instances, where models appear to be insufficiently reliable, an entirely empirical approach to compound removal or transformation is taken.

BioWin biodegradability predictions

Biodegradability was predicted by BioWin (versions 1 to 7) using the procedures specified above. Results are summarized in Table S6 of the supplementary information. Per the Methods section, we selected results obtained with BioWin4 as biodegradability predictors for further use. Those results consist of estimated (compound-dependent) times required for primary metabolic transformations on a semi-quantitative scale. Predicted transformation times were ranked and divided into five groups ranging in duration from days to months for the 55 selected TOrCs (Fig. 1). The wide range of biodegradability indices of the 55 TOrCs considered reflects the diversity present among their molecular structures. In particular, PAHs were less biodegradable than other groups. Predicted hormone biodegradabilities were generally lower than those of pesticides, herbicides and pharmaceuticals.

The pH-7 octanol-water partition coefficient (D_{ow}), which is frequently used to represent conditional hydrophobicity (at circumneutral pH) was examined here as a potential contributor to TOrC biodegradability. BioWin4 results are presented as a function of $\log D_{ow}$ values in Fig. 2. Results of the statistical analysis suggest that compound hydrophobicity does not contribute to (BioWin4) biodegradability. Nevertheless, influent-to-effluent reduction in compound concentration occurs in part as a consequence of biosorption and sludge separation, so that BioWin predictions may not be an adequate indication of overall process performance. That is,

removal of less biodegradable, hydrophobic TOrCs during conventional secondary treatment may be due primarily to adsorption on biosolids. TOrCs such as EE2 (26) and triclosan (54), for example, which have low BioWin4 indices but high D_{ow} values, are, in general, efficiently removed during conventional biological treatment. Although sorption of TOrCs is usually considered a minor contributor to removal during biological treatment (Radjenović et al. 2009; Khan and Ongerth 2004), sorption to sludge solids increases dramatically for compounds with $\log K_{ow} > 4$ (Byrns 2001; Khan and Ongerth 2004; Thompson et al. 2011).

To minimize the effects of biosorption among reported data, TOrCs with $\log D_{ow} \geq 3.5$ were eliminated from further consideration. For the remaining TOrCs, levels of compound removal that exceeded 80% of influent-to-effluent measurements during activated sludge treatment, as reported by Rojas et al. (2013), were plotted as a function of the compound-specific BioWin4 index (Fig. 3). The objective was to better examine the relationship between observed efficiencies of biochemical transformation and BioWin4 predictions of biodegradability—i.e., to exclude compounds with a strong tendency to adsorb on biosolids. Even though the Spearman correlation coefficient increased, the relationship between the BioWin4 index and observed removals during activated sludge treatment was weak ($\rho = 0.27$). This is contradictory to the results of Blair et al. (2013), who found that BioWin4 indices were well correlated with observed removals of PPCPs. It is possible that the wide variety of operating conditions during conventional wastewater treatment is partly responsible for the apparent lack of correlation, although the inherent complexity of biodegradation processes probably would make finding successful correlations difficult.

UV₂₅₄ direct photolysis

Direct UV photo-attenuations were calculated under the conditions presented in the Methods section for all 45 TOrCs for which both quantum yield and molar absorptivity literature data at 254 nm were found. Results are shown for both clean matrix and wastewater effluent simulations (Fig. 4). Six out of 45 of the TOrCs studied were transformed at more than 50% level during low-pressure UV irradiation in treated wastewater under the conditions of the simulations. Fourteen were transformed at more than 50% level under the same conditions in the pure water matrix. The differences shown in Figure 4 between clean water and wastewater clearly indicate the relatively high impact that light shading has on photolytic transformations, since light shading was the only effect included in the matrix effects during the modeling of the process. Once reactor characteristics and operating conditions are set, including EBC parameters, Eq (2) shows that direct-photolysis removal efficiencies depend on just two parameters: ϵ_{254} and Φ_{254} . The influence of these parameters is shown in Fig. 5. The straight-line shape of the removal contours in the log-log scale is a consequence of the low concentrations on TOrCs used in the simulations. Since the initial concentration of TOrCs is in all cases 10 nM, compounds with sufficiently low molar absorptivity will satisfy $\text{Abs}_{254} \ll 1$. For that case, neglecting the higher order terms in a Taylor series expansion of the exponential term in Eq (2) yields

$$\frac{d[\text{TOrC}]}{dt} \approx -2.303\Phi_{\text{TOrC}-254}I_0(\epsilon_{\text{TOrC}-254}[\text{TOrC}]\ell) \quad \text{Eq (11)}$$

which, after integration, leads to

$$\ln \frac{[\text{TOrC}]}{[\text{TOrC}]_0} = -2.303\Phi_{\text{TOrC}-254}\epsilon_{\text{TOrC}-254}I_0\ell t \quad \text{Eq (12)}$$

Note that under these conditions, TOrC removal depends on the product between quantum yield and extinction coefficient, so that this combination of the two parameters represents a single independent variable.

In the wastewater matrix, if the solution absorbance at 254 nm is overwhelmed by EBC—i.e.

$\varepsilon_{\text{TOrC-254}}[\text{TOrC}] \ll \varepsilon_{\text{EBC-254}}[\text{EBC}]$, Eq (2) can be simplified to

$$\frac{d[\text{TOrC}]}{dt} \approx -\Phi_{\text{TOrC-254}}\varepsilon_{\text{TOrC-254}}[\text{TOrC}]I_o \frac{[1 - 10^{-(\varepsilon_{\text{EBC-254}}[\text{EBC}]_c)\ell}]}{\varepsilon_{\text{EBC-254}}[\text{EBC}]_c} \quad \text{Eq (13)}$$

If EBC concentration is unchanged by UV irradiation, Eq (13) can be integrated yielding

$$\ln \frac{[\text{TOrC}]}{[\text{TOrC}]_o} = -\Phi_{\text{TOrC-254}}\varepsilon_{\text{TOrC-254}}I_o \frac{[1 - 10^{-(\varepsilon_{\text{EBC-254}}[\text{EBC}]_c)\ell}]}{\varepsilon_{\text{EBC-254}}[\text{EBC}]_c} t \quad \text{Eq (14)}$$

Consequently, the log transformed TOrC residuals are also proportional to the product of their molar absorptivity and quantum yield at 254 nm. To establish the validity of these approximations for the treatment process considered here, predicted residual fractions of 45 TOrCs in pure water and effluent, calculated from Eq (2), were plotted as a function of the TOrC-dependent product of ε_{254} and Φ_{254} and compared to results of Eq (12) and Eq (14) (Fig. 6). In both pure water and effluent, the straight-line shape of the relation presented establishes the validity of each approximation throughout the range of experimental conditions simulated and for each of the compounds tested. Matrix effects are exceptionally important, as indicated by differences between the clean water and effluent lines.

Advanced oxidation

Transformations of TOrCs by UV/H₂O₂ AOP treatment were simulated using the plug-flow reactor configuration and operating conditions specified in the Methods section. The

concentration of H₂O₂ added to both the clean water and effluent matrices was 5 ppm. A third set of calculations was performed in which the shading effect of the wastewater matrix was neglected by artificially imposing $\epsilon_{\text{EBC-254}} = 0$. That calculation represents a hypothetical situation designed to expose the effect of ^{*}OH scavenging by matrix organics. Results of the simulations are presented in Fig. 7. Under the conditions selected for the simulations, AOP removal efficiency in pure water was high (> 80%, but mostly close to 100%) for all TOxCs. Although photosensitivities—i.e. the product of ϵ_{254} and Φ_{254} , among the 42 selected TOxCs ranged from < 2 LEin⁻¹cm⁻¹ (2,4-D, ID #2) to over 4500 LEin⁻¹cm⁻¹ (ketoprofen, ID #32), the range of second-order reaction rate constants for the same compounds with ^{*}OH is roughly 10⁹ to 10¹⁰ M⁻¹s⁻¹, close to the diffusion limit, accounting for the predicted AOP efficiency in the clean matrix. In the effluent matrix (secondary effluent), however, both shading and scavenging of ^{*}OH by matrix organics are predicted to inhibit TOxC removal efficiencies. Consequently, TOxC removal efficiencies were only marginally improved by the addition of H₂O₂ to the wastewater matrix. This can be seen by comparison of results in Figs. 4 and 7 (black bars for direct photolysis in Fig. 4 versus cyan bars in Fig. 7, which accounted for shading and radical scavenging effects.) As mentioned, the pure water efficiencies are uniformly high (gray bars in Fig.7). Effects of radical quenching by reaction with wastewater constituents are as shown (yellow vs. gray bars), as are the combined effects of wastewater quenching and shading (reaction plus UV absorbance; cyan bars).

Carbon adsorption

A correlation between $\log K_{ow}$ and adsorption performance is usually acknowledged in the literature (Hu et al. 1997; Westerhoff et al. 2005). The same idea was pursued by plotting AdDesignSTM (PSDM) predicted bed volumes fed to breakthrough (BVF) in organic free water—i.e. without fouling adsorbent by NOM, as a function of $\log D_{ow}$ for the 35 TOrCs with available $\log D_{ow}$ values (Fig. 8). The results indicate that $\log D_{ow}$ is a poor indicator of the predicted performance of carbon adsorption. The lack of correlation may be due at least in part to the lack of a consistent isotherm parameter database. The Freundlich parameters assembled in this study represent values taken over 15 different types of activated carbon at pH values ranging from 2.0 to 8.0. Nevertheless, correlation between $\log D_{ow}$ and adsorption performance was not substantially improved by applying Freundlich parameters from a single source (detailed information available in Table S7 and Fig. S17).

The BVF to breakthrough for 43 TOrCs with available Freundlich parameters and related physicochemical information were calculated for the conditions specified in the Methods section to investigate potential impact of fouling on treatment efficiency. The results are shown in Fig. 9. The water matrices used were either NOM-free water or Rhine River (Germany) water, which contains a significant anthropogenic input. Those waters were among the selections available in AdDesignSTM under “Fouling of GAC”.

In the presence of fouling by NOM, calculated BVFs ranged from approximately 10^2 to 10^6 . Values for diclofenac (19) and caffeine (11) were $> 5 \times 10^6$. Conversely, E3 (25) was predicted to break through first at ~ 200 bed volumes. All other TOrCs were scattered between 10^3 and 10^6 .

As expected, fouling of the activated carbon by NOM in the matrix inhibits TOrC separation, which is particularly noted for pesticides and herbicides. The pore and surface diffusion model (PSDM) from AdDesignS™ reduces the Freundlich capacity parameter (K) to reflect the fouling process. Fouling effects are specific to water quality characteristics, sorbate types and adsorbent properties (Bhuvendralingam 1992). When the fluid matrix and adsorber conditions are fixed, TOrC Freundlich capacity parameters are corrected by the PSDM using empirical equations that are sorbate and sorbent specific.

Membrane separations

Membrane TOrC rejection at 50% NaCl rejection was determined from linear regression lines specific to each TOrC. Examples of the regression are shown in Fig. 10. Only membrane separation literature data that were accompanied by NaCl rejection data were used in the analysis that follows. In addition, TOrCs lacking the five independent data points deemed sufficient for determination of the compound-specific rejection at 50% NaCl rejection were also neglected. Twenty TOrCs survived these screening criteria. Compound-specific rejections at the 50% NaCl rejection conditions are presented in Fig. 11.

To determine whether rejection data were influenced by TOrC molecular dimensions or hydrophobicity, compound-specific rejections (Fig. 11) were examined as a function of $\log D_{ow}$, molecule length and thickness for each compound. Only TOrC thickness proved to be a reasonable predictor of compound removal. The relationship is shown in Fig. 12. Figures illustrating potential relationships between membrane separation efficiency and either compound molecular length or hydrophobicity are omitted for brevity. (For details see Fig. S18.)

A reciprocal function

$$y = 102.2 - \frac{4.481}{(x - 0.1)} \quad \text{Eq (15)}$$

was obtained by fitting the data representing rejections as a function of molecule thickness (Fig. 12). Coefficients were determined for the line of best fit using the MATLAB Curve Fitting Tool. From the curve and mathematical treatment, it is evident that molecules with thickness < 0.25 nm penetrate RO/NF membranes under conditions that result in 50% (and presumably higher) NaCl penetration. Solutes with molecular thicknesses > 0.3 nm are generally well removed ($> 75\%$) under the same conditions.

Direct sunlight photolysis

Sunlight-driven TOrC attenuations have been attributed to both direct and indirect photolysis. The indirect mechanism involves light-dependent formation of reactive intermediate species from “sensitizer” compounds that contribute to residual EfOM in wastewater effluent (Lee et al. 2013; Jasper and Sedlak 2013; Dong et al. 2015). Despite their potential importance, the current state of the art does not support rational quantification of indirect photolysis matrix effects due to EfOM; consequently, they are omitted from the following analysis. Furthermore, parameters governing direct photochemical transformations of TOrCs in sunlight (i.e. ϵ_λ and quantum efficiencies from 300 to 400 nm) are limited. Only 17 out of the 55 selected TOrCs could be analyzed here based on literature data. Results are presented in Fig. 13. As in direct UV photolysis, the shading effect of the effluent matrix is predicted to reduce photolytic efficiency in

direct sunlight significantly. Important exceptions included acetaminophen (3), norfloxacin (40) and sulfamethoxazole (51), each of which is exceptionally sensitive to sunlight.

TOrC removals in sunlight versus UV irradiance were sometimes inconsistent. That is, a subset of the TOrCs analyzed was significantly more sensitive to sunlight than UV exposure (e.g., acetaminophen). The reverse was true for an additional set of the compounds analyzed (e.g., testosterone). Detailed information is provided in supplemental materials (Fig. S19).

Implication for process design

Based on the foregoing, it is possible to comment on the efficacy of individual unit operations including conventional wastewater biotreatment, candidate tertiary processes and sunlight photolysis on the fates of the most prevalent TOrCs during and immediately after treatment of municipal wastes. Compound-specific TOrC treatment performance in effluent wastewater matrix of engineered and natural processes investigated in this study are shown in Table 7. Somewhat arbitrarily, process- and compound-specific TOrC removal efficiencies were characterized as high, medium or low according to the criteria presented in Table 8. A scoring system was developed utilizing qualitative evaluation results based on the results in Table 7 to provide semi-quantitative estimation for TOrCs removal efficiencies in wastewater effluent matrix of two proposed treatment sequences: (i) conventional secondary treatment followed by UV/H₂O₂ AOP followed by activated carbon followed by RO/NF, and (ii) conventional secondary treatment followed by UV/H₂O₂ AOP followed by activated carbon. In this scoring system, three qualitative attenuation levels—i.e. high, medium and low, of a single TOrC during each engineered processes were arbitrarily set as 2, 1 and 0, respectively. Removal scores of a

TOrC during each selected engineered processes are independently summed, yielding a final score of the TOrC for selected treatment sequence. Results of this evaluation are presented in Tables 9. For sequence (i), one can consider such treatment strategy is good, fair or poor for removing a TOrC when final scores are > 5 , 3-5, or < 3 , respectively. When applying sequence (ii), final scores for good, fair or poor removal are > 4 , 2-4, or < 2 , respectively.

Limitations of the analysis

Due to the paucity of detailed matrix effects as well as degradation mechanism of TOrCs under direct and indirect UV photolysis, the UV254-based TOrC removals calculated in this study only considered light scattering and *OH quenching of matrix by simply using an EBC, and neglected potential impact from by-products and interactions among matrix compounds with targets and by-products. Similarly, for sunlight process, UVA shading is the only matrix effect considered in the treated effluent, where indirect sunlight photolysis via ROS—e.g., *OH and singlet oxygen as well as photo-excited DOMs may play an important role on attenuations of TOrCs under natural conditions.

Given the fact that adsorption isotherm constants can vary with adsorbent type and solution pH, PSDM predicted sorptive removals may not be accurate enough to reflect TOrC relative attenuation during activated carbon processes without a consistent isotherm parameter database (Freundlich parameters used in this study obtained from the literature and represented over 15 different types of activated carbon and pH values ranging from 2.0 to 8.0). Besides, without comparing to experimentally-determined results, prediction accuracy of PSDM considering matrix effect still remains questionable since AdDesignSTM simply utilizes empirical equations

to manipulate Freundlich capacity parameter based on matrix and chemical types to represent fouling of adsorbent by NOM.

Additionally, the validity of applying the correlation obtained between the rejection results of 20 out the 55 (< 40%) selected TOrCs and their molecular thickness data to estimate membrane treatment performance for the rest 33 compounds will remain unknown until enough experimental results are available.

The scoring system proposed in this study simply combines efficiencies of select processes independently neglecting potential influence of effluent quality/composition of each process on the following unit(s) in the treatment train. For instance, the aforementioned *OH quenching by background organic matter during UV/H₂O₂ AOP may lead to less fouling potential in the activated carbon process.

Conclusions

The remarkable effort of Grady on developing a systematic approach to rationalize engineered biotransformation of xenobiotic organic compounds during conventional wastewater treatment provided a heuristic guideline for scientists and engineers, stimulating broad-scale thinking relative to substantial environmental engineering problems. Besides the roles of available tools in reactor engineering, Grady emphasized the importance of databases of intrinsic kinetic parameters. Most importantly, Grady proposed that in most engineering applications, transformations of multiple xenobiotic compounds could be treated independently, using a single-substrate kinetic approach. This idea was followed up in the present study where removal efficiencies of 55 selected TOrCs were individually investigated in a single-substrate—i.e. a

representative wastewater effluent during engineered (conventional and tertiary treatments) and natural processes using currently available tools. The potential relationships between treatment performance and compound physicochemical properties were tested to explore the physicochemical and biological determinants of TOrC removal efficiencies in a variety of engineered and natural processes, including one of the most common AOPs (H_2O_2 photolysis). Other common AOPs (e.g. Ozonation, TiO_2 catalysis, Fenton's reactions) would need to be considered in a more thorough investigation of optimal treatment strategies.

It is apparent that simply utilizing QSAR calculated biodegradability (e.g. BioWin simulations) to estimate overall fate of TOrCs during conventional wastewater treatment is not absolutely reliable, which confirms observations reported previously (Rojas et al., 2013, and references therein).

All tertiary treatments which can be impacted by background organic matter present in the water matrix are capable of attenuating a broad spectrum of TOrCs, highly depending on compound's related physicochemical properties. Due to lack of good understanding of matrix effects as well as degradation mechanism of TOrCs during photon-driven tertiary treatment—e.g. UV-based advanced oxidation and sunlight photolysis, removals were simulated without considering the potential impact from by-products and interactions among matrix organics with targets and by-products. Even under these conditions, the effects of radical scavenging and light shading by organic matrix compounds have an important impact on TOrC treatment. Quantification of matrix interferences both in terms of physical effects (such as light absorption) and chemical

effects (degradation mechanisms, radical scavenging, production of reactive oxygen species)

remains a challenging key point in the evaluation of treatment technologies.

References

- Bhuvendralingam, S. (1992). "A decision algorithm for optimizing granular activated carbon adsorption process design." *Doctor of Philosophy Dissertation*, Michigan Technological University, Ann Arbor.
- Bielski, B. H. J., Cabelli, D. E., Arudi, R. L., and Ross, A. B. (1985). "Reactivity of HO₂/O⁻ radicals in aqueous solution." *J. Phys. Chem. Ref. Data*, 14(4), 1041-1100.
- Blair, B. D., Crago, J. P., Hedman, C. J., Treguer, R. J., Magruder, C., Royer, L. S., and Klaper, R. D. (2013). "Evaluation of a model for the removal of pharmaceuticals, personal care products, and hormones from wastewater." *Sci. Total Environ.*, 444, 515-521.
- Boethling, R. S., Gregg, B., Frederick, R., Gabel, N. W., Campbell, S. E., and Sabljic, A. (1989). "Expert systems survey on biodegradation of xenobiotic chemicals." *Ecotoxicol. Environ. Saf.*, 18(3), 252-267.
- Boethling, R. S., Howard, P. H., Meylan, W., Stiteler, W., Beauman, J., and Tirado, N. (1994). "Group contribution method for predicting probability and rate of aerobic biodegradation." *Environ. Sci. Technol.*, 28(3), 459-465.
- Boethling, R. S., Lynch, D. G., and Thom, G. C. (2003). "Predicting ready biodegradability of premanufacture notice chemicals." *Environ. Toxicol. Chem.*, 22(4), 837-844.
- Brown, W. H., Foote, C. S., Iverson, B. L., and Anslyn, E. (2011). *Organic Chemistry*, Cengage Learning, Belmont, U.S.A.
- Buxton, G. V., Greenstock, C. L., Helman, W. P., and Ross, A. B. (1988). "Critical review of rate constants for reactions of hydrated electrons, hydrogen atoms and hydroxyl radicals (-OH/-O-) in aqueous solution." *J. Phys. Chem. Ref. Data*, 17(2), 513-886.
- Byrns, G. (2001). "The fate of xenobiotic organic compounds in wastewater treatment plants." *Water Res.*, 35(10), 2523-2533.
- Carpenter, K., Cottrell, H. J., Silva, W. H., Heywood, B. J., Leeds, W. G., Rivett, K. F., and Soundy, M. L. (1964). "Chemical and biological properties of two new herbicides—ioxynil and bromoxynil." *Weed Res.*, 4, 175-195.
- Celis, R., Hermosín, M. C., Cox, L., and Cornejo, J. (1999). "Sorption of 2,4-dichlorophenoxyacetic acid by model particles simulating naturally occurring soil colloids." *Environ. Sci. Technol.*, 33(8), 1200-1206.
- Colburn, T., Dumanoski, D., and P., M. J. (1996). *Our stolen future: Are we threatening our fertility, intelligence, and survival? - A scientific detective story*, Dutton, New York.
- Comerton, A. M., Andrews, R. C., Bagley, D. M., and Hao, C. (2008). "The rejection of endocrine disrupting and pharmaceutically active compounds by NF and RO membranes as a function of compound and water matrix properties." *J. Membr. Sci.*, 313(1-2), 323-335.

- Daughton, C. G., and Ternes, T. A. (1999). "Pharmaceuticals and Personal Care Products in the Environment: Agents of Subtle Change?" *Environ. Health Perspect.*, 107(Suppl 6), 907-938.
- Dong, B., Kahl, A., Cheng, L., Vo, H., Ruehl, S., Zhang, T., Snyder, S., Sáez, A. E., Quanrud, D., and Arnold, R. G. (2015). "Fate of trace organics in a wastewater effluent dependent stream." *Sci. Total Environ.*, 518-519, 479-490.
- Fono, L. J., Kolodziej, E. P., and Sedlak, D. L. (2006). "Attenuation of wastewater-derived contaminants in an effluent-dominated river." *Environ. Sci. Technol.*, 40(23), 7257-7262.
- Grady, C., Jr. (1990). "Biodegradation of Toxic Organics: Status and Potential." *J. Environ. Eng.*, 10.1061/(ASCE)0733-9372(1990)116:5(805), 805-828.
- Hiller, E., Khun, M., Zemanová, L., Jurkovič, L., and Bartaľ, M. (2006). "Laboratory study of retention and release of weak acid herbicide MCPA by soils and sediments and leaching potential of MCPA." *Plant Soil Environ.*, 52(12), 550-558.
- Howard, P. H., Boethling, R. S., Stiteler, W. M., Meylan, W. M., Hueber, A. E., Beauman, J. A., and Larosche, M. E. (1992). "Predictive model for aerobic biodegradability developed from a file of evaluated biodegradation data." *Environ. Toxicol. Chem.*, 11(5), 593-603.
- Howard, P. H., Hueber, A. E., and Boethling, R. S. (1987). "Biodegradation data evaluation for structure/biodegradability relations." *Environ. Toxicol. Chem.*, 6(1), 1-10.
- Hu, J., Aizawa, T., and Magara, Y. (1997). "Evaluation of adsorbability of pesticides in water on powdered activated carbon using octanol-water partition coefficient." *Water Sci. Technol.*, 35(7), 219-226.
- Jasper, J. T., and Sedlak, D. L. (2013). "Phototransformation of wastewater-derived trace organic contaminants in open-water unit process treatment wetlands." *Environ. Sci. Technol.*, 47(19), 10781-10790.
- Jones, O. A., Voulvoulis, N., and Lester, J. N. (2005). "Human pharmaceuticals in wastewater treatment processes." *Crit. Rev. Env. Sci. Technol.*, 35(4), 401-427.
- Jones, O. A., Voulvoulis, N., and Lester, J. N. (2007). "The occurrence and removal of selected pharmaceutical compounds in a sewage treatment works utilising activated sludge treatment." *Environ. Pollut.*, 145(3), 738-744.
- Khan, S. J., and Ongerth, J. E. (2004). "Modelling of pharmaceutical residues in Australian sewage by quantities of use and fugacity calculations." *Chemosphere*, 54(3), 355-367.
- Kidd, K. A., Blanchfield, P. J., Mills, K. H., Palace, V. P., Evans, R. E., Lazorchak, J. M., and Flick, R. W. (2007). "Collapse of a fish population after exposure to a synthetic estrogen." *Proc. Nat. Acad. Sci. U.S.A.*, 104(21), 8897-8901.
- Knaak, J. B., Dary, C. C., Okino, M. S., Power, F. W., Zhang, X., Thompson, C. B., Tornero-Velez, R., and Blancato, J. N. (2008). "Chemical Engineering Science Parameters for

- carbamate pesticide QSAR and PBPK/PD models for human risk assessment.” *Reviews of Environmental Contamination and Toxicology*, D. M. Whitacre, ed., Springer, New York, 53-212.
- Kolpin, D. W., Furlong, E. T., Meyer, M. T., Thurman, E. M., D., Z. S., Barber, L. B., and Buxton, H. T. (2002). “Pharmaceuticals, hormones, and other organic wastewater contaminants in U.S. streams, 1999-2000: a national reconnaissance.” *Environ. Sci. Technol.*, 36(6), 1202-1211.
- Ku, Y., Chang, J., and Cheng, S. (1998). “Effect of solution pH on the hydrolysis and photolysis of diazinon in aqueous solution.” *Water, Air, Soil Pollut.*, 108(3), 445-456.
- Lapworth, D. J., Baran, N., Stuart, M. E., and Ward, R. S. (2012). “Emerging organic contaminants in groundwater: A review of sources, fate and occurrence.” *Environ. Pollut.*, 163, 287-303.
- Lee, E., Glover, C. M., and Rosario-Ortiz, F. L. (2013). “Photochemical formation of hydroxyl radical from effluent organic matter: Role of composition.” *Environ. Sci. Technol.*, 47(21), 12073-12080.
- Li, Y. F., Zhang, X. Q., Hu, W. Y., Li, Z., Liu, P. X., and Zhang, Z. Q. (2013). “Rapid screening of drug-protein binding using high-performance affinity chromatography with columns containing immobilized human serum albumin.” *J. Anal. Methods Chem.*, 2013, 1-7.
- Margot, J., Kienle, C., Magnet, A., Weil, M., Rossi, L., de Alencastro, L. F., Abegglen, C., Thonney, D., Chèvre, N., Schäfer, M., and Barry, D. A. (2013). “Treatment of micropollutants in municipal wastewater: ozone or powdered activated carbon?” *Sci. Total Environ.*, 461-462, 480-498.
- Maruya, K. A., Schlenk, D., Anderson, P. D., Denslow, N. D., Drewes, J. E., Olivieri, A. W., Scott, G. I., and Snyder, S. A. (2014). “An adaptive, comprehensive monitoring strategy for chemicals of emerging concern (CECs) in California's aquatic ecosystems.” *Integr. Environ. Assess. Manage.*, 10(1), 69-77.
- Meylan, W., Boethling, R., Aronson, D., Howard, P., and Tunkel, J. (2007). “Chemical structure-based predictive model for methanogenic anaerobic biodegradation potential.” *Environ. Toxicol. Chem.*, 26(9), 1785-1792.
- Miège, C., Choubert, J. M., Ribeiro, L., Eusèbe, M., and Coquery, M. (2009). “Fate of pharmaceuticals and personal care products in wastewater treatment plants -conception of a database and first results.” *Environ. Pollut.*, 157(5), 1721-1726.
- Myers, J. L., and Well, A. D. (2003). *Research Design and Statistical Analysis*, Lawrence Erlbaum Associates, Mahwah, New Jersey.
- Perry, R., Green, D., and Maloney, J. (1984). *Perry's Chemical Engineers' Handbook*, McGraw-Hill, New York.

- Petrović, M., and Barceló, D. (2007). *Analysis, fate and removal of pharmaceuticals in the water cycle*, Elsevier, Oxford, U.K.
- Posthumus, R., Traas, T. P., Peijnenburg, W. J., and Hulzebos, E. M. (2005). "External validation of EPIWIN biodegradation models." *SAR QSAR Environ. Res.*, 16(1-2), 135-148.
- Purdom, C. E., Hardiman, P. A., Bye, V. V. J., Eno, N. C., Tyler, C. R., and Sumpter, J. P. (1994). "Estrogenic effects of effluents from sewage treatment works." *Chem. Ecol.*, 8(4), 275-285.
- Radjenović, J., Petrović, M., and Barceló, D. (2009). "Fate and distribution of pharmaceuticals in wastewater and sewage sludge of the conventional activated sludge (CAS) and advanced membrane bioreactor (MBR) treatment." *Water Res.*, 43(3), 831-841.
- Rivas, J., Gimeno, O., Borralho, T., and Sagasti, J. (2011). "UV-C and UV-C/peroxide elimination of selected pharmaceuticals in secondary effluents." *Desalination*, 279(1-3), 115-120.
- Rojas, M. R., Leung, C., Bonk, F., Zhu, Y., Edwards, L., Arnold, R. G., Sáez, A. E., and Klečka, G. (2013). "Assessment of the effectiveness of secondary wastewater treatment technologies to remove trace chemicals of emerging concern." *Crit. Rev. Env. Sci. Technol.*, 43(12), 1281-1314.
- Rojas, M. R., Leung, C., Whitley, D., Zhu, Y., Arnold, R. G., and Sáez, A. E. (2011). "Advanced oxidation of trace organics in water by hydrogen peroxide solar photolysis." *Ind. Eng. Chem. Res.*, 50(22), 12479-12487.
- Rosario-Ortiz, F. L., Mezyk, S. P., Doud, D. F. R., and Snyder, S. A. (2008). "Quantitative correlation of absolute hydroxyl radical rate constants with non-isolated effluent organic matter bulk properties in water." *Environ. Sci. Technol.*, 42(16), 5924-5930.
- Rücker, C., and Kümmerer, K. (2012). "Modeling and predicting aquatic aerobic biodegradation – a review from a user's perspective." *Green Chem.*, 14(4), 875-887.
- Schwarzenbach, R. P., Gschwend, P. M., and Imboden, D. M. (2003). *Environmental Organic Chemistry*, John Wiley & Sons, Hoboken, New Jersey.
- Senseman, S. A. (2007). *Herbicide handbook*, Weed Science Society of America, Lawrence, U.S.A.
- Stevens-Garmon, J., Drewes, J. E., Khan, S. J., McDonald, J. A., and Dickenson, E. R. (2011). "Sorption of emerging trace organic compounds onto wastewater sludge solids." *Water Res.*, 45(11), 3417-3426.
- Sui, Q., Cao, X., Lu, S., Zhao, W., Qiu, Z., and Yu, G. (2015). "Occurrence, sources and fate of pharmaceuticals and personal care products in the groundwater: A review." *Emerg. Contam.*, 1(1), 14-24.

- Sumpter, J. P. (1995). "Feminized responses in fish to environmental estrogens." *Toxicol. Lett.*, 82/83, 737-742.
- Thompson, K., Zhang, J., and Zhang, C. (2011). "Use of fugacity model to analyze temperature-dependent removal of micro-contaminants in sewage treatment plants." *Chemosphere*, 84(8), 1066-1071.
- Tunkel, J., Howard, P. H., Boethling, R. S., Stiteler, W., and Loonen, H. (2000). "Predicting ready biodegradability in the Japanese ministry of international trade and industry test." *Environ. Toxicol. Chem.*, 19(10), 2478-2485.
- U.S. EPA (2009). "Occurrence of contaminants of emerging concern in wastewater from nine publicly owned treatment works." U.S. Environmental Protection Agency Office of Water, Washington, DC.
- U.S. EPA (2010). "Treating contaminants of emerging concern: A literature review database." U.S. Environmental Protection Agency Office of Water, Washington, DC.
- U.S. EPA (2016). "Estimation Programs Interface Suite™ for Microsoft® Windows, v 4.11." United States Environmental Protection Agency, Washington, DC, U.S.A.
- Urase, T., and Kikuta, T. (2005). "Separate estimation of adsorption and degradation of pharmaceutical substances and estrogens in the activated sludge process." *Water Res.*, 39(7), 1289-1300.
- Volman, D. H., and Chen, J. C. (1959). "The photochemical decomposition of hydrogen peroxide in aqueous solutions of allyl alcohol at 2537 Å." *J. Am. Chem. Soc.*, 81(16), 4141-4144.
- Weinstein, J., and Bielski, B. H. J. (1979). "Kinetics of the interaction of HO₂ and O₂- radicals with hydrogen peroxide. The Haber-Weiss reaction." *J. Am. Chem. Soc.*, 101(1), 58-62.
- Westerhoff, P., Yoon, Y., Snyder, S., and Wert, E. (2005). "Fate of endocrine-disruptor, pharmaceutical, and personal care product chemicals during simulated drinking water treatment processes." *Environ. Sci. Technol.*, 39(17), 6649-6663.
- Wols, B. A., and Hofman-Caris, C. H. M. (2012). "Review of photochemical reaction constants of organic micropollutants required for UV advanced oxidation processes in water." *Water Res.*, 46(9), 2815-2827.
- Zhang, D., Yan, S., and Song, W. (2014). "Photochemically induced formation of reactive oxygen species (ROS) from effluent organic matter." *Environ. Sci. Technol.*, 48(21), 12645-12653.

Table 1. List of the 55 TOrCs selected for this study, including octanol-water partition coefficients (K_{ow}) and pK_a , reported at ambient or near-ambient conditions

TOrCs	TOrC ID	CAS Number	Molecular Weight	General Class	log K_{ow}	pK_a
1,4-Dichlorobenzene (1,4-DCB)	1	106-46-7	147.00	Deodorizer	3.44	—
17 α -Ethinyl estradiol (EE2)	26	57-63-6	296.41	Hormone	3.67	10.3 ^b
17 β -Estradiol (E2)	24	50-28-2	272.39	Hormone	4.01	10.3 ^b
2,4-Dichlorophenoxyacetic acid (2,4-D)	2	94-75-7	221.04	Herbicide	2.81	2.6 ^e
Acetaminophen	3	103-90-2	151.17	Antipyretic	0.46	9.5 ^b
Anthracene	4	120-12-7	178.24	PAH	4.45	—
Atrazine	5	1912-24-9	215.69	Herbicide	2.61	3.2 ^b
Benzo(a)pyrene	6	50-32-8	252.32	PAH	6.13	—
Benzophenone	7	119-61-9	182.22	UV blocker	3.18	—
Bezafibrate	8	41859-67-0	361.83	Lipid regulator	4.25 ^a	3.6 ^c
Bisphenol A	9	80-05-7	228.29	Plasticizer	3.32	9.8 ^b
Bromoxynil	10	1689-84-5	276.92	Herbicide	3.39 ^a	4.1 ^f
Caffeine	11	58-08-2	194.19	Stimulant	-0.07	-0.92 ^b
Carbamazepine	12	298-46-4	236.28	Anti-epileptic	2.45	16.0 ^b
Carbofuran	13	1563-66-2	221.26	Pesticide	2.32	12.3 ^g
Chlorpyrifos	14	2921-88-2	350.59	Insecticide	4.96	—
Ciprofloxacin	15	85721-33-1	331.35	Antibiotic	0.28	6.1 ^c
Clofibric acid	16	882-09-7	214.65	Metabolite	2.57	2.8 ^c
Diazinon	18	333-41-5	304.35	Insecticide	3.81	2.4 ^h
Diclofenac	19	15307-86-5	296.15	Anti-inflammatory	4.51	4.0 ^b
Diphenhydramine	20	58-73-1	255.36	Antihistamine	3.27	9.0 ^d
Diuron	21	330-54-1	233.10	Herbicide	2.68	—
Doxycycline	22	564-25-0	444.44	Antibiotic	-0.02	—
Estriol (E3)	25	50-27-1	288.39	Hormone	2.45	10.3 ^b
Estrone (E1)	23	53-16-7	270.37	Hormone	3.13	10.3 ^b

Table 1. (Continued)

TOrCs	TOrC ID	CAS Number	Molecular Weight	General Class	log K _{ow}	pKa
Fluoranthene	27	206-44-0	202.26	Various	5.16	—
Gemfibrozil	28	25812-30-0	250.34	Lipid regulator	4.77 ^a	4.4 ^b
Ibuprofen	29	15687-27-1	206.29	Anti-inflammatory	3.97	4.9 ^b
Indomethacin	30	53-86-1	357.80	Anti-inflammatory	4.27	4.5 ^c
Iopromide	31	73334-07-3	791.12	Contrast medium	-2.05	—
Ketoprofen	32	22071-15-4	254.29	Anti-inflammatory	3.12	4.5 ^c
Linuron	33	330-55-2	249.10	Herbicide	3.2	—
MCPA	34	94-74-6	200.62	Herbicide	3.25	3.1 ⁱ
Mefenamic acid	35	61-68-7	241.29	Anti-inflammatory	5.12	—
Metolachlor	36	51218-45-2	283.80	Herbicide	2.9	—
Metoprolol	37	51384-51-1	267.37	Betablocker	1.88	9.6 ^d
N,N-Diethyl-toluamide (DEET)	17	134-62-3	191.28	Insecticide	2.18	—
Naproxen	38	22204-53-1	230.27	Anti-inflammatory	3.18	4.2 ^b
Nonylphenol	39	25154-52-3	220.36	Detergent metabolite	5.76	10.3 ^c
Norfloxacin	40	70458-96-7	319.34	Antibiotic	-1.03	6.3 ^d
Octylphenol	41	1806-26-4	206.33	Detergent metabolite	5.5	9.9 ^c
Phenanthrene	42	85-01-8	178.24	PAH	4.46	—
Phenol	43	108-95-2	94.110	Disinfectant	1.46	9.9 ^j
Progesterone	44	57-83-0	314.47	Hormone	3.87	19.3 ^k
Propachlor	45	1918-16-7	211.69	Herbicide	2.18	—
Pyrene	46	129-00-0	202.26	PAH	4.88	—
Ranitidine	47	66357-35-5	314.41	Antacid	0.27	2.7 ^c
Roxithromycin	48	80214-83-1	837.07	Antibiotic	2.75 ^a	9.0 ^c
Simazine	49	122-34-9	201.66	Herbicide	2.18	1.6 ^l
Sulfamerazine	50	127-79-7	264.30	Antibiotic	0.14	7.4 ^c
Sulfamethoxazole	51	723-46-6	253.28	Antibiotic	0.89	6.2 ^b

Table 1. (Continued)

TOrCs	TOrC ID	CAS Number	Molecular Weight	General Class	log K _{ow}	pKa
Testosterone	52	58-22-0	288.43	Hormone	3.32	19.4 ^b
Tetracycline	53	60-54-8	444.44	Antibiotic	-1.3	3.3 ^c
Triclosan	54	3380-34-5	289.55	Disinfectant	4.76	8.1 ^c
Trimethoprim	55	738-70-5	290.32	Antibiotic	0.91	7.2 ^b

^aK_{ow} values were estimated by KOWWIN program in the EPI Suite™.

^bpKa data from Stevens-Garmon et al. (2011).

^cpKa data from Rojas et al. (2013).

^dpKa data from Petrović and Barceló (2007).

^epKa data from Celis et al. (1999).

^fpKa data from Carpenter et al. (1964).

^gpKa data from Knaak et al. (2008).

^hpKa data from Ku et al. (1998).

ⁱpKa data from Hiller et al. (2006).

^jpKa data from Brown et al. (2011).

^kpKa data from Li et al. (2013).

^lpKa data from Senseman (2007).

Table 2. Photochemical properties (quantum yield at 254 nm, $\Phi_{\text{TOrC-254}}$, molar absorptivity at 254 nm, $\epsilon_{\text{TOrC-254}}$, and reaction rate constant with $^*\text{OH}$, $k_{\text{TOrC-}^*\text{OH}}$) for the 55 TOrCs in this study.

TOrCs	$\Phi_{\text{TOrC-254}}$ $\times 10^{-2}$ mol/Ein	$\epsilon_{\text{TOrC-254}}$ $\times 10^3$ M ⁻¹ cm ⁻¹	$k_{\text{TOrC-}^*\text{OH}}$ $\times 10^9$ M ⁻¹ s ⁻¹	$\Phi_{\text{TOrC-sunlight}}$ $\times 10^{-2}$ mol/Ein
1,4-DCB	60.0	0.118	8.00 (± 3.68)	1.70
2,4-D	0.950	0.173	3.51 (± 1.81)	—
Acetaminophen	0.390 (± 0.297)	6.70 (± 2.16)	9.70	34.5 (± 14.9)
Anthracene	14.9 (± 7.4)	1.07 (± 0.04)	7.83 (± 4.21)	—
Atrazine	4.77 (± 1.37)	3.51 (± 0.58)	3.22 (± 2.31)	—
Benzo(a)pyrene	16.4 (± 21.2)	1.08	25.2 (± 0.2)	—
Benzophenone	—	—	8.85 (± 0.21)	—
Bezafibrate	—	0.950	7.70 (± 0.42)	—
Bisphenol A	0.655 (± 0.276)	0.750	8.00 (± 3.11)	—
Bromoxynil	4.00	4.97	8.45 (± 0.40)	—
Caffeine	0.180 (± 0.030)	4.81	6.40 (± 0.71)	—
Carbamazepine	0.060 (± 0.009)	6.06 (± 0.03)	6.53 (± 3.36)	0.003 (± 0.002)
Carbofuran	1.66	0.800	1.73	—
Chlorpyrifos	1.60	0.650	4.54 (± 0.52)	—
Ciprofloxacin	1.19 (± 0.22)	17.2 (± 6.8)	5.94 (± 1.72)	—
Clofibric acid	27.5 (± 37.4)	0.927 (± 0.930)	4.95 (± 1.95)	0.376 (± 0.250)
DEET	—	1.21	4.95 (± 0.18)	—
Diazinon	4.95 (± 2.87)	2.95 (± 1.34)	8.70 (± 0.42)	—
Diclofenac	29.2 (± 8.6)	4.77 (± 1.16)	8.38 (± 1.25)	6.58 (± 4.00)
Diphenhydramine	12.5	0.388	6.26 (± 1.19)	—
Diuron	1.43 (± 0.41)	16.1 (± 0.4)	8.65 (± 5.73)	—
Doxycycline	0.803 (± 1.201)	48.4 (± 63.7)	4.62 (± 4.41)	—
E1	17.5 (± 24.7)	0.370 (± 0.036)	—	2.96

Table 2. (Continued)

TOrCs	$\Phi_{\text{TOrC-254}}$ $\times 10^{-2}$ mol/Ein	$\epsilon_{\text{TOrC-254}}$ $\times 10^3$ M ⁻¹ cm ⁻¹	$k_{\text{TOrC-}^*\text{OH}}$ $\times 10^9$ M ⁻¹ s ⁻¹	$\Phi_{\text{TOrC-sunlight}}$ $\times 10^{-2}$ mol/Ein
E2	5.50 (± 1.70)	0.403 (± 0.024)	9.70 (± 6.22)	0.480
E3	—	0.234	—	0.480
EE2	5.59 (± 1.95)	0.931 (± 1.193)	10.3 (± 0.7)	0.480
Fluoranthene	44.7	0.311	17.6	—
Gemfibrozil	—	3.45	10.0 (± 0.6)	—
Ibuprofen	13.9 (± 7.5)	0.269 (± 0.018)	6.86 (± 0.48)	0.023 (± 0.028)
Indomethacin	—	14.9	—	0.043 (± 0.006)
Iopromide	3.90 (± 0.40)	21.0 (± 0.2)	3.30 (± 0.60)	—
Ketoprofen	29.8 (± 8.7)	15.3 (± 0.2)	6.89 (± 2.14)	—
Linuron	1.86 (± 2.47)	13.4 (± 0.1)	4.30	—
MCPA	14.9	0.352	6.60	—
Mefenamic acid	0.470 (± 0.140)	5.07 (± 0.61)	11.0	0.008 (± 0.007)
Metolachlor	45.6 (± 21.8)	0.564 (± 0.086)	6.96 (± 2.00)	—
Metoprolol	3.47 (± 4.12)	0.565 (± 0.333)	7.51 (± 0.80)	—
Naproxen	2.77 (± 2.05)	4.00 (± 0.70)	8.86 (± 0.65)	3.10 (± 0.71)
Nonylphenol	24.3 (± 15.7)	0.400	11.0 (± 2.0)	0.300
Norfloxacin	0.340 (± 0.030)	16.0	1.00	4.30
Octylphenol	—	—	14.0 (± 2.0)	—
Phenanthrene	0.690 (± 0.050)	40.5	13.4	—
Phenol	2.55 (± 0.64)	0.750 (± 0.325)	8.57 (± 4.77)	—
Progesterone	2.20 (± 0.50)	17.0 (± 0.4)	0.850	—
Propachlor	12.7 (± 1.0)	0.421	4.45 (± 0.21)	—
Pyrene	0.385	18.2	—	—
Ranitidine	—	—	15.0 (± 2.0)	0.530
Roxithromycin	—	—	5.40 (± 0.30)	0.020

Table 2. (Continued)

TOrcs	$\Phi_{\text{TOrc-254}}$ $\times 10^{-2}$ mol/Ein	$\epsilon_{\text{TOrc-254}}$ $\times 10^3$ M ⁻¹ cm ⁻¹	$k_{\text{TOrc-}\cdot\text{OH}}$ $\times 10^9$ M ⁻¹ s ⁻¹	$\Phi_{\text{TOrc-sunlight}}$ $\times 10^{-2}$ mol/Ein
Simazine	8.30	3.33	2.45 (± 0.50)	—
Sulfamerazine	—	—	7.80 (± 0.30)	—
Sulfamethoxazole	3.62 (± 0.86)	13.9 (± 4.3)	5.81 (± 1.72)	79.0 (± 41.0)
Testosterone	12.9 (± 13.6)	15.1 (± 0.8)	—	4.15 (± 0.77)
Tetracycline	0.380	8.82 (± 6.66)	7.70 (± 1.20)	—
Triclosan	34.0 (± 7.0)	1.80	5.45 (± 0.06)	4.00
Trimethoprim	0.118 (± 0.011)	3.51 (± 0.80)	7.09 (± 1.49)	—

Note: For parameters with more than one literature value, averages and standard deviations (in parentheses) are reported.

Properties are reported at ambient or near-ambient conditions. An expanded version of this table with corresponding sources is presented in the supplementary materials (Tables S1 and S2)

Table 3. Properties used in AdDesignS™ for the 43 TOrcs in this study with available Freundlich isotherm constants, reported at ambient or near-ambient conditions.

TOrcs	Molar Volume m ³ /kmol	Boiling Point °C	Solubility mg/L	Vapor Pressure Pa	Freundlich Parameters K (mg/g)(L/mg) ^{1/n} 1/n	
1,4-DCB	0.133 ^a	174 ^b	8.13 × 10 ¹	2.32 × 10 ^{2d}	121	0.47
2,4-D	0.189 ^a	329	6.77 × 10 ²	1.10 × 10 ^{-2d}	43.9	0.34
Acetaminophen	0.121	341	1.40 × 10 ⁴	2.59 × 10 ⁻⁴	153	0.35
Anthracene	0.196 ^a	340 ^b	4.00 × 10 ⁻²	8.71 × 10 ^{-4d}	376	0.70
Atrazine	0.163	313	3.47 × 10 ¹	3.85 × 10 ^{-5d}	289	0.29
Benzo(a)pyrene	0.259 ^a	495 ^b	0.00 × 10 ⁰	7.32 × 10 ^{-7d}	33.6	0.44
Bezafibrate	0.287	538	1.22 × 10 ^{0c}	8.16 × 10 ⁻⁹	141	0.19
Bisphenol A	0.259 ^a	220 ^b	1.20 × 10 ²	3.03 × 10 ⁻⁵	20.7	0.18
Bromoxynil	0.124	329	1.30 × 10 ²	6.29 × 10 ^{-6d}	201	0.18
Caffeine	0.133	431	2.16 × 10 ⁴	9.77 × 10 ⁻⁷	239	0.04
Carbamazepine	0.187	410.	1.12 × 10 ²	1.17 × 10 ⁻⁵	430.	0.38
Carbofuran	0.187	311	3.20 × 10 ²	6.47 × 10 ^{-4d}	266	0.41
Chlorpyrifos	0.237	377	1.12 × 10 ⁰	2.71 × 10 ^{-3d}	11.3	0.70
Ciprofloxacin	0.227	567	3.00 × 10 ⁴	3.80 × 10 ⁻¹¹	32.2	0.45
Clofibric acid	0.170	321	5.83 × 10 ^{2c}	1.01 × 10 ⁻²	71.0	0.25
Diazinon	0.261	366	4.00 × 10 ¹	1.20 × 10 ^{-2d}	3.63	0.33
Diclofenac	0.207	424	2.37 × 10 ⁰	8.19 × 10 ⁻⁶	304	0.08
Diphenhydramine	0.249	345	3.06 × 10 ³	7.73 × 10 ⁻⁴	95.7	0.80
Diuron	0.179	354	4.20 × 10 ¹	9.20 × 10 ^{-6d}	279	0.22
E1	0.232	392	3.00 × 10 ¹	6.79 × 10 ⁻¹	610.	0.41
E2	0.233	395	3.90 × 10 ⁰	2.65 × 10 ⁻⁷	2.65	0.33
E3	0.230	432	4.41 × 10 ^{2c}	1.25 × 10 ⁻⁹	0.310	0.78

Table 3. (Continued)

TOrCs	Molar Volume m ³ /kmol	Boiling Point °C	Solubility mg/L	Vapor Pressure Pa	Freundlich Parameters K (mg/g)(L/mg) ^{1/n} 1/n	
EE2	0.245	411	1.13 × 10 ¹	2.60 × 10 ⁻⁷	2.15	0.28
Fluoranthene	0.162	384 ^b	2.60 × 10 ⁻¹	1.23 × 10 ^{-3d}	664	0.61
Ibuprofen	0.200	323	2.10 × 10 ¹	2.48 × 10 ⁻²	122	0.17
Iopromide	0.364	885	2.38 × 10 ^{1c}	2.12 × 10 ⁻²⁶	71.7	0.30
Ketoprofen	0.212	404	5.10 × 10 ¹	1.95 × 10 ⁻⁴	1.14	0.23
Linuron	0.185	366	7.50 × 10 ¹	1.91 × 10 ^{-4d}	159	0.23
MCPA	0.153	287 ^b	6.30 × 10 ²	7.87 × 10 ^{-4d}	29.5	0.29
Mefenamic acid	0.201	398	2.00 × 10 ¹	7.77 × 10 ⁻⁶	9.54	0.59
Metolachlor	0.258	282 ^b	5.30 × 10 ²	4.19 × 10 ^{-3d}	233	0.13
Naproxen	0.192	380.	1.59 × 10 ¹	1.69 × 10 ⁻⁴	12.1	0.37
Nonylphenol	0.236	295 ^b	6.35 × 10 ⁰	3.15 × 10 ^{-3d}	250.	0.37
Norfloxacin	0.237	553	1.78 × 10 ^{5c}	1.11 × 10 ⁻⁹	300.	0.17
Phenanthrene	0.196 ^a	340. ^b	1.15 × 10 ⁰	1.61 × 10 ^{-2d}	215	0.44
Phenol	0.088	182 ^b	8.28 × 10 ⁴	4.67 × 10 ^{1d}	21.0	0.54
Pyrene	0.210 ^a	404 ^b	1.40 × 10 ⁻¹	6.00 × 10 ^{-4d}	389	0.39
Ranitidine	0.265	415	2.47 × 10 ^{4c}	1.87 × 10 ⁻⁴	404	0.21
Simazine	0.148	307	6.20 × 10 ⁰	2.95 × 10 ^{-6d}	150.	0.23
Sulfamethoxazole	0.173	414	6.10 × 10 ²	1.73 × 10 ⁻⁵	227	0.22
Tetracycline	0.270	745	2.31 × 10 ²	2.77 × 10 ⁻¹⁹	105	0.56
Triclosan	0.194	374	1.00 × 10 ¹	6.20 × 10 ⁻⁴	3.03	0.62
Trimethoprim	0.221	449	4.00 × 10 ²	1.00 × 10 ⁻⁶	142	0.18

Note: An expanded version of this table with corresponding sources is presented in the supplementary materials (Table S3)

^aMolar volume values were obtained from Software to Estimate Physical Properties in ETDOT10 package.

^bBoiling point values (1 atm) used experiment data provided by EPI Suite™.

^cWater solubility values were estimated by WSKOW v1.41 program in the EPI Suite™ at room temperature.

^dVapor pressure values used experimental data provided by EPI Suite™ at room temperature.

Table 4. Molecular structures for 20 TOrCs with at least five reported values of membrane rejections during RO treatment that were accompanied by NaCl rejection data

TOrCs	Length nm	Thickness nm
Acetaminophen	0.933	0.186
Atrazine	1.21	0.228
Bisphenol A	1.23	0.220
Caffeine	0.819	0.186
Carbamazepine	1.03	0.207
DEET	1.09	0.187
Diclofenac	1.08	0.329
E1	1.18	0.316
E2	1.16	0.315
E3	1.21	0.377
EE2	1.26	0.605
Gemfibrozil	1.27	0.438
Ibuprofen	1.14	0.228
Ketoprofen	1.34	0.315
Mefenamic acid	1.08	0.186
Naproxen	1.27	0.332
Progesterone	1.27	0.376
Simazine	1.21	0.186
Sulfamethoxazole	1.40	0.290
Trimethoprim	1.31	0.218

Note: Geometric parameters were estimated using Materials Studio 4.0. Molecular length is the maximum distance between any two atoms in a single compound. Molecular thickness is the maximum distance between any two atoms on planes perpendicular to the direction of molecular length. An expanded version of this table for all 55 TOrCs, including molecular structures, is presented in the supplementary information (Figures S1 to S10).

Table 5. Summary of input/output characteristics of BioWin Models

Version	Description							Classification Accuracy for Validation Set Chemicals ^a
	O ₂ Condition	Output Data	Output Classification	Training Set	Regression Method	Independent Variables	Model Algorithm	
BioWin1	Aerobic	Probability of rapid biodegradation	≥ 0.5 Biodegrades fast < 0.5 Does NOT biodegrade fast	Database consisted of results from 4 types of test method-specific records for 186 chemicals evaluated as “biodegrades fast” and 109 chemicals as “does not biodegrade fast”	Linear (least squares)	36 substructures + molecular weight	$Y_j = a_0 + \sum_{n=1}^{36} a_n f_n + a_m M_w + e_j$ $= \begin{cases} 1, & \text{if biodegrades fast} \\ 0, & \text{if does not biodegrade fast} \end{cases}$	54% (165/305)
BioWin2	Aerobic	Probability of rapid biodegradation	≥ 0.5 Biodegrades fast < 0.5 Does NOT biodegrade fast	Database consisted of results from 4 types of test method-specific records for 186 chemicals evaluated as “biodegrades fast” and 109 chemicals as “does not biodegrade fast”	Non-linear (maximum likelihood)	36 substructures + molecular weight	$Y_j = \frac{\exp(a_0 + \sum_{n=1}^{36} a_n f_n + a_m M_w)}{1 + \exp(a_0 + \sum_{n=1}^{36} a_n f_n + a_m M_w)}$ $= \begin{cases} 1, & \text{if biodegrades fast} \\ 0, & \text{if does not biodegrade fast} \end{cases}$	67% (203/305)
BioWin3	Aerobic	Ultimate biodegradation rates	5.0 hours; 4.0 days; 3.0 weeks; 2.0 months; 1.0 longer	Time required for ultimate (transformation to CO ₂ and H ₂ O) biodegradation of 200 chemicals on scales (hours = 5, days = 4, weeks = 3, months = 2, longer = 1) scored by 17 experts from survey study	Linear (least squares)	36 substructures + molecular weight	$Y_j = a_0 + \sum_{n=1}^{36} a_n f_n + a_m M_w + e_j$	87% (265/305)

BioWin4	Aerobic	Primary biodegradation rates	5.0 hours; 4.0 days; 3.0 weeks; 2.0 months; 1.0 longer	Time required for primary (initial metabolic step) biodegradation of 200 chemicals on scales (hours = 5, days = 4, weeks = 3, months = 2, longer = 1) scored by 17 experts from survey study	Linear (least squares)	36 substructures + molecular weight	$Y_j = a_0 + \sum_{n=1}^{36} a_n f_n + a_m M_w + e_j$	83% (253/305)
BioWin5	Aerobic	Probability of ready biodegradability	≥ 0.5 Readily degradable < 0.5 Not readily degradable	Database consisted of results from MITI test for 254 chemicals evaluated as “readily biodegradable” and 335 chemicals as “not readily biodegradable”	Linear (least squares)	42 substructures + molecular weight	$Y_j = a_0 + \sum_{n=1}^{42} a_n f_n + a_m M_w + e_j$ $= \begin{cases} 1, & \text{if readily biodegradable} \\ 0, & \text{if not readily biodegradable} \end{cases}$	83% (252/305)
BioWin6	Aerobic	Probability of ready biodegradability	≥ 0.5 Readily degradable < 0.5 Not readily degradable	Database consisted of results from MITI test for 254 chemicals evaluated as “readily biodegradable” and 335 chemicals as “not readily biodegradable”	Non-linear (maximum likelihood)	42 substructures + molecular weight	$Y_j = \frac{\exp(a_0 + \sum_{n=1}^{42} a_n f_n + a_m M_w)}{1 + \exp(a_0 + \sum_{n=1}^{42} a_n f_n + a_m M_w)}$ $= \begin{cases} 1, & \text{if readily biodegradable} \\ 0, & \text{if not readily biodegradable} \end{cases}$	83% (254/305)
BioWin7	Anaerobic	Probability for methanogenic biodegradation	≥ 0.5 Biodegrades fast < 0.5 Does not Biodegrade fast	Results from serum bottle test for 82 chemicals evaluated as “pass” and 87 chemicals as “fail”	Linear (least squares)	37 substructures	$Y_j = a_0 + \sum_{n=1}^{37} a_n f_n + e_j$ $= \begin{cases} 1, & \text{if serum bottle test pass} \\ 0, & \text{if serum bottle test not pass} \end{cases}$	89.9% (152/169)

^aValidation set applied for classification accuracy test was described by Boethling et al. (2003) for the first six BioWin models (BioWin1 to BioWin6); and Meylan et al. (2007) for BioWin7.

Table 6. Summary of reactions and related parameters used to simulate UV₂₅₄-based treatment performance of TOrCs

Reaction ID	Reaction	Kinetic Parameters	Reference
R1	$\text{H}_2\text{O}_2 + \text{h}\nu \rightarrow 2 \text{ }^*\text{OH}$	$\epsilon_{\text{H}_2\text{O}_2-254} = 18.7 \text{ M}^{-1}\text{cm}^{-1}$ $\Phi_{\text{H}_2\text{O}_2-254} = 0.5 \text{ mol/Ein}$	Volman and Chen (1959)
R2	$\text{}^*\text{OH} + \text{H}_2\text{O}_2 \rightarrow \text{O}_2^{\bullet-} + \text{H}_2\text{O} + \text{H}^+$	$k_2 = 2.7 \times 10^7 \text{ M}^{-1}\text{s}^{-1}$	Buxton et al. (1988)
R3	$\text{}^*\text{OH} + \text{HO}_2^- \rightarrow \text{O}_2^{\bullet-} + \text{H}_2\text{O}$	$k_3 = 7.5 \times 10^9 \text{ M}^{-1}\text{s}^{-1}$	Buxton et al. (1988)
R4	$\text{}^*\text{OH} + \text{HO}_2^* \rightarrow \text{O}_2 + \text{H}_2\text{O}$	$k_6 = 6.6 \times 10^9 \text{ M}^{-1}\text{s}^{-1}$	Buxton et al. (1988)
R5	$\text{}^*\text{OH} + \text{O}_2^{\bullet-} \rightarrow \text{O}_2 + \text{OH}^-$	$k_7 = 8.0 \times 10^9 \text{ M}^{-1}\text{s}^{-1}$	Buxton et al. (1988)
R6	$\text{}^*\text{OH} + \text{}^*\text{OH} \rightarrow \text{H}_2\text{O}_2$	$k_8 = 5.5 \times 10^9 \text{ M}^{-1}\text{s}^{-1}$	Buxton et al. (1988)
R7	$\text{O}_2^{\bullet-} + \text{H}_2\text{O}_2 \rightarrow \text{}^*\text{OH} + \text{O}_2 + \text{OH}^-$	$k_{10} = 0.13 \text{ M}^{-1}\text{s}^{-1}$	Bielski et al. (1985)
R8	$\text{O}_2^{\bullet-} + \text{HO}_2^* \rightarrow \text{HO}_2^- + \text{O}_2$	$k_{12} = 9.7 \times 10^7 \text{ M}^{-1}\text{s}^{-1}$	Bielski et al. (1985)
R9	$\text{HO}_2^* + \text{HO}_2^* \rightarrow \text{H}_2\text{O}_2 + \text{O}_2$	$k_{13} = 8.6 \times 10^5 \text{ M}^{-1}\text{s}^{-1}$	Weinstein and Bielski (1979)
R10	$\text{HO}_2^* + \text{H}_2\text{O}_2 \rightarrow \text{}^*\text{OH} + \text{O}_2 + \text{H}_2\text{O}$	$k_{14} = 3.7 \text{ M}^{-1}\text{s}^{-1}$	Bielski et al. (1985)
R11	$\text{H}_2\text{O}_2 \leftrightarrow \text{HO}_2^- + \text{H}^+$	$k_{18} = 2.51 \times 10^{-2} \text{ s}^{-1}$ $k_{18r} = 1 \times 10^{10} \text{ M}^{-1}\text{s}^{-1}$	Perry et al. (1984)
R12	$\text{HO}_2^* \leftrightarrow \text{O}_2^{\bullet-} + \text{H}^+$	$k_{19} = 1.58 \times 10^5 \text{ s}^{-1}$ $k_{19r} = 1 \times 10^{10} \text{ M}^{-1}\text{s}^{-1}$	Perry et al. (1984)
R13	$\text{TOrC} + \text{h}\nu \rightarrow \text{products}$	$\epsilon_{\text{TOrC-254}}$ $\Phi_{\text{TOrC-254}}$	Table 2
R14	$\text{TOrC} + \text{}^*\text{OH} \rightarrow \text{products}$	$k_{\text{TOrC-}^*\text{OH}}$	Table 2
R15	$\text{EBC} + \text{}^*\text{OH} \rightarrow \text{products}$	$k_{\text{EBC-}^*\text{OH}} = 8.6 \times 10^8 \text{ M}^{-1}\text{s}^{-1}$	Rosario-Ortiz et al. (2008)

Note: Average values of $\epsilon_{\text{TOrC-254}}$, $\Phi_{\text{TOrC-254}}$ and $k_{\text{TOrC-}^*\text{OH}}$ from Table 2 were used in modeling.

Table 7. Summary of treatment efficiency of different processes investigated in this study on attenuating TORCs

TORCs	Conventional activated sludge process ^a	UV254 photolysis	UV/H ₂ O ₂ AOP	Activated carbon	RO/NF	Direct sunlight photolysis
	Levels of influent-to-effluent removal of TORCs observed with > 80% frequency (%)	Predicted liquid removal (%)	Predicted liquid removal (%)	Bed volumes to breakthrough	Rejection (%) at 50% rejection of NaCl	Predicted liquid removal (%)
1,4—DCB	—	11	16	1.56×10^5	42 ^b	—
2,4—D	—	0	3	2.76×10^4	51 ^b	—
Acetaminophen	86	4	11	2.04×10^5	0	100
Anthracene	—	22	26	1.12×10^5	38 ^b	—
Atrazine	—	23	25	1.16×10^5	55	—
Benzo(a)pyrene	—	24	37	7.14×10^4	38 ^b	—
Benzophenone	67	—	—	—	0 ^b	—
Bezafibrate	49	—	—	2.69×10^5	84 ^b	—
Bisphenol A	69	1	6	1.01×10^5	36	—
Bromoxynil	—	27	31	1.37×10^5	0 ^b	—
Caffeine	84	1	6	7.10×10^5	70	—
Carbamazepine	3	1	5	3.72×10^5	77	0
Carbofuran	—	2	3	6.30×10^4	86 ^b	—
Chlorpyrifos	—	2	5	7.14×10^3	80 ^b	—
Ciprofloxacin	11	27	31	4.20×10^4	81 ^b	—
Clofibric acid	5	33	35	2.18×10^5	86 ^b	—
DEET	—	—	—	—	71	—
Diazinon	—	21	25	2.35×10^3	82 ^b	—
Diclofenac	5	89	89	6.07×10^5	91	26

Table 7. (Continued)

TOrcs	Conventional activated sludge process	UV254 photolysis	UV/H ₂ O ₂ AOP	Activated carbon	RO/NF	Direct sunlight photolysis
	Levels of influent-to- effluent removal of TOrcs observed with > 80% frequency (%)	Predicted liquid removal (%)	Predicted liquid removal (%)	Bed volumes to breakthrough	Rejection (%) at 50% rejection of NaCl	Predicted liquid removal (%)
Diphenhydramine	—	7	12	1.74×10^4	86 ^b	—
Diuron	—	30	35	6.36×10^4	50 ^b	—
Doxycycline	—	46	47	—	89 ^b	—
E1	45	10	—	3.82×10^5	81	5
E2	45	3	10	2.42×10^4	91	22
E3	78	—	—	1.95×10^2	71	—
EE2	45	8	15	2.51×10^4	92	12
Fluoranthene	—	20	29	2.19×10^5	38 ^b	—
Gemfibrozil	36	—	—	—	81	—
Ibuprofen	70	6	10	2.67×10^5	68	1
Indomethacin	11	—	—	—	83 ^b	21
Iopromide	—	73	73	7.37×10^4	88 ^b	—
Ketoprofen	30	100	100	1.35×10^4	94	—
Linuron	—	32	34	9.31×10^4	50 ^b	—
MCPA	—	8	12	2.85×10^4	50 ^b	—
Mefenamic acid	—	4	11	1.31×10^4	67	3
Metolachlor	—	33	36	1.44×10^5	86 ^b	—
Metoprolol	—	3	8	—	64 ^b	—
Naproxen	55	16	21	4.86×10^4	97	39
Nonylphenol	45	14	21	1.78×10^5	50 ^b	0

Table 7. (Continued)

TOrcs	Conventional activated sludge process	UV254 photolysis	UV/H ₂ O ₂ AOP	Activated carbon	RO/NF	Direct sunlight photolysis
	Levels of influent-to- effluent removal of TOrcs observed with > 80% frequency (%)	Predicted liquid removal (%)	Predicted liquid removal (%)	Bed volumes to breakthrough	Rejection (%) at 50% rejection of NaCl	Predicted liquid removal (%)
Norfloxacin	31	8	9	4.22×10^5	67 ^b	100
Octylphenol	53	—	—	—	50 ^b	—
Phenanthrene	—	36	41	2.25×10^5	38 ^b	—
Phenol	—	3	9	5.09×10^4	38 ^b	—
Progesterone	—	45	45	—	95	—
Propachlor	—	8	11	—	67 ^b	—
Pyrene	—	10	—	3.57×10^5	38 ^b	—
Ranitidine	22	—	—	3.76×10^5	50 ^b	86
Roxithromycin	21	—	—	—	93 ^b	36
Simazine	—	35	36	1.06×10^5	43	—
Sulfamerazine	—	—	—	—	79 ^b	—
Sulfamethoxazole	26	55	56	2.82×10^5	57	100
Testosterone	72	95	—	—	86 ^b	9
Tetracycline	52	5	10	7.12×10^4	94 ^b	—
Triclosan	50	62	63	4.14×10^3	20 ^b	4
Trimethoprim	18	1	6	2.35×10^5	81	—

^aData from Rojas et al. 2013.

^bEvaluation based on calculated compound rejection.

Table 8. Summary of treatment evaluation of different processes investigated

Unit Operation	Index	Determinants of process efficiency level		
		High	Medium	Low
Conventional activated sludge process	Influent-to-effluent removal (%)	> 75	25–75	< 25
UV254 Photolysis	Predicted liquid removal (%)	> 75	25–75	< 25
UV/H ₂ O ₂ AOP	Predicted liquid removal (%)	> 75	25–75	< 25
Activated carbon	Bed volumes fed to breakthrough	> 10 ⁵	10 ⁴ –10 ⁵	< 10 ⁴
RO/NF	Compound rej. @ NaCl Rej. = 50%	> 75	25–75	< 25
Sunlight photolysis	Predicted liquid removal (%)	> 75	25–75	< 25

Note: For compounds without enough reported data, their rejection percentages at NaCl rejection = 50% were calculated using Eq (15) based on compound molecular thickness data, which is provided in Figs. S1 to S10.

Table 9. Scoring system of semi—quantitative estimation for TOrCs removal efficiencies of proposed treatment sequence (i): conventional secondary treatment, UV/H₂O₂ AOP and activated carbon, and (ii): conventional secondary treatment, UV/H₂O₂ AOP, activated carbon and RO/NF

TOrCs	Final Score	
	Sequence (i)	Sequence (ii)
Acetaminophen	4	4
Bisphenol A	3	4
Caffeine	4	5
Carbamazepine	2	4
Ciprofloxacin	2	4
Clofibric acid	3	5
Diclofenac	4	6
E2	2	4
EE2	2	4
Ibuprofen	3	4
Ketoprofen	4	6
Naproxen	2	4
Nonylphenol	3	4
Norfloxacin	3	4
Sulfamethoxazole	4	5
Tetracycline	2	4
Triclosan	2	2
Trimethoprim	2	4

Figure Captions

Fig. 1. Predicted semi-quantitative biodegradation indices (BioWin4) for 55 TOrCs. TOrC IDs in this and following figures are summarized in Table 1. The number designations for specific TOrCs in Fig. 1 are preserved throughout the paper.

Fig. 2. Calculated BioWin4 biodegradation indices as a function of $\log D_{ow}$. Compound IDs correspond to those in Fig. 1. The Spearman correlation coefficient (ρ) is shown.

Fig. 3. Relationship between levels of removal of TOrCs observed with > 80% frequency (from Rojas et al. 2013) as a function of the BioWin4 (bioremediation) index. Only TOrCs with $\log D_{ow} < 3.5$ were considered to minimize the effect of sorptive removal. The Spearman correlation coefficient (ρ) is shown. Data correspond to measurements from full-scale wastewater treatment plants.

Fig. 4. Predicted influent-to-effluent removal of 45 TOrCs in pure water and secondary effluent by direct photolysis during UV-254 treatment. Conditions for the simulation were as indicated in the Methods section. In all cases, $[TOrCs]_o = 10$ nM.

Fig. 5. Predicted UV-254 direct photolysis removals of TOrCs at 10 nM initial concentration in secondary effluent as a function of compound-specific molar absorptivity and quantum yield at 254 nm. Simulation results for specific TOrCs are as shown. Compound identities are indicated by number as described in Fig. 1. Conditions for the simulations are described in the Methods section.

Fig. 6. Residual (fractional) concentrations of 45 TOrCs from simulations of direct UV-254 photolysis under representative conditions in clean water and treated wastewater. The solid and dashed lines were generated using Eq (12) and Eq (14), respectively.

Fig. 7. Predicted fractional TOrC attenuations during UV/H₂O₂ for 42 TOrCs with reported $\Phi_{TOrC-254}$, $\epsilon_{TOrC-254}$ and $k_{TOrC-\cdot OH}$ values in three different matrices: PW = pure water, SE = secondary effluent, HSE effluent w/o shading = hypothetical secondary effluent neglecting light shading effect. Operating conditions are representative of practice: commercial size PFR with low pressure UV, 30 s residence time, $[TOrCs]_o = 10$ nM, $[H_2O_2]_o = 5$ ppm (Methods section).

Fig. 8. AdDesignSTM (PSDM) predicted BVF to breakthrough for TOrCs in organic free water versus compound-specific $\log D_{ow}$ values (Table 1). The Spearman correlation coefficient (ρ) for the hypothesized relationship is shown.

Fig. 9. Calculated BVF to breakthrough using AdDesignSTM (PSDM) for 43 TOrCs in either organic free water—i.e. without fouling, or Rhine River (Germany) water with anthropogenic input. Both are options within “Fouling of GAC” of the PSDM. In all cases, $[TOrCs]_o = 10$ nM.

Fig. 10. Relationship between TOrC and NaCl rejections for specific TOrCs. Examples include TOrCs with molecule thickness < 2.5 nm: atrazine and bisphenol A; and thickness > 0.3

nm: EE2 and ketoprofen. Compound thicknesses, as defined in the text, are in parentheses. Solid lines are linear fit of the data. Similar analyses for other compounds are provided in Fig. S1—S5.

Fig. 11. NF/RO rejections of individual TOrCs under conditions that resulted in 50% rejection of NaCl. Compounds analyzed in this fashion were limited to the 20 TOrCs for which sufficient experimental data were available (Methods section).

Fig. 12. Compound rejection under conditions for which NaCl rejection = 50% versus molecule thickness. Solid line is a fit of the experimental data shown.

Fig. 13. Predicted removals of 17 TOrCs in pure water and wastewater effluent due to direct photolysis in sunlight. The assumed period of exposure is 8 hours. Other conditions in the simulations were as indicated in the Methods section.

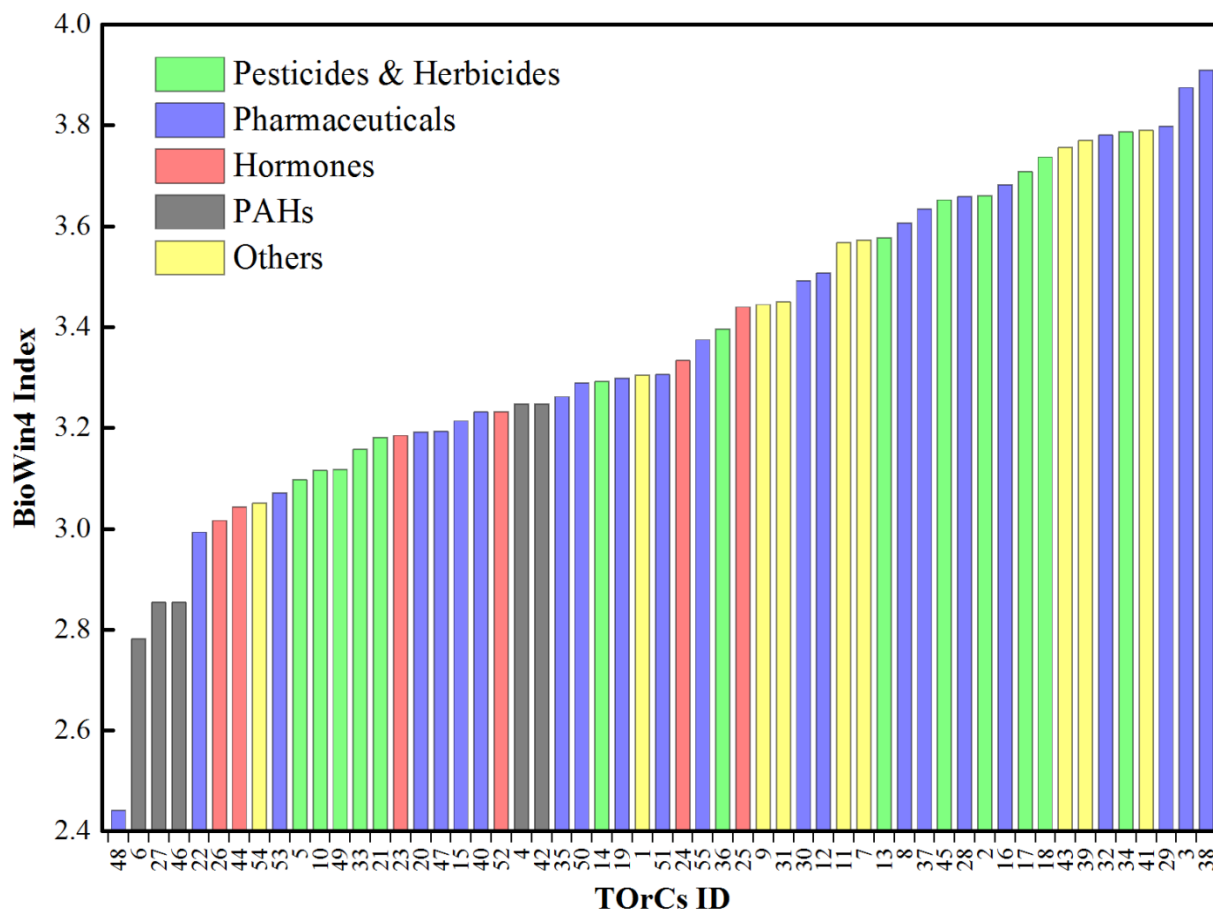


Fig. 1. Predicted semi-quantitative biodegradation indices (BioWin4) for 55 TOxCs: Index values for primary biodegradation indicate primary degradation times as follows: 5.00 → hours, 4.00 → days, 3.00 → weeks, 2.00 → months. TOxC IDs in this and following figures are:

1	1,4-DCB	12	Carbamazepine	23	E1	34	MCPA	45	Propachlor
2	2,4-D	13	Carbofuran	24	E2	35	Mefenamic acid	46	Pyrene
3	Acetaminophen	14	Chlorpyrifos	25	E3	36	Metolachlor	47	Ranitidine
4	Anthracene	15	Ciprofloxacin	26	EE2	37	Metoprolol	48	Roxithromycin
5	Atrazine	16	Clofibric acid	27	Fluoranthene	38	Naproxen	49	Simazine
6	Benzo(a)pyrene	17	DEET	28	Gemfibrozil	39	Nonylphenol	50	Sulfamerazine
7	Benzophenone	18	Diazinon	29	Ibuprofen	40	Norfloracin	51	Sulfamethoxazole
8	Bezafibrate	19	Diclofenac	30	Indomethacin	41	Octylphenol	52	Testosterone
9	Bisphenol A	20	Diphenhydramine	31	Iopromide	42	Phenanthrene	53	Tetracycline

10	Bromoxynil	21	Diuron	32	Ketoprofen	43	Phenol	54	Triclosan
11	Caffeine	22	Doxycycline	33	Linuron	44	Progesterone	55	Trimethoprim

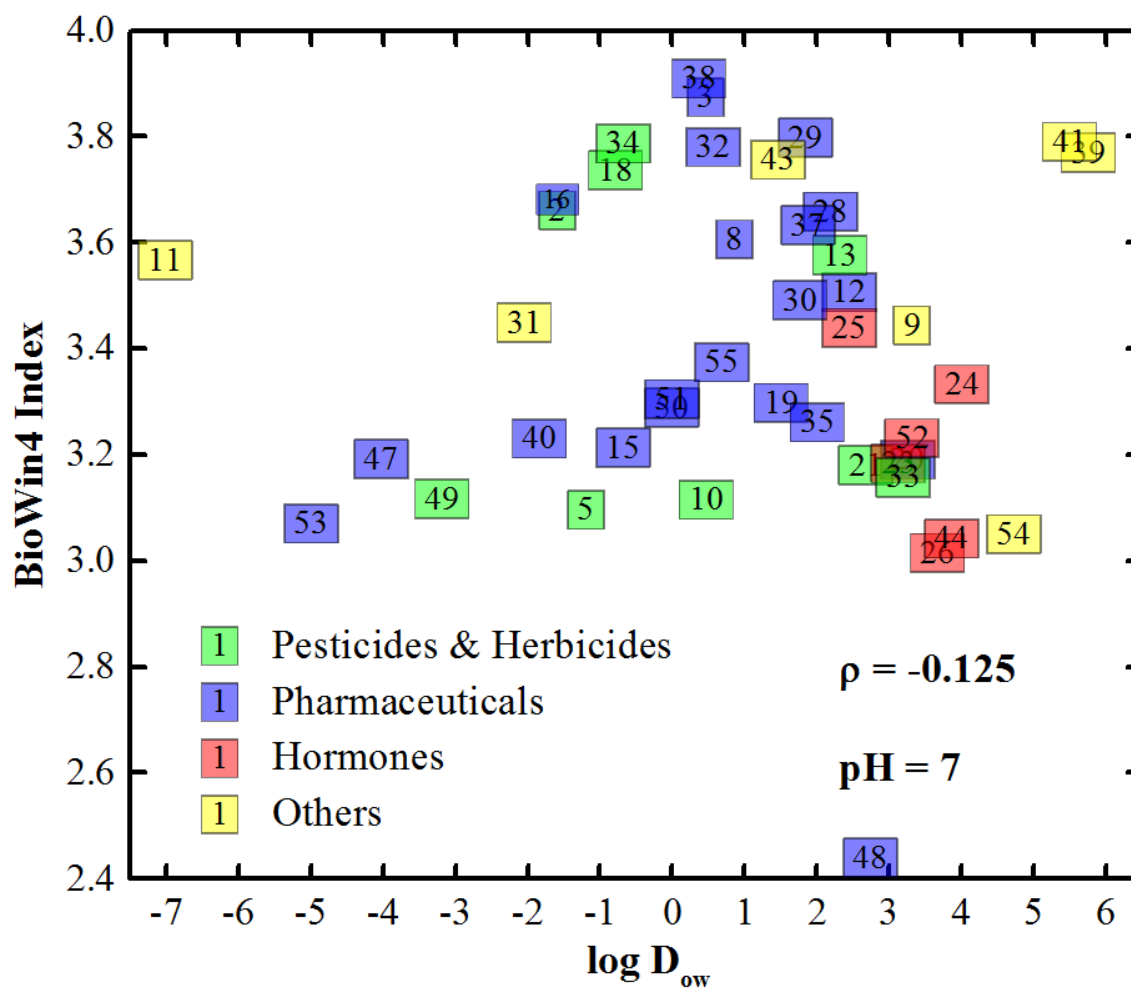


Fig. 2. Calculated BioWin4 biodegradation indices as a function of log D_{ow}. Compound IDs correspond to those in Fig. 1. The Spearman correlation coefficient (ρ) is shown.

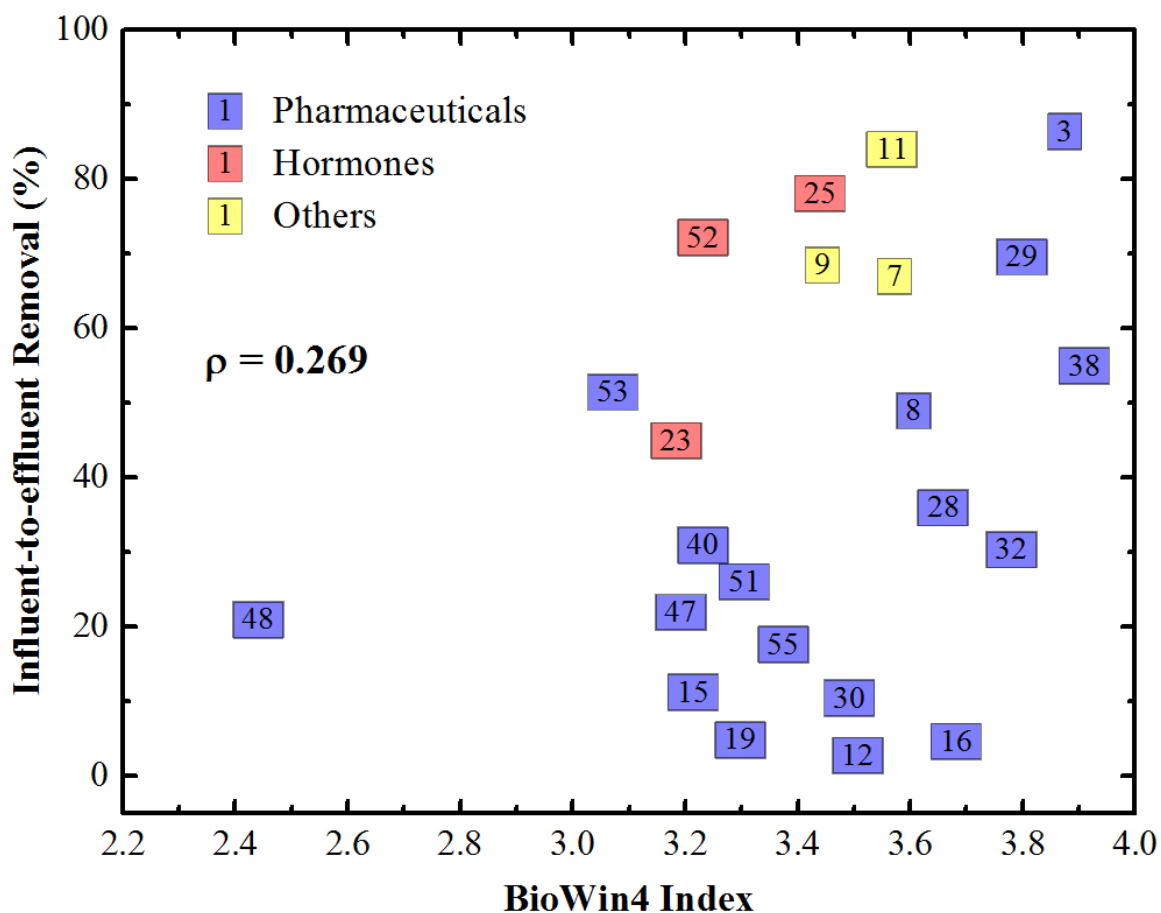


Fig. 3. Relationship between levels of removal of TOrCs observed with > 80% frequency (from Rojas et al. 2013) as a function of the BioWin4 (bioremediation) index. Only TOrCs with $\log D_{ow} < 3.5$ were considered to minimize the effect of sorptive removal. The Spearman correlation coefficient (ρ) is shown.

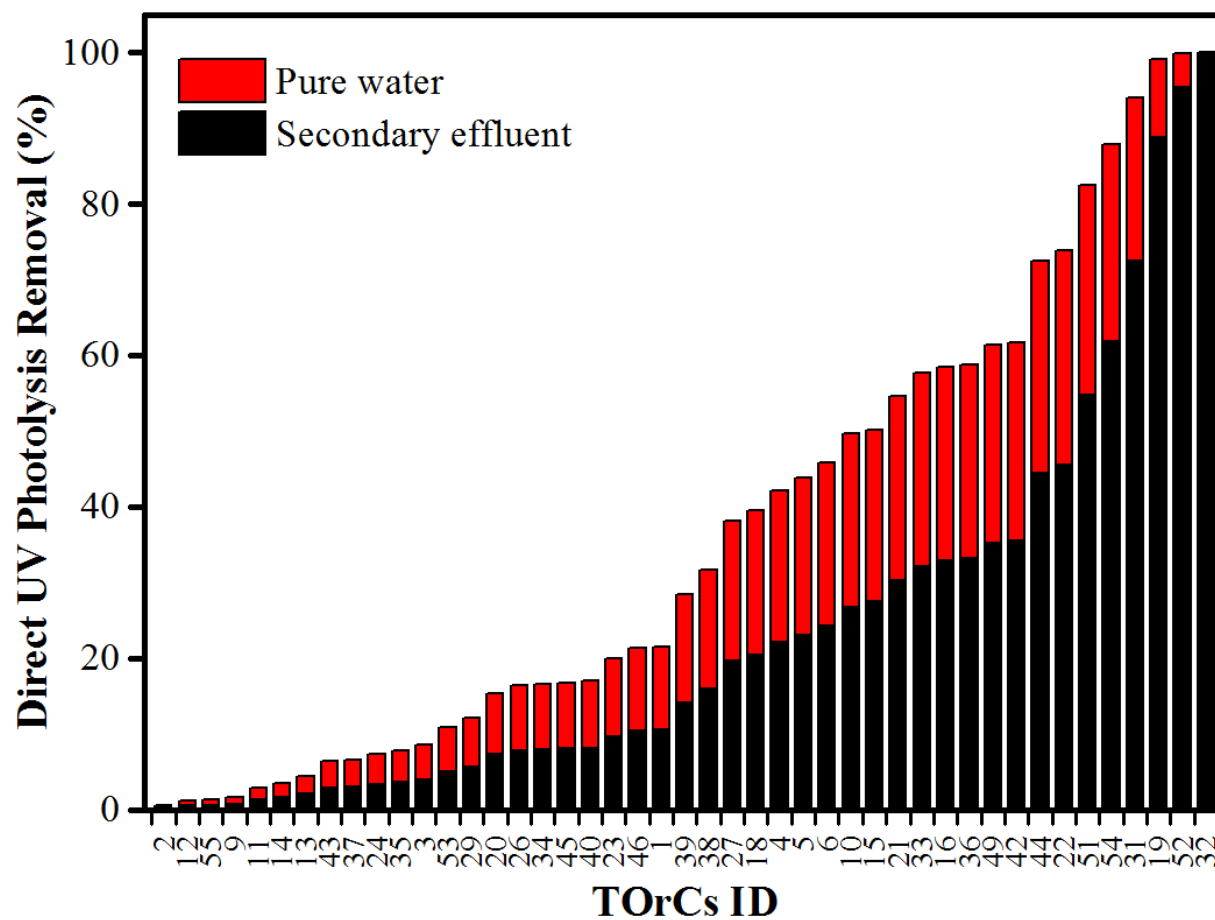


Fig. 4. Predicted influent-to-effluent removal of 45 TOrcs in pure water and secondary effluent by direct photolysis during UV-254 treatment. Conditions for the simulation were as indicated in the Methods section. In all cases, $[\text{TOrcs}]_0 = 10 \text{ nM}$.

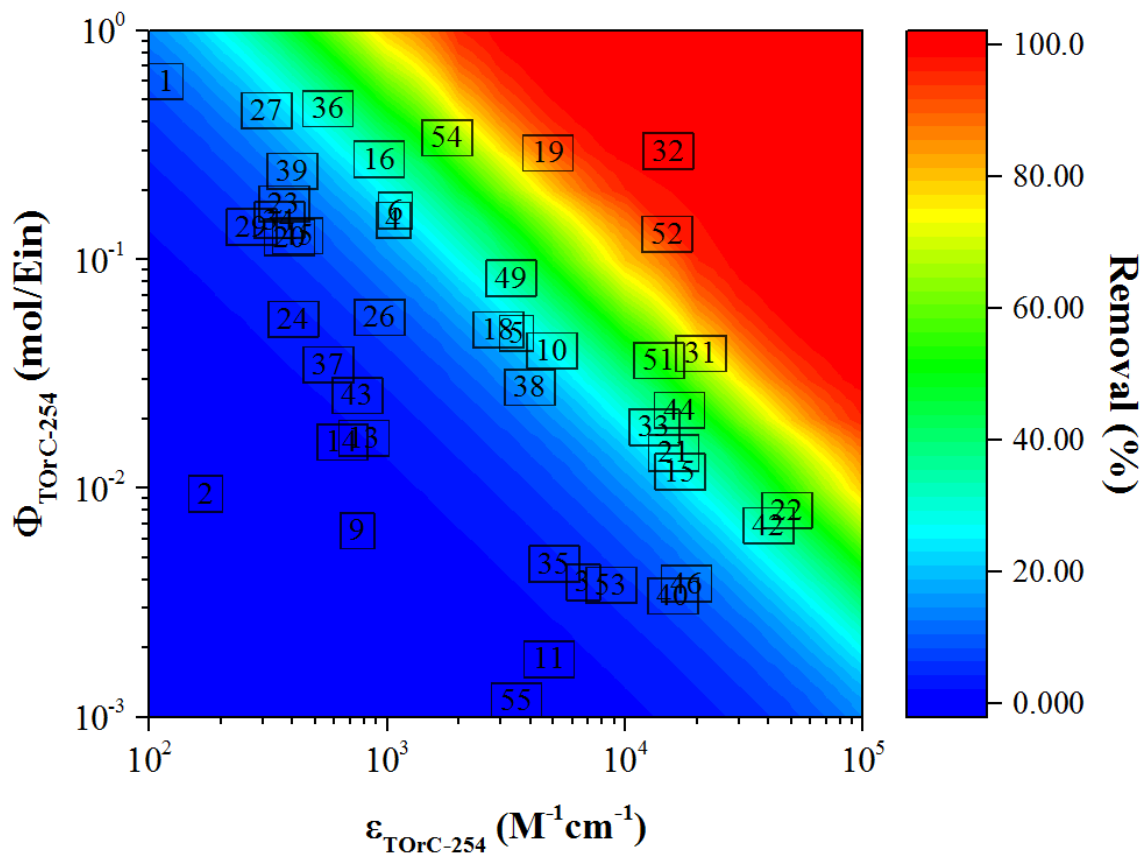


Fig. 5. UV-254 direct photolysis removals of TOxCs at 10 nM initial concentration in secondary effluent as a function of compound-specific molar absorptivity and quantum yield at 254 nm. Simulation results for specific TOxCs are as shown. Compound identities are indicated by number as described in Fig. 1. Conditions for the simulations are described in the Methods section.

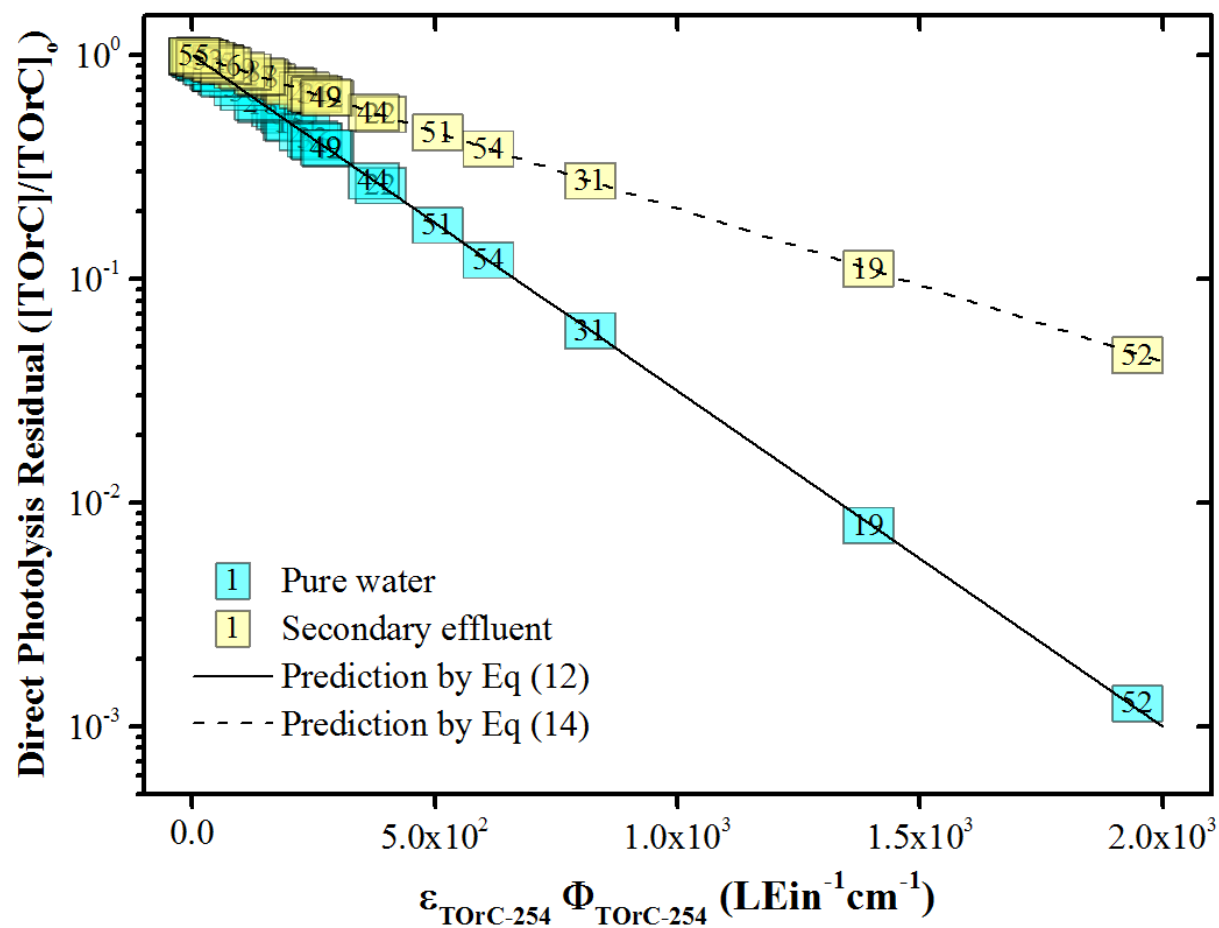


Fig. 6. Residual (fractional) concentrations of 45 TOrCs during simulation of direct UV-254 photolysis under representative conditions in clean water and treated wastewater. The solid and dashed lines were generated using Eq (12) and Eq (14), respectively.

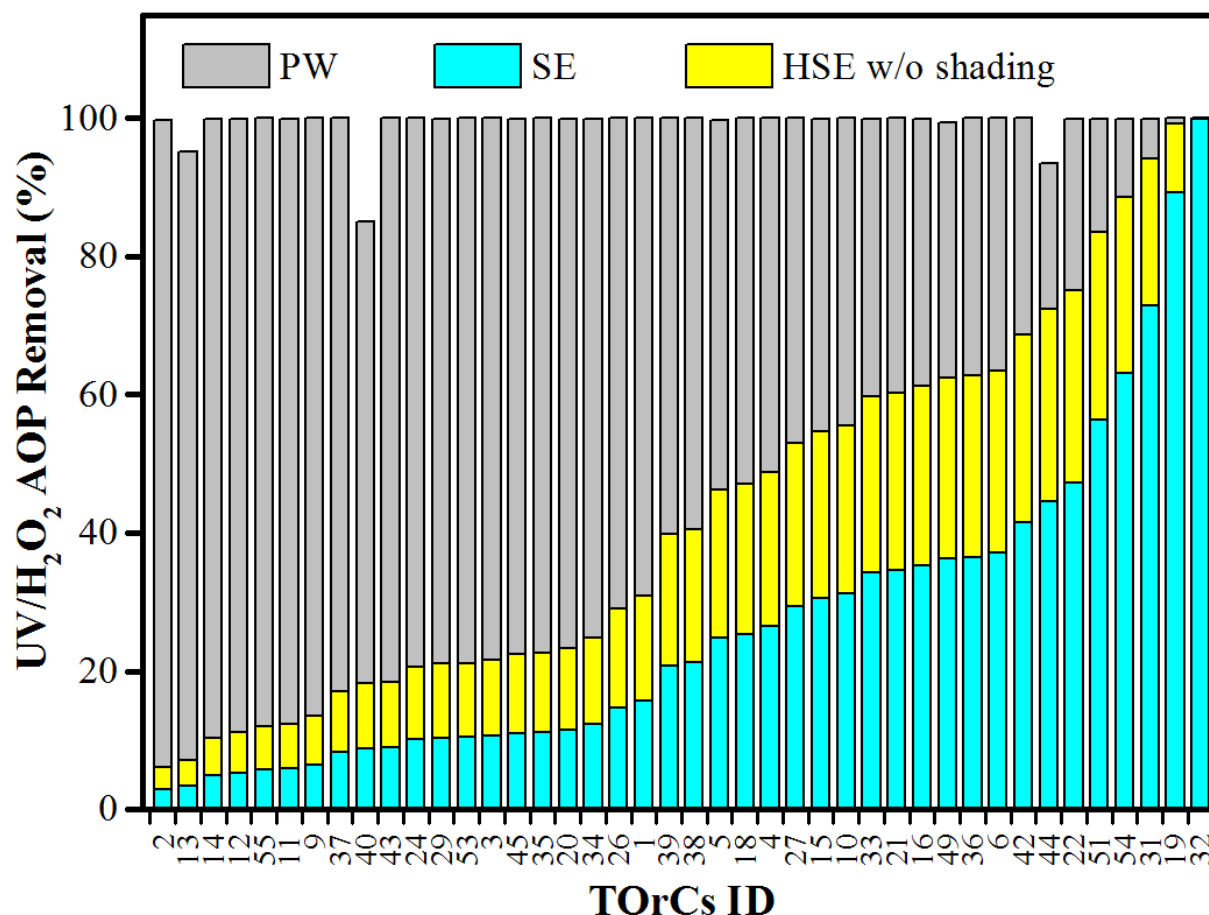


Fig. 7. Predicted fractional TOxC attenuations during UV/H₂O₂ for 42 TOxCs with reported $\Phi_{\text{TOxC-254}}$, $\epsilon_{\text{TOxC-254}}$ and $k_{\text{TOxC} \cdot \text{OH}}$ values in three different matrices: PW = pure water, SE = secondary effluent, HSE effluent w/o shading = hypothetical secondary effluent neglecting light shading effect. Operating conditions are representative of practice: commercial size PFR with low pressure UV, 30 s residence time, $[\text{TOxCs}]_0 = 10 \text{ nM}$, $[\text{H}_2\text{O}_2]_0 = 5 \text{ ppm}$ (Methods section).

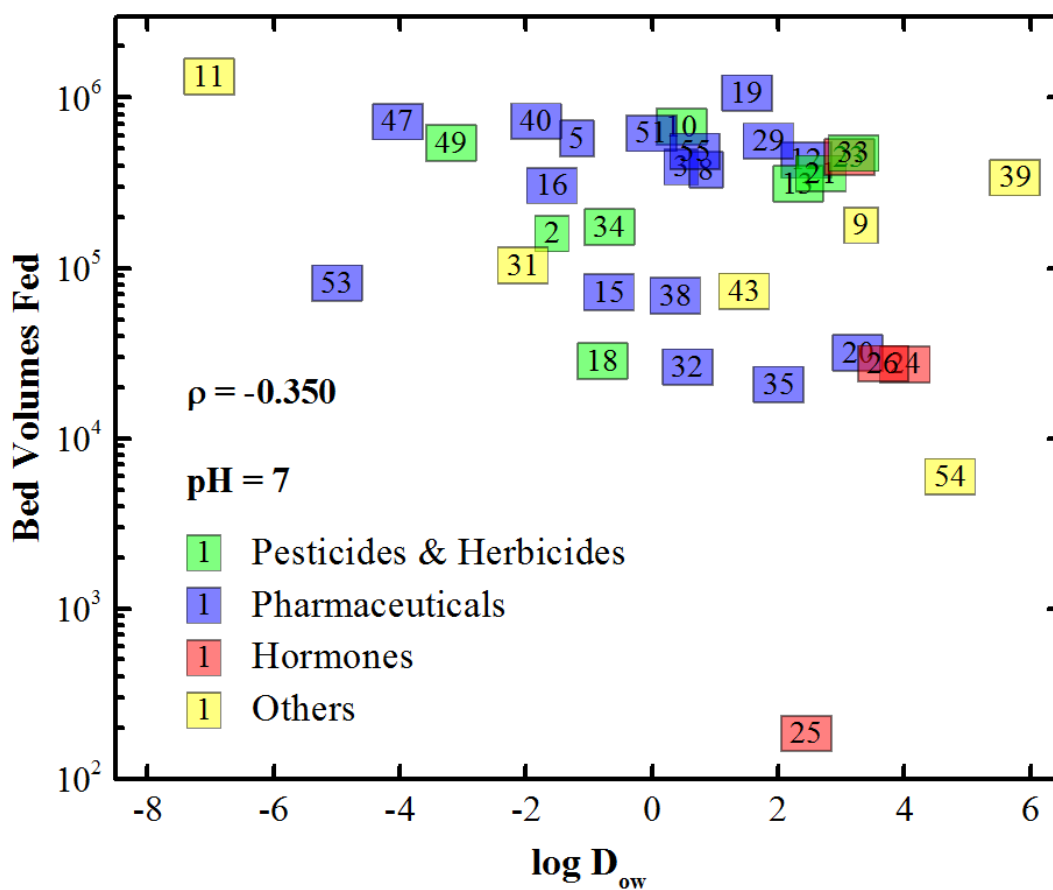


Fig. 8. AdDesignSTM (PSDM) predicted BVF to breakthrough for TORCs in organic free water versus compound-specific log D_{ow} values (Table 1). The Spearman correlation coefficient (ρ) for the hypothesized relationship is shown.

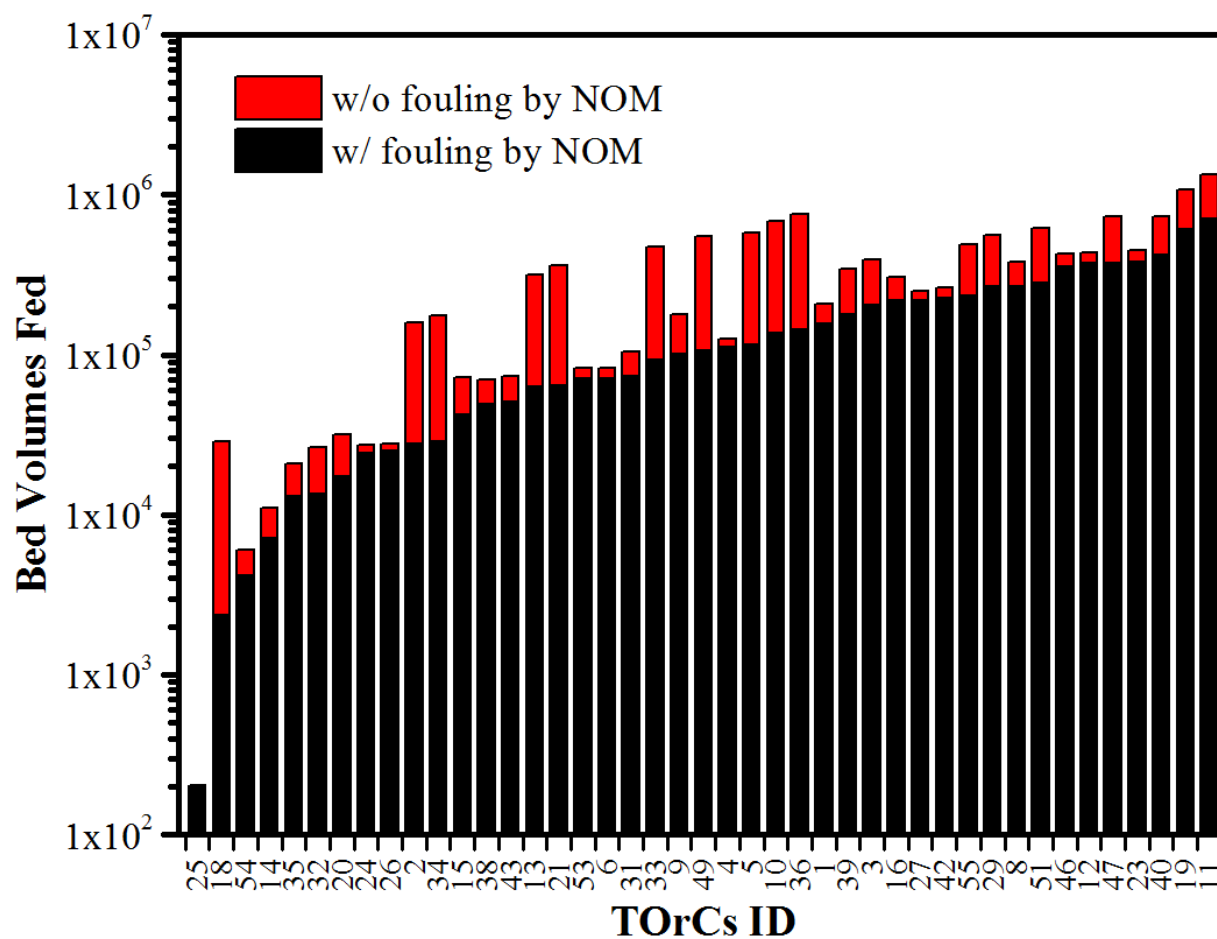


Fig. 9. Calculated BVF to breakthrough using AdDesignS™ (PSDM) for 43 TOrCs in either organic free water—i.e. without fouling, or Rhine River (Germany) water with anthropogenic input. Both are options within “Fouling of GAC” of the PSDM. In all cases, $[\text{TOrCs}]_0 = 10 \text{ nM}$.

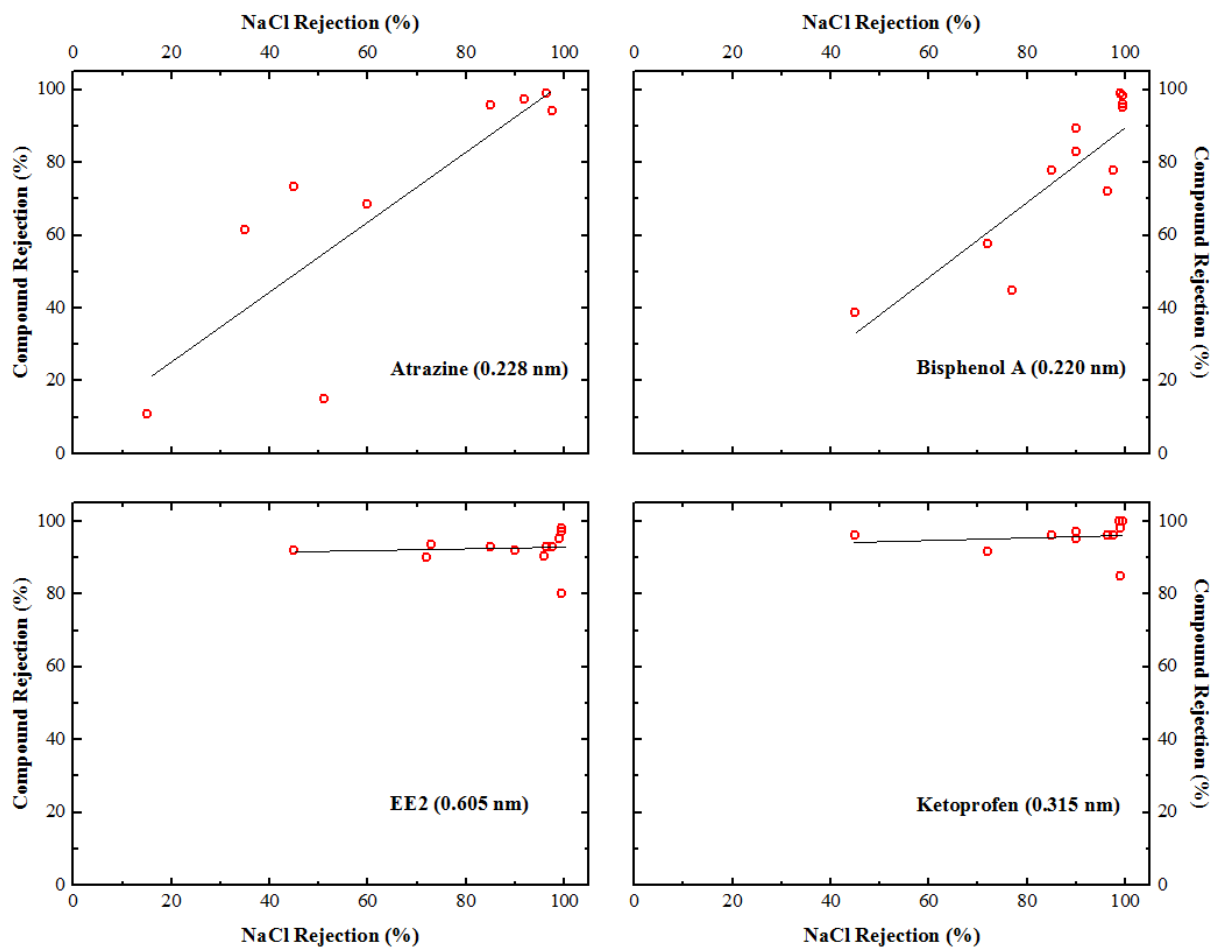


Fig. 10. Relationship between TORC and NaCl rejections for specific TORCs. Examples include TORCs with molecule thickness < 2.5 nm: atrazine and bisphenol A; and thickness > 0.3 nm: EE2 and ketoprofen. Compound thicknesses, as defined in the text, are in parentheses. Similar analyses for other compounds are provided in Fig. S11—S15.

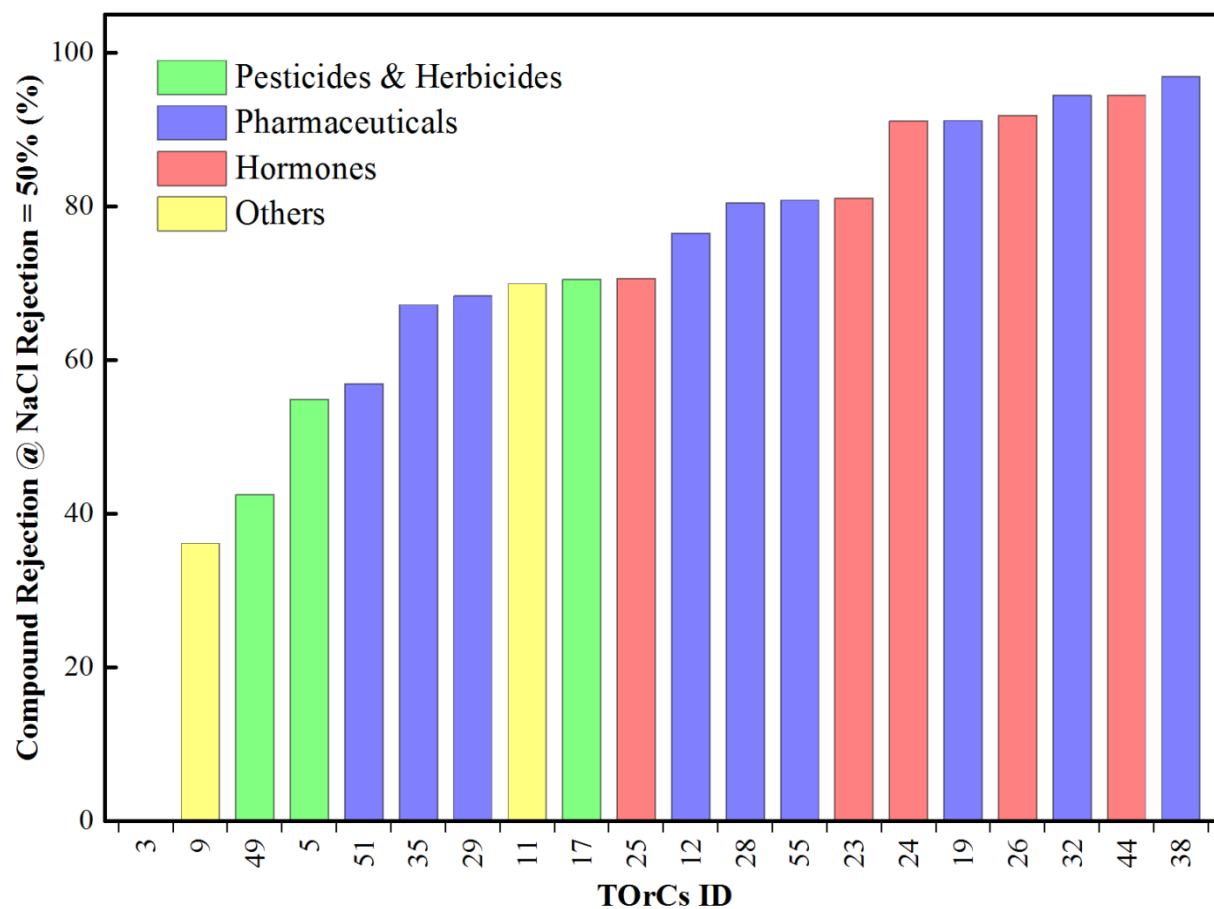


Fig. 11. NF/RO rejections of individual TORCs under conditions that resulted in 50% rejection of NaCl. Compounds analyzed in this fashion were limited to the 20 TORCs for which sufficient data were available (Methods section).

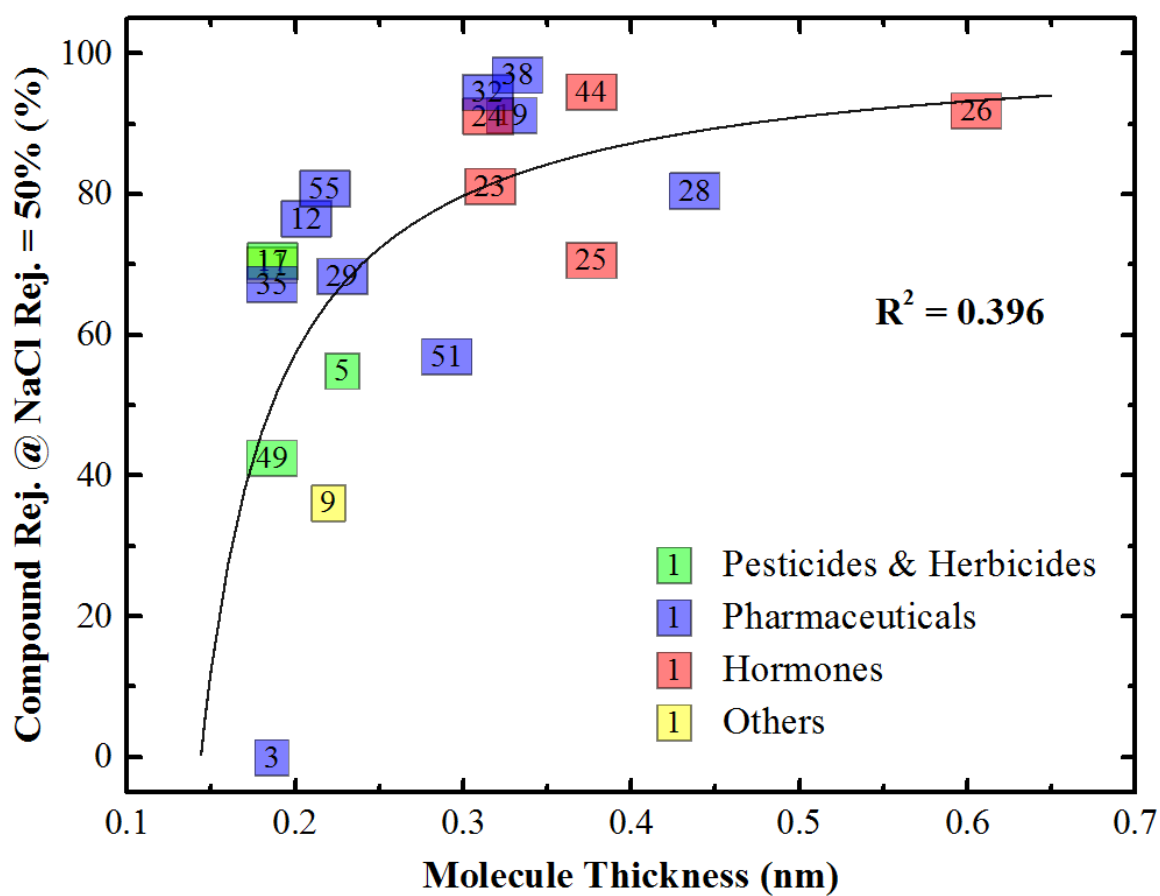


Fig. 12. Compound rejection under conditions for which NaCl rejection = 50% versus molecule thickness.

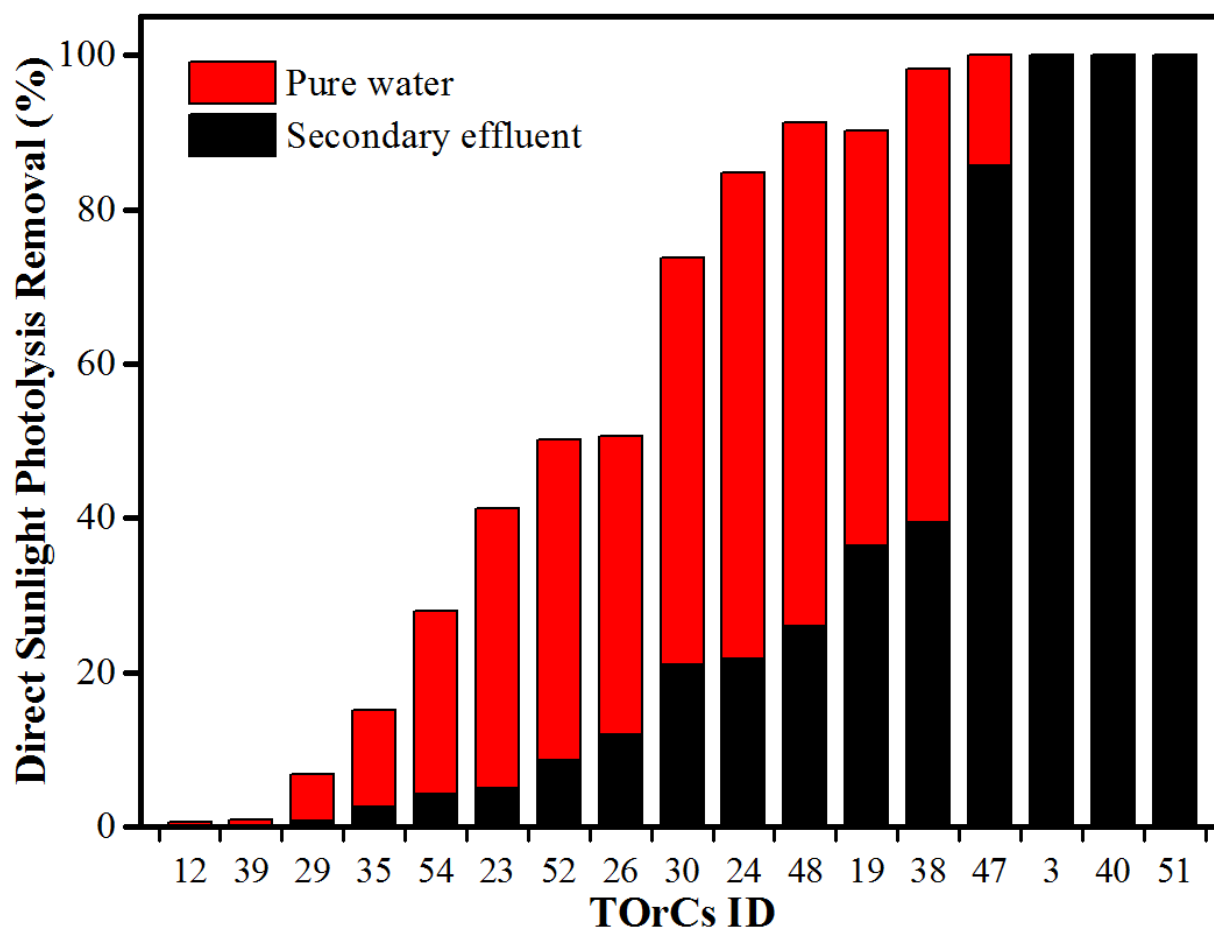


Fig. 13. Predicted removals of 17 TOxCs in pure water and wastewater effluent due to direct photolysis in sunlight. The assumed period of exposure is 8 hours. Other conditions in the simulations were as indicated in the Methods section

REFERENCES

- Andreozzi, R., Marotta, R. & Paxéus, N., 2003. Pharmaceuticals in STP effluents and their solar photodegradation in aquatic environment. *Chemosphere*, 50(10), pp.1319–1330.
- Blough, N. & Zepp, R., 1995. Reactive Oxygen Species in Natural Waters. *Active Oxygen in Chemistry*, 2(0 2), pp.280–333.
- Brillas, E., Sir?os, I. & Oturan, M.A., 2009. Electro-fenton process and related electrochemical technologies based on fenton's reaction chemistry. *Chemical Reviews*, 109(12), pp.6570–6631.
- Canonica, S. et al., 1995. Transformation Kinetics of Phenols in Water: Photosensitization by Dissolved Natural Organic Material and Aromatic Ketones. *Environmental science & technology*, 29(7), pp.1822–1831.
- Crittenden, J.C. et al., 1999. A kinetic model for H₂O₂/UV process in a completely mixed batch reactor. *Water Research*, 33(10), pp.2315–2328.
- Dong, B. et al., 2015. Fate of trace organics in a wastewater effluent dependent stream. *Science of the Total Environment*, 518–519, pp.479–490.
- Fenton, H.J.H., 1894. Oxidation of Tartaric Acid in presence of Iron. *journal of the chemical society, transactions*, pp.899–910.
- Fono, L.J., Kolodziej, E.P. & Sedlak, D.L., 2006. Attenuation of wastewater-derived contaminants in an effluent-dominated river. *Environmental Science and Technology*, 40(23), pp.7257–7262.
- Glaze, W.H., Kang, J.-W. & Chapin, D.H., 1987. The Chemistry of Water Treatment Processes Involving Ozone, Hydrogen Peroxide and Ultraviolet Radiation. *Ozone: Science & Engineering*, 9(4), pp.335–352.
- Glaze, W.H., Lay, Y. & Kang, J.-W., 1995. Advanced Oxidation Processes. A Kinetic Model for the Oxidation Hydrogen Peroxide and U V Radiation. *Industrial & Engineering Chemistry Research*, 37, pp.2314–2323.
- Kruihof, J.C., Kamp, P.C. & Martijn, B.J., 2007. UV/H₂O₂ treatment: A practical solution for organic contaminant control and primary disinfection. *Ozone-Science & Engineering*, 29(4), pp.273–280.
- Lam, M.W., Tantuco, K. & Mabury, S.A., 2003. PhotoFate: A new approach in accounting for the contribution of indirect photolysis of pesticides and pharmaceuticals in surface waters. *Environmental Science and Technology*, 37(5), pp.899–907.
- Länge, R. et al., 2001. Effects of the synthetic estrogen 17 alpha-ethinylestradiol on the life-cycle of the fathead minnow (*Pimephales promelas*). *Environmental toxicology and chemistry*, 20(6), pp.1216–1227.

- Lee, C. & Yoon, J., 2004. Determination of quantum yields for the photolysis of Fe(III)-hydroxo complexes in aqueous solution using a novel kinetic method. *Chemosphere*, 57(10), pp.1449–1458.
- Li, M. et al., 2012. Impact of reflection on the fluence rate distribution in a UV reactor with various inner walls as measured using a micro-fluorescent silica detector. *Water Research*, 46(11), pp.3595–3602.
- Lin, A.Y.-C. & Reinhard, M., 2005. Photodegradation of Common Environmental Pharmaceuticals and Estrogens in River Water. *Environmental Toxicology and Chemistry*, 24(6), p.1303.
- Machulek, A. et al., 2009. Photolysis of ferric ions in the presence of sulfate or chloride ions: implications for the photo-Fenton process. *Photochemical & photobiological sciences : Official journal of the European Photochemistry Association and the European Society for Photobiology*, 8(7), pp.985–991.
- Miège, C. et al., 2009. Fate of pharmaceuticals and personal care products in wastewater treatment plants - Conception of a database and first results. *Environmental Pollution*, 157(5), pp.1721–1726.
- Moreira, F.C. et al., 2016. Tertiary treatment of a municipal wastewater toward pharmaceuticals removal by chemical and electrochemical advanced oxidation processes. *Water Research*, 105, pp.251–263.
- Nadtochenko, V.A. & Kiwi, J., 1998. Photolysis of FeOH₂⁺ and FeCl₂⁺ in Aqueous Solution. Photodissociation Kinetics and Quantum Yields. *Inorganic Chemistry*, 37(20), pp.5233–5238.
- Navntoft, C. et al., 2008. Effectiveness of solar disinfection using batch reactors with non-imaging aluminium reflectors under real conditions: Natural well-water and solar light. *Journal of Photochemistry and Photobiology B: Biology*, 93(3), pp.155–161.
- Oturan, M.A. & Aaron, J.-J., 2014. Advanced Oxidation Processes in Water/Wastewater Treatment: Principles and Applications. A Review. *Critical Reviews in Environmental Science and Technology*, 44(23), pp.2577–2641.
- Rojas, M.R. et al., 2011. Advanced oxidation of trace organics in water by hydrogen peroxide solar photolysis. *Industrial and Engineering Chemistry Research*, 50(22), pp.12479–12487.
- Rojas, M.R. et al., 2010. Modeling of advanced oxidation of trace organic contaminants by hydrogen peroxide photolysis and fentons reaction. *Industrial and Engineering Chemistry Research*, 49(22), pp.11331–11343.
- Song, W., Ravindran, V. & Pirbazari, M., 2008. Process optimization using a kinetic model for the ultraviolet radiation-hydrogen peroxide decomposition of natural and synthetic organic compounds in groundwater. *Chemical Engineering Science*, 63(12), pp.3249–3270.

- Tokumura, M. et al., 2016. Comprehensive study on effects of water matrices on removal of pharmaceuticals by three different kinds of advanced oxidation processes. *Chemosphere*, 159, pp.317–325.
- Wang, Z. & Liu, J., 2014. New insight into photochemical oxidation of Fe(II): The roles of Fe(III) and reactive oxygen species. *Catalysis Today*, 224, pp.244–250.
- Yang, Q., Pehkonen, S.O. & Ray, M.B., 2005. Light distribution model for an annular reactor with a cylindrical reflector. *Industrial and Engineering Chemistry Research*, 44(10), pp.3471–3479.
- Zepp, R. G.; Holgne, J.; Bader, H., 1987. Nitrate-Induced Photooxidation of Trace Organic Chemicals in Water. *Environmental science & technology*, 21(5).
- Zepp, R.G. et al., 1977. Singlet oxygen in natural waters. *Nature*, 267(5610), pp.421–423.